HAL
archives-ouvertes.fr

Multiscale cytometry of 3D cell cultures in microfluidic hydrogel arrays

Raphaël Tomasi

▶ **To cite this version:**

Raphaël Tomasi. Multiscale cytometry of 3D cell cultures in microfluidic hydrogel arrays. Cellular Biology. Université Paris-Saclay, 2016. English. ¡ NNT : 2016SACLX114 ¿.

HAL Id: tel-01496291

https://pastel.archives-ouvertes.fr/tel-01496291

Submitted on 27 Mar 2017

HAL is a multi-disciplinary open access archive for the deposit and dissemination of scientific research documents, whether they are published or not. The documents may come from teaching and research institutions in France or abroad, or from public or private research centers.

L'archive ouverte pluridisciplinaire **HAL**, est destinée au dépôt et à la diffusion de documents scientifiques de niveau recherche, publiés ou non, émanant des établissements d'enseignement et de recherche français ou étrangers, des laboratoires publics ou privés.

NNT : 2016SACLX114

Thèse de doctorat de l'Université Paris-Saclay préparée École Polytechnique

École doctorale n°573
INTERFACES - Approches interdisciplinaires: fondements, applications et innovations
Spécialité de doctorat: Biologie

par

M. Raphaël F.-X. TOMASI

Cytométrie multi-échelle de cultures cellulaires 3D dans des tableaux de billes de gel microfluidiques

Thèse présentée et soutenue à l'École Polytechnique, le 16 décembre 2016.

Composition du Jury :

M. Alexis GAUTREAU	Directeur de recherche	École Polytechnique	Président du jury
M. Matthieu PIEL	Directeur de recherche	Institut Curie	Rapporteur
Mme. Valérie TALY	Directrice de recherche	Université Paris Descartes	Rapportrice
M. Andrew J. DEMELLO	Professeur	ETH Zurich	Examinateur
M. Jean-Philippe STEPHAN	Directeur de département	Servier	Examinateur
M. Charles N. BAROUD	Professeur	École polytechnique	Directeur de thèse

Multiscale cytometry of 3D cell cultures in microfluidic hydrogel droplet arrays

Raphaël F.-X. Tomasi

Remerciements

Une fois ma soutenance passée, le vendredi 16 décembre 2016, je finalise le dépôt du présent manuscrit et je me rends compte du chemin parcouru depuis mon arrivée au LadHyX en février 2013 pour un stage de master. Je tiens à remercier les personnes suivantes, qui ont de près ou de loin contribué à l'aboutissement de ce travail et sans qui cette expérience n'aurait pas été la même.

Charles Baroud, pour la confiance qu'il a placé en moi tout au long de ces 4 années en me donnant ce sujet de master qui a conduit à cette thèse, en me laissant une grande indépendance, en m'envoyant travailler un mois au MIT, en me confiant plusieurs collaborations, en me faisant participer à de nombreuses conférences en France et à l'étranger ou encore en rédigeant ensemble plusieurs brevets. Bien sûr aussi pour tout ce qu'il m'a appris notamment dans la démarche scientifique et le fait d'apporter un point de vue physique et quantitatif dans la biologie. Enfin, pour l'entente que nous avons eu en travaillant ensemble et l'ambiance qui existe dans cette équipe de recherche.

Gabriel Amselem et Sébastien Sart, pour notre collaboration constante. Ce travail est en grande partie aussi le votre. Gabriel, pour avoir initié le projet "CellGel", pour m'avoir appris les bases de l'analyse d'images avec Matlab, pour ses idées et avis toujours pertinents et pour son soutien constant le long de ses années. Sébastien, pour avoir eu la patience de nous apprendre la biologie, pour sa force de conviction et le nombre incalculable d'expériences qu'il a menées pendant ce travail.

Caroline Frot, pour gérer la logistique de l'équipe, pour sa bonne humeur constante et surtout son aide précieuse pour réaliser nos moules microfraisés, toujours urgents et souvent annoncés à la dernière minute.

Tiphaine Champetier, pour avoir eu la patience de faire son stage de master avec moi et pour tout le travail qu'elle a accompli sur la formation de librairies de gouttes qui a été essentiel pour la fin de ma thèse.

Les autres membres l'équipe microfluidique, passés ou présents, pour notre entraide, pour nos discussions scientifiques (ou pas scientifiques), pour instaurer une ambiance de travail idéale qui donne envie de se donner le matin et pour avoir supporté ma musique en microfab pendant de longues heures: Etienne Fradet, Nicolas Taccoen, Morgan Grivel, Cyprien Guermonprez, Elie Abiraad, Micaela Tamara Vitor, Benoit Drogue, Antonie Barizien, Irma Liascukiene, Charles Fosseprez, Adrien Saint-Sardos, Yu-Ting Kao et Mani Sai Suryateja Jammalamadaka.

L'ensemble des membres du LadHyX, pour créer une entité si particulière dont nous sommes fiers d'être membres, pour l'APSaLadHyXa, les séminaires, les BBQs et les quelques verres que nous avons eu le loisir de partager.

Particulièrement, les résidents du bâtiment 65, membres du LMS et de l'équipe d'Abdul Barakat avec qui nous partageons bureaux et espaces expérimentaux, pour apporter leur conseils, leur bonne humeur et pour les soirées que nous avons faites ensemble.

L'ensemble du personnel administratif et technique du laboratoire pour son efficacité en toutes circonstances, nous sauvant la mise bien des fois: Daniel Guy, Toai Vu Do Chi, Antoine Garcia, Sandrine Laguerre, Thérèse Lescuyer, Magali Tutou, Delphine l'Huiller.

Les membres de Stilla et Instent avec qui nous intéragissont régulièrement au labo et qui nous inspirent: Rémi Dangla, Magali Droniou, Jordan Madic, Franz Bozsak, Myline Cottance, Pierluca Messina, Elena Gusarova, Bruno Carreel.

Loïc Tadrist et Lionel Guillou, mes co-bureaux qui ont soutenu leur thèse avant moi, pour tout ce que nous avons partagé ensemble et tout ce qui a rendu cette période agréable.

Matthieu Piel et Valérie Taly, pour avoir accepté d'être examinateurs de ma thèse, pour leur relecture précise et leur commentaires pertinents.

Alexis Gautreau en tant que président de mon jury, Andrew deMello et Jean-Philippe Stephan en tant qu'examinateurs, pour avoir accepté d'être membres de mon jury et pour la qualité des discussions que nous avons eues durant ma soutenance.

Patrick Doyle et Rathi Srinivas pour m'avoir acceuilli un mois au MIT à Boston, ainsi que Sébastien Teychené, Pascale Dupuis-Williams et Laurent Mugherli pour nos collaboration enrichissantes.

Mes amis, de l'ESPCI, du rugby ou de tous horizons pour tout le bon temps passé ensemble et leur soutien tout au long de ma thèse.

Enfin ma famille, et notamment mes parents et mon frère pour leur support constant et leur présence à ma soutenance.

Résumé

Les conditions du corps humain ne sont pas reproduites fidèlement par la culture cellulaire traditionnelle en 2D. Ceci a par exemple des conséquences majeures pour l'industrie pharmaceutique dont les tests en laboratoire ne permettent pas de prédire l'effet réel chez un patient. Ainsi, seulement 10 % des médicaments qui entrent en phase clinique sont finalement acceptés. Il existe néanmoins des modèles 3D *in vitro* qui permettent de mieux reproduire le microenvironnement des cellules *in vitro*. Par exemple, les sphéroïdes sont des boules de cellules adhérentes, qui communiquent entre elles, produisent leur propre matrice extra-cellulaire et ont un phénotype hautement fonctionnel. Le but de cette thèse est d'utiliser les techniques de manipulation de gouttes en microfluidique pour construire une platforme de culture 3D hautement intégrée qui permettent d'effectuer des tests cellulaires réalistes *in vitro* à haut débit.

Dans la première partie de ce manuscrit, les techniques microfluidiques et d'analyse d'images qui ont été mises en oeuvre sont détaillées. D'abord, le contrôle du confinement des gouttes via l'utilisation de rails et de pièges, technologie développée prècédemment au LadHyX, permet de construire efficacement des tableaux de gouttes immobilisées à haute densité. Ensuite, lorsque ces gouttes contiennent des cellules, celles-ci se réorganisent dans chaque piège après immobilisation pour former un unique sphéroïde dont la taille est contrôlée. L'utilisation d'une solution d'agarose, en maintenant mécaniquement le sphéroïde dans son piège après gélification, permet d'allonger le temps de culture et de perfuser le tableau avec des solutions aqueuses, par exemple pour de l'immuno-cyto-chimie. Un sphéroïde en culture dans la puce microfluidique peut alors être sélectivement extrait du tableau sans altérer sa viabilité en faisant fondre la bille d'agarose correspondante grâce à un laser infra-rouge. L'immobilisation des sphéroïdes permet aussi de les imager facilement au cours du temps, en fluorescence ou en lumière blanche. Un code d'analyse d'image a été développé pour détecter chaque piège ainsi que les cellules qu'il contient. Des mesures précises peuvent ainsi être obtenues sur la morphologie et le signal fluorescent, au niveau de la population totale, mais aussi au niveau de chaque sphéroïde et même au niveau des cellules individuelles qui sont détectées au sein des sphéroïdes. Cette technique d'analyse est appelée cytométrie multi-échelle.

La seconde partie de ce manuscrit se concentre sur deux exemples d'applications biologiques de cette plateforme microfluidique. D'abord des sphéroïdes de cellules hépatocytaires sont formés et caractérisés en détail. Les cellules sont encapsulées dans des gouttes de moins de 20 nL, et les sphéroïdes obtenus ont un diamètre moyen de 73 μm et présentent un haut niveau de circularité. Ces cellules ont une viabilité similaire dans les sphéroïdes et en 2D. En 3D dans la puce microfluidique, leur prolifération est réduite et leur production d'albumine est plus grande, ce qui prouve que les sphéroïdes formés se comportent

bien comme des tissus hautement fonctionnels. La corrélation entre le niveau d'albumine intra-cellulaire et la morphologie des sphéroïdes permet de mettre en lumière plusieurs résultats biologiques intéressants, comme la forte production d'albumine pour les sphéroïdes ayant un haut niveau de circularité ou l'augmentation du signal fluorescent d'albumine dans les cellules proches du bord du sphéroïde. Enfin, le contrôle spatial de la perfusion du tableau avec un médicament permet sur une même puce d'étudier différentes conditions d'exposition temporelle à chacun des 3 niveaux d'analyse. Le second type cellulaire utilisé pour valider cette technique microfluidique est la cellule souche mésenchymale humaine. Ces cellules ont un grand potentiel thérapeutique, notamment via la sécreation de nombreux facteurs anti-inflammatoires ou immnuno-modulatoires. Si l'aggrégation de ces cellules a été demontrée comme étant à l'origine d'une augmentation de la production de certains de ces facteurs, les mécanismes moléculaires régulant ce phénomène sont encore incertains. Dans ce travail, nous avons regardé les hétérogéneités spatiales dans l'expression de la caspase-3 (Casp3) et la cyclooxygenase-2 (COX2), deux protéines impliquée dans la sécrétion de la molécule anti-inflammatoire protaglandine E2 (PGE-2), dans des sphéroïdes de 140 μm de diamètre. Un jour après aggrégation, nous observons une activation de Casp3 au centre des sphéroïdes puis, 2 jours plus tard, une propagation de cette activation vers le bord des sphéroïdes. COX2 montre constamment une expression plus intense sur les couches externes des sphéroïdes. D'autres expériences sont requises pour relier ces observations à la production de PGE2.

La troisième partie de ce manuscrit montre comment le design des pièges peut être modifié pour appliquer des conditions différentes dans chacune des gouttes du tableaux. Ces nouveaux pièges permettent notamment d'immobiliser séquentiellement deux gouttes de dimensions différentes qui sont alors en contact et peuvent avoir des contenus différents. Ces gouttes peuvent être coalescées grâce à l'utilisation d'un agent déstabilisant. Une première preuve de concept est obtenue en mélangeant de manière combinatoire des gouttes colorées sur un tableau de piège. Cette technique peut être utilisée pour soumettre des sphéroïdes d'hépatocytes à différentes concentrations d'acétaminophène sur une même puce et ainsi déterminer la limite de toxicité correspondante. Ces pièges peuvent aussi être utilisés pour faire coalescer des gouttes contenant des sphéroïdes de différents types cellulaires afin d'aboutir à la formation de microtissus complexes à l'organisation contrôlée.

Les techniques dévelopées dans cette thèse permettent la culture de sphéroïdes dans des gouttes microfluidiques sur une plateforme hautement intégrée. En effet, la plateforme permet la production des sphéroïdes, leur culture à long terme, leur coloration pour de l'imagerie de fluorescence, le contrôle dynamique et spatial de leur microenvironnement ainsi que la récupération sélective d'un des sphéroïdes du tableau. Grâce au format microfluidique, nous béneficions du contrôle des écoulements, des faibles volumes mis en jeu et du haut débit de production des gouttes. L'analyse d'image détaillée a permis d'extraire des données quantitatives, sur des dizaines de milliers de sphéroïdes individuellement et sur des centaines de milliers de cellules sans devoir séparer les sphéroïdes. Ainsi les paramètres fonctionnels et morphologiques peuvent être corrélés pour mieux comprendre l'influence

de l'organisation tridimensionnelle des cellules sur leur fonctionalité biologique. Ce travail peut mener à des dévelopements importants dans beaucoup de domaines tels que l'analyse de la toxicité des médicaments, le criblage de médicaments à haut débit, le traitement personnalisé du cancer, l'ingénierie tissulaire ou la modélisation de maladies.

Mots clefs: **microfluidique, cellules mammifères adhérentes, culture cellulaire 3D, gouttes d'hydrogel, analysis d'images haut débit, cytométrie, hépatocytes, toxicité des médicaments, cellules souches mésenchymales, ingénierie tissulaire.**

Contents

Introduction

Mammalian cells have been cultured and extensively studied on two dimensional (2D) conditions for decades. Indeed, plastic plates allow easy handling and imaging. Although the Petri dish has allowed researchers to greatly increase the knowledge on molecular cell biology, a flat surface fails to reproduce *in vivo* conditions. This difference was only recognized recently [1] and most of the laboratory equipment still relies on 2D culture.

This has a dramatic impact on drug discovery for the pharmaceutical industry. Indeed, the development of a new drug is a long and expensive process, beginning with performing an *in vitro* screen of a large library of compounds (sometimes hundreds of thousands of molecules) against a target of interest. Then, before entering the clinical stage, the toxicity of potential hits is investigated with *in vitro* and *in vivo* tests. Nevertheless, only 1 in 10 drugs that enter the clinical stage get a final approval [2]. This extremely high failure rate represents a huge waste of resources and indicates that the pre-clinical stage, relying on 2D cell culture, fails to reproduce the conditions of the human body (pharmacodynamics and pharmacokinetics).

In order to create more relevant culture conditions in the laboratory, we first need to recall the impact of the micro-environment on the cellular phenotype. The micro-environment represents all the molecular, mechanical and cellular factors that can regulate the cell behavior. First, the cells of the human body are embedded in a natural hydrogel called the extra-cellular matrix (ECM). The ECM is composed of many different biological molecules, like collagen or proteoglycans, that create a fibrous material on which the cells can adhere via transmembrane proteins called integrins [3]. The ECM also plays a role as reservoir of growth factors and regulate their delivery to cells. Like many transmembrane proteins, integrins are the starting points of mechano-transduction. Consequently, cells are sensitive to mechanical cues. For instance, the substrate stiffness has been demonstrated to play a major role in stem cell differentiation [4]. Cells also sense other types of mechanic forces like compression or to the shear stress of a flow. Finally, the three dimensional (3D) *in vivo* environment favors the interactions between the cells, of similar or different types. These interactions can either be direct through membrane proteins for creating cellular junctions [5] or indirect, for instance, via the secretion of soluble factors that can affect the phenotype of neighboring cells (paracrine interaction) [6].

Several approaches can be used to recapitulate some aspects of the 3D micro-environment *in vitro*. For instance, the ECM can be replaced by an hydrogel [7]. Biological hydrogels like collagen or Matrigel™ [8] are gelated by temperature control and often used for migration assays [9]. Alternatively, synthetic hydrogels can be engineered and provide a high level of flexibility [10] regarding composition and properties. Also, paracrine interactions are classically reproduced by using Transwell inserts in wells that allow to study the communication between two cellular types in close proximity but physically separated by a porous membrane.

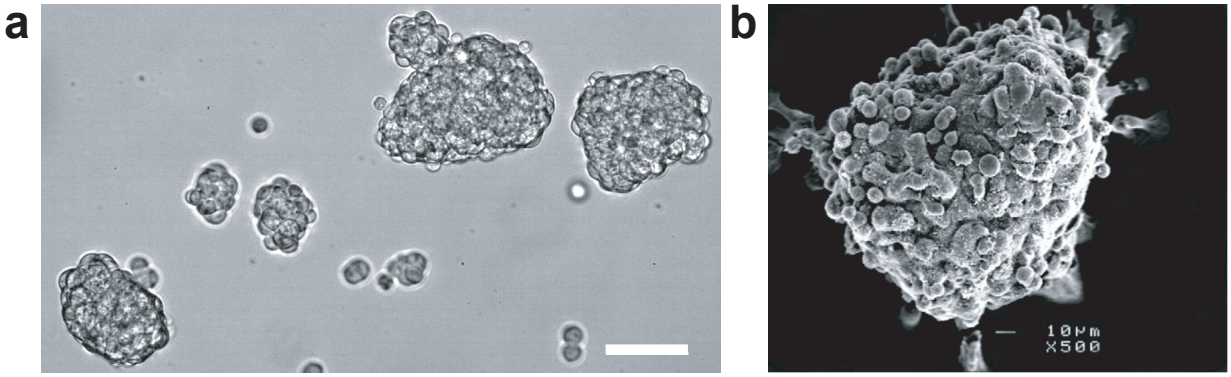

Figure 1: Spheroids. **(a)** Spheroids in suspension. Scale bar is 50 μm. **(3)** Electron micrograph of an hepatocyte spheroid, reproduced from Kelm *et al.* [11]. Scale bar is 10 μm

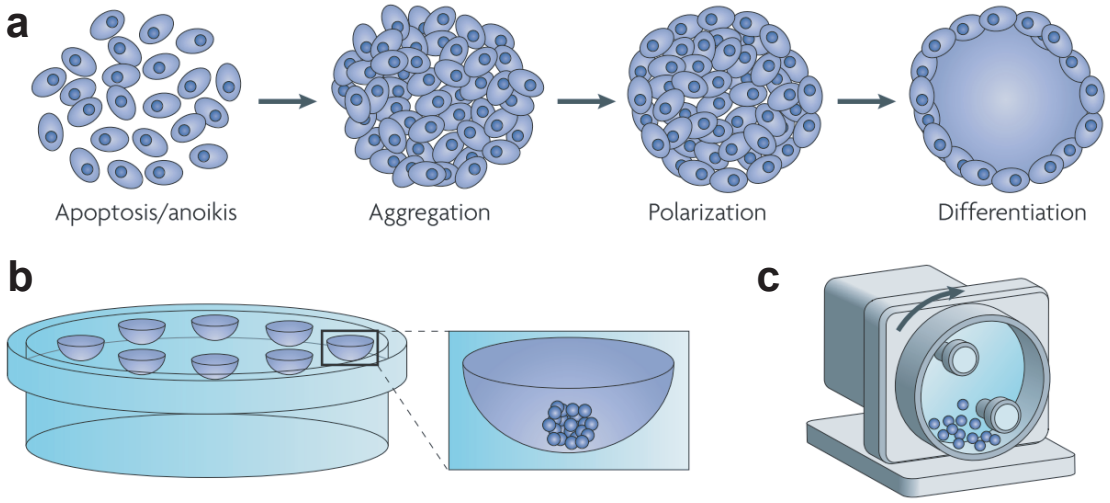

Figure 2: Spheroid formation. **(a)** During aggregation, cells establish reciprocal interactions and reorganize to form a functional microtissue. Spheroids can be produced by hanging drop technique **(b)** or in bioreactors like rotating-wall vessels **(c)** or stirred tanks. Reproduced from Pampaloni *et al.* [12].

The production of spheroids is becoming more and more popular in the scientific community. Spheroids are functional 3D microtissues generated by the aggregation of adherent

cells (see Fig.1 and Fig.2 **(a)**). Cells are able to establish junctions and produce their own ECM, therefore, they can closely mimick *in vivo* conditions [11]. Classically, spheroids are produced by the hanging drop method (Fig.2 **(b)**) which consists in placing a droplet of cell suspension on the top of a Petri dish and flip it over to allow the cells to settle at the bottom of the suspended droplets. Spheroids can also be formed in low attachment plates, agitated bioreactors (Fig.2 **(c)**) or microwells [13].

Thanks to their high biological relevance and ease of production, spheroids can be expected to become soon the gold standard in drug toxicity and screening assays [14, 15, 16]. Nowadays, the 2D format remains the norm in the pharmaceutical industry.

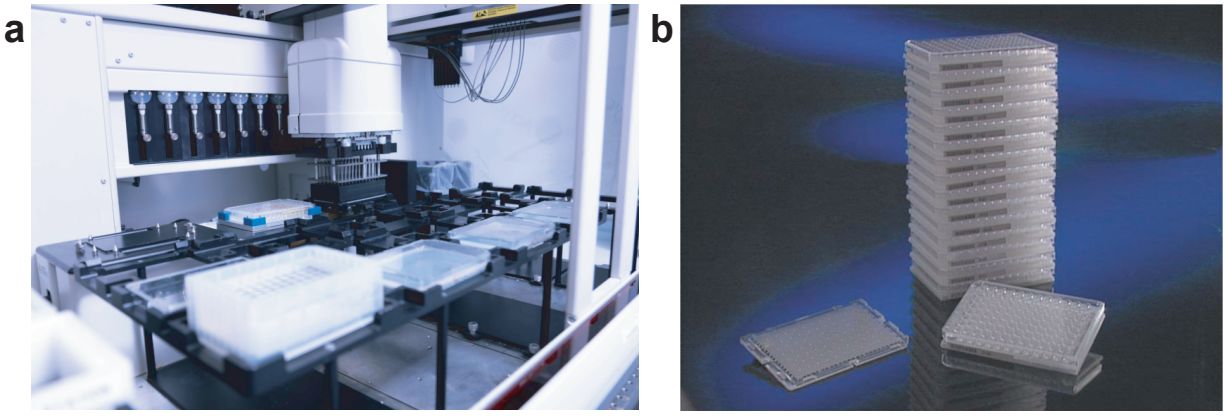

Figure 3: Microtiter plates and screening robots. **(a)** Photograph of a pipetting robot, reproduced from the NewCastle University website (http://research.ncl.ac.uk/bioht/equipment/equipment.html). **(b)** Photograph showing one 1,536 well plate (left) capable of screening as many conditions as a stack of 16 plates with 96 wells, reproduced from Burbaum *et al.* [17].

Drug screening is currently performed on microtiter plates. This format has many advantages. First, microtiter plates are cheap and disposable. Then, the wells are physically separated one from another, allowing the screening of different conditions in a single plate. Finally, the filling of a well or the recovery of its content can be simply done by pipetting. These operations have been automatized by pharmaceutical companies [18] with the development of pipetting robots (see Fig.3 **(a)**) capable of handling many different titerplates. In order to increase the throughput of these operations, the classical 96 well plate format has been extended to 386, 1,536 (see Fig.3 **(b)**) and even 3,456 wells [18] on the same area of 110 cm^2.

Nevertheless, the miniaturization of the microtiter plate format has limits. When increasing the well density, the volume of liquid in each well decreases up to a point where evaporation becomes significant [17] and the recovery of a well content becomes challenging. Therefore, the number of wells per plate rarely exceeds 1,536 and the quest for a higher

throughput has been replaced by the acquisition of more detailed biological data provided by the high-content screening techniques [19].

These limitations are the consequences of the open format of the microtiter plates. Droplet microfluidics provides an interesting alternative to the classical microtiter plates. Indeed, the laminar flows encountered at the microscopic scale allow a precise control of the hydrodynamics that is not possible at larger scale due to the appearance of turbulent flows. For instance, it is very easy to produce highly monodisperse droplets at a very high throughput in a two phase system [20]. These droplets are typically in the nano- or picoliter range and if their content is immiscible with the continuous phase they can be used as separated reactors, similarly to the wells in a microtiter plate.

Droplet microfluidics has two major advantages over traditional 2D formats. First, the production of monodisperse droplets at very high frequencies (typically in the kilohertz range) allows to create millions of separated bioreactors in less than 1 hour. Then, there is a drastic cost reduction associated with the high throughput and extremely low reagent consumption of droplet microfluidics. The expenses can be reduced by a factor of 1.10^6 [21]. These advantages have motivated a strong research effort for reproducing the basic handling operations in the microfluidic format [22], like transport [23], mixing [24], washing [25], sorting [21] or the addition of new reagents [26].

Today, droplet microfluidic is reaching a maturation phase and focuses more and more on applications. In biology, most applications are related to biochemistry [27] or single cell encapsulation and screening [28], for instance for genomic profiling [29]. New applications are also possible thanks to the high throughput capabilities of droplet microfluidics, like the directed evolution of enzymes [21]. In most of these applications, droplet microfluidics is basically used as an improvement over classical flow cytometers and the applications related to the culturing of mammalian cells in microfluidic droplets remains limited [30].

The reasons that prevented droplet microfluidics from extending to long-term adherent cell culture are threefold. First, the droplet observation over long times scales is challenging. Indeed, droplets can evaporate through the external oil [31]. They are also simply difficult to image and track if not immobilized. Second, the nutrient availability in a confined volume is low. Third, most of the mammalian cells are adherent and need to adhere to a substrate in order to survive and to avoid anoikis.

In order to overcome the nutrient availability issue, Yu *et al.* [32] proposed to encapsulate cells in alginate beads, as shown in Fig.4 **(a)**. The encapsulation was performed in oil inside a first microfluidic chip. The beads were then collected off chip and dispersed in aqueous medium. Finally, the beads were injected into a second microfluidic chip for their immobilization and for cell culture (see Fig.4 **(b)**). The porous alginate matrix allows the diffusion of fresh nutrients to the cells and, as a result, enables culture for several days.

Nevertheless, the alginate is an hydrogel which cannot be digested by cells and on which

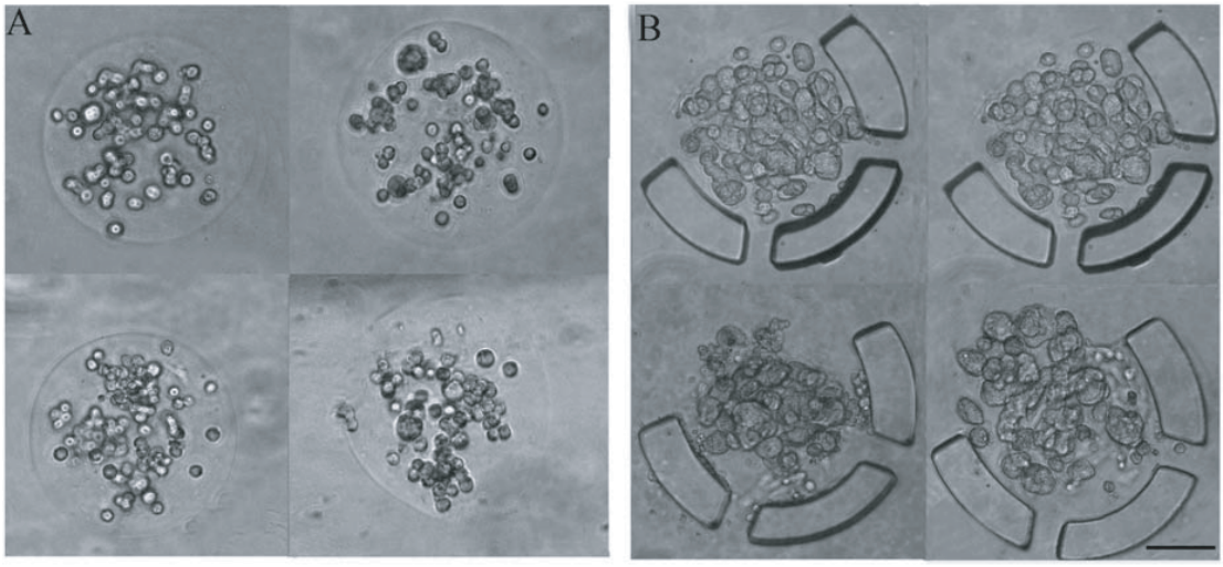

Figure 4: Encapsulation of cells in alginate beads. Images of cells in alginate beads right after encapsulation **(a)** and after 4 days of culture following the immobilization of the beads in microfluidic hydrodynamic traps **(b)**. Reproduced from Yu *et al.* [32]. Scale bar is 100 μm.

they cannot adhere, as a result, the cells shown in Fig.4 are isolated from one another and cannot reorganize properly to create a functional spheroid. These cells maintained a high viability for extended culture periods because of their high degree of tumorigenicity that allow them to grow without proper adherence.

Forming or encapsulating spheroids into microfluidic droplets is an interesting approach for solving anoikis. Indeed, the cells inside a spheroid can adhere one to another and create their own ECM on which they can adhere. At the beginning of my PhD in September 2013, the examples of production of spheroids in microfluidic hydrogel droplets were scarce [33, 34]. Alternatively, they were some example of spheroid production in single phase microfluidic systems [35, 36]. Since then, the bibliography on the subject has become more abundant, we will quickly discuss it in the conclusion of the first part of this manuscript.

Another approach for the high-throughput and reliable production of size controlled spheroids is the adaptation of microtiter plates, either for low adhesion microwells [37] (Fig.5 **(a)**) or parallelized hanging drops [38] (Fig.5 **(b)**). This has already led to the commercialization of several products as the gravityPLUS^{TM} Hanging drop system (InSphero), the Perfecta3D® Hanging drop plate (3D Biomatrix) or the AggreWell^{TM} plate (STEMCELL technologies). These formats are easy to handle and compatible with pippeting robots but not with perfusion experiments. In addition, the hanging drop plates still suffer from a low density, leading to low integration and high consumption of costly

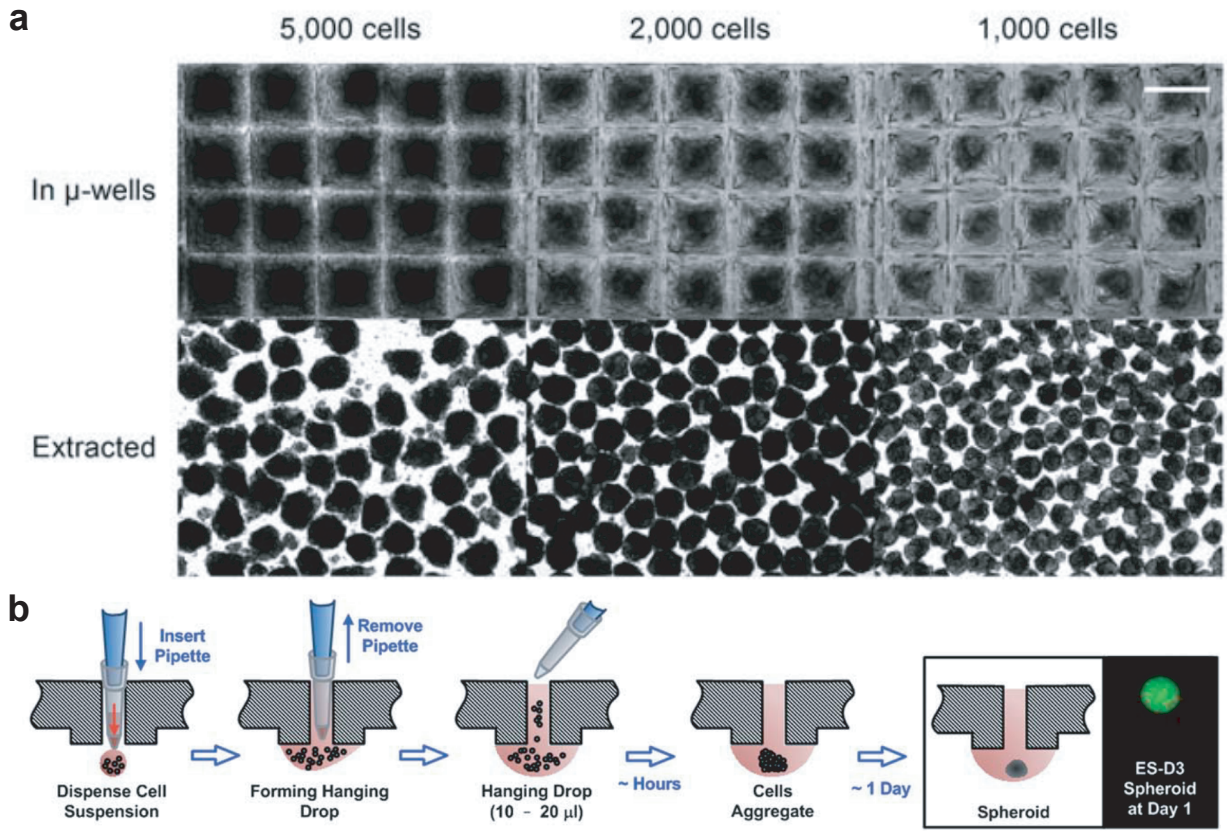

Figure 5: Adaptation of the microtiter plate to 3D cell culture. **(a)** Formation of human embryoid bodies in poly(dimethylsiloxane) (PDMS) microwells at various cellular concentrations. Reproduced from Ungrin *et al.* [37]. Scale bar is 400 μm. **(b)** Schematic protocol for the formation of spheroids in hanging drop plates. Reproduced from Tung *et al.* [38].

reagents such as fluorescent antibodies. Indeed, the density of a 384 well plate is almost 5 wells/cm^2, one, if not two, orders of magnitude below what is possible with the microfluidic format. Although the low adhesion microwells can achieve high density formation of monodisperse spheroids they do not support selective extraction.

In this PhD work, we aim at adapting droplet microfluidics to 3D cell culture in order to form and analyze biologically relevant microtissues in a high-density and controled manner. In part I, we explain how we overcome the issues raised by the encapsulation of adherent cells into microfluidic droplets. First, we use the droplet manipulation techniques previously developed in the group [23] to create static droplets array, allowing easy manipulation and observation. Then, we adapt this protocol for the *in situ* formation and detailed analysis of spheroids in hydrogel droplets. In part II, we present the results of two biological studies performed with our microfluidic platform, using successively hepatocytes and human mesenchymal stem cells s. In part III, we enhance the droplet manipulation techniques to be able to apply many different conditions in the droplets of a single chip.

Part I

Droplet microfluidic as a tool for 3D cell culture and image analysis

In this first part, we detail the technical tools that have been developed in my PhD work to create and analyze 3D cell cultures in microfluidic droplets.

Chapter 1 is dedicated to creation of microfluidic high-density droplet arrays. We will first come back to the main physical principles of droplet microfluidics by introducing surface tension and surfactant stabilization. We will also review the droplet manipulation techniques that have been previously discovered and optimized in the LadHyX laboratory, notably with the PhD work of Rémi Dangla and Étienne Fradet. Then, we will discuss the design of a microfluidic chip integrating gradients of confinement to create high-density droplet arrays. The droplet production and the optimization of the array filling will be successively highlighted.

Chapter 2 will shed light on the specific protocol allowing spheroid formation and culture in a high-density droplet array. We will first see how the encapsulation of multiple single cells can lead to the formation of monodisperse spheroids. Then, we will explain why the use of agarose hydrogel droplets plays a major role in performing long-term culture of these microtissues. In addition, we will discuss the ability to perform immuno-staining as well as the controlled stimulation and recovery of the spheroids in the droplet array.

Finally, chapter 3 is focused on the image analysis that allows us to extract quantitative data from the experiments in a detailed and high-throughput manner. First, the concept of multiscale cytometry will be introduced and the image acquisition protocols will be discussed. Then, we will detail the detection protocol and explain how we ensure to select real spheroids from all the detected objects. Moreover, there will be an emphasis on the extraction of data from single cells inside the spheroids.

Chapter 1

A microfluidic chip for creating high-density droplet arrays

1.1 Guiding microfluidic droplets in large 2D chambers: rails and anchors

1.1.1 Surface tension and droplet stability

Droplet microfluidics can be a very useful tool for biological reactions. However, creating and manipulating small droplets constitutes an important challenge. Indeed, emulsions are highly metastable. It means that a system of two immiscible fluids is not at the thermodynamic equilibrium when separated into a dispersed and a continuous phase. So where does the instability of an emulsion come from ?

In a liquid phase, molecules can interact and share energy with their neighbors. This interaction is optimized when the molecules are identical. At the interface of a droplet, the molecules of the dispersed phase have direct neighbors from the continuous phase and thus, their interactions are not optimized to minimize their energy. It results in a surface energy γ called surface tension, expressing the energetic cost of a particular interface. This cost is payed when the emulsion is created, for instance by the work of a vigorous mixing of the two phase system (that is what happens when mixing the oil and vinegar to prepare a salad dressing).

A newly created emulsion tends to come back to its equilibrium state by droplet coalescence. Indeed, when two droplets merge they reduce their surface by ΔS and consequently save an energy equaled to $\gamma \Delta S$. Thankfully, the thermodynamic evolution of an emulsion can be kinetically stopped via the addition of surfactants. Surfactants are amphilic

molecules that adsorb to liquid-liquid interfaces. In the present work, we create aqueous droplets in fluorinated oil thanks to a commercialy available PEG-di-Krytox™ surfactant (Fig.1.1). This molecule has an hydrophilic head and a fluorophilic tail and it is directly diluted into the fluorinated oil. It adsorbs at the water/oil interface with the hydrophilic head pointing at the aqueous phase and the fluorophilic tails in the external oil. At this stage, it is worth noting that the surfactants that we use in this work have been specifically designed for biological applications since they prevent biomolecule adsorption at the interface as well as cellular adhesion [39].

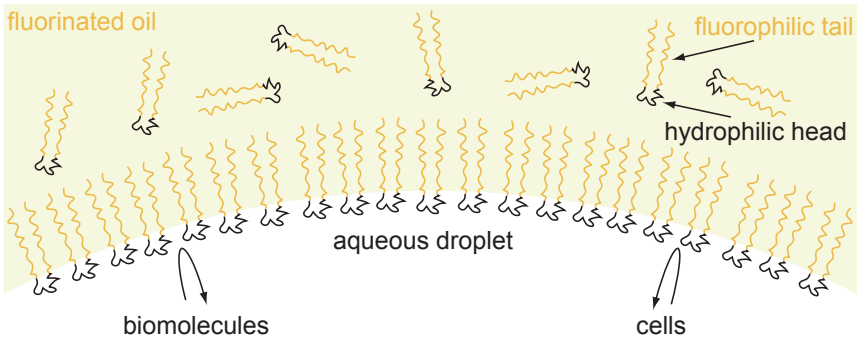

Figure 1.1: Surfactants. Schematic view of the surfactant adsorption at the interface of an aqueous droplet in fluorinated oil.

Once adsorbed, they bring two main stabilizing properties to the emulsion. First, the value of the surface tension γ is decreased, reducing the cost of the interface creation and thus, facilitating the droplet formation. Second, they induce Marangoni stresses that help preventing the coalescence [40].

Therefore, even if emulsions are thermodynamically unstable, their evolution can be kinetically stopped by the addition of surfactants that adsorb at the interfaces and prevent droplet coalescence. With the dramatic increase of the contact surface between the two immiscible phases, the surface tension plays a major role in emulsions. In the following subsection, we show how surface tension can be used to efficiently guide droplets in microfluidic chambers.

1.1.2 Gradients of confinements

A small droplet sitting on a non-wetting plate minimizes its energy by adopting a spherical shape. If this droplet is squeezed between two non-wetting parallel plates, it will adopt a pancake shape. The work of the squeezing force balances the increase in surface energy. That is what happens in our microfluidic chips: we create droplets squeezed between the top and bottom walls and, consequently, they have a high surface energy. Any opportunity to relax to a more spherical shape will be favorable as the surface energy will be reduced. If there

is a hole etched in the chamber floor or ceiling, the droplet will decrease its confinement by entering the hole cavity, therefore reducing its surface energy. Exiting the hole would mean to increase again its surface energy by going back to a pancake shape. Thus, the droplet is experiencing a gradient of confinement that results in a trapping force maintaining the droplet in place against an external flow. These holes are called anchors [41] and are characterized by their diameter and depth (Fig.1.2 **(a)**).

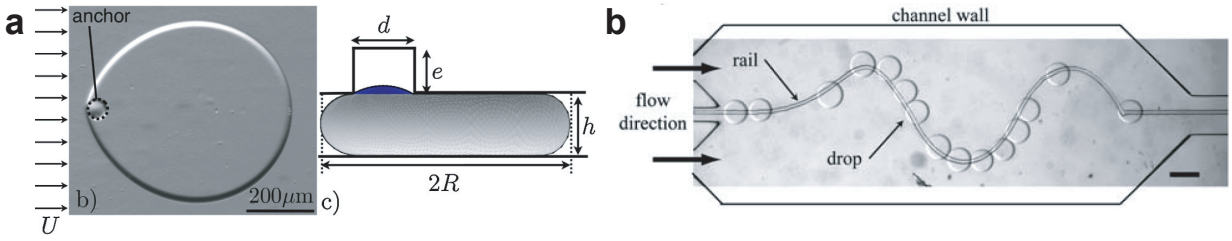

Figure 1.2: Anchors and rails. **(a)** Top and side view of a large droplet immobilized on a small anchor (reproduced from Dangla *et al.* [41]). **(b)** Top view of droplets guided by a rail in a large 2D chamber (reproduced from Abbyad *et al.* [23]).

The same principle can be applied with a groove instead of a hole. The droplet is submitted to a gradient of confinement when it enters the groove. If there is an external flow the droplet remains on the groove but can, depending on the flow direction, slide accross its length as it keeps the surface energy reduction constant. These grooves are called rails [23] (Fig.1.2 **(b)**) and they can have various shapes to guide droplets along the chamber width.

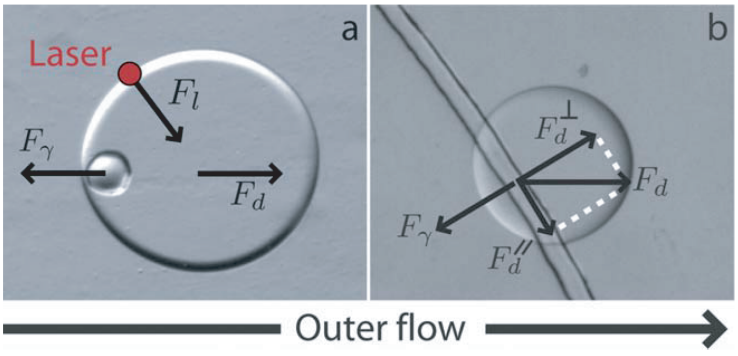

Figure 1.3: Force balance on trapped droplets. The visquous drag F_d can be balanced by the trapping force F_γ exerted by an anchor **(a)** or a rail **(b)** on a confined droplet. An infra-red laser spot (red dot) can change this balance by applying a repealing force F_l (reproduced from Fradet *et al.* [42]).

Investigating the forces that apply on a droplet submitted to a gradient of confinement provides a more detailed picture of the situation (Fig.1.3). First, while there is an external oil flow, the droplet is submitted to a visquous drag F_d. It has the same direction than

the flow and its magnitude scales like $\mu U \frac{R^2}{h}$, where μ is the oil viscosity, U is the mean oil velocity, R is the apparent radius of the droplet and h is the chamber height. For parallel top and bottom walls without surface patterning, this is the force responsible for the droplet movement. Therefore, trapping a droplet can only be achieved if F_d is balanced by another force.

Fig.1.3 **(a)** shows the case of a droplet immmobilized on an anchor. As previously described, the entrance of the droplet into the anchor cavity results in the reduction of its surface energy. Overcoming this energy reduction requires a force F_γ^{max}, that scales like $\frac{\gamma \Delta S}{d}$ [41], where γ is the surface tension, ΔS is the surface reduction and d is the characteristic length scale over which the energy surface changes. Therefore, as long as $F_d \leq F_\gamma^{max}$, the anchor applies a force F_γ opposed to the flow direction and of equal magnitude than F_d. In this case, the droplet is immobilized by the anchor against the outer flow. A larger droplet or an increased oil flowrate would create a higher drag force that could overcome F_γ^{max}. In this case, the droplet would not be trapped by the anchor.

In the case of a rail (Fig.1.3 **(b)**), the trapping force F_γ is perpendicular to the rail direction, thus, only the perpendicular component $F_d^{\perp}$ of the drag can be balanced and the other component ($F_d^{\parallel}$) can drive the droplet along the rail.

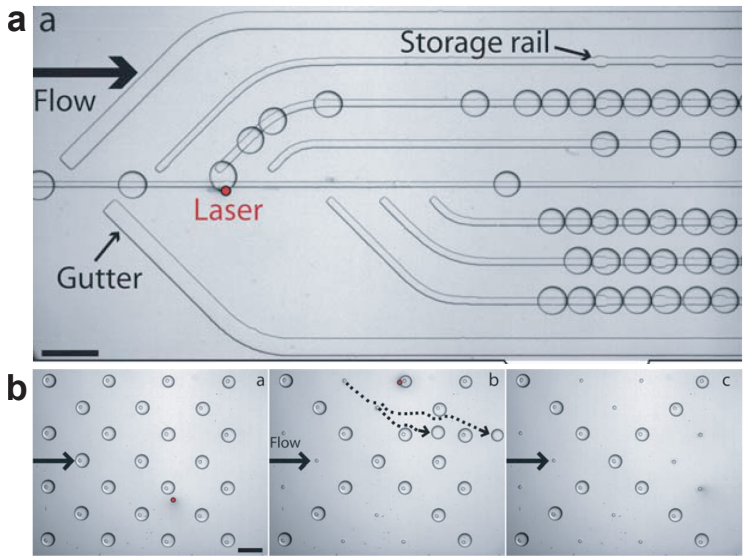

Figure 1.4: Combining laser forcing and confinement gradients. **(a)** Image of the selective filling of a rail. Scale bar is 600 μm.**(b)** Time lapse images showing the selective detrapping of droplets in an anchor array submitted to an external oil flow. The dashed lines represent 2 droplet trajectories. Scale bar is 400 μm. All images reproduced from Fradet *et al.* [42].

An interesting additional feature is the use of an infra-red laser capable of applying a force on the droplet on demand [43] (Fig.1.2 **(c)**, left). The laser induces a change in the surfactant concentration at the interface which, via Marangoni stress, results in a force F_l

(FIG.1.3 **(a)**) driving the droplet away from the laser spot. If the drag force F_d is sufficiently high or the maximum trapping force F_γ^{max} sufficiently low, the capilary trapping can be overcome. This feature can be used to selectively fill the rows of an array by forcing a rail change (FIG.1.4 **(d)**) or selectively remove a droplet from a trap (FIG.1.4 **(e)**).

Rails and anchors are easy to create using classical microfabrication techniques (see appendix A.1) and provide passive control of confined droplets in large Hele-Shaw chambers (with a height much smaller than the chamber width). The magnitude of the trapping force is determined by the pattern geometry. In the following subsection, we discuss in detail the parameters controlling the trapping efficiency of anchors.

1.1.3 Anchor dimensions and trapping efficiency

By entering an anchor, a confined droplet decreases its surface energy. The magnitude of the trapping force exerted by the anchor depends on the efficiency of the surface reduction. A droplet that only enters slightly an anchor will experience a low trapping force.

FIG.1.5 **(a)** defines the geometrical parameters of the problem: h is the chamber height, d and Δh are respectively the anchor diameter and depth, R is the apparent droplet radius from a top view, δh is the entrance height of the droplet in the anchor cavity. While $\delta h \leq \Delta h$, the portion of the droplet inside the anchor cavity is a spherical cap with a free radius of curvature r. This radius of curvature reaches its minimum value r_{min} when the anchor depth Δh is larger than $\frac{d}{2}$. In this case, $r_{min} = \frac{d}{2}$ (see FIG.1.5 **(b)**). The case where the droplet enters the anchor cavity with $r < r_{min}$ without touching the anchor walls is unphysical.

To understand to what extend a droplet enters the anchor cavity, v we need to discuss the curvature equilibrium of a trapped droplet. Laplace's relation gives us:

$$P_{int} - P_{ext} = \gamma \mathscr{C} \tag{1.1.1}$$

with P_{int} and P_{ext} the pressures inside and outside the droplet, γ the surface tension of the water/oil interface and $\mathscr{C}$ its curvature. It means that the curvature of the interface of the droplet indicates the pressure difference between the interior and exterior.

In order to have a trapped droplet in its equilibrium state, the pressure must be identical in every part of the droplet. Nevertheless, we can separate a droplet trapped in an anchor into two different parts whose curvature is governed by independent geometric parameters. First, in the chamber, the radius of curvature between the top and bottom wall is $\frac{h}{2}$. In the other direction, the radius of curvature is governed by the droplet size and, by neglecting the radius change in height, it is equal to R. Consequently, the curvature of the droplet in the chamber is $\frac{1}{R} + \frac{2}{h}$. Second, there is a curvature in the anchor cavity. In the case of FIG.1.5 **(a)**, the spherical cap has a radius of curvature r and thus a curvature $\frac{2}{r}$. If the two

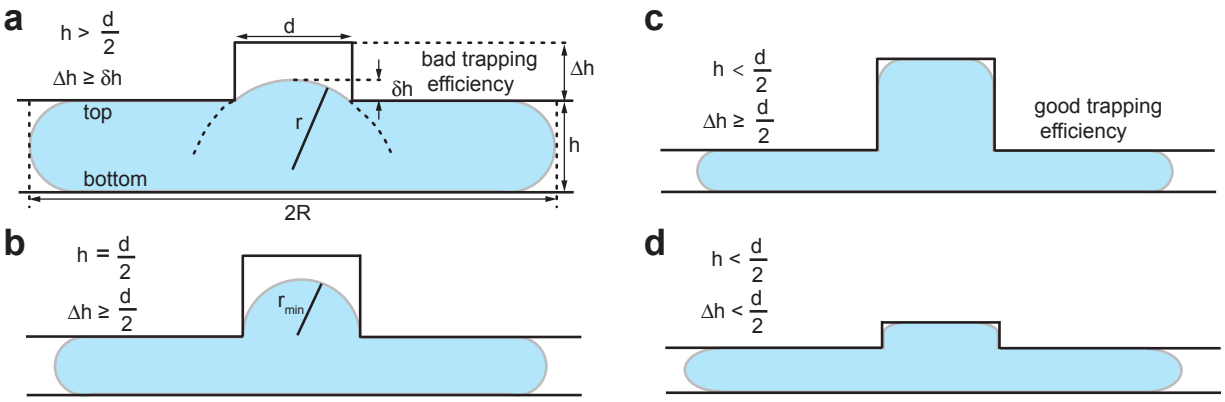

Figure 1.5: Trapping efficiency. Side view of droplets anchored with different geometrical parameters. **(a)** Definition of the geometrical parameters in the case of a bad trapping efficiency. **(b)** Maximum entrance that can be achieved with the equilibrium of the equation 1.1.3. **(c)** Maximum trapping efficiency with a droplet fully entering a deep anchor. **(d)** Intermediate trapping efficiency in a low depth anchor.

parts of the droplet have different curvatures and if we assume a constant pressure P_{ext} outside the droplet, the pressure inside the droplet should not be constant. Thus, at the equilibrium state, these the curvatures in the chamber and inside the anchor cavity must have the same value and the equilibrium condition is:

$$\text{equilibrium} \iff \begin{cases} \dfrac{1}{R} + \dfrac{2}{h} = \dfrac{2}{r} \\ \\ r \geq \dfrac{d}{2} \end{cases} \tag{1.1.2}$$

This relation is valid as long as the droplet enters the anchors cavity with a free interface *i.e.* as long as the anchor depth Δh is higher than the entrance of the drop δh.

In the case of large droplets ($R \gg h$), the equilibrium condition in (1.1.2) simplifies greatly:

$$\text{equilibrium with } R \gg h \iff \begin{cases} h = r \\ r \geq \dfrac{d}{2} \end{cases} \tag{1.1.3}$$

Consequently, the height of the chamber h defines the radius of the free spherical cap in the anchor cavity. In the case where h is large ($h > \frac{d}{2}$, see Fig.1.5 **(a)**), the droplet only enters slightly into the anchor cavity resulting in a bad trapping efficiency. If h becomes smaller, the droplet entrance increases resulting in a higher trapping efficiency, until the limit case where $h = \frac{d}{2}$ (Fig.1.5 **(b)**).

At this point, nothing prevents to design a chip with an even smaller chamber height ($h < \frac{d}{2}$). In this case, the pressure drop induced by the curvature of the pancake droplet

in the chamber cannot be balanced by the the free curvature created at the entrance in the anchor cavity (which has a maximum value of $\frac{2}{r_{min}} = \frac{4}{d}$). Therefore, the droplet enters completely into the anchor cavity and will balance the extra pressure by pushing against the anchor walls (Fig.1.5 **(c)**). It creates a very high trapping efficiency since the droplet would need to deform to a large extend to exit the anchor. This trapping efficiency is further controlled by the depth of the anchor Δh. Indeed, even in the case of a complete entrance in the anchor cavity, if the anchor depth is low (typically $\Delta h < \frac{d}{2}$) the droplet does not need to deform much to escape the anchor (Fig.1.5 **(d)**).

In summary, a high trapping efficiency can be achieved for a chamber height smaller than the anchor radius and a large anchor depth:

$$\text{high trapping efficiency for } R \gg h \iff \begin{cases} h > \dfrac{d}{2} \\ \\ \Delta h \gtrsim \dfrac{d}{2} \end{cases} \tag{1.1.4}$$

Without assuming anything about the droplet radius and without neglecting the radius change accros the height of the chamber, the exact curvature of the pancake is $\frac{\pi}{4}\frac{1}{R} + \frac{2}{h}$ [41] and the condition for high trapping efficiency becomes:

$$\text{high trapping efficiency} \iff \begin{cases} h > \dfrac{d}{2 - \dfrac{\pi d}{8R}} \\ \\ \Delta h \gtrsim \dfrac{d}{2} \end{cases} \tag{1.1.5}$$

The condition (1.1.5) is even less stringent than the condition (1.1.4) for large droplets because we had neglected the curvature of the pancake in the chamber plane, adding an extra pressure and thus helping the droplet to enter the anchor cavity.

In the following work, we use the condition (1.1.4) for designing high efficiency anchors.

1.2 Experimental setup and design of the microfluidic chip

The microfluidic chips that are used in this work are made of PDMS on glass slides, as discussed in appendix A.1. Fig.1.6 shows an image of a typical experimental setup. The microfluidic chip is placed on an inverted microscope and each inlet is connected to a

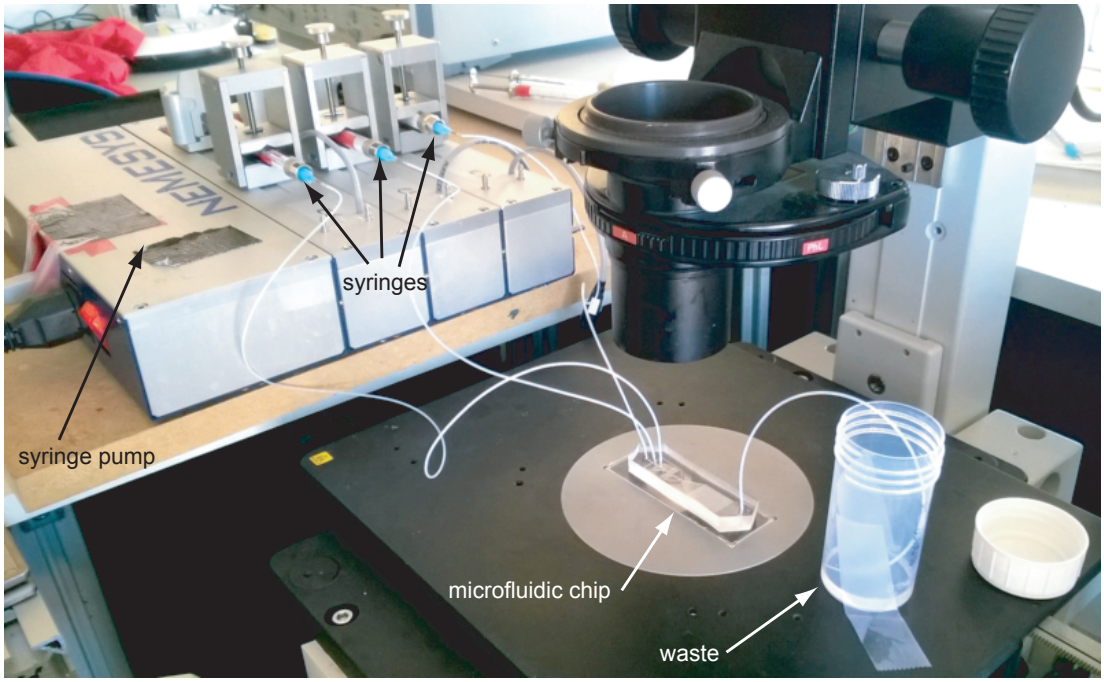

Figure 1.6: Experimental setup. Photograph of a typical experimental setup.

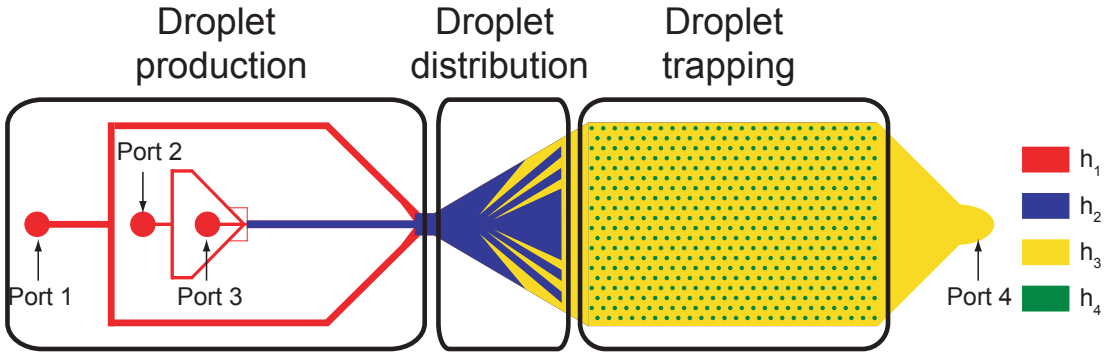

Figure 1.7: General principles of the chip design. h_1, h_2, h_3 and h_4 represent four different heights in the increasing order. The ports are areas where a hole is created in the PDMS chip for fluidic connexions.

syringe. The syringes are actuated with a programmable syringe pump providing a constant flowrate for each solution. The outlet of the chip is connected to a waste container.

The design of the microfluidic chips used in this thesis follows some general principles represented in Fig.1.7. First, every chip has different heights since the control of the droplet confinement will allow to guide and trap the droplets. Then, there are 4 different fluidic ports that allow fluidic connections between the microfluidic chip and the syringes or the waste container. Each of them can be used as an inlet or an outlet. Also, every chip is

divided into 3 stages that have different roles. First, a droplet production stage allows to create monodisperse microfluidic droplets. 3 ports and the jonction where the droplets are produced are located in this area. Most of the time, there are one aqueous and two oil syringes connected to the ports during the droplet production: one oil syringe controlling the oil flowrate at the junction and the other one controlling the oil flowrate at the entrance of the chamber. This stage will be discussed in section 1.3. Alternatively, the droplet production can be performed off chip and in this case a pre-formed emulsion can be directly injected into the chamber (see chapter 6). Second, there is a droplet distribution stage, where are located rails that disperse the droplets homogeneously across the chamber width. Third, the main chamber constitutes the droplet trapping area where are located the anchors. In our microfluidic chips it has a 2 cm^2 area (1.2 cm x 1.7 cm). The distribution and trapping stages will be discussed in section 1.4. Finally, there is at least one port after the trapping chamber that can be either used as an inlet or an outlet, depending on the protocol.

1.3 Droplet production

1.3.1 Combination of flow-focusing and step emulsification

Many techniques are available to produce monodisperse microfluidic droplets [20, 44]. One of the most commonly used is the flow focusing junction (Fig.1.8 **(a)**). In this case, the dispersed phase is injected at the center of the junction and two channels bring the continuous phase flow in opposite sides in order to regularly pinch the dispersed phase. The size of the produced droplets depends on the balance between the viscous drag and capillary forces and thus relies heavily on the flowrate values. The droplet breaking can be helped by adding a small restriction right after the junction (width w in Fig.1.8 **(a)**). When properly optimized, the advantages of this type of junction are twofolds: it is capable of producing highly monodisperse droplets at very high throughput (typically in the kHz range) and the droplet size is easily tunable over a wide range without changing the geometry. Two drawbacks of this type of junction are that even a slight change in the flowrates can affect significantly the droplet size and there is a transition time before reaching the steady state, during which the droplet size is not controlled.

Droplets can also be produced by step emulsification (Fig.1.8 **(b)**). Usually, the dispersed phase is injected at constant flowrate in a chamber where the continuous phase can be stationnary. The droplet breaking mecanism comes from a sharp increase of the channel height that changes the curvature balance in the aqueous thread [45]. The monodispersity of the produced droplets is also very high and their size is mostly determined by the ratio between the height of the step Δh and the height of the injector h and also, but to a smaller extent, by the injection flowrate. Increasing $\frac{\Delta h}{h}$ results in the production of smaller

droplets.

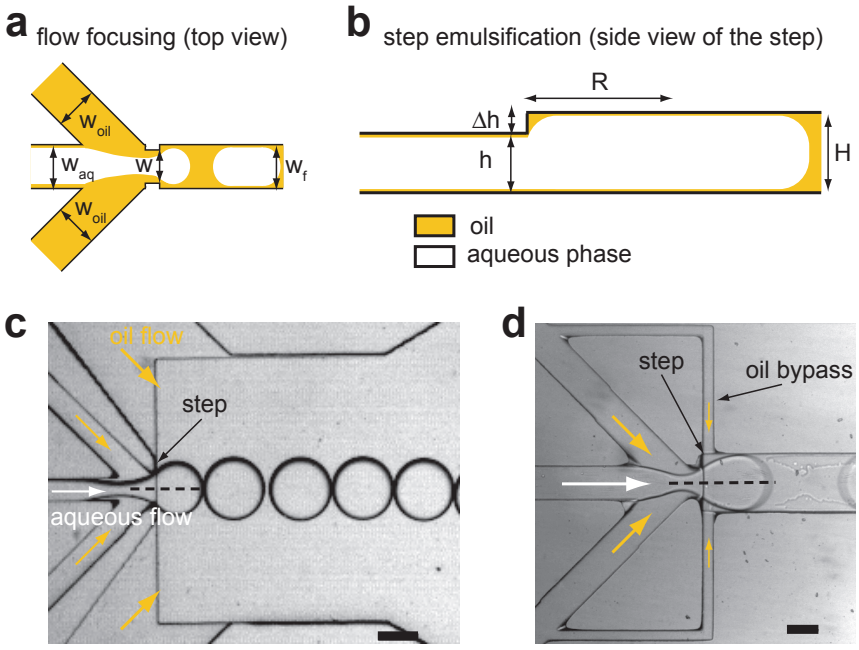

Figure 1.8: Combining flow focusing and step emulsification **(a)** Schematic top view of a flow focusing junction. **(b)** Schematic side view of a step emulsification droplet production.**(c-d)** Junctions combining flow focusing and step emulsification techniques, without **(c)** and with **(d)** oil bypasses. The black dashed lines represent the location of the section schematically represented in **(b)**.

In this work, we chose to add a step right at the droplet breakup location of a flow focusing junction [46] (Fig.1.8 **(c)**). This combines advantages from the two techniques. First, the passive breaking induced by the step increases the reproductibility of the droplet production (even in the case of a high viscosity dispersed phase) and suppresses any observable transition time. Then, the active control of the continuous phase flowrate allows to keep a high versatility on the droplet size. In most of our junctions, the width of the aqueous and oil inlets was 200 μm and the short restriction following the junction was set to 150 μm. Then, the height of the step determines the range of droplet size that can be produced.

We also found that adding two bypass channels between each oil channel reaching the droplet producing junction and the droplet breakup area can be useful (Fig.1.8 **(d)**). The width of these bypasses controls which proportion of the oil flowrate goes into the junction and into the bypasses. They help the droplet breaking by increasing the overall oil flowrate right at the step location but their main advantage is that they ensure that the produced droplets are well separated in the emulsification channel that we discuss in the next subsection.

1.3.2 Droplet stability and emulsification channel

We know from subsection 1.1.1 that surfactants help stabilizing droplets by preventing coalescence but the kinetics of the surfactant adsorption at the interface also needs to be taken into account [47]. Indeed, in case of high-throughput production, low surfactant concentration or large droplet surface, the characteristic time of absorption can become significant. If two droplets enter in contact before their surface is sufficiently covered by surfactant molecules they will probably coalesce. To overcome this issue, Baret *et al.* [47] suggest to add a channel whose width w is smaller than the droplet diameter between the droplet production and the entrance of a chamber in which they can enter in contact (Fig.1.9 **(a)**). This way, droplets in the emulsification channel are separated by oil plugs and therefore cannot touch one another. During the travelling time in this channel, determined by its length, the surfactant can adsorb without risking coalescence. Fig.1.9 **(b)** shows images of a chip with a straight emulsification channel. As previously stated, the bypass channels role is to ensure that sufficiently large oil plugs separate the droplets. The usefulness of this emulsification channel is demonstrated in Fig.1.9 **(c)** when we see coalescence happening for a similar droplet size and at the same surfactant concentration but in the absence of such a channel. The length, as well as the covering efficiency, can be further increase in our design by building a serpentine emulsification channel (Fig.1.9 **(d-e)**).

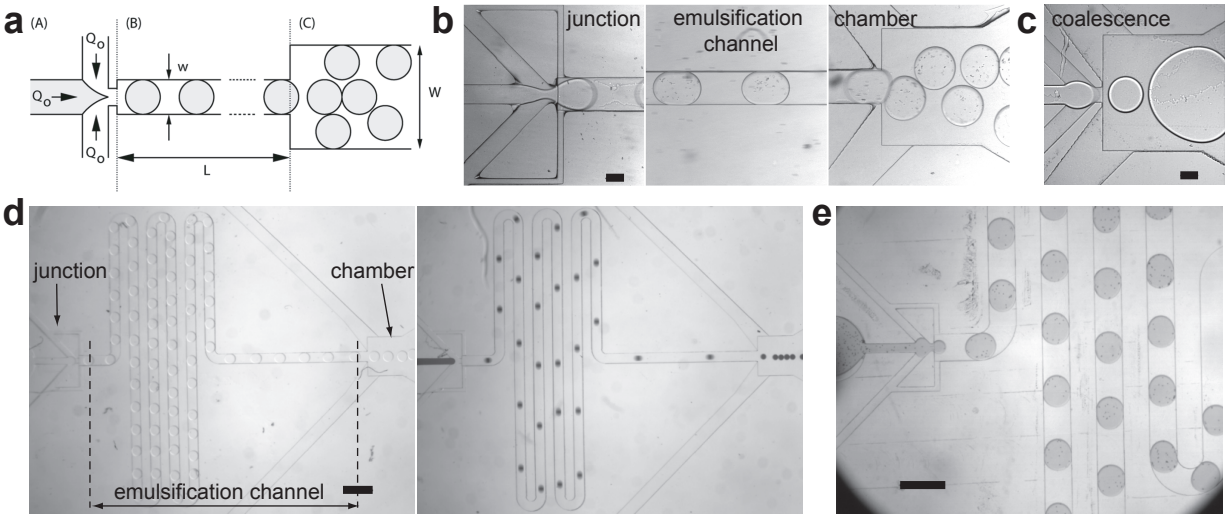

Figure 1.9: Emulsification channel. **(a)** Schematic principle of the emulsification channel (reproduced from Baret *et al.* [47]). w is the width of the emulsification channel. **(b)** Images of the droplet production at different stages for a straight emulsification channel. w = 350 μm. Scale bar is 200 μm. **(c)** Droplet production with the same surfactant concentration as in **(b)** but without an emulsification channel. Scale bar is 200 μm. **(d-e)** Droplet production with a serpentine emulsification channel for various droplet sizes. Scale bars are 1 mm. **(d)** w = 325 μm. **(e)** w = 600 μm.

As previously stated, controlling the flowrates at the junction allows to produce droplets

of different sizes with the same geometry (Fig.1.9 **(d)**). The width of the emulsification channel, of the oil bypass and the step depth can also be adjusted to produce significantly bigger droplets in a reproducible manner (Fig.1.9 **(e)**).

In the microfluidic chips used in the present work, the droplet production frequency ranges typically from 1 to 20 Hz, depending on the droplet size. The use of an emulsification channel allows the production of stable microdroplets, even for low surfactant concentrations. It is also useful being able to save this costly reagent.

1.4 Creating a large droplet array

1.4.1 Array density

The techniques discussed previously allow to produce highly monodisperse droplets that are going to be trapped in the 2 cm^2 anchor array of our microfluidic chip. The anchor locations can be entirely chosen during the design of the chip, though, we chose to build high-density arrays with the anchors disposed homogeneously across the chamber, following a repeating unit. The geometrical properties of the array are the repeating unit shape, the number of columns and rows, the anchor diameter d and the pitch of the array a (see Fig.1.10 **(a)**). First, the array can be built on different patterns, for instance with a squared or hexagonal geometry. Then, the anchor diameter and array pitch will determine the array density: for instance $\frac{1}{a^2}$ for a squared pattern or $\frac{2}{a^2\sqrt{3}}$ for an hexagonal one (1.15 times as dense as the square pattern). Fig.1.10 **(b-f)** shows images from 5 different arrays with increasing densities, up to 2,887 anchors/cm^2 (for $d = 50$ μm and $a = 200$ μm).

There are few factors that limit the array density. First, the spacing between the anchors must be large enough to let non-anchored droplets flow in between filled anchors. Then, if we want to ensure an efficient trapping, we need to have a sufficiently thin chamber compared to the anchor diameter (see condition (1.1.4)). Therefore, building small efficient anchors can be challenging from a microfabrication point of view. With our techniques, 50 μm wide anchors can be considered as a lower limit. In practice, the anchor diameter is determined by the application. For instance, small anchors are well adapted for encapsulating single cells but bigger ones are needed for building microtissues in droplets. Then, if we want the highest density achievable with a given anchor diameter, we need to find the minimum spacing that allows to let the droplets flow in between filled anchors. Once these parameters are set, the number of rows and columns are determined by the chamber width (1.2 cm) and length (1.7 cm).

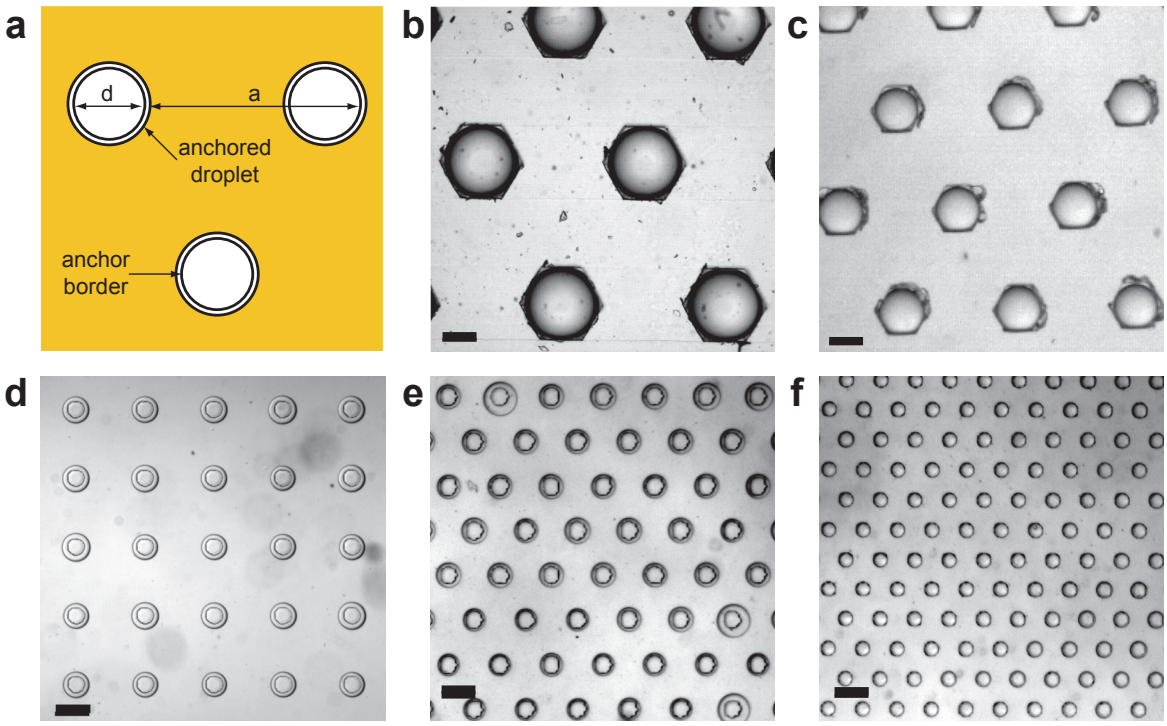

Figure 1.10: Droplet arrays with increasing densities. **(a)** Schematic representation of 3 aqueous droplets in oil trapped on anchors in a array with an hexagonal symmetry. d is the anchor diameter and a is the array pitch. **(b-f)** Images of droplet arrays with various densities. Array densities: **(b)** 128, **(c)** 250, **(d)** 625, **(e)** 1,283 and **(f)** 2,887 anchors/cm^2. Scale bars are 200 μm.

1.4.2 Efficient filling and washing of the droplet array

Droplets could directly flow into a trapping chamber but the addition of a distribution stage greatly enhance the filling efficiency by allowing droplets to quickly fill all the traps in the array. Indeed, the droplets enter the chamber through a single channel and consequently they have difficulties going to the anchors located on the sides of the chamber. In other words, they would only fill the anchors in the central region of the array.

Fig.1.11 shows how rails (see section 1.1.2) can deviate the droplets in order to distribute them homogeneously across the chamber width. These rails have several geometrical characteristics that have been optimized. First, they are regions of higher height compared to the channel in which the droplets are produced, and consequently, they guide the droplets by reducing their confinement. These rails are also directly opened to the trapping chamber which has exactly the same height. It means that the droplets can freely go through the exit of the rail to enter the trapping chamber at a deviated position across its width. Moreover, these rails have a diverging shape with a pointy end that widens until it reaches the trapping chamber. It builds a confinement gradient that captures the droplets going over

the rail beginning. Thus, the location of the rail beginning has to be optimized in order to ensure that a comparable number of droplets enters each rail. In addition, the control of the oil flowrate at the entrance of the chamber can play a role in this distribution. If it is too high, the injected droplets will be focused in the center of the channel and will not reach the rails, or at least the ones the sides. If it is too low, droplets will be well distributed but the filling of the droplet array will be longer. Finally, the number and direction of the rails have to be optimized depending on the droplet size and anchor spacing to be able to fill each area of the trapping chamber quickly.

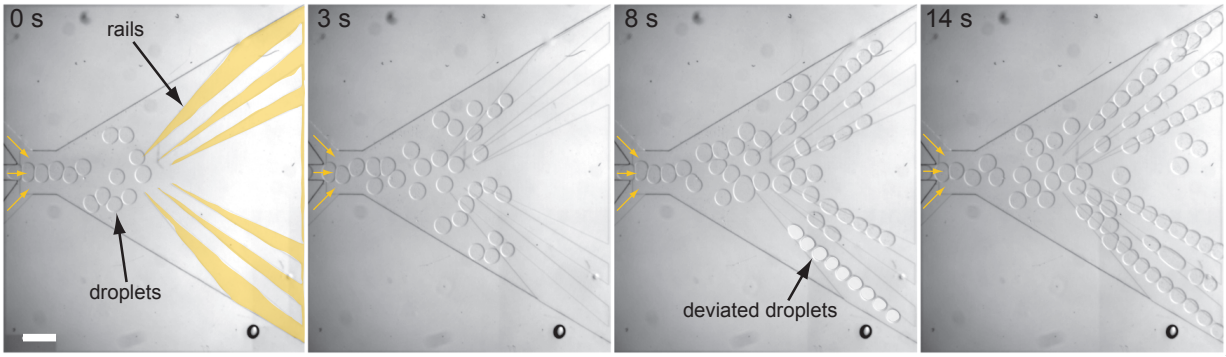

Figure 1.11: Distribution stage. Time lapse images of 6 diverging rails in the distribution stage. Yellow arrows represents the direction of the oil flowrate. Yellow and white overlays highlight respectively surface patterns in the oil chamber and aqueous droplets. Scale bar is 1 mm.

The homogeneous distribution of the droplets along the chamber width allows to efficiently fill the anchor array. Fig.1.12 **(a)** shows time lapse images of the filling of few anchors. At first, the anchors are empty, then droplets driven by the external oil flow fill the first anchors and the following ones move in between the filled anchors to reach the ones that are left. It is worth noting that, in the case displayed on Fig.1.12 **(a)**, the anchored droplets first look bigger than the anchors and, few tens of seconds later, seem to have completely enter the anchor cavity. This situation is schematically displayed in Fig.1.12 **(b)**. When a droplet enters an efficient anchor, it wants to fill entirely the anchor cavity. Therefore, a significant volume of oil has to be replaced by the aqueous droplet and the only way out is through the lubrication film between the anchor edge and the droplet. It constitutes a very thin channel with a high hydrodynamic resistance that slows down the oil emptying and thus the droplet entrance. This process is facilitated if the anchor has an angular shape, like an hexagon or a square, because in this case the droplet cannot entirely fill the wedge in each anchor corner, leaving a gutter that can be used by the oil for escaping the anchor more easily. These gutters are absent with cylindrical anchors and in this particular case, some droplets are even unable to completely enter the anchor cavity.

For an array of 500 efficient anchors that have a 250 μm diameter and with a 5 Hz droplet production rate we found that the time needed to fill all the anchors and remove

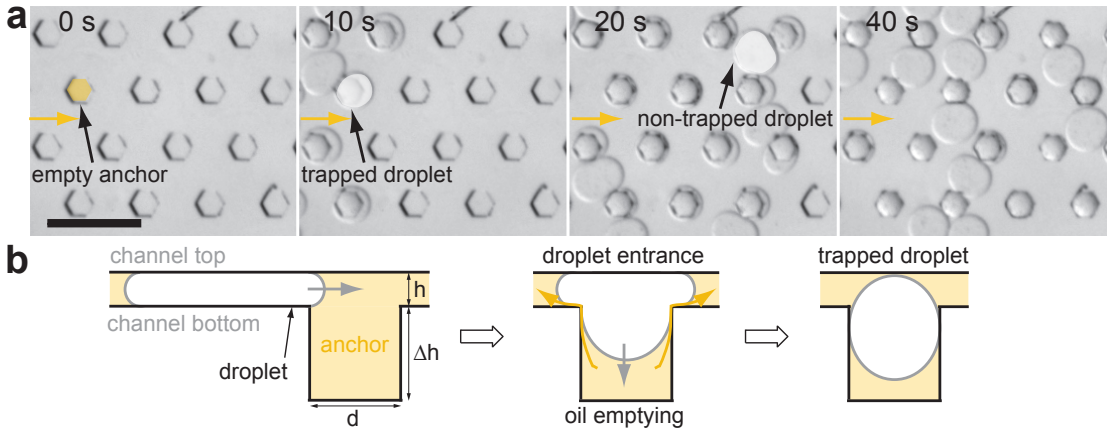

Figure 1.12: Filling of the array. **(a)** Time lapse images of the filling of 16 anchors with aqueous droplets. **(b)** Schematic side view of a droplet entering an efficient an deep anchor. Grey and yellow arrows represent respectively the droplet movement and the oil flow. d and Δh are the anchor diameter and depth, h is the height of the chamber.

the non-trapped droplets is about 5 minutes. It corresponds to a total number of produced droplets of about 800.

1.4.3 Spatial control of the array filling

The distribution stage can also be modified to control which area of the anchor array is filled with droplets. Fig.1.13 **(a)** shows a scheme of the distribution stage with an extra oil inlet that can be used to change the droplet trajectory (see colored droplets in Fig.1.13 **(b)**) by the addition of a large oil side flow. As a consequence, droplets are directed towards the 3 rails on the opposite side of the extra oil inlet (Fig.1.13 **(c)**) and fill the anchors on the right side of a chamber. After discarding the non-trapped droplets we can stop the extra oil flow and create droplets with another solution (non colored droplets). They will distribute homogeneously across the chamber width but since the anchors on the right side are already filled with colored droplets, they will only be trapped by the anchors on the left side. This simple protocol allows the formation of a spatially controlled droplet array (Fig.1.13 **(d-e)**).

This feature could probably be further developed by having two opposite extra oil inlets that could be independently controlled and by optimizing the rails design in order to spatially control the trapping of more than 2 droplet populations.

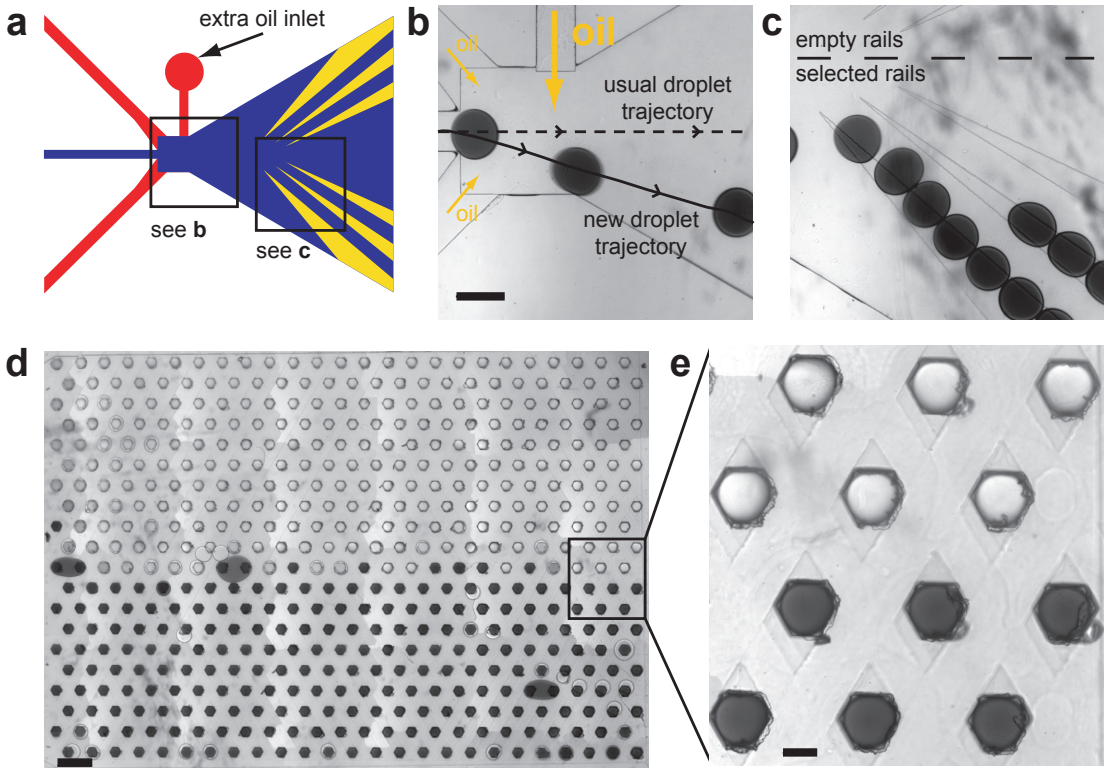

Figure 1.13: Deviated droplets for a control filling of the array. **(a)** Scheme of the entrance of the chamber with an extra oil inlet. The two black squares represent the location of the images in **(b)** and **(c)**. **(b)** Image of the entrance of the chamber with a large flowrate coming from the extra oil inlet that changes the droplet trajectory. Scale bar is 500 μm. **(c)** Image of the rails area. **(d)** Image of the 500 anchors of the chamber at the end of the selective filling with two droplet populations. Scale bar is 1 mm. **(e)** Zoomed image from **(d)** on 12 anchored droplets. Scale bar is 200 μm.

Chapter 2

Spheroid formation and culture in trapped hydrogel droplets

2.1 From cell encapsulation to spheroid formation

In this section, we explain how we create 3D cell cultures from cells encapsulated in microfluidic droplets. The basic principle is shown in Fig.2.1 **(a)**. First, multiple cells are encapsulated in microfluidic droplets that are immobilized on a high-density anchor array. These anchors provide efficient trapping (see condition (1.1.4)). Then, as soon as the external oil flowrate is stopped, the cells sediment. As the droplets have a smaller volume than the anchor, they enter completely the anchor cavity and have an almost hemispherical interface at the bottom. Consequently, the cells gather at the bottom center of each droplet. Then, they adhere one to another and reorganize to form a spheroid.

Fig.2.1 **(b)** shows a typical cell encapsulation with a junction combining flow focusing and step emulsification (see subsection 1.3.1). We can see about 200 encapsulated cells per droplet. This number is determined by the cell concentration and follows a Poisson distribution. In this case, the exact number of encapsulated cells should go roughly from 180 to 220. Then, these droplets are trapped on the anchor array, as explained in section 1.4. As soon as the non-trapped droplets have exited the microfluidic chip, the external oil flowrate is stopped which allows the cell sedimentation. We did not see sedimentation before because the oil flowrate induces recirculations inside the droplets that constantly move the cells around. Fig.2.1 **(c)** shows that the typical time scale of this sedimentation is about one minute and the nice centering of the sedimented cells confirms that the bottom interface of the droplets is hemispherical. The sedimentation process is complete after 5 minutes. At this point, the microfluidic chip that was observed on a temperature-controlled microscope is brought in a cellular incubator at 37°C. After about 20 hours of culture, we obtain one single well-formed spheroid per droplet (Fig.2.1 **(d)**).

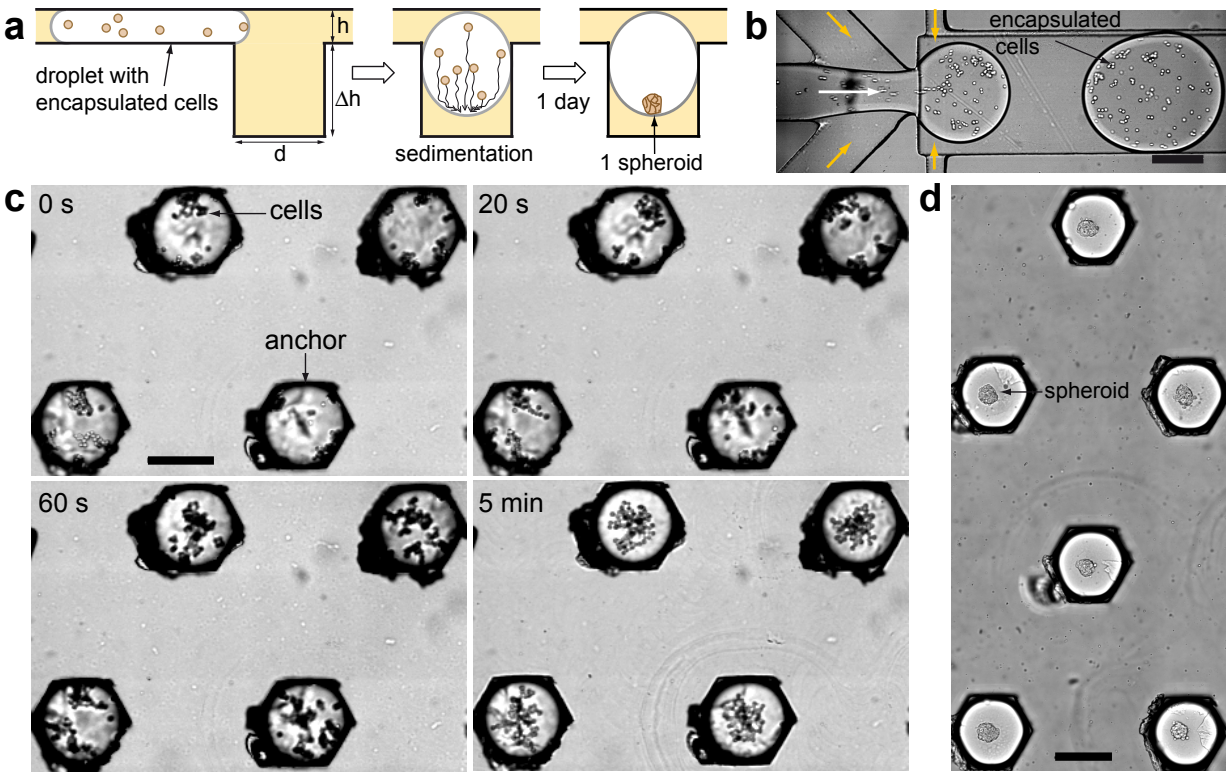

Figure 2.1: Cell encapsulation and spheroid formation. **(a)** Schematic side view of an anchor, from the droplet trapping to the spheroid formation. **(b)** Image showing the cell encapsulation at the microfluidic junction. Yellow and white arrows represent respectively the oil and aqueous flowrates. **(c)** Timelapse images of 4 anchors during the cell sedimentation. The external oil flowrate is stopped at $t = 0$ s. **(d)** 6 anchored droplets, each encapsulating one spheroid after an overnight incubation in oil. Scale bars are 200 μm.

The parameters of this experiment depend on the cellular type and application. For instance, the higher the cell concentration, the bigger the spheroids will be. Interestingly, the Poisson statistics only has a very limited impact on our spheroid formation while it is a critical point for single cell encapsulation [48]. If the spheroids would have been created off chip, then encapsulated and trapped on an anchor array, we would have had to optimize the concentration in order to minimize the number of empty droplets and droplets with multiple spheroids. Here, we have a single spheroid in almost all of our droplets. Also, if the sedimentation step is always the same, the dynamics of the spheroid formation process, and consequently the time needed for the incubation, depends on the cellular type. It typically ranges from few hours to a couple of days.

2.2 Spheroid culture and phase change

Doing 3D cell culture experiments can only be relevant if the culturing time can extend to at least several days. Though, the nutrient availability in the confined volume of a microfluidic droplet (typically 10 nL) is low. In our case, the nutrients will be depleted in a couple of days. In this section, we explain how the use of agarose can help us solve this issue and culture the spheroids for long-term periods.

Agarose is a purified algae extract that constitutes an hydrogel. The repeating unit is a disaccharide and it forms linear chains. The gelation, relying on the formation of H-bonds, is thermo-sensitive and reversible. The agarose powder can be dissolved at high temperature and gelates at low temperature. An interesting feature is that there is a thermal hysteresis of the sol/gel transition: the agarose melts and gelates at different temperatures, also these temperatures depend on the hydrogel concentration. Many types of agarose are available with various gelling and melting temperatures. In this work, we use an ultra-low gelling agarose, at a 0.9 %(w/w) concentration, which melts above 60°C and gelates below 15°C. It means that once melted it remains liquid at 37°C. Similarly, it remains solid at 37°C after gelation.

The cell encapsulation is actually done in liquid agarose droplets, diluted with culture medium. All the steps discussed in the previous section are performed at 37°C, so the agarose that was melted before the experiment above 60°C remains liquid, allowing the cells to reorganize into spheroids. After the spheroid formation, the microfluidic chip is kept 30 minutes at 4°C. It allows a complete agarose gelation and the cells are not affected by the cooling during this short period of time. At this point, the spheroids are embedded in solid agarose beads, so they are mechanically immobilized.

This immobilization allows us to remove the external oil and replace it by culture medium without risking flushing the spheroids out of the chip, which would have been the case with aqueous droplets. Adding an hydrogel matrix ensures to keep the spheroids in place. This phase change is done by filling the chamber with medium via the fluidic port located at the end of the trapping chamber (on the right side of Fig.1.7). This port was used as an outlet for the droplet production and trapping and is now used as an inlet for the medium filling. Furthermore, since the hydrogel is a highly porous structure, the nutrient and molecules in the surrounding culture medium can diffuse throughout the agarose matrix and reach the spheroids. The culturing time can now be extended.

Nevertheless, the process of replacing the external oil phase by an aqueous medium requires the optimization of several parameters. First, the anchors need to be very efficient in order to avoid removing the trapped gelated beads from the anchors with the oil/medium interface. Fig.2.2 shows images of the phase change in two different geometrical configurations. In the case of Fig.2.2 **(a)**, we can see that the gelated agarose beads are removed from their trap by the moving interface, which is not the case for the beads in Fig.2.2 **(b)**.

The difference relies on the trapping efficiency. In first case, the anchor diameter is 75 μm with a 65 μm height chamber. Therefore, the condition of efficient trapping is not met (see condition (1.1.4)). In the second case, the anchors have a 100 μm diameter and the chamber has a 50 μm height, so each droplet completely fills the anchor cavity (see condition (1.1.5)).

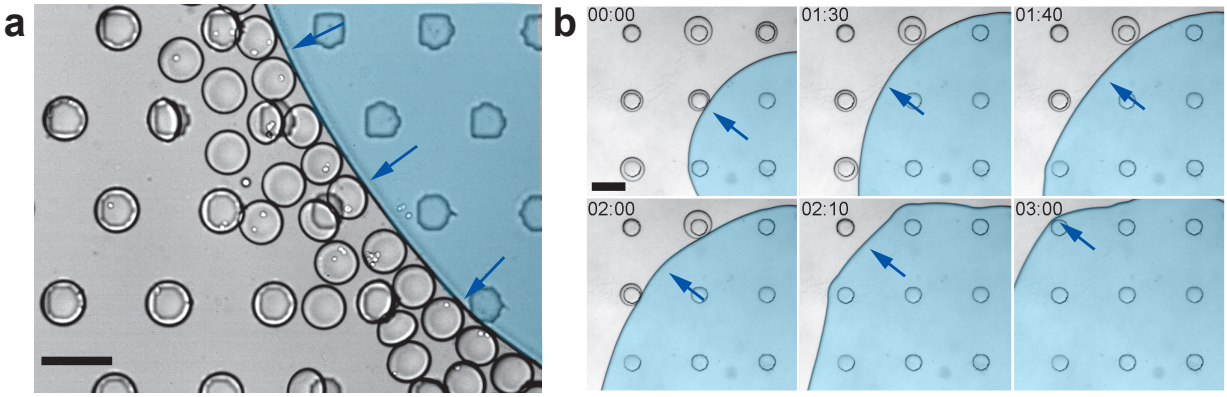

Figure 2.2: Influence of the trapping efficiency on the phase change. Phase change for a low **(a)** and high **(b)** trapping efficiency. Blue overlays highlight the aqueous phase and blue arrows show the movement of the water/oil interface. Scale bars are 200 μm.

A second parameter is the removal of the surfactant. When doing a phase change, we want the aqueous phase to merge with the agarose beads in order to bring the spheroids fresh medium. This merging is prevented by the surfactants (see subsection 1.1.1) which are still adsorbed at the interface of each agarose bead. This way, the aqueous phase will go around the agarose beads, filling the chamber without perfusing them. To avoid this phenomenon, we perfuse thoroughly the agarose beads with oil without any surfactant prior to the phase change. By doing so, we quickly decrease the surfactant concentration in the oil. Thus, the adsorption/desorption balance at the interface is driven towards the desorption of the surfactant. This process can be quite long since the desorption rate of the surfactant is known to be very low [49]. In our case, we usually perfuse a 50 μL chamber with 2 mL of pure oil at a 40 μL/min flowrate.

The efficiency of this surfactant removal is also controlled with the initial surfactant concentration. Fig.2.3 shows micrographs of anchors trapping agarose beads after the oil removal and the perfusion with a fluorescein solution. In Fig.2.3 **(a)** we can see that all 7 displayed beads are well perfused with fluorescein. The increase of the intensity in the beads is explained by higher depth of the anchors compared to the chamber. Fig.2.3 **(b)** shows a different configuration. First, we can see that the 3 beads at the middle of the image have been avoided by the aqueous phase. We still see the interface indicating the presence of an oil film separating the beads from the exterior. Then, in the other 4 anchors, the one on the bottom left is well perfused, as indicated by the high fluorescein intensity, but the other 3 are also isolated from the external phase. The fluorescence intensity distribution

indicates that the aqueous phase is only above and around the bead, but there is still an oil film preventing the perfusion of these beads (see the schematic side view of one of these anchors in Fig.2.3 **(b)**). In Fig.2.3 **(a)** and **(b)** the protocol for the surfactant removal and phase change was completely identical. This difference between the two cases comes from the surfactant concentration in the oil used for the droplet production: 0.5 % (w/w) in **(a)** and 4 % (w/w) in **(b)**. This demonstrates that the phase change is easier in the case of low surfactant concentration. It also emphasizes the utility of the emulsification channel (see subsection 1.3.2) that allows production of stable droplets at low surfactant concentrations. It is interesting to notice that the situations described in Fig.2.3 **(b)** happen more often for the last beads of the array to be reached by the aqueous phase. This can be explained by the accumulation at the aqueous phase interface of the remaining surfactants coming from the coalesced beads. After the merging with many beads, the interface of the aqueous phase has collected a sufficient amount of remaining surfactants to make other merging events more difficult.

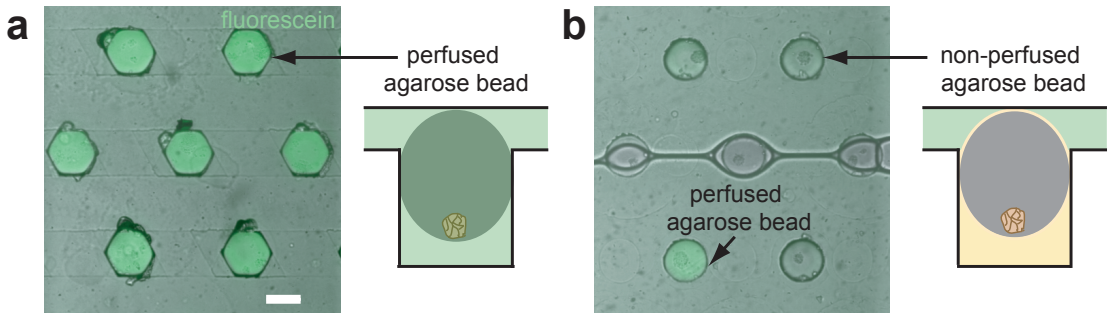

Figure 2.3: Influence of the surfactant concentration on the efficiency of the phase change. Micrographs of 7 anchored agarose beads encapsulating spheroids with schematic side view of highlighted anchors. The phase change has been conducted similarly with a fluorescein aqueous solution. The droplets in **(a)** and **(b)** were produced respectively with a high and low surfactant concentration. Scale bar is 200 μm.

Therefore, producing hydrogel droplets with an emulsification channel in a low surfactant concentration oil, trapping them in efficient anchors and perfusing the array with pure oil for removing the surfactant molecules are three conditions that allow an efficient phase change.

If we can facilitate the merging of the aqueous phase with the immobilized beads, we also need to make sure that the aqueous phase will homogeneously fill the entire array, leaving no area in oil. In this regard, reducing the surfactant concentration before the phase change does not help. Indeed, it favors the apparition of wetting points where the interface will be stuck, potentially preventing the perfusion of large areas of the array. We can ensure that the aqueous phase will extend across the entire chamber width before reaching the anchors by adding a filling chamber. This is the area of the microfluidic chip that extends from the fluidic port at the end of the trapping chamber (on the right side of Fig.1.7, now

used as an inlet for the aqueous phase) to the edge of the trapping chamber (see cyan area in Fig.2.4 **(a)**). If this area has a height higher than the trapping chamber there is a step right before the first anchors that guides the medium interface (Fig.2.4 **(b)**). Indeed, since crossing the step means increasing the confinement, it costs energy and the medium first fills entirely the filling chamber. Then, since it is the only option left, the energy barrier is crossed and the array can be perfused similarly across its width. We found that the addition of the filling chamber significantly increases the reproducibility of the phase change from one microfluidic chip to another. The design of these filling chambers was also optimized by successively widening and narrowing the chamber right before the step. This specific design helps ensuring a reproducible phase change, with all the anchors of the trapping chamber being perfused. In contrast, Fig.2.4 **(c)** shows the design of a microfluidic chip which has a simple triangular filling chamber, directly joining the inlet of the aqueous phase to the corners of the trapping area. This design favors an incomplete phase change across the array, as demonstrated by Fig.2.4 **(d)** which shows images of 2 selected areas of the trapping chamber after the phase change. Since the non-wetting aqueous phase cannot completely fill the wedges at the extremities of the trapping, it fails to reach the anchors that are close to these corners.

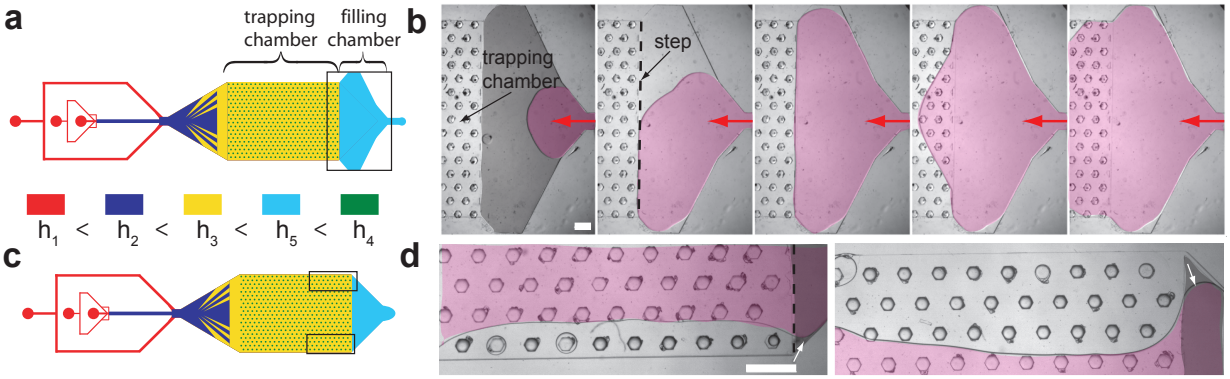

Figure 2.4: Guiding the medium filling with a step. **(a)** Schematic representation of the chip design. The filling chamber is the cyan area and it has a height h_5 heigher than the height h_3 of the trapping chamber in yellow. The black rectangle represents the location of the images in **(b)**. **(b)** Time lapse images of the medium perfusion with a filling chamber. The red arrows represent the medium flow. **(c)** Schematic representation of the chip design with a triangular filling chamber. **(d)** Images of the corners of the trapping chamber after the phase change. White arrows show the curvature of the aqueous phase in the wedges of the triangular filling chamber. Red and black overlays highlight respectively the aqueous medium and the filling chamber. The black dashed lines show the location of the step. Scale bars are 1 mm.

In this section, we showed that the formation of spheroids in agarose droplets allows to extend the 3D culture beyond what the nutrient depletion in microfluidic droplets would normally permit. After gelation of the agarose beads, the spheroids are mechanically held in the place and therefore the external phase can be exchanged from oil to fresh medium

without flushing out the cells. The efficiency of this phase change can be optimized with geometrical (design of the anchors and of the filling chamber) and chemical parameters (initial surfactant concentration and removal). After the phase change, the oil has been removed and the entire chamber is filled with fresh medium. The culture can be kept under static conditions for several days, with potentially medium renewal every 2 or 3 days.

2.3 Spheroid perfusion and stimulation

After the phase change, the microfluidic chip is only filled with an aqueous phase. As a result, every molecule that will be introduced in the chamber will be able to diffuse towards the spheroids. In this section, we discuss some applications related to the perfusion of the spheroid array.

2.3.1 *In situ* immuno-cyto-chemistry

The immobilization of the spheroids allows to perform *in situ* immuno-cyto-chemistry. Immuno-cyto-chemistry is a technique for visualizing specific proteins in cells. It relies on the specificity of a primary antibody directed against the target of interest. Either this antibody is labeled with a fluorescent dye, or the detection is made possible via the use of a secondary fluorescent antibody, directed against the primary. The labeling protocols can be tedious since there can be many steps, even prior to the antibody incubation.

For instance, these are the successive steps for an immuno-staining procedure with a primary and secondary antibody:

- PBS washing (Phosphate-Bufferred Saline);
- paraformaldehyde incubation: fixation step that kills the cells by polymerizing them, thus creating an immobilized network of antigens;
- PBS washing;
- Triton X-100 incubation: permeabilization step that facilitates the diffusion of reagents inside the cells;
- PBS washing;
- Fetal Bovin Serum (FBS) incubation: blocking step where serum proteins interact with antigens in a non-specific way. It prevents the non-specific binding of antibodies that will therefore only interact with the target of interest;

- PBS washing;
- primary antibody incubation: the primary antibody binds with the targeted antigen;
- PBS washing;
- secondary antibody incubation: the secondary antibody is fluorescently labelled and binds to the primary antibody. As several secondary antibodies can bind to a single primary antibody, there is an amplification of the biological signal;
- PBS washing.

In this example, there are 11 successive steps. In this manuscript, this is the staining procedure used for cyclooxygenase-2 in chapter 5. When a fluorescent dye is directly bound to the primary antibody, there is no need for a secondary antibody and the staining procedure is consequently a bit quicker. This is the case of the albumin staining in chapter 4 (see also Fig.2.5). Most of the time these immuno-cyto-chemistry procedures are coupled with DAPI staining, which is a fluorescent dye that binds to DNA. A slightly different procedure is used with BrdU (BromodeoxyUridine) staining. BrdU is a synthetic nucleoside that is incubated with the cells and can replace thymidine in the DNA replication. BrdU can be stained with a fluorescent antibody after a reduction step of the bromide group. Therefore, BrdU staining requires an extra step after the cells fixation and permeabilization and before the antibody incubation (see chapter 4). Finally, we also used viability staining, which is easier to perform since it does not require the fixation, permeabilization and blocking steps of an immuno-cyto-chemistry procedure. LIVE/DEAD® reagent was used in chapter 4 and NucBlue® Live reagent was used in section 4.8 and chapter 5 and 7.

Though, in the context of spheroids cultured in suspension or hanging drops, these protocols require many pipetting steps, separated with washing and potentially centrifugation. These handling steps in microplates can affect the microtissue integrity. With our microfluidic chip, we simply flow the solutions one by one in the chamber and respect the different incubation times under static conditions. All staining, incubation and washing steps can be performed on chip. In addition, the staining procedure is a step where the high reduction of the reagent consumption in microfluidics compared to microplates has a direct impact. Indeed, fluorescent labels and antibodies are very costly reagents.

For the experiments shown in chapter 4, the staining protocol is done manually, by changing the injection syringe at each step. In chapter 5, the protocol has been entirely automated with a computer-controlled perfusion system (see appendix C). The details of the protocols and reagents that have been used can be found in appendix A.4.

Our spheroids are immobilized in 0.9 % (w/w) agarose beads. At this concentration, the pore size of the gelated network should be about 500 nm [50, 51]. In comparison the antibodies have a typical size of 14 nm, consequently the diffusion of biomolecules in agarose

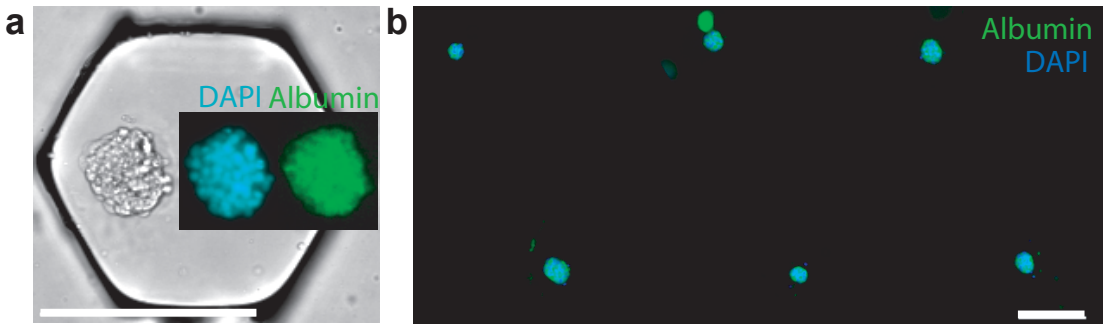

Figure 2.5: *In situ* IMMUNO-CYTO-CHEMISTRY ON TRAPPED SPHEROIDS. Fluorescent image of 1 **(a)** and 6 spheroids **(b)** trapped in the agarose beads of an anchor array. The spheroids are stained with DAPI (cyan **(a)**, blue **(b)**) and for intra-cellular albumin (green, see chapter 4). Scale bars are 200 μm.

is not hindered by the gelated mesh. This has been confirmed during this PhD work by many staining experiments, as shown in FIG.2.5;

2.3.2 Selective perfusion

We can also perfuse the spheroid array with a molecule that will have an impact on the cells biology. For instance a drug can be used for toxicity experiment or different culture medium compositions can be tested. If it is straightforward to perfuse the entire array with one particular solution, for instance by comparing the effects with a control chip, we can also selectively perfuse some of the spheroids of the array by taking advantage of the microfluidic flows. In order to do so, we need to have several fluidic ports for the different aqueous solutions [52].

FIG.2.6 **(a)** shows a spheroid array where only 2 rows are perfused with a fluorescein solution. There are 3 different inlets, one for the fluorescein in the middle and two for the aqueous medium on the sides. Adjusting independently the flowrates allows to choose which rows of the array are perfused (FIG.2.6 **(b)**). This is a very versatile system since the number of perfused rows is controlled by the relative magnitude of the fluorescein flowrate. The higher it is, the more rows will be perfused.

This technique can be used to apply different conditions in the same spheroid array as long as the solutions keep flowing for the duration of the experiment. The number of inlets and solutions can vary depending on the application. Section 4.8 will detail the experimental aspects and describe the results obtained with a similar system for a drug perfusion experiment on hepatocyte spheroids.

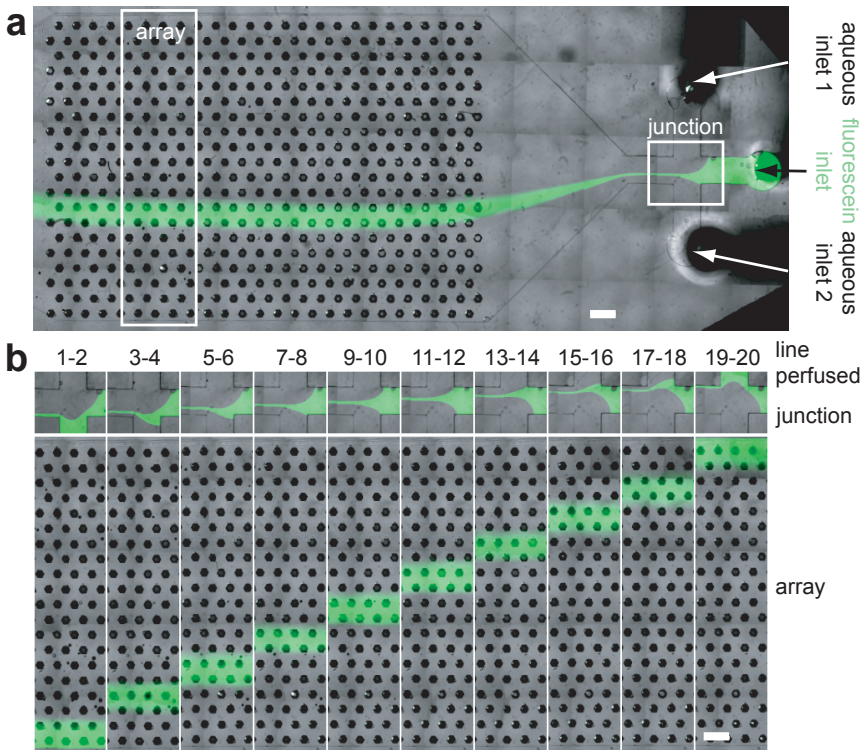

Figure 2.6: Line by line perfusion of the array. **(a)** Micrograph of the entire anchor array showing the three inlets added at the end of the chamber. A fluorescein solution and an aqueous buffer flow respectively through the middle and side inlets. The white rectangles represent the location of the images shown in **(b)**. **(b)** The first row of images represents the junction of the three aqueous inlets while the second row shows a portion of the array. Each column stands for different flowrate leading to different lines perfused with the fluorescein solution. Scale bars are 1 mm.

2.4 Selective recovery of viable spheroids

One more feature of this microfluidic chip is the ability to selectively recover viable spheroids from the array. It also relies on the properties of the agarose hydrogel.

As discussed in subsection 1.1.2, an infra-red laser can be used to change the droplet trajectory. Since the infra-red wavelengths are well absorbed by water, an infra-red laser efficiently and locally heats the aqueous medium that it goes through [53]. The temperature rise is sufficiently high to melt the agarose.

Fig.2.7 **(a)** shows a schematic view of the spheroid recovery with an infra-red laser. The position of the focused laser spot is controlled via a computer with a custom LabVIEW code that controls galvanometric mirors [42]. The agarose bead of a selected spheroid is melted with the infra-red laser within a few seconds. Thus, the spheroid is released and can be

taken away by a medium flow (Fig.2.7 **(b)**). The spheroid is driven out of the chip and can be recovered in a centrifuge tube for further downstream analysis. Moreover, we confirmed that this recovery process does not affect the spheroid viability with LIVE/DEAD® staining (Fig.2.7 **(c)**) and replating experiments (Fig.2.7 **(d)**) on recovered spheroids. Even if the temperature rise during the exposure to the infra-red laser is very high, we carefully avoid to directly shoot the spheroid with the laser and the melting operation only lasts a few seconds.

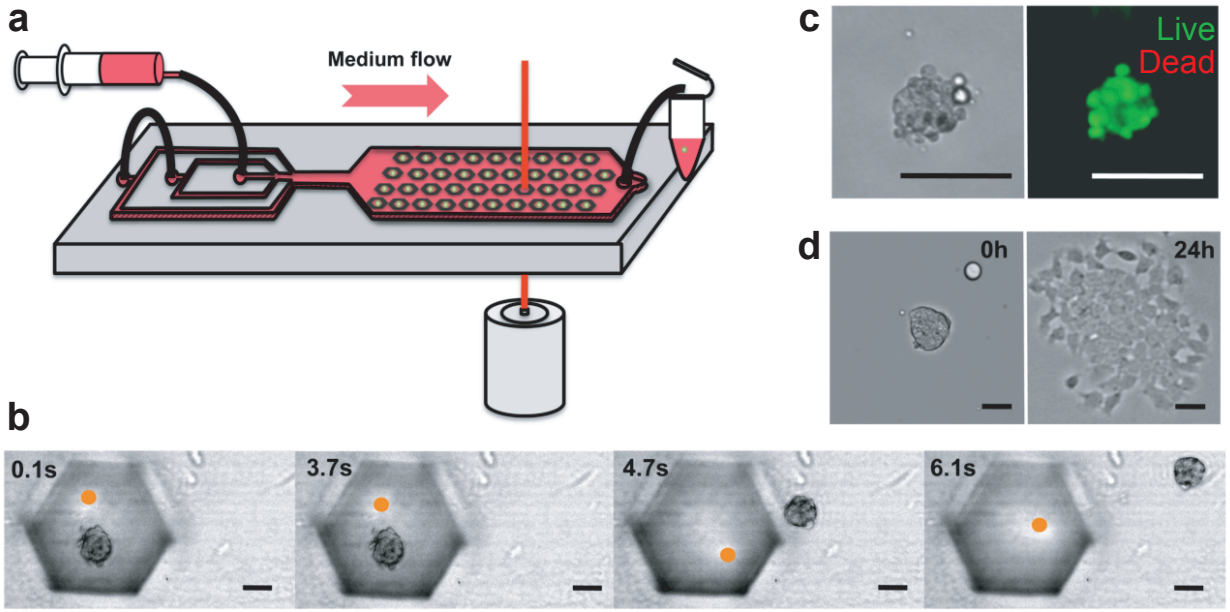

Figure 2.7: Selective recovery of viable spheroids. **(a)** Schematized protocol of the selective recovery. A culture medium flow transports the spheroid out of the chip, where it is collected in a 1.5 mL tube. **(b)** Time lapse images of the spheroid recovery. The laser beam location is represented by an orange dot. **(c)** Bright field image and LIVE/DEAD® staining of a recovered spheroid. **(d)** Bright field image of a recovered spheroid immediately after replating (0 h) and 24 h post-replating in 2D dish. All scale bars are 50 μm.

Chapter 3

Image analysis for multiscale cytometry

This chapter concludes the presentation of the technical aspects of my PhD work. In order to characterize and study the spheroids that are created in agarose droplet arrays, we need quantitative data. In this regard, fluorescent imaging is an attractive approach for several reasons. First, our microfluidic format is well adapted to immuno-cyto-chemistry, as discussed in the section 2.3. Then, the image acquisition in our system is facilitated because every spheroid is immobilized in its anchor, even to a further extend once the agarose droplets are gelated. In addition, using a motorized microscope allows to acquire efficiently detailed images of all the spheroids cultured in a microfluidic chip. These images can be acquired either after a given culturing time or at regular intervals for studying the dynamics of a process. Finally, the reading of the fluorescence levels directly gives quantitative data correlated to biological parameters.

The data that is extracted from the images comes from an automated image analysis procedure developed on the Matlab® software. The data is organized and presented at different levels of details (see Fig.3.1):

- **population level.** This represents data that is averaged over the entire population, like most of the standard biological quantitative results. It gives a general trend but completely misses the heterogeneity inside the population that can be of paramount importance in many applications.

- **spheroid level.** This is the case where one quantitative value is obtained for each spheroid, like a mean fluorescent signal. It allows to clearly see the spreading of the data over the population and spot the interesting outliers. In a single microfluidic chip, as we create one spheroid per anchor, we can obtain one data for each of the anchors of the array (typically several hundreds).

– **cellular level.** In this case, we used the details of the acquired images to detect and analyze separately all the observable cells of all the spheroids. It provides biological relevant information at a very high throughput (typically several thousands of analyzed cells in a single microfluidic chip) and *in situ*. It means that we have access to the cellular level data without breaking the spheroid structure and looking at the cells individually. Therefore we can benefit from the structural information of the organoids to explain the biological results that are observed at the spheroid level.

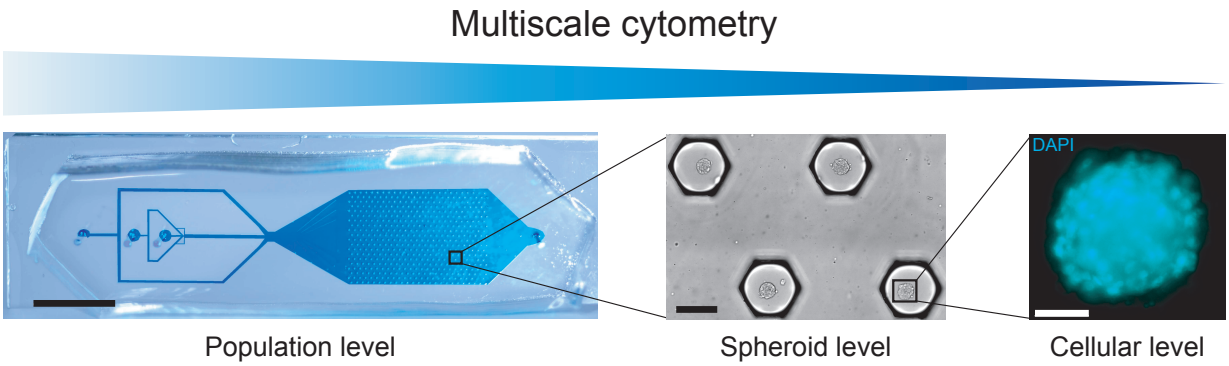

Figure 3.1: Multiscale cytometry. Images of a microfluidic chip (population level, scale bar is 1 cm), 4 anchors filled with agarose beads encapsulating spheroids (spheroid level, scale bar is 200 μm) and a fluorescent image of the DAPI signal inside a spheroid (cellular level, scale bar is 50 μm).

As this image analysis technique allows to extract quantitative data from cells with different levels of details and in a high-throughput manner we call it **multiscale cytometry**.

Before going through the details of this hierarchical analysis procedure, we first discuss the inherent difficulties of imaging fuorescent 3D microtissues and the optimization of the image acquisition protocol.

3.1 Image acquisition

3.1.1 Imaging spheroids with fluorescence microscopy

The objective magnification, the optics and camera determine the XY resolution of an image, *i.e.* the pixel size in microns. For imaging 3D fluorescent microtissues, we also need to understand the Z resolution of our images, in the direction perpendicular to the chip plane. In this regard, confocal microscopy is a powerful tool since it only selects the fluorescent light coming from a single plane, resulting in very high Z resolutions (typically in

the order of one micron). Fig.3.2 **(a)** shows 4 different confocal slices of a spheroid created in our microfluidic chip and stained with DAPI. We can clearly see the different cell layers. The nuclei are well defined and the out of focus intensity is low. In Fig.3.2 **(b)**, every pixel value is the maximum over all the confocal slices. It gives an idea of the distribution of all the nuclei in the spheroids. Nevertheless, the images analyzed in the present work were obtained on a regular fluorescence microscope. In this case, the Z resolution is much lower (typically in the order of few tens of microns), as shown in Fig.3.2 **(c)**, which shows typical fluorescent images. They were taken with a 10X objective, corresponding to a depth of field of 15 microns, which is the order of magnitude of a cell diameter. Though, there is a high a out of focus intensity.

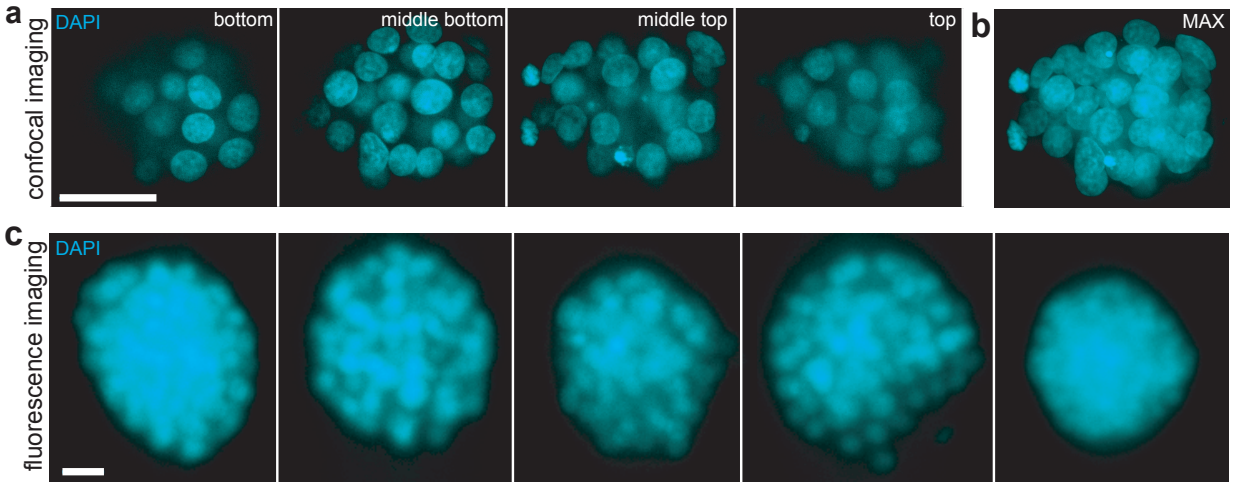

Figure 3.2: Imaging fluorescent spheroids. **(a)** Confocal slices of a spheroid stained with DAPI, acquired with a spinning disk confocal microscope. **(b)** Maximum projection of all the confocal slices of the spheroid shown in **(a)**. **(c)** 5 spheroids imaged with regular fluorescent microscopy. Scale bars are 20 μm.

It is interesting to see that the images from Fig.3.2 **(c)** look more like the one in Fig.3.2 **(b)** than the individual slices in Fig.3.2 **(a)**. It indicates that the fluorescence images we acquired bear the mark of the cells above and below the focus plane. Experimentally, it is also confirmed by the fact that there is only one plane with a good focus, unlike what is seen for the same spheroids on a confocal microscope.

This discussion depends highly on the magnification of the objective. A higher magnification will lead to a smaller depth of field and a lower out of focus intensity. But a higher magnification means a smaller field of view and consequently, a higher acquisition time. A balance needs to be found between the precision of the image and the duration of the acquisition.

3.1.2 Acquisition protocol

The easiest way to acquire images over the entire trapping chamber is to use the motorized stage to image the entire area (see Fig.3.3 **(a-b)**). The single images are taken with a small overlap and are rearranged during the final stitching to reconstruct the large image. In the example shown in Fig.3.3 **(b)**, 486 images are taken with a 10X objective (1.6 μm/pixel), forming an array of 18 rows and 27 columns. This protocol provides a complete image of the trapping chamber, which can be interesting if we want to look at something in between the anchors. It is straightforward to implement but in the end more than 80 % of the pixels of the stitched image are outside the anchors.

One way to optimize the number of useful pixels is to only take images centered on the anchors, as shown in Fig.3.3 **(c)**. Their periodic spatial arrangement allows to easily record their locations. Recorded images are voluntarily bigger than the anchors to allow for small drifting, in case the axis of the anchor array are not exactly parallel to the axes of the motorized stage. After acquisition, the anchors are automatically cropped from the single images and rearranged to create a montage, saving their spatial coordinates in the original array (Fig.3.3 **(d)**). This protocol can provide more detailed images, since there is only one field of view per anchor needed. Meanwhile, the acquisition time depends only on the number of anchors, so it is only quicker than the previous protocol if there are less anchors than fields of view needed to image the entire array. In Fig.3.3 **(d)**, there are 270 anchors, forming an array of 15 rows and 18 columns. Thus the images are acquired much quicker than in the previous case, and also with a higher spatial resolution (0.64 μm/pixel).

The results presented in chapter 4 were obtained by acquiring an image of the entire array. In chapter 5, there are fewer but bigger anchors so we used the single trap acquisition protocol.

Independently of the previous discussion, the two acquisition methods can be adapted to the temporal sampling of the experiments. Either there is one single acquisition step after a given culturing time, giving a snapshot of the spheroids behavior, or the acquisition is repeated regularly to follow dynamically the biological evolution of the system. In this last case, the time interval between two acquisitions has to be shorter than the time needed to image all the anchor array once. The time needed for getting multiple fluorescence channels images on several hundreds of anchors is typically between 30 min and 1 hour. If, as discussed earlier, we acquire only one image per anchor, this acquisition time is cannot be decreased. If we image the entire chamber, we can use a lower magnification, assuming that it is acceptable for the image analysis. It will result in a broader field of view and consequently in a quicker acquisition time and smaller interval between the time points. Another approach for increasing the acquisition frequency is to only image a subset of anchors. It reduces the number of different spheroids that are monitored but does not compromise on the image quality.

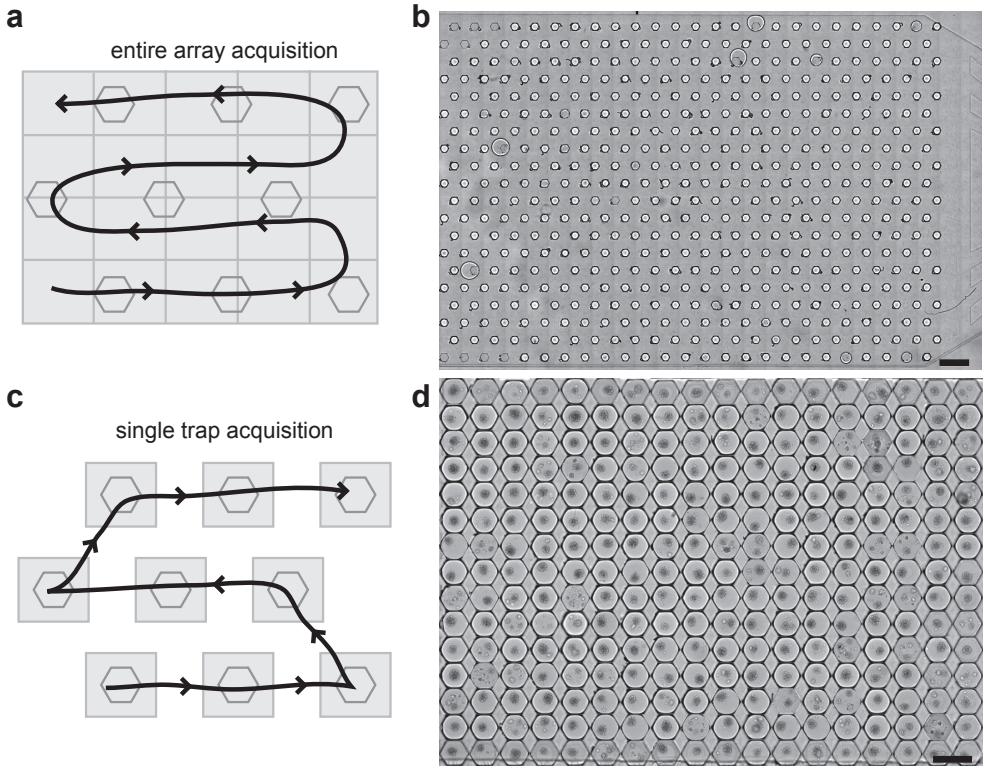

Figure 3.3: Acquisition protocol. Either the entire anchor array can be imaged (**(a-b)**, 500 anchors with a 250 μm diameter) or a montage from the single trap acquisition can be created (**(c-d)**, 270 anchors with a 400 μm diameter). Scale bars are 1 mm.

There are also different techniques to ensure getting a good focus for each spheroid of the array. In the ideal case, there is only one focus plane needed for the entire array. Indeed, since all droplets have similar sizes, all cells sediment at the same level and therefore all spheroids are formed in the same plane. Nevertheless, there are some cases, likely depending on the cell type and spheroid size, where the spheroids end up at different Z positions. In this case, we can use an autofocus technique that scans Z positions over a given range to find and record the best image. It increases the acquisition time but greatly enhances the overall image quality.

3.2 Detection and analysis protocol

After the acquisition, the images are analyzed with a custom Matlab® code. In this section, we detail the first step of the analysis and discuss the overall procedure for extracting quantitative data.

3.2.1 Anchor detection

Every spheroid is immobilized in an anchor, therefore, the first step of the analysis protocol is the detection of all the anchors of the array. Although, we could use the fact that the periodic arrangement of the anchors is known, we chose to look for the anchors individually in order to have a reliable detection whatever the trapping array.

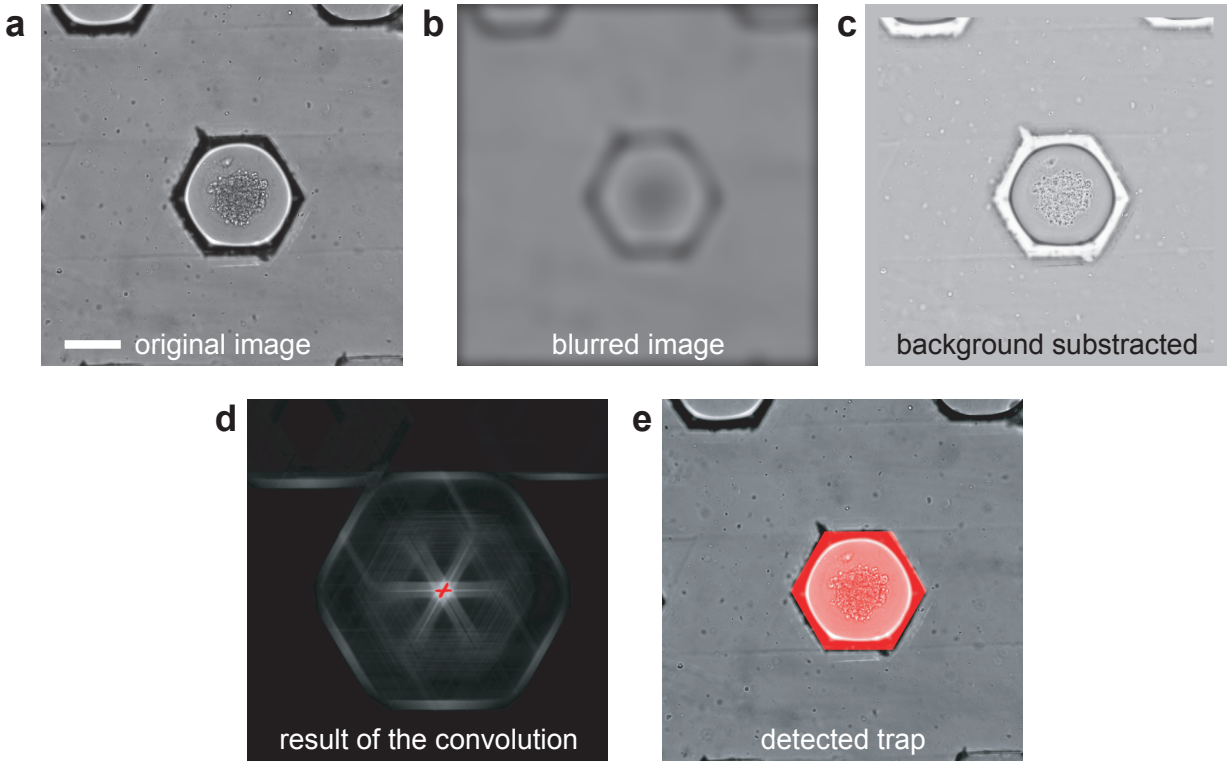

Figure 3.4: Anchor detection procedure. **(a)** Original image with an agarose bead encapsulating a spheroid in an 400 μm hexagonal anchor. Scale bar is 200 μm. **(b)** Image after a Gaussian blur. **(c)** Image after background substraction and inversion. **(d)** Result of the convolution with a properly sized hexagonal mask. The red pixels are above the threshold. **(e)** Original image with a red overlay showing the detected trap.

The detection protocol is shown on a single anchor in Fig.3.4. First, there is a pre-processing before actually trying to detect the anchor center. The original image (Fig.3.4 **(a)**) is blurred by a Gaussian convolution in order to extract the background of the image (Fig.3.4 **(b)**). This background is subtracted from the original image and inverted (Fig.3.4 **(c)**). This way, the anchor edge appears clearly with a high intensity (in white on the image) in the result image. Then, there is the actual detection step. Since the exact size and shape of the anchor is known, the pre-processed image is convoluted with a mask of the anchor edges. The result of the convolution is shown in Fig.3.4 **(d)**, where the white pixels intensity indicates a high value of the convolution. When the mask is centered on the

anchor location, it fits the high intensity edges that are seen in Fig.3.4 **(c)**, giving a high result on the convoluted image. Consequently, thresholding the result of the convolution allows to find the location of the center of the anchor (shown in red on Fig.3.4 **(d)**) and to create a mask of the anchor, as shown in red in Fig.3.4 **(e)**.

If only demonstrated here for a single anchor, this detection technique works similarly for the image of an entire array, whatever the spatial arrangement of the anchors, but as long as they have the same size and shape. If needed, this detection could be easily upgraded to detect even different anchors in the same image.

When imaging the entire trapping chamber, as discussed in subsection 3.1.2, this detection is performed on the overall reconstructed image. When imaging single anchors, this detection is performed on the single images in order to crop properly the anchor that will be incorporated in the final montage, on which the anchor detection is not repeated.

3.2.2 Cellular detection

The anchors of the array contain the droplets encapsulating the cells. As a result, after the anchor detection, the cells are detected in each anchor. The detection procedure is done either in bright field when there is no other channel or directly with the fluorescent signal.

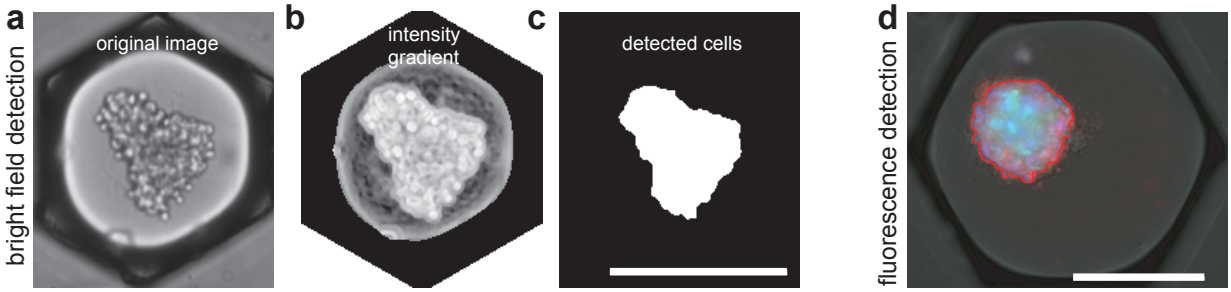

Figure 3.5: Cell detection procedure. **(a-c)** Detection of cells in bright field. The intensity gradient **(b)** is extracted from the original image **(a)** and thresholded to detect the cells **(c)**. **(d)** Micrograph showing the detection of cells with the fluorescent signal. The red line shows the edge of the detected spheroid. Scale bars are 200 μm.

On the first hand, the principle of the bright field detection is shown in Fig.3.5 **(a-c)**. The intensity gradient is extracted from the original image (Fig.3.5 **(a)**) in each detected anchor (Fig.3.5 **(b)**). The pixels representing the cells often have very different intensities from their neighbors, therefore, they have a high gradient value. Simply thresholding the gradient image allows to detect the cells (Fig.3.5 **(c)**). This procedure is automated but it can give wrong results, mostly when the cells are too close to the anchor walls. In this case, a manual check of the detection is needed. On the other hand, the fluorescence signal provides

a more reliable detection method because the signal difference between the cells and the background is usually much higher (Fig.3.5 **(d)**). When several fluorescence channels are required, we can either choose to combine them for the detection or to select some of them. The threshold is chosen automatically with the function *graythresh* of Matlab®, which chooses the value minimizing the variance of the pixels above and the variance of the pixels below the threshold.

3.2.3 Analysis protocol

The detection of the anchors and the cells are the cornerstones of the image analysis protocol. Once the cells have been detected, we can extract data that are correlated to biological parameters. Before discussing in details the parameters acquired from the cells, we look at the overall analysis protocol in 2 different typical experimental cases, first when a single fluorescence image (possibly with multiple channels) is acquired after a given culturing time and second, when multiple images are acquired in bright field at regular intervals to follow dynamically the spheroid formation.

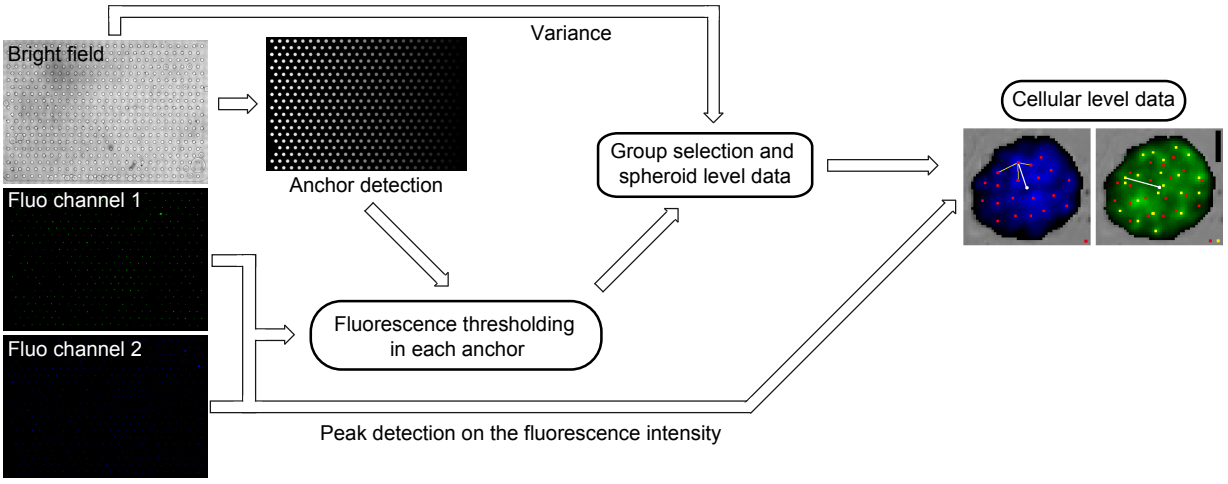

Figure 3.6: Analysis protocol for a fluorescent spheroid array. An image of the entire array is taken in bright field and with two (or more) fluorescent channels. The anchors are detected on the bright field image, allowing an automatic thresholding for the fluorescent channels in each anchor. This detection, with variance calculations, allows the sorting of the detected objects among the different groups based on morphological criteria. The cellular level data is acquired by fluorescence peak detection in each spheroid.

The general principle of the analysis for a fluorescence acquisition is shown in Fig.3.6. First, the images are acquired in bright field and in fluorescence. The anchors are detected on the bright field image and the fluorescent intensity allows to easily detect the cells. At this stage, we can extract many quantitative data, like morphological and fluorescence

parameters at the spheroid level. This dataset is used find the real spheroids among all the detected objects, as discussed later in subsection 3.3.2. Finally, once the spheroid data is sorted, we can use their fluorescent signal to extract data at the cellular level.

Alternatively, Fig.3.7 shows the analysis protocol for the example of the dynamic following of the spheroid formation. In this case, there is a time lapse acquisition, only in bright field. The images of the array are regularly acquired and at each time point, the anchors are detected and tracked overtime. The tracking of the anchors ensures that they are correctly followed through time in case some of them are not detected at every time point. Then, in each anchor, the cells are detected and tracked over time, in case there are several detected spheroids in a single anchor. This way, morphological measurements that are obtained at each time point can be computed over time.

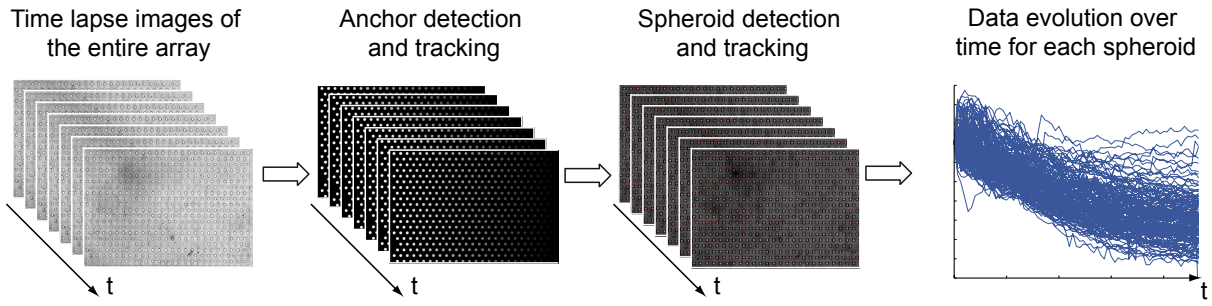

Figure 3.7: Image analysis for a time lapse acquisition in bright field. Images of the array are taken at regular intervals. After anchor and cell detection, as well as tracking over time, data is extracted for each spheroid at each time point.

These two procedures can be combined for live fluorescent staining. In this case, Fig.3.6 represents the analysis that is done at each time point. The spheroid and cellular level data can be computed over time by the tracking of the detected spheroids.

3.3 Group selection and spheroid-level data

After the detection step, we have in each anchor a binary image of the cells. These binary objects can be directly used for extracting morphological data such as the area and the perimeter. In this section, we explain which are the morphological parameters that we measure and how they are used to sort all the detected objects in different categories and reliability select the actual spheroids.

3.3.1 Morphological data

The easiest morphological parameter to compute is the equivalent diameter d. Whatever the shape of the object, d is defined as the diameter of the disk that has the same area (see Fig.3.8 **(a)**). Therefore:

$$d = 2\sqrt{\frac{\mathcal{A}}{\pi}} \tag{3.3.1}$$

where $\mathcal{A}$ is the projected area of the detected object.

Fig.3.8 shows three examples from the same microfluidic chip. d can be assimilated to the diameter of the spheroid only when it is well reorganized in 3D. Indeed, for a similar number of cells, a flat non reorganized aggregate will have a bigger projected area, and thus a bigger equivalent diameter than the corresponding well formed spheroid.

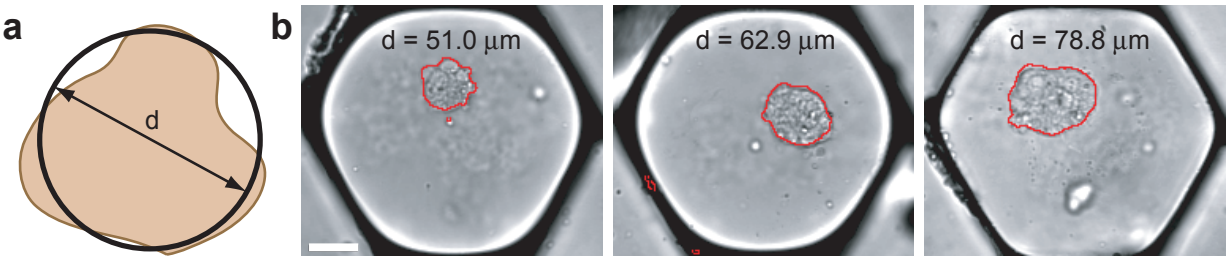

Figure 3.8: Mesurement of the spheroid diameter. **(a)** Schematic representation of the equivalent diameter d. **(b)** Images of 3 spheroids with increasing equivalent diameters. The red lines show the edge of the detected spheroids. Scale bar is 50 μm.

Then, we can try to have quantitative measures for the spheroid shape. For instance, the shape index $\mathcal{SI}$ quantifies the circularity:

$$\mathcal{SI} = \frac{4\pi\mathcal{A}}{\mathcal{P}^2} \tag{3.3.2}$$

where $\mathcal{A}$ is the projected area and $\mathcal{P}$ is the perimeter (see Fig.3.9 **(a)**). $\mathcal{SI}$ goes from 0 for a line to 1 for a disk. Fig.3.9 **(b)** shows 3 cell aggregates with increasing shape index. We can see that a low shape index value, typically below 0.5, corresponds to an aggregate that is not well reorganized (left). In contrast, an almost spherical spheroid has a shape index value above 0.9 (right). Intermediate values can be obtained, even for apparently well formed spheroids, if there are some non adherent single cells outside the spheroid border but still detected as part of the same object (middle).

Another measure of an object shape is given by the inertia ratio $\mathcal{I}$. By assuming a constant mass density over the object, we can calculate the moment of inertia matrix with the XY coordinates. $\mathcal{I}_1$ and $\mathcal{I}_2$ are the eigenvalues of this matrix. Physically, they

represent the principal axis of rotation (see Fig.3.9 **(c)**). $\mathcal{I}$ is the ratio of the smallest over the largest:

$$\mathcal{I} = \frac{\mathcal{I}_2}{\mathcal{I}_1} \tag{3.3.3}$$

where $\mathcal{I}_1$ and $\mathcal{I}_2$ are the first and second principal moments of inertia. Therefore, the inertia ratio is equal to 1 if there is an axis of rotational symmetry perpendicular to the object plane. Fig.3.9 **(d)** shows different cases from the same chip. We can see that there is a low inertia ratio value when 2 distinct spheroids that look about to merge are detected in the same object (left). This object has 2 axis with very different lengths. In the other two images, there is only one spheroid that is detected and thus the inertia ratio value is higher. The middle spheroid has a lower value because it has a more ovoidal shape than the spheroid on the right image.

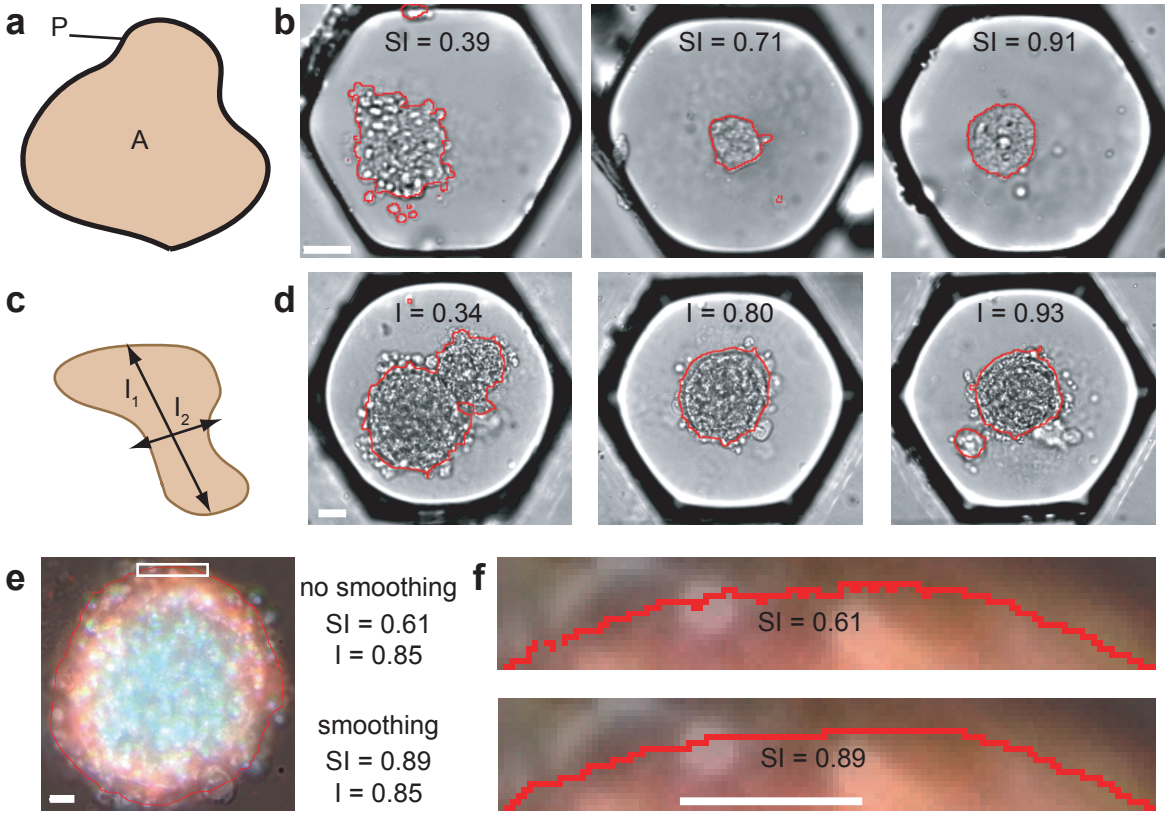

Figure 3.9: Quantification of the spheroid shape. **(a)** Definition of the perimeter $\mathcal{P}$ and the projected area $\mathcal{A}$ needed to compute the shape index $\mathcal{SI}$. **(b)** Images of 3 spheroids with increasing shape index. Scale bar is 50 μm. **(c)** Schematic definition of the first and second principal axis of inertia. **(d)** Images of 3 spheroids with increasing inertia ratios. Scale bar is 50 μm. **(e)** Micrograph showing the edge detection for 2 detection methods on a fluorescent spheroid. The white rectangles indicate the location of the zoomed images in **(f)**. Scale bars are 20 μm. The red lines show the edge of the detected spheroids.

The shape index can be strongly influenced by the pixel size and the analysis protocol so the values given by the automated analysis need to be checked by looking at the general aspect of the considered spheroid. Indeed, Fig.3.9 **(e)** shows a micrograph of a fluorescent spheroid, whose shape index and inertia ratio are calculated with or without an artificial smoothing of the detected spheroid border. A zoomed image is shown in both cases in Fig.3.9 **(f)**. We can see that the raw detection (top) leads to a border with a high roughness and consequently, to an overestimated measure of the perimeter. When the border is smoothed before analysis, the perimeter has a lower and more appropriate value. Meanwhile, the projected area remains similar regardless of the smoothing step, so the shape index is underestimated when there is no smoothing step. As the spheroid displayed in Fig.3.9 **(e)** looks well round, a high shape index value (0.89) seems appropriate, which justifies the use of the border smoothing. This need appears when the pixel size is very small compared to the perimeter. As the inertia ratio does not rely on the detailed shape of the border but more on the overall shape of the object it is not affected by the smoothing of the spheroid border.

To conclude, on the first hand, the shape index provides a quantitative measure of the circularity of the object. It is highly dependent on the roughness of the border. On the other hand, the inertia ratio quantifies the revolution symmetry of the object.

3.3.2 Groups and selection criteria

The morphological parameters that were previously discussed are used to sort all the detected objects into different groups. Fig.3.10 shows images explaining this sorting process.

The different groups are:

- **Discarded objects.** All the detected groups of pixels that have an equivalent diameter smaller than 6 μm, and therefore cannot correspond to cells, or objects that have a low variance value, indicating that they are not in focus (see top image of Fig.3.10 **(b)**).

- **Cell units.** Objects well in focus with an equivalent diameter between 6 and 40 μm. They correspond to single cells or aggregates that are too small to be considered as spheroids. Two cell units are shown in the bottom image of Fig.3.10 **(b)**.

- **Cell aggregates.** Objects in focus with a diameter higher than 40 μm and a low shape index (typically below 0.5) or inertia ratio. They correspond for instance to non reorganized aggregates (see the middle image of Fig.3.10 **(b)**).

- **Spheroids.** Objects in focus, with a diameter higher than 40 μm, a high shape index

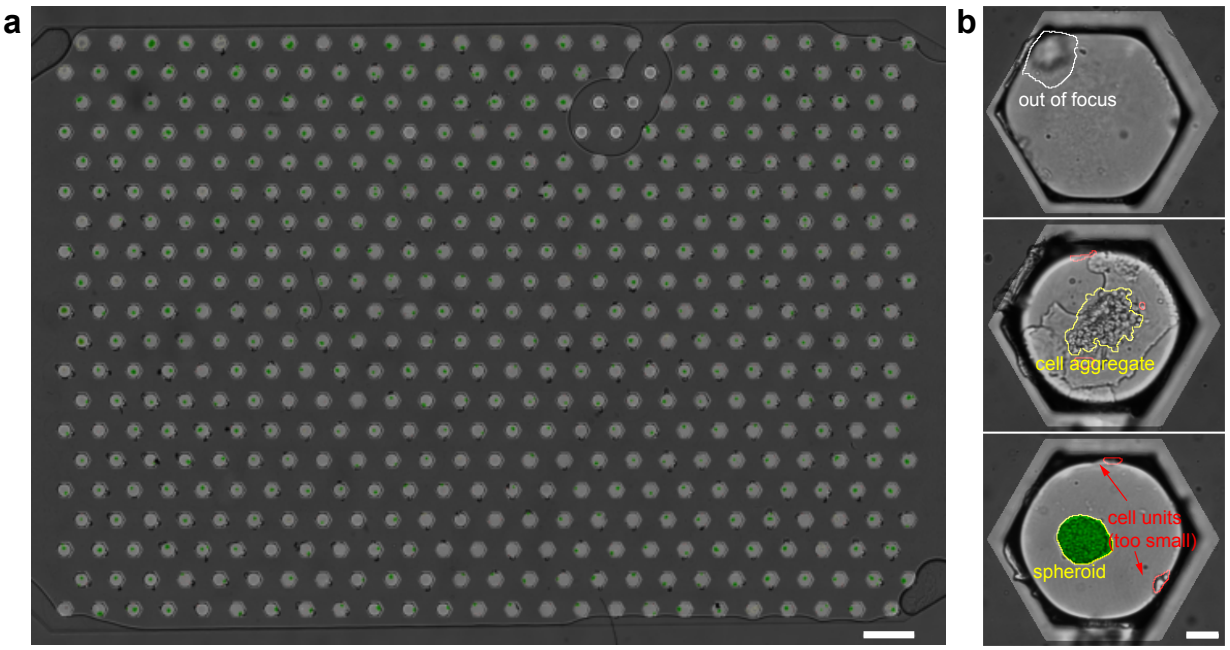

Figure 3.10: Group selection. **(a)** Image analysis on an entire array of 500 anchors with a 250 μm diameter. Anchors are highlighted and spheroids are colored in green. Scale bar is 1 mm. **(b)** Selected anchors showing a discarded object (top),a cell aggregate (middle), a spheroid and some cell units (bottom). Scale bar is 50 μm.

and inertia ratio. They are well reorganized microtissues (see the bottom image of Fig.3.10 **(b)**).

3.3.3 Fluorescent signal

After the cell detection and the group sorting, we can extract data from the fluorescence intensity of the spheroids. This fluorescence intensity will have a biological meaning depending on the staining. Here, we describe the protocol that allows to get a fluorescent signal at the spheroid level.

First, we define the fluorescent signal as the difference between the fluorescent intensity and background:

$$S = I - I_0 \tag{3.3.4}$$

where S is the fluorescent signal, I is the raw fluorescent intensity ans I_0 is the fluorescent background. The fluorescent background is determined locally in each anchor. Fig.3.11 **(b)** shows the fluorescent intensity inside the anchor shown in bright field in Fig.3.11 **(a)**. As discussed in subsection 3.2.2, the Matlab® function *graythresh* is used for setting a fluorescent threshold that minimizes the variance of the pixels above and below this value.

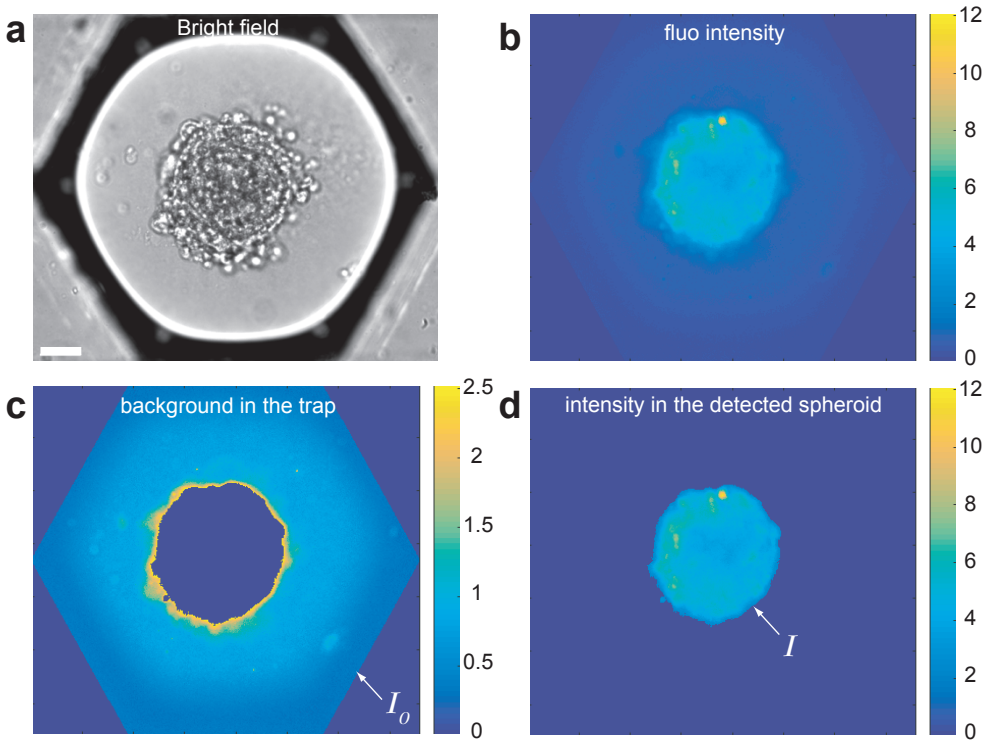

Figure 3.11: Automatized fluorescence detection. **(a)** Bright field image of a spheroid trapped in a 400 μm anchor. Scale bar is 50 μm. **(b)** Fluorescent intensity in the hexagonal trap. The automatized threshold separates the trap between the background intensity area (**(c)**, I_0) and the intensity of the detected spheroid(**(d)**, I). Color bars are in arbitrary units.

Fig.3.11 **(c)** highlights the pixels of the anchor that are below this fluorescent threshold. They represent the background fluorescence coming from the agarose and PDMS. The fluorescent background I_0 is simply the mean value of these pixels. The pixels that are close to the spheroid (in yellow on Fig.3.11 **(c)**) have a value typically twice as high as the other pixels of the background but it does not affect much the value of I_0 since they only represent a small portion of the pixels of the background. Similarly, the fluorescent intensity I is the mean value of the pixels above the fluorescent threshold, which correspond to the spheroid (see Fig.3.11 **(d)**). This protocol allows to determine the fluorescent background locally for each anchor, and thus, we take into account any spatial change in the fluorescent background across the array, whether it comes from the camera or the intrinsic fluorescent background. The resulting fluorescent signal S is a spheroid level data, as it is an average on all the pixels of the spheroid.

Alternatively, the fluorescent intensity can be used for extracting other kinds of spheroid level data, like the viability. The viability value is determined with the following for-

mula:

$$\text{viability}(\%) = \frac{\mathcal{A} - N_{\text{DEAD pixels}}}{\mathcal{A}} \tag{3.3.5}$$

where $\mathcal{A}$ is the projected area (in pixels) and $N_{\text{DEAD pixels}}$ is the number of pixels that are above the threshold for the DEAD signal. In this regard, Fig.3.12 shows a typical example with LIVE/DEAD® staining on an hepatocyte spheroid. The combination of the pixels above the threshold in both channels is used to determine the projected area of the spheroid.

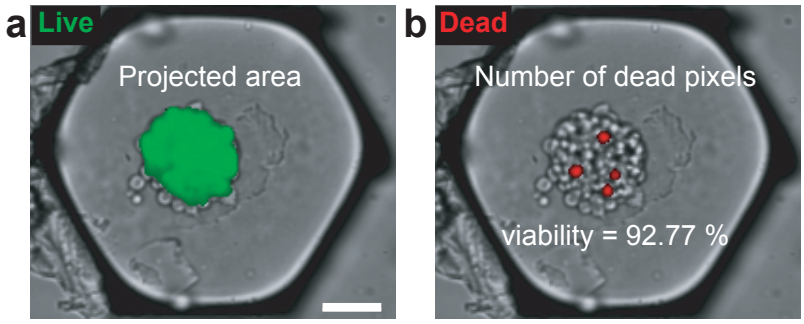

Figure 3.12: Determination of the spheroid viability. Micrographs showing the Live intensity (**(a)**, in green) and the Dead intensity (**(b)**, in red) overlayed on the bright field image of a spheroid trapped in a 250 μm anchor. Scale bar is 50 μm.

3.4 Fluorescence analysis for cellular level data

As discussed in the introduction of this chapter, data can be extracted at the cellular level by looking at single cells inside the spheroids. In this section, we detail the single cell detection protocol and show two different procedures to extract quantitative data from the fluorescent signal at the cellular level. Both of them rely on the detection of local fluorescence maxima.

3.4.1 Detection of the cell nuclei

The easiest way to detect single cells inside a spheroid is to use a nuclear fluorescent signal. Indeed, the nuclei are at the center of each cell and consequently are well separated. Fig.3.13 shows the detection results based on the DAPI fluorescent intensity. In Fig.3.13 **(a)**, the cell centers are simply detected by finding the regional maxima of fluorescence. For each detected cell center, we can compute its distance r to the spheroid center, that can be normalized by R, the equivalent radius of the spheroid.

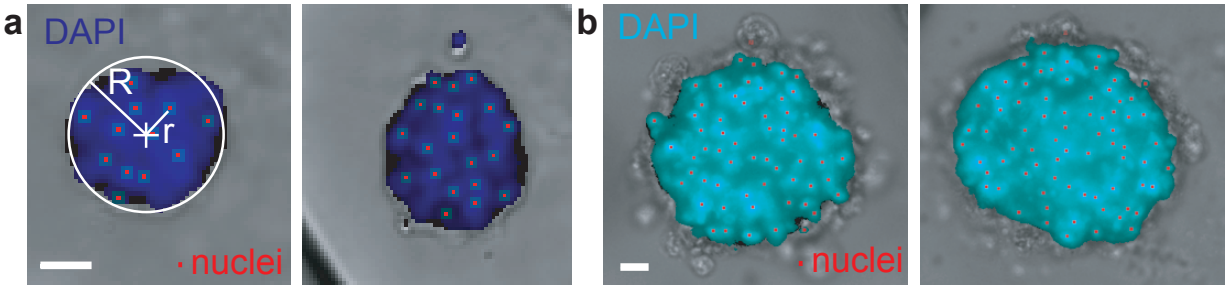

Figure 3.13: Detection of the cell nuclei. Images from the analysis showing the fluorescent intensity only for the pixels of the spheroids, surrounded by the bright field image. **(a)** Nuclei detection on small spheroids with 1.6 μm/pixel. R is the equivalent radius and r is the distance from a nucleus to the spheroid center. **(b)** Nuclei detection on larger spheroids with 0.64 μm/pixel. Red dots represent the center of the detected nuclei. Scale bars are 20 μm.

Fig.3.13 **(b)** shows a similar detection but with more detailed images. When a single nucleus is represented by many pixels, a simple look at the regional maxima can lead to the detection of several maxima. A Gaussian blur of the DAPI image allows to reliably detect the cell centers.

3.4.2 Thresholding the fluorescent signal in the cell nuclei

Once the cell centers are detected, we can extract the fluorescent signal coming from a nuclear staining at the cellular level. For each detected nucleus, we simply average the values of the pixels neighboring the location of the detected nucleus center, the number of considered neighbors depending on the pixel size. Below, we describe a procedure to binarize this fluorescent signal, creating a negative and a positive population among the detected nuclei.

Fig.3.14 shows the example of the BrdU analysis (see subsection 2.3.1) on hepatocyte spheroids at the cellular level. If the cell that was synthetizing new DNA during the BrdU incubation, it has incoporated BrdU as a replacement for thymidine. Therefore the BrdU fluorescent intensity is proportional to the DNA content and it is normalized by the DAPI signal. For these two channels, the signal is calculated by subtracting the local background from the raw intensity (see 3.3.3). Fig.3.14 is the histogram of the BrdU / DAPI ratio for all the detected nuclei of one microfluidic chip. We see that most of the values are below 0.06. Though, some values are three times higher. By looking at the shape of the first peak, a threshold can be automatically set to define the population that has a positive BrdU signal (in green on Fig.3.14).

In this particular case, the $BrdU^+$ nuclei represent 18.03 % of the detected nuclei in the

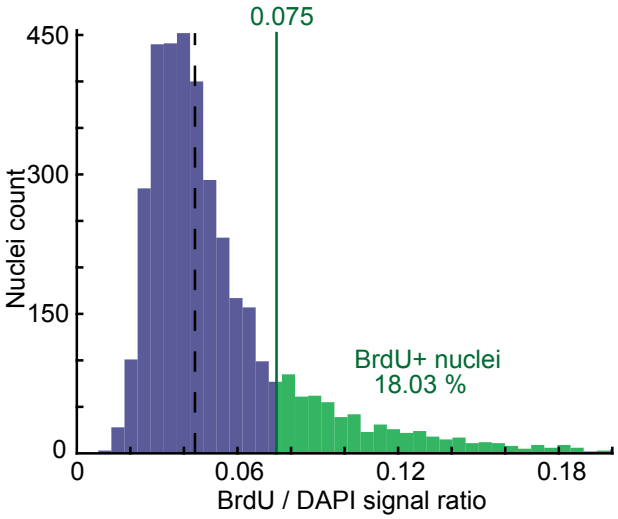

Figure 3.14: Analysis of a nuclear fluorescent signal. BrdU / DAPI signal ratio histogram for one experiment ($n_{spheroids} = 258, n_{nuclei} = 3.832$). The BrdU$^+$ population is highlighted in green. The dashed line indicates the median of the distribution.

chip. This result is a population level data, obtained by a cellular level analysis. We could also extract the ratio of BrdU$^+$ nuclei at the spheroid level (see Fig.4.17 **(b)**) by counting the number of positive nuclei per spheroid.

3.4.3 Detection of a localized fluorescent signal in a cell inside a spheroid

The approach that was previously used with the DAPI intensity for detecting the cell nuclei can be extend to other fluorescent staining procedures for locating the regional maxima of the fluorescent intensity inside the cells. With the careful signal processing presented below, we are able to extract biologically relevant signal values for each of these maxima at the cellular level.

This procedure is illustrated with the albumin signal in Fig.3.15. Albumin is a protein that is produced in the cell cytoplasm of hepatocytes before secretion. The distribution of the related fluorescent intensity is highly inhomogeneous in the cell cytoplasm. In 2D, we clearly see one albumin peak per cell, therefore, it might correspond to the location of the Golgi apparatus where many vesicles filled with albumin must travel. The biological interest of albumin will be further discussed in chapter 4. Fig.3.15 **(a)** is a schematic representation of an image of a spheroid stained for albumin. The pixels corresponding to the maxima are in dark blue, their direct neighbors are in cyan and the other pixels of the spheroid are in gray. Compared to the pixels of the albumin peaks, we can say that the gray pixels represent the fluorescent background of albumin inside the spheroid and consequently we

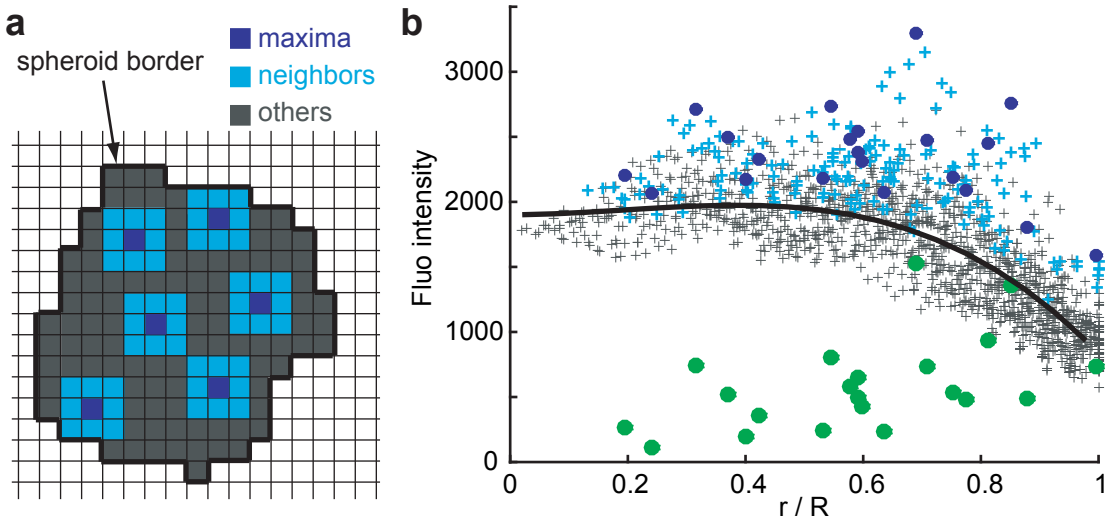

Figure 3.15: Analysis of a cytoplasmic inhomogeneous fluorescent signal. **(a)** Schematic representation of the image of one spheroid. The dark blue pixels represent the location of the fluorescent maxima, the cyan pixels are the pixels neighboring these maxima and the intra-spheroid background pixels are shown in gray. **(b)** The intensity of the pixels from a spheroid is computed with r/R. Each blue dot is a local maximum and the cyan crosses are its neighboring pixels. The grey crosses are the other pixels. The black line represent a polynomial fit of the grey crosses. The green dots represent the peak signal, obtained by subtracting the fitted background from the peak intensity.

can use their value to transform the raw fluorescent intensity of the albumin peaks into relevant fluorescent signals.

This is what is done in Fig.3.15 **(b)** that shows the intensity evolution of the pixels of one spheroid with the normalized distance to the spheroid center r/R (see Fig.3.13 **(a)**). $r/R = 0$ at the center of the spheroid and $r/R = 1$ on its edge. The raw intensity of the detected albumin peaks is represented by the large dark blue disks. The intensity of the pixels neighboring each peak location is shown with cyan crosses. The intensity of the other pixels of the spheroid is represented with gray crosses. As the value of these background pixels (grey crosses) varies with r/R, the fluorescent background inside each spheroid is calculated by fitting their intensity with a polynomial: $ax^3 + bx^2 + c$ with $x = r/R$. Finally, the albumin peak signal is obtained, at a given r/R value, by subtracting the corresponding value of the background fit from the raw peak signal. This signal is represented on the graph with large green disks.

The calculus of this cellular level fluorescent signal takes into account the influence of the out of focus intensity inherent to the imaging of 3D microtissues with non confocal microscopes (see subsection 3.1.1). As the microtissue has a spherical shape it is not surprising to observe a background intensity that is maximum at the center of the spheroid (black

line in Fig.3.15 **(b)**). This procedure is used in chapter 4 for the cellular level data of the albumin signal and also in chapter 5 for the accurate measure of the caspase-3 signal.

3.5 Interpolating the cellular shape with a Voronoi analysis

The knowledge of the nuclei locations can also be used to extrapolate the cellular shape with a mathematical operation called the Voronoi transformation. This gives access to a new set of morphological data at the cellular level, like the cell diameter or the layer classification. In this last section, we describe the Voronoi operation, discuss its biological interest and its integration in the analysis protocol.

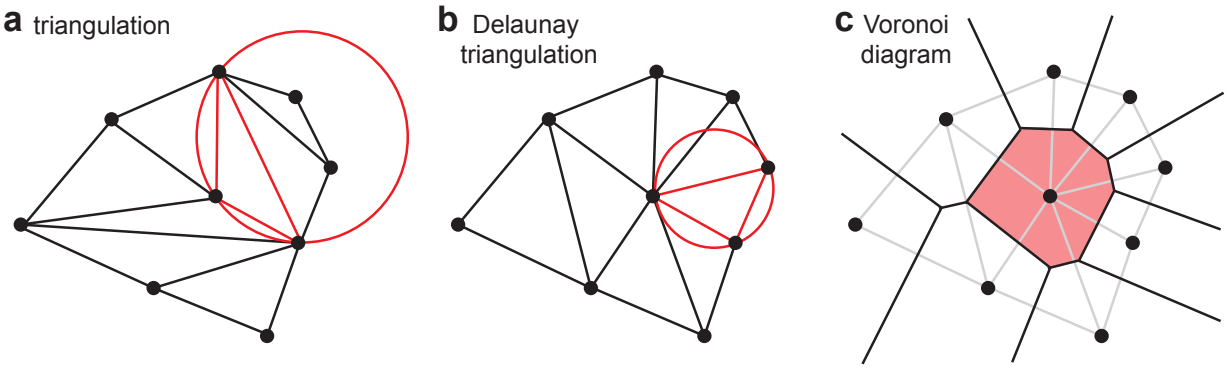

Figure 3.16: Delaunay triangulation and Voronoi diagram. Simple triangulation **(a)** and Delaunay triangulation on 9 points (black dots). The red circles represent the circumcircles associated with the red triangles. **(c)** Voronoi diagram (black) corresponding to the previous Delaunay triangulation (grey). One Voronoi cell is overlayed in red.

Fig.3.16 **(a)** first presents the principle of a triangulation. The area between a given set of points (black dots) in the 2D plane can be filled with non intersecting triangles. It is called a triangulation of the plane. The Delaunay triangulation is the triangulation where the circumcircles of each triangle do not contain any of the other data points (shown in red in Fig.3.16 **(a)** and **(b)**). Therefore, Fig.3.16 **(a)** represents one of the many possible triangulations between the 9 given points and Fig.3.16 **(b)** shows the unique Delaunay triangulation. The Voronoi diagram (Fig.3.16 **(c)**) is the dual graph of the Delaunay triangulation. It separates the 2D plane into Voronoi cells (one is highlighted with a red overlay), one for each point. There is only one given point (black dot) in each Voronoi cell and each Voronoi cell defines the area of the plane that is closest to this given point. Each edge of the Voronoi cells is the perpendicular bisector of a segment of the corresponding Delaunay triangulation. Voronoi diagrams can have practical implications. For instance, let us imagine that the Voronoi diagram of Fig.3.16 **(c)** represents the map of a country and

that each data point stands for the location of an airport. If an emergency that requires landing happens to a plane flying in the red area, the closest airport to land will be the airport at the center of the red voronoi cell.

If the given points are cell centers, the Voronoi diagram provides a good approximation of the cell shape. Fig.3.17 shows the Voronoi tansformation on a confocal slice of a cellular spheroid. First, the DAPI intensity and cell centers are displayed on Fig.3.17 **(a)**. The white lines constitute the Delaunay triangulation of these cells. In Fig.3.17 **(b)**, we can see in red the phalloidin that binds to the actin. In the case of a spheroid, the actin is mainly cortical, meaning that it is located close to the cell membrane (that will be discussed in section 4.4). The corresponding Voronoi diagram is shown in white and we can see that it is a fairly good approximation of the cell shape.

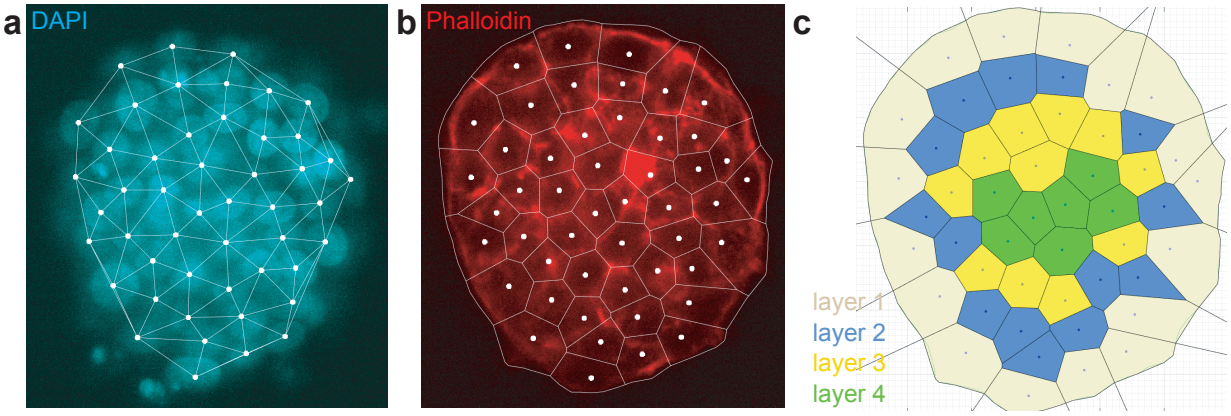

Figure 3.17: Voronoi diagram on cells. **(a)** Delaunay triangulation (white) on detected cells overlayed with the corresponding confocal DAPI slice (cyan). **(b)** Corresponding Voronoi diagram (white) overlayed with the confiocal phalloidin slice (red). White disks represent the center of the detected cell centers. **(c)** Voronoi cells colored according to the layer assignment.

It is worth noting that a Voronoi diagram is not usually closed, normally the edges join at the infinite point. In our analysis, we incorporated a border, corresponding to the edge of the detected spheroid, that cuts the Voronoi cells corresponding to the outermost layer of the spheroid. This step can lead to apparent detection errors for the spheroids whose border has some concave portions. Indeed, we implemented a custom code for creating a concave hull around the detected spheroid border that helps defining a more representative border (see Fig.3.18 **(a)**). Nevertheless, the area of some cells of the outermost layer can be overestimated (Fig.3.18 **(b)**).

This Voronoi analysis gives a insight into the spheroid structure by providing new cellular level data. For instance, the number of cellular neighbors (in the observation plane) can be easily calculated for each cell by counting the Delaunay segments that meet at a each cell center. The Voronoi cells can also be used to calculate the equivalent diameter of each

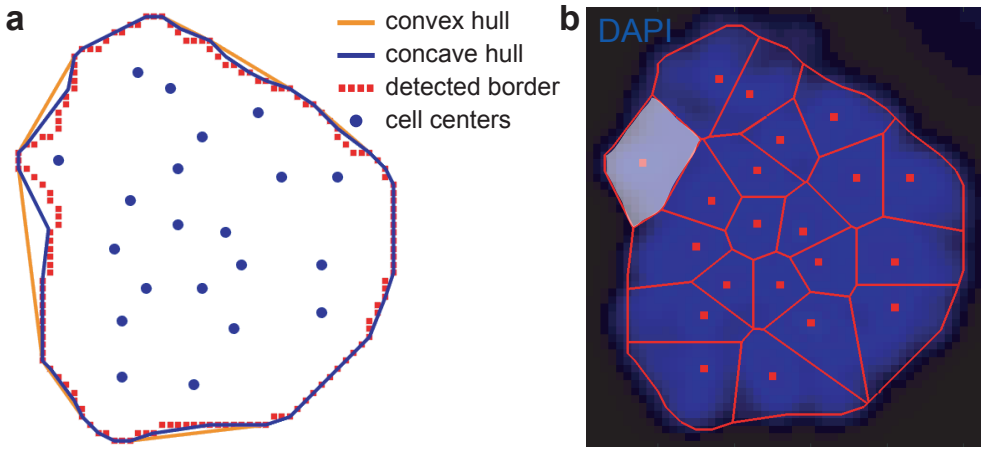

Figure 3.18: Adding a border to the Voronoi diagram. **(a)** Convex (orange) and concave (blue) hull around a spheroid border. **(b)** The concave hull delimits the edges of the Voronoi diagram. The Voronoi cell highlighted in white has a slightly overestimated area.

detected cell inside the spheroid. Moreover, we can assign a cell layer number to each detected cell, as shown in Fig.3.17 **(c)**, the layer 1 being the outermost cell layer.

Finally, the Voronoi cells can be used for the fluorescent signal at the cellular level. We can simply average the values of the pixels of each Voronoi cell to get a mean fluorescent intensity per cell. In the context of the peak detection described in subsection 3.4.3, each detected peak can now be assigned to a cell, allowing, for instance to correlate its intensity with the cellular size.

The image analysis techniques that are described in this chapter are not limited to 3D cell culture. Indeed, the same protocols can be used for extracting quantitative data from images of 2D cultures (see for instance the viability and proliferation data in chapter 4). The only difference is that the detected cells are not sorted into structural groups, thus, data is acquired at the cellular level and can be average at the population level.

Conclusion of Part I

In this first part, we presented a highly integrated microfluidic platform for 3D cell culture, stimulation and analysis. Cells are encapsulated in liquid agarose droplets at 37°C. The droplets are produced with a junction combining flow focusing and step emulsification and their stability is ensured by the surfactant adsorption which takes place in the emulsification channel. Droplets are then guided with rails to fill homogeneously the trapping chamber, whose density can be optimized depending on the application. If the trapped droplets are smaller than the anchors, the cells sediment when the external flow is stopped. They gather at the bottom of each droplet, where they can rearrange to form a single spheroid. If the trapping efficiency is high enough, gelating the agarose droplets and removing the surfactant allows to exchange the external oil with culture medium without displacing the hydrogel beads. Fresh nutrients can diffuse throughout the hydrogel matrix and the culturing time can be extended. Since there is only one single aqueous phase in the microfluidic chip, we can perfuse the chamber consecutively with different solutions, for instance for an immuno-staining protocol. Perfusion can also be used to set different culture conditions in the same chamber. This overall protocol is summarized schematically in Fig.3.19.

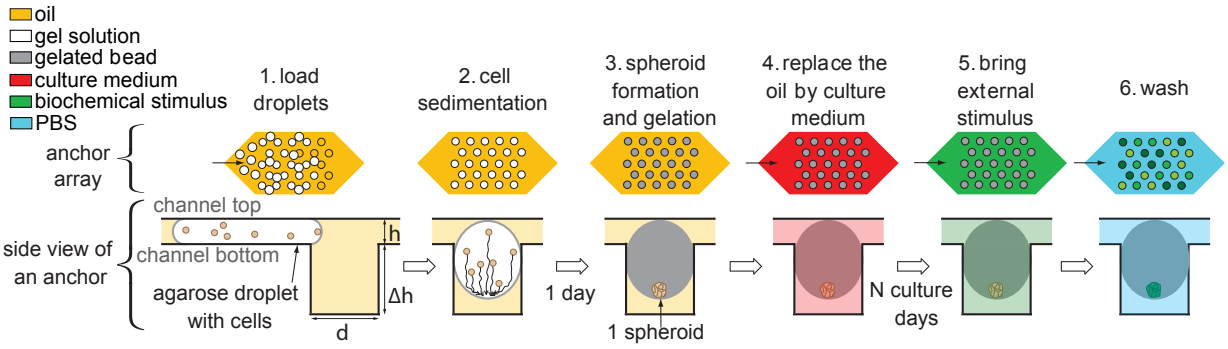

Figure 3.19: Protocol of a typical experiment. Schematic view of the different steps of the protocol with the trapping chamber (top) and the side view of an anchor (bottom). The black arrows indicate the presence of a flow in the chamber.

Agarose helps immobilizing the spheroids and facilitates the perfusion and imaging

steps. In addition, the selective melting of an agarose bead with an infra-red laser enables controlled recovery of an intact spheroid off chip.

Despite this protocol requires several time scales, from a second to a week, all the operations are well integrated in the same microfluidic platform. Several droplets are produced every second and they need a few minutes to reach and fill the entire anchor array. After 5 minutes under static conditions, the sedimented cells can start to reorganize into spheroids overnight. The gelation and phase change take a couple hours and enables to continue the cell culture for days. These time scales are represented on a logarithmic axis on Fig.3.20.

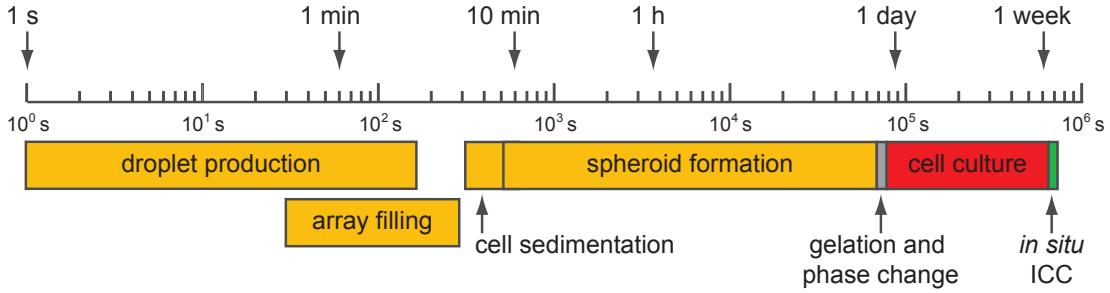

Figure 3.20: Time scales of a typical experiment. Logarithmic representation, from 1 second to 1 week, of the protocol for a 1 week culture experiment followed by an *in situ* immuno-cyto-chemistry (ICC).

The image acquisition protocol can also be excetuted at different time scales. We can either choose to follow dynamically a process like the spheroid formation in real time or to only extract data after a given culture time. This versatility is made possible by the immobilization of the droplets over the entire experiment course.

After acquisition, the image analysis can provide multiscale cytometry of the 3D cell culture. Results can be computed at the population level like usual biological results, such as a mean viability or a production level of a given protein. Data can also be quantitatively extracted in a high-throughput manner at the spheroid level in order to study morphological parameters and fluorescent signals individually. Specific methods have also been developed to measure data at the cellular level inside the spheroids.

Between the beginning of my PhD and the time I wrote this manuscript, many approaches were developed in the literature for the high-throughput and reliable production of size controlled spheroids in microfluidics. First, microarrays can be implemented in monophasic formats which allow perfusion. For instance, Frey *et al.* [54] have incorporated flow perfusion in micro-hanging droplets connected one another with microfluidic channels. Although this open format allows selective recovery, the created spheroid array suffers from a low density. Alternatively, non adhesive wells have been used in microfluidic channels to capture the injected cells after sedimentation and to create monodisperse spheroids [55, 56].

The immobilization of the spheroids under flow conditions facilitates medium exchange, dynamic monitoring and *in situ* fluorescent staining.

Second, spheroids have been created in microfluidic droplets, for instance in alginate capsules [57] or in double emulsions [58]. In the latter case, nutrient can diffuse throughout the oil layer isolating the droplet from the continuous aqueous phase. Spheroid encapsulation also allows to use biologically relevant hydrogels. As an example, Siltanen *et al.* [59] demonstrated the control of the differentiation of mouse embryoid bodies encapsulated in a PEG/heparin hydrogel droplets which can immobilize specific growth factors. However, the spheroids were observed off chip, which limits the control over the culture conditions. In addition, the phase change or the immuno-cyto-chemistry procedures usually requires to physically separate the droplet production from the observation. In our case, this issue is overcome by the use of capillary anchors that ensures an efficient and passive trapping of the droplets. The trapping efficiency is sufficient to perform the replacement of the external oil by an aqueous phase *in situ* without moving the hydrogel embedded spheroids from their anchor. We believe that the integration of this phase change is a unique feature of this microfluidic chip.

Consequently, there is currently a strong effort for developing a versatile microfluidic platform for 3D cell culture. Nevertheless, there is, to the best of our knowledge, no platform able to combine efficiently the advantages of droplet microfluidics (high-throughput, low volumes, controlled perfusion), microarrays (immobilization, selective extraction) and hydrogels droplets (phase change after gelation, encapsulation).

The main advantage of our microfluidic platform lies in its high level of integration and high versatility. Similar to microarrays, we can create size controlled spheroids on a static high-density pattern. We can even selectively extract one viable spheroid of the array like a micropipette would do. We also benefit from the microfluidic format that allows the encapsulation in hydrogel droplets, as well as the controlled and selective perfusion of some parts of the array. In addition, image analysis can provide quantitative in-depth and high-throughput results at every stage of the experiment.

There are some very recent examples of the integration of the phase change on hydrogel droplets encapsulating adherent cells [60, 61] but they lack the universality that we previoulsy demonstrated. By relying on serial designs they limit the perfusion protocols available in a large chamber and do not enable the selective recovery of a single spheroid. They also do not provide a biological analysis comparable to what is obtained with multi-scale cytometry in the following part of this PhD thesis.

Part II

High-throughput and multiscale cytometry on cellular spheroids

In this second part, we present the biological results obtained on 3D cell cultures of two different cell types. It constitutes a proof-of-concept for the technology discussed in Part I. The results obtained by multiscale cytometry are presented at the population, spheroid and cellular level.

Chapter 4 is dedicated to hepatocyte spheroids. First, we analyze dynamically the spheroid formation process and discuss the influence of this culture format. Then, we investigate the morphological characteristics of the spheroids. We demonstrate that these spheroids are viable, proliferative and functional and the correlation between functionality and morphological parameters is investigated at the spheroid and cellular level. Furthermore, we perform a spatially and dynamically controlled perfusion of an hepatocyte spheroids array with a drug known for its effects on the liver. The results are analyzed at each time point with multiscale cytometry which provides an insight on the drug effect at different scales.

In chapter 5, we use our microfluidic platform for creating well organized spheroids with human mesenchymal stem cells (hMSCs), as demonstrated by a detailed morphological analysis. We investigate the expression of caspase-3 (Casp3) and cyclooxygenase-2 (COX2), 2 enzymes involved in the regulation of the therapeutic properties of hMSCs in 3D. First, the activation of Casp3 undergoes dynamic changes at the spheroid and cellular level. Second, we emphasize a consistent higher COX2 expression in the cells close to the spheroid edge.

Chapter 4

Hepatocyte spheroids: fonctional microtissues for drug toxicity experiments

4.1 Introduction to liver function and tissue organization

The liver is a vital organ located just below the diaphragm at the height of the stomach (Fig.4.1 **(a)**). It is the heaviest and largest gland of the human body and it supports many fonctions.

Liver anatomy and cellular types. The liver has a strong hierarchical architecture. It is divided into macroscopic lobes but its mesoscopic functional unit is the liver lobule (Fig.4.1 **(b)**). These cellular structures have an hexagonal shape around a central vein and are subdivided into liver sinusoids joining the edges to the centers of the hexagons. The sinusoid is the place where the oxygen-rich blood from the hepatic artery and the nutrient-rich blood from the portal vein (coming from the gastro-intestinal tract) mix (Fig.4.1 **(c)**). The liver sinusoidal endothelial cells create a highly porous barrier between the sinusoid lumen and the liver cells. About 60 % of the liver cells are parenchymal hepatocytes which are responsible for most of the liver functions. They are further separated from the sinusoidal endothelial cells by a protein-enriched interface called the space of Disse (Fig.4.1 **(d)**) where are located the hepatic stellate cells that are activated in case of liver

injury. Finally, Kupffer cells are specialized macrophages that play a major role in red blood cells recycling.

Many gradients are maintained across the liver sinusoid. For instance the bile acids are secreted by the hepatocytes and driven to the bile ductules at the edges of the lobules. There is also an oxygenation gradient from the hepatic arteriole to the central vein.

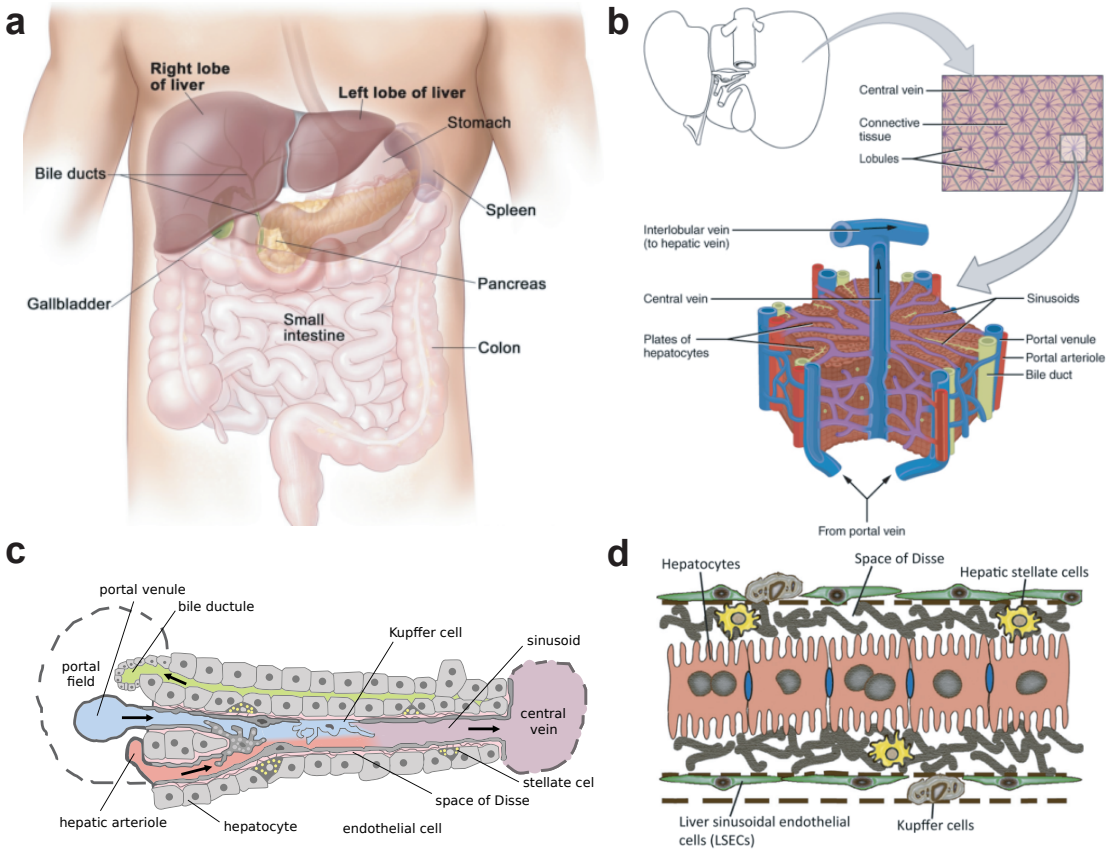

Figure 4.1: Hierarchical liver anatomy. **(a)** Organ level (reproduced from *http://anatomy-bodychart.us/*). Liver lobule **(b)** and liver sinusoid **(c)** (reproduced from *Wikipedia*). **(d)** Cellular level organization (reproduced from Vu *et al.* [62]).

Hepatocytes and liver function. Hepatocytes are the most important liver cells since they represent about 80 % of the liver volume and cumulate many critical functions. First, they secrete bile acids that are collected in the bile ductules and then injected at the entrance of the intestine via the duodenum to help the digestion. Then, they transform a lot of glucose to glycogen via the glycogenesis, a critical process in energy storage and release. Hepatocytes are also responsible of the blood detoxification thanks to enzymes such as the cytochromes P450 (known as CYPs). For instance, most of the drugs that enter the blood stream are metabolised by the hepatocytes, making them natural models

for drug testing purposes. Finally, these cells produce a lot of useful hormones or proteins such as albumin. Albumin is the most common protein in blood serum and is responsible for osmotic homeostasis or the transport of many molecules in the bloodstream.

Reproducing liver functions *in vitro* with hepatocyte spheroids. Primary cells harvested from rat undergo a rapid dedifferenciation when cultured in 2D [63]. Indeed, the expression levels of many molecules involved in liver-specific functions decrease rapidly in hepatocytes cultured in 2D conditions, compared to *in vivo* levels. Meanwhile, hepatocyte spheroids (also known as hepatospheres) maintain significantly higher expression levels than cells cultures in 2D for at least 10 days of culture. For instance, hepatocyte spheroids have been showed to produce high levels of albumin for weeks [64] and also maintain high expression of transcription factors (hepatocyte nuclear factor HNF-4) or enzymes (such as CYP1A1 or enzymes involved in the urea cycle) [65]. The higher involvement of cellular junction (for instance with E-cahderins or connexin-32) in 3D conditions is a major factor to explain the increased functionality over 2D conditions [66, 5]. This observation has a critical impact on toxicity studies since 2D models are strongly limited to reproduce *in vivo* conditions. As a result there is a strong effort to engineer functional liver models [67], for instance by combining 3D conditions and co-culture with hepatocytes and stellate cells [68].

In this chapter, we use H4-II-EC3 cells (a rat hepatoma cell line) as a model of hepatocytes. We allow them to create spheroids in microfluidic droplets and monitor their albumin production as a marker of their functionality [69].

4.2 Chip and trap design

Specific anchors were designed for creating hepatocyte spheroids (Fig.4.2 **(a)**). They have a 250 μm diameter (d) and depth (Δh) while the trapping chamber has a 95 μm height (h). This geometry provides a strong anchoring force since $h < \frac{d}{2}$ (see condition (1.1.4)). Contrary to all the other features of this chip, the anchors are located at the bottom of the chamber (see appendix A.1 for details). These anchors are included in a chip (Fig.4.2 **(b)**) whose design follows the principles discussed in section 1.2. The droplet production stage (Fig.4.2 **(c)**) is constituted of a junction for combining flow-focusing and step emulsification techniques with 50 μm wide spacers. The height before and after the step are respectively 65 and 80 μm. The 200 μm wide inlets are followed by a 150 μm restriction and a 450 μm wide straight emulsification channel in which the surfactant can adsorb at the water/oil interface without risking any coalescence (see subsection 1.3.2). The droplets are then guided across the chamber width with 6 diverging rails having a 95 μm height. In the trapping chamber (Fig.4.2 **(d)**) 500 hexagonal anchors are arranged on an hexagonal pattern with a 680 μm pitch. It allows the non-trapped droplets to flow in between filled anchors and gives a

trapping density of 250 anchors/cm^2. A picture of the actual microfluidic chip is shown in Fig.4.2 **(e)**.

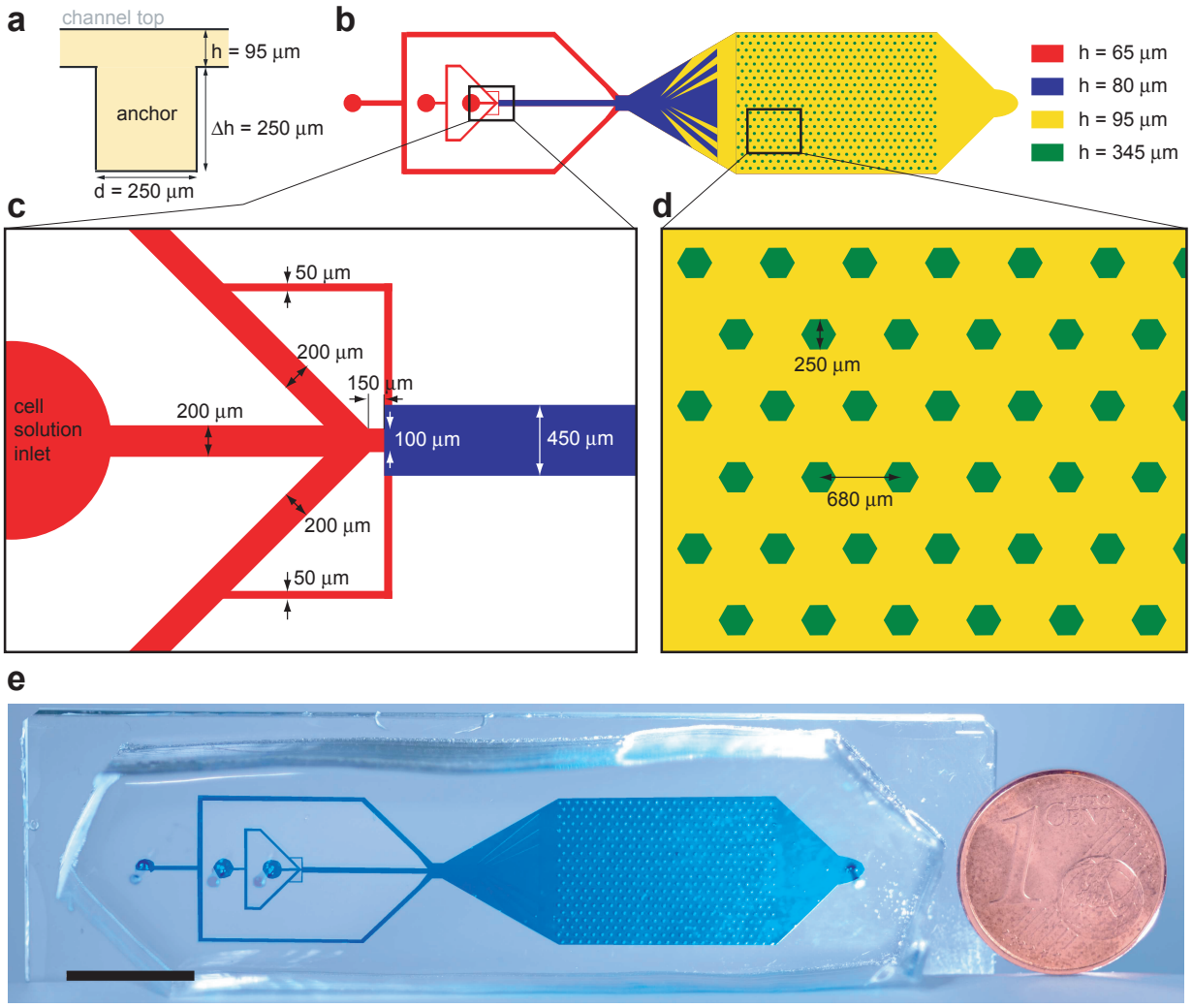

Figure 4.2: Trap and chip design. **(a)** Side view of an anchor with dimensions. Schematic top view of the whole chip **(b)**, the junction **(c)** and the anchors **(d)**. **(e)** Picture of the actual chip. Scale bar is 1 cm.

With this geometry the total anchor volume is 18.7 nL. The volume of the droplets produced in this chapter was experimentally measured to 16 nL, ensuring an almost hemispherical interface at the bottom of the trapped droplets. The H4-II-EC3 cells are encapsulated at a concentration of 12.10^6 cells/mL giving an average of 192 cells encapsulated per droplet.

4.3 Dynamics of the spheroid formation

The H4-II-EC3 cells are encapsulated in 0.9 % (w/w) agarose droplets that are trapped in the anchor array previously described (see section 4.2). Then, as explained in section 2.1, the cells sediment and aggregate in each droplet to create spheroids. The results of the observation and analysis of this process are described in this section.

4.3.1 Real-time monitoring of the aggregation

The microfluidic chip is kept at 37°C after the cell sedimentation in order to keep the agarose liquid and thus allow the cell reorganization. As every droplet is now immobilized in the anchor array, the spheroid formation process can be followed in real time by imaging the chip for 24 hours with the motorized stage of the microscope. Fig.4.3 **(a)** shows time lapse images of the cellular reorganization in one anchor. The red line shows the edge of the aggregate detected by image analysis. At the beginning of the acquisition, the cells are well sedimented at the bottom of the droplet and form a rough aggregate that quickly becomes smaller as the cells start to interact with each other. After 23 hours, a round spheroid that has a much smaller projected area can be observed. The decrease of the projected area over time is computed and shown in Fig.4.3 **(b)**. As the total cellular volume can be considered as constant during the process, the decrease of the projected area is an indication of the reorganization in the third dimension. The dynamics of this particular spheroid formation follows an exponential decay with a characteristic time of 13.3 hours.

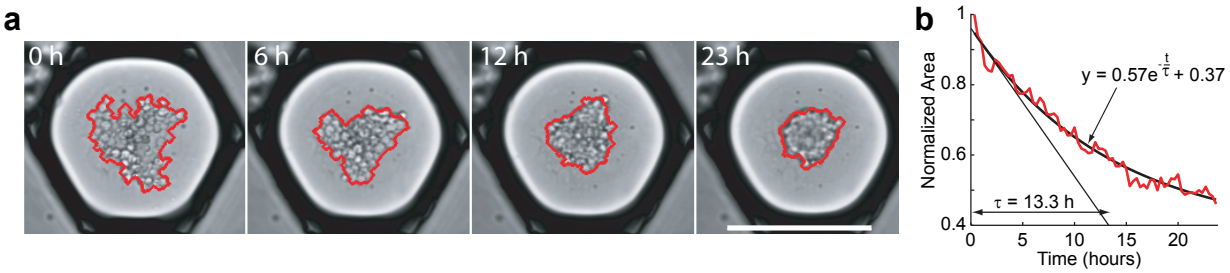

Figure 4.3: Single analysis of the spheroid formation. **(a)** Time lapse of spheroid formation in one anchor. The red line shows the edge of the detected pattern. **(b)** Evolution of the projected area of the spheroid displayed in **(a)** over time, normalized by its value at $t = 0$. The black curve shows an exponential fit, with a characteristic shrinking time τ of 13.3 hours.

This analysis can be performed in parallel for all the anchors of the array, as shown in Fig.4.4 **(a)** for 152 spheroids in the same microfluidic chip. The trend observed in Fig.4.3 **(b)** is reproducible since it describes well the behavior of most of the curves. Nevertheless, a few curves look rather flat, indicating that some aggregates do not reorganize into spheroids.

Similarly, the evolution of the shape index over time is shown in Fig.4.4 **(b)**. In spite of a substantial noise coming the image analysis (see 3.3.1 for details) there is an overall increase indicating the formation of a round structure and the smoothing of its interface during the process.

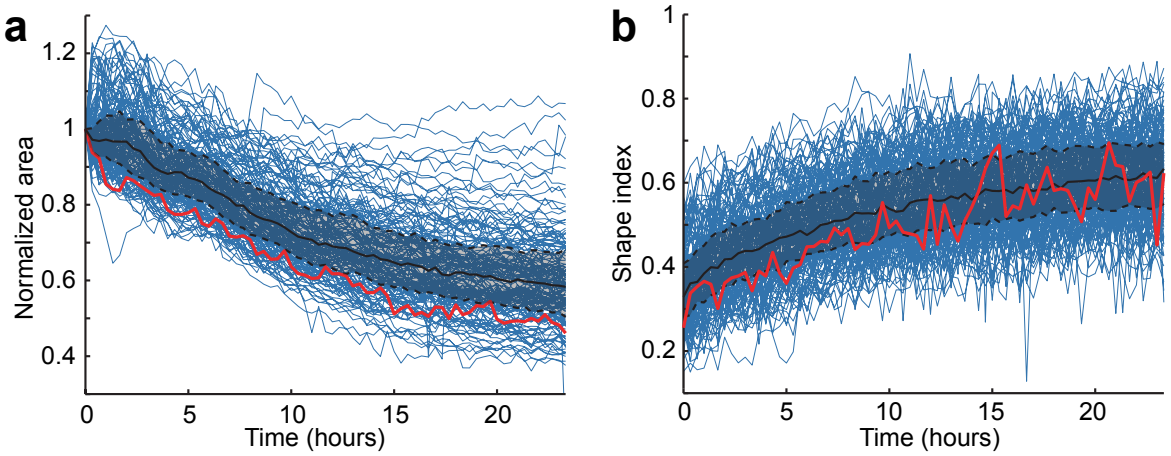

Figure 4.4: Followup of the spheroid formation. Normalized area **(a)** and shape index **(b)** evolution ($n_{spheroids} = 152$) with time. Each blue line represents one spheroid . The red line corresponds to the spheroid in Fig.4.3 **(b)**. Black lines: median. Dashed lines: first and third quartiles.

These measurements can be used to obtain more detailed information. For instance, Fig.4.5 **(a)** quantifies the reproductibility of the shrinkage speed. The median characteristic time τ of shrinkage is 11.2 hours, which is in good agreement with data obtained with similar cells [70]. The fact that the agarose is gelated in our experiments (see section 2.2) after about 20 hours of culture, so roughly after twice the characteristic shrinking time, ensures to get well formed spheroids in the agarose beads. However, the τ distribution shows some high values ($\tau > 20$ hours) corresponding to the aggregates that do not form spheroids. Fig.4.5 **(b)** provides a possible explanation for the slow aggregation of these cells. First, the correlation between the initial and final detected areas in each anchor indicates that many spheroids exhibit an overall shrinkage close to 60 %. Nevertheless, the aggregates well above this line have a low shrinking rate and interestingly all have a high initial area. It suggests that the cell concentration was higher in these particular droplets, potentially leading to a lack of nutrients or exogenous factors to initiate an efficient reorganization. Finally, Fig.4.5 **(c)** shows a dynamic followup of the size distribution. The shrinking is indicated by a shift towards the smaller areas. It also looks like there is a decrease of the polydispersity as the width of the distribution becomes smaller over the shrinking process.

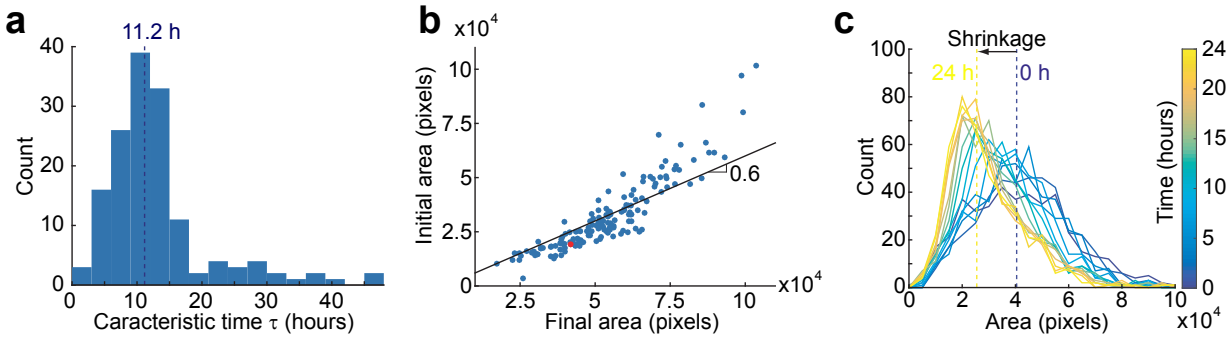

Figure 4.5: Analysis of the spheroid formation data. **(a)** Histogram of the characteristic shrinking time for the analyzed spheroids ($n_{spheroids} = 152$). **(b)** Initial projected areas versus the final areas after the spheroid formation. Each dot corresponds to one spheroid, while the red dot is the spheroid showed in Fig.4.3 **(a)**. **(c)** Area histogram of the 500 detected spheroids over time. Dashed lines: medians.

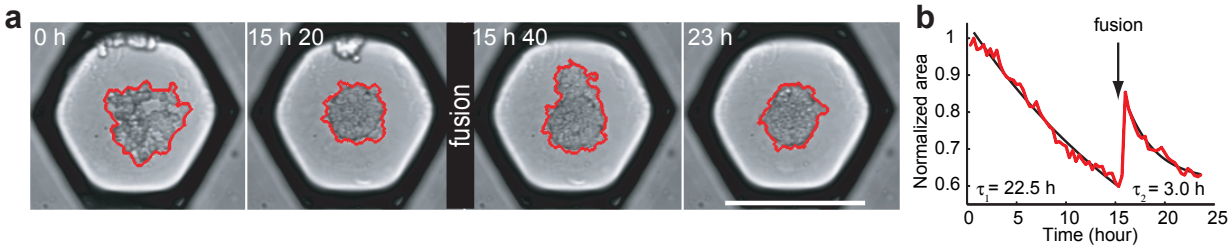

Figure 4.6: Spheroid fusion event. **(a)** Time lapse of the spheroid formation in one trap, with a fusion event between the second and third frame. **(b)** Corresponding time evolution of the normalized area, with two exponential fits shown in black before and after the fusion.

4.3.2 Fusion events during the spheroid formation

Although the droplet array is constituted of 500 anchors, the analysis presented in 4.3.1 only shows the data extracted from 152 anchors. Indeed, many anchors have been discarded because the spheroid formation process is often discontinuous. Many times the cells do not all sediment at the bottom of the agarose droplets but some of them stay close to the anchor side walls. Such a case is described in Fig.4.6 **(a)**. Two separated aggregates can be seen in the first two frames of the time lapse but between the second and third frame the aggregate that was forming close the the anchor side wall fell to the bottom of the droplet, entering in contact with the first aggregate. Then, these aggregates merged into a single spheroid. When analyzing these fusion events, only the largest aggregate is chosen for the data extraction. Consequently, a fusion event is identified when there is a strong discontinuity in the evolution of the projected area, as shown in Fig.4.6 **(b)**. The height of the discontinuity corresponds to the projected area of the aggregate that is added to the previous one. These fusion events can occur with two but also with three and more small

aggregates. It is interesting to notice that most of the time the dynamics of the spheroid formation is accelerated after a fusion event, leading to a characteristic time post fusion τ_2 smaller than the initial one τ_1.

4.4 Morphological characterization of the hepatocyte spheroids

In this section, we describe and discuss the morphological parameters of the hepatocyte spheroids created on chip. We also emphasize the role of the agarose gelation and its effect on the spheroid formation.

4.4.1 Production of monodisperse spheroids

Droplet microfluidics allows the fine control of the spheroid size. The polydispersity histogram for the different detected populations (see 3.3.2) in 35 microfluidic chips combined is shown in Fig.4.7. First, over 10,000 hepatocyte spheroids were detected and analyzed. They have a mean diameter of 72.9 μm, with a Gaussian distribution. The 26.6 % coefficient of variation (CV) indicates a high level of monodispersity for this kind of organoids.

Encapsulating the cells at a higher concentration for a constant droplet volume will produce bigger spheroids. On the contrary, we will have smaller spheroids with a lower initial concentration. The main parameter that influences the CV is the pre-aggregation of the cells in the tubing before the microfluidic channels. As a result, the cell concentration varies from one droplet to another, leading to different spheroid sizes. This effect could be limited by decreasing the cell concentration in the droplets, thus producing smaller spheroids or by creating larger anchors for a similar spheroid size.

In addition, we see a high number of cell units (defined as having a diameter between 10 and 40 μm). The peak between 10 and 20 μm corresponds to single cells and the part between 20 and 40 μm to aggregates that are too small to be considered as spheroids. The cell aggregates (having a low shape index) tend to appear slightly bigger than the spheroids since they are probably flatter (so a larger projected area) than the fully reorganized spheroids.

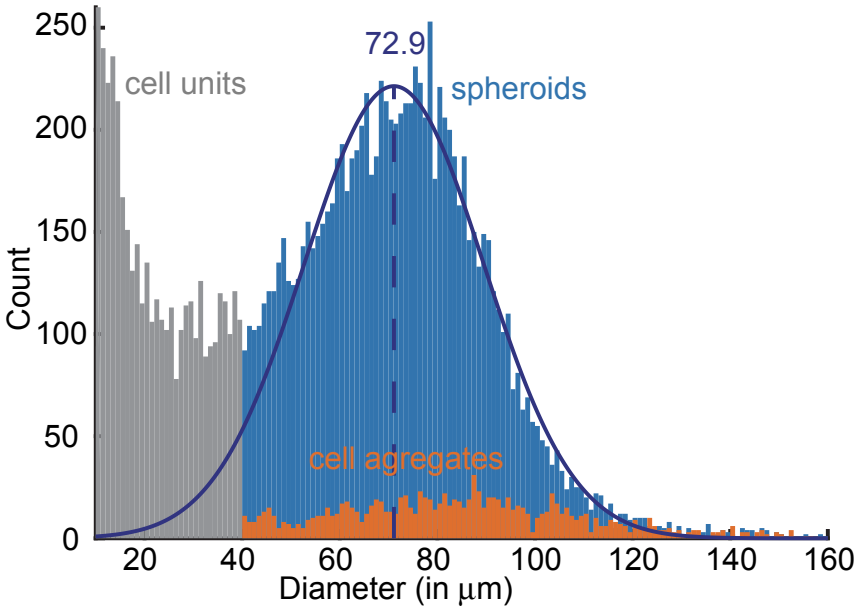

Figure 4.7: Polydispersity. Size distribution of all spheroids (blue, 35 chips, $n_{spheroids}$ = 10,113), cell aggregates (orange, $n_{cell\ aggr}$ = 1,189) and cell units (gray, $n_{cell\ units}$ = 4,146). The blue curve represents a Gaussian fit of the spheroid distribution. Dashed line: mean for the spheroids.

4.4.2 Influence of the agarose gelation on the spheroid formation and culture

Before the agarose gelation, the cells are encapsulated in viscous droplets. Therefore, they can reorganize and stick to one another by draining the fluid separating them. On the contrary, when the agarose is gelated, the cells are embedded in a solid network that they cannot digest, on which they cannot adhere and whose pore size is about 500 nm [50, 51]. So the reorganization of the cells after the agarose gelation must be very limited. It is illustrated in Fig.4.8 which shows no significant change in the spheroid diameter over the culturing time. This contrasts to classical spheroid culture techniques where the culture medium is liquid and where the spheroid growth is continuous [71].

Setting the gelation time of the agarose droplets before the end of the spheroid formation process allows to voluntarily stop the reorganization. Results from these blockage experiments are presented on Fig.4.9 when three conditions are compared (Fig.4.9 **(a)**). 2 experiments were carried out with different gelation moments to show the effect of a disrupted spheroid formation. In the control experiments (D+1), the cells were allowed to reorganize overnight in liquid agarose. The agarose was gelated 20 hours after the droplet loading and the external oil was replaced by culture medium. In the blocking experiments, the spheroid formation was disrupted by gelating the agarose 6 hours (H+6) or 3 hours

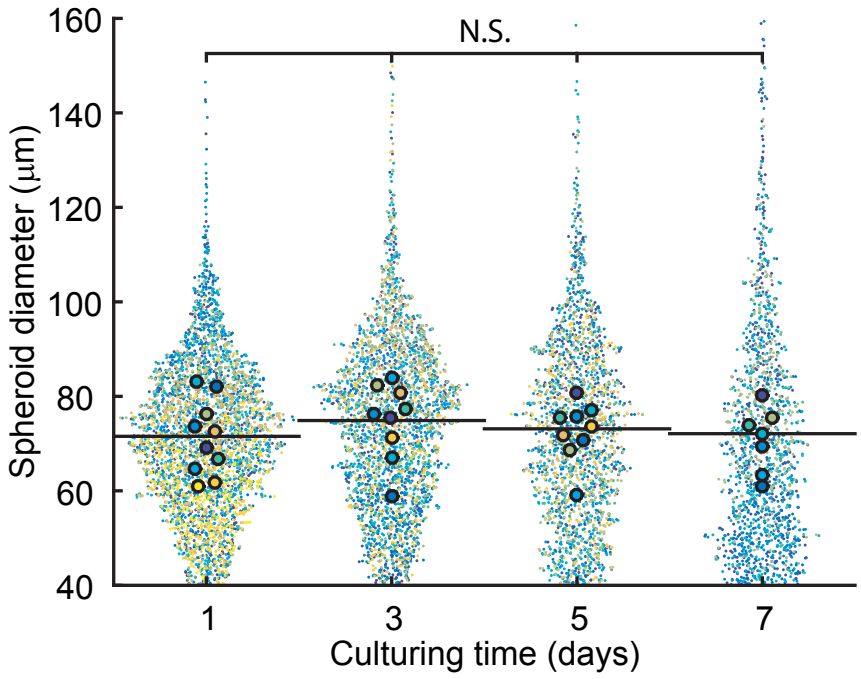

Figure 4.8: Violin plot of the spheroid diameter evolution over time. For each time point, one color corresponds to one chip. Each chip was only analyzed once (no dynamic monitoring). Large colored dots show the mean across each chip while the smaller colored dots represent individual spheroids. Each time point mean is represented by a black line. D+1/D+3/D+5/D+7: n_{chips} = 10/9/9/7; $n_{total\ spheroids}$ = 10,113.

(H+3) after the cell loading. The external phase change always occurred 20 hours after the beginning of the experiment. The cells are then fixed prior to fluorescent staining and image analysis. LIVE/DEAD® staining on the blockage experiments showed no observable effect on cell viability. Fig.4.9 **(b)** shows to what extend a premature gelation affects the shape index of the created spheroids. In the control, there are over 90 % of spheroids created at the end of the experiment while this proportion drops to almost 50 % in the H+3 experiment (Fig.4.9 **(c)**). Finally, an earlier gelation induces a broadened distribution of shape index values with a lower median (Fig.4.9) **(d)**.

Taken together, the results presented in this subsection show that the gelation of the surrounding agarose has an impact on the spheroid behavior. Since the cells are unable to digest or remodel the gelated network, they are physically held in the agarose beads. It defines a constant size for the spheroids over time and the control of the gelation time can be used to block the spheroid formation process and produces aggregates that are not completely reorganized.

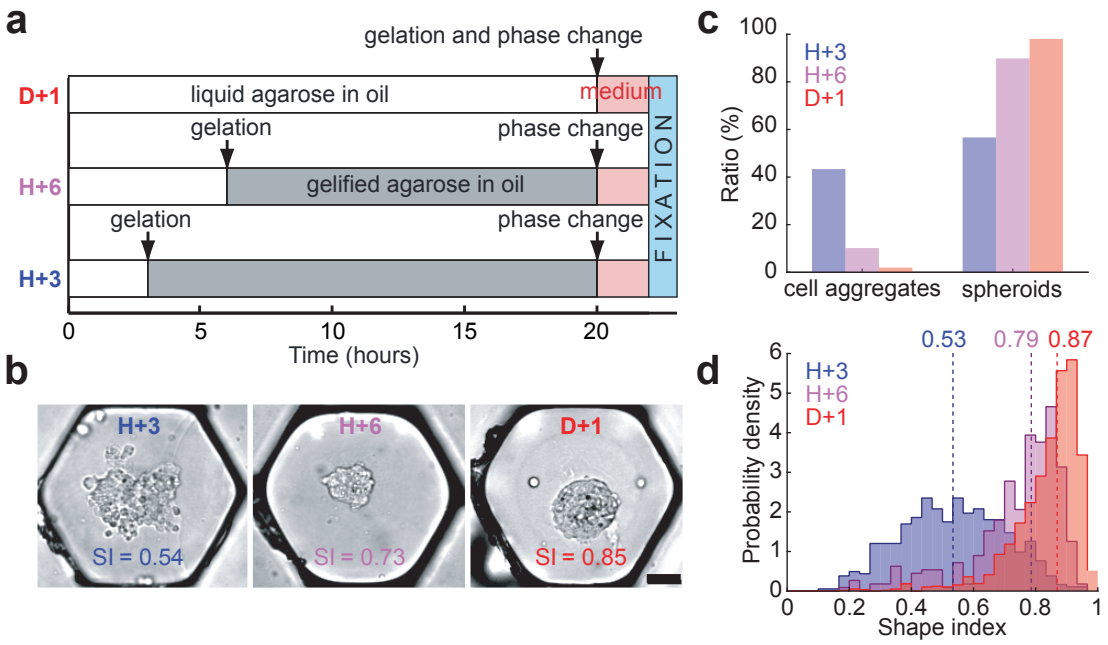

Figure 4.9: Influence of a premature gelation on the spheroid shape index. **(a)** Timeline explaining the experimental protocol. **(b)** Bright field images of one spheroid per condition, with a representative shape index value. Scale bar is 50 μm. **(c)** Evolution of cell aggregates to spheroids ratio. Evolution of the shape index **(d)** with the gelation time. Dashed lines: medians. D+1: red, $n_{spheroids} = 1{,}712$, $n_{cell\ aggr} = 34$, $n_{chips} = 5$, H+6: purple, $n_{spheroids} = 301$, $n_{cell\ aggr} = 34$, $n_{chip} = 1$, H+3: blue, $n_{spheroids} = 311$, $n_{cell\ aggr} = 238$, $n_{chip} = 1$.

4.4.3 Distribution of the cellular size and density across the spheroid structure

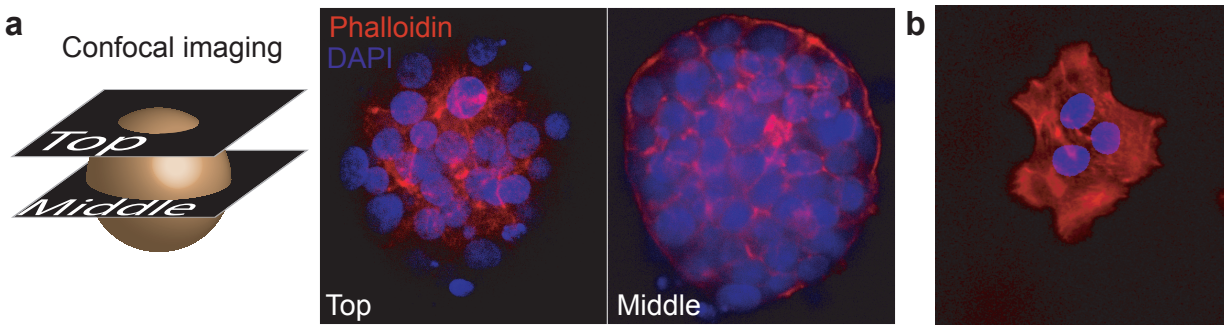

Figure 4.10: Actin staining. Actin organization in one spheroid **(a)** on chip (confocal slices at two vertical positions), and cells in 2D **(b)**.

A first view of the cellular organization in hepatocyte spheroids can be obtained by observing the organization of actin. Fig.4.10 **(a)** shows two confocal slices of an hepatocyte

spheroid created on chip where the F-actin is stained with phalloidin (in red). In the middle plane we mostly see cortical actin close to the cell membranes while the actin organization looks more fibrillar on top of the microtissue. In Fig.4.10 **(b)**, we can see 3 cells cultured in 2D that mostly have cytoplasmic actin fibers. This observation is consistent with previously reported results [72]. These observations suggest that the 3D organization of the cells inside a spheroid plays a major role in the regulation of their phenotype. Before being able to correlate the functionality with morphological parameters at the cellular level, we need to understand quantitatively the spheroid structure.

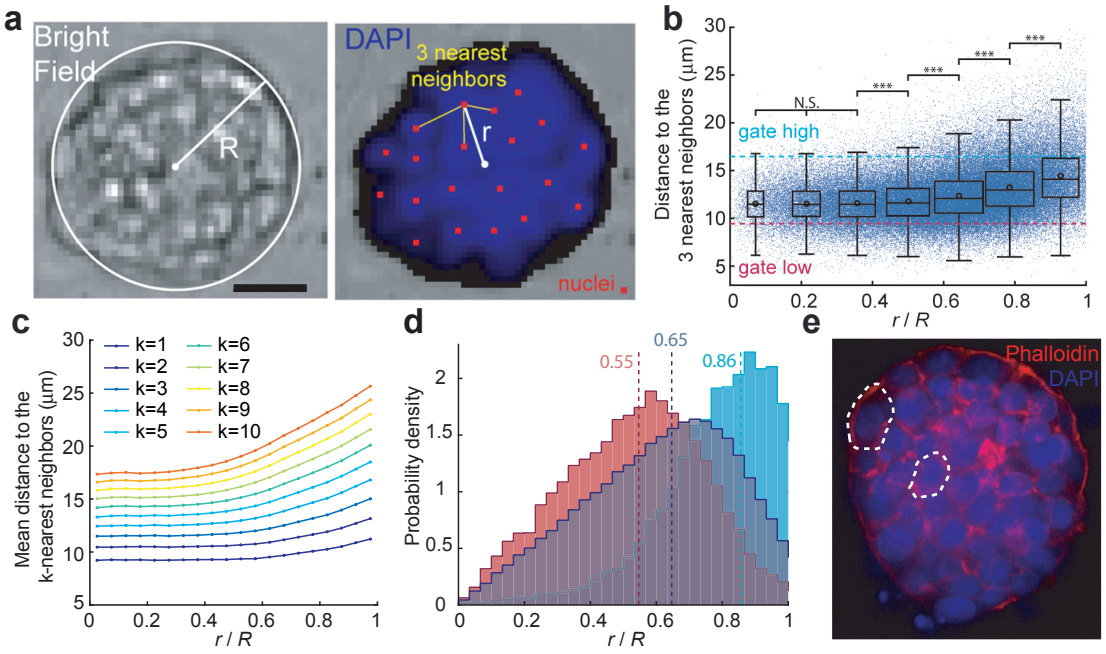

Figure 4.11: Morphology of the spheroids at the cellular level. **(a)** Images for a spheroid in bright field (left) and stained for DAPI (right). The detected nuclei locations are shown with red pixels. Scale bar is 50 μm. **(b)** Mean distance between each cell and its 3 nearest neighbors with r/R (n_{cells} = 128,973, $n_{spheroids}$ = 6,236). The cyan and magenta dashed lines represent the first and last deciles of the data. **(c)** Trends for different values of the number of neighbors k. **(d)** Location histograms of all the nuclei (dark blue) and of the two gated populations in **(b)** (magenta: below the first decile, cyan: above the last decile). Dashed lines: medians. **(e)** Confocal image of the mid-plane of a spheroid stained with phalloidin (red) and DAPI (blue). Dashed lines emphasize two representative cells.

A higher level of detail can be obtained by looking quantitatively at the geometrical parameters of the cells inside the spheroids. It provides an insight into the 3D cellular organisation of the microtissues. We first used the DAPI signal to detect the cell centers and for each of them calculated their normalized distance to the spheroid center r/R (see 3.4.1). $r/R = 0$ at the spheroid center and $r/R = 1$ at the spheroid border. The mean distance between each cell and its 3 nearest neighbors is also calculated and its evolution

with r/R is shown in Fig.4.11 **(b)**. We can see a clear an continuous increase of this distance from 11.5 μm to 14.4 μm when coming closer to the spheroid edge. This trend is very reproducible, does not depend on the number of neighbors that are considered (Fig.4.11 **(c)**) and is further confirmed by the location histograms of the cells having the 10 % highest and lowest values of the mean distance to the 3 nearest neighbors (Fig.4.11 **(d)**). Taken together, these results show that there is a cell density gradient oriented towards the spheroid center, with an constant high cell density in the spheroid core, with r/R values from 0 to 0.4, and a significant decrease for r/R from 0.4 to 1. Eventually, confocal imaging of the spheroids also show a smaller cellular size in the core compared the the edge (Fig.4.11 **(e)**).

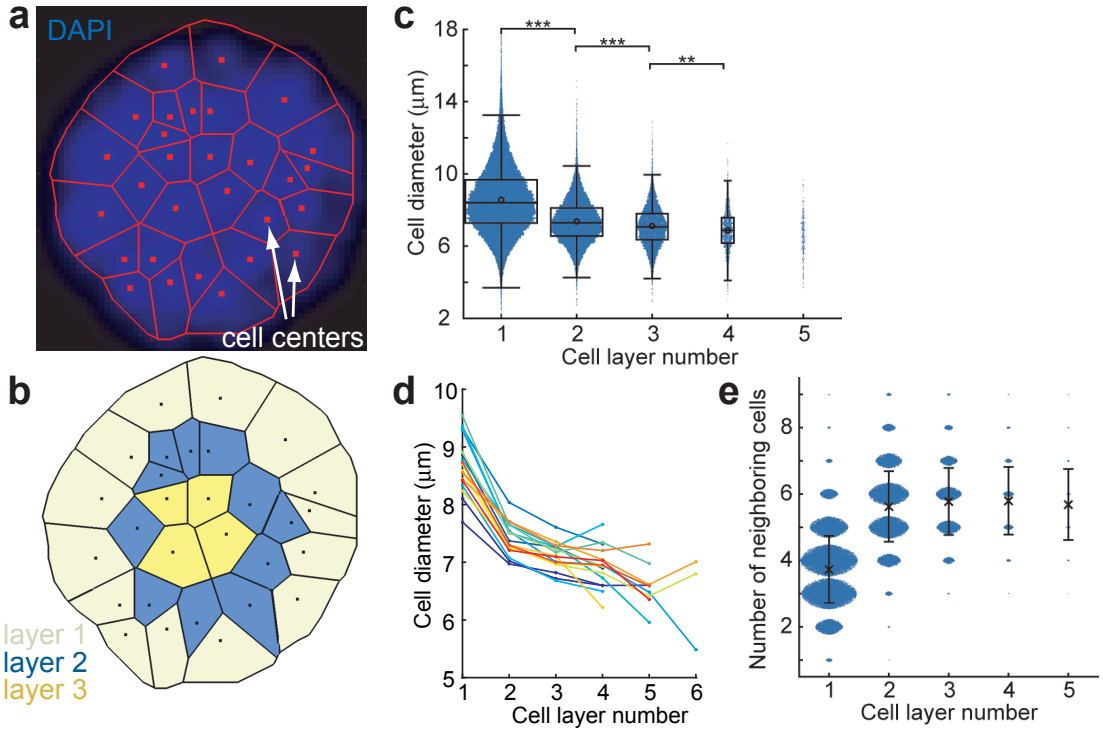

Figure 4.12: Data extracted from the Voronoi analysis. **(a)** Image of a spheroid stained with DAPI and overlayed with its corresponding Voronoi cells (in red). **(b)** Corresponding scheme showing the cell layer attribution. **(c)** Violin plot of the cell diameter with the cell layer number (n_{cells} = 100,139, $n_{spheroids}$ = 4,654). **(d)** Evolution of the cell diameter trends gathered in **(c)** for each microfluidic chip. **(e)** Scaterred plot showing the number of neighboring cells with the cell layer number. The area of the circles at each intersection (i,j) is proportional to the number of cells in the layer i that have j neighbors. The black crosses and error bars represent respectively the mean number of neighbors per cell layer and the corresponding standard deviation.

The Voronoi analysis described in 3.5 can be used to study the spheroids morphology from a different angle. Fig.4.12 **(a-b)** shows the transformation on a typical spheroid having

three different cell layers and Fig.4.12 **(c)** quantifies the cell diameter for each cell layer (the layer 1 being the outermost layer). We first see that very few cells belong to the layers 4 an 5, indicating that most of the hepatocyte spheroids in this study only have 3 layers. Then, we can see a continuous and significant decrease of the cell diameter, from 8.6 μm in layer 1 to 6.9 μm in layer 4. This trend is also very reproducible (Fig.4.12 **(d)**) and the biggest difference is between the first two layers. The measured diameters in the first layer might be slightly overestimated due to the difficulty encountered in detecting rightfully the spheroid edge (see Fig.3.18). The number of detected neighbors is also calculated for each cell layer in Fig.4.12 **(e)**. The mean number of neighbors is very close to 6 for the inner layers, even for the second layer, while it is closer to 4 for the outermost layer. It shows that in the observation plane the cells in the inner layer have an hexagonal shape.

Taken together, these cellular level data reveal the existence a cell density gradient inside the spheroid. In the spheroid core, cells are small and present an hexagonal shape while close to the spheroid edge, the cells are bigger and exhibit a lower density.

4.5 Viability of the hepatocyte spheroids

In order to validate our microfluidic 3D culture model and before infer anything about the spheroid biology we need to first investigate the viability of our microtissues.

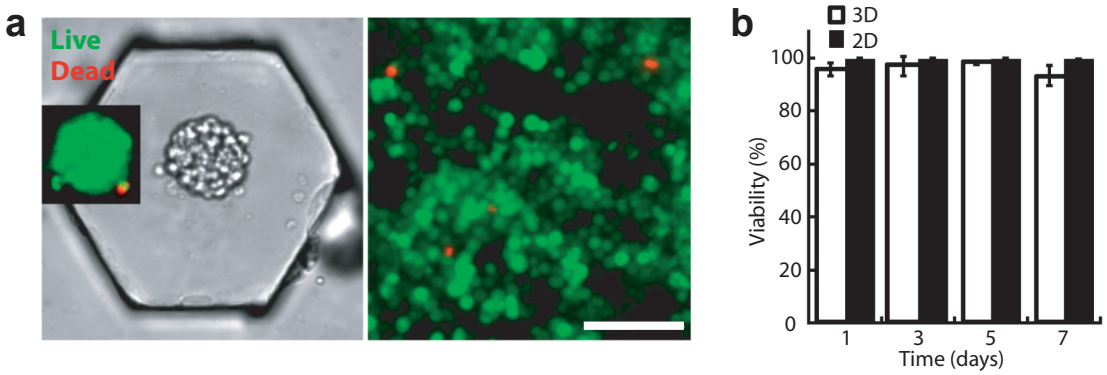

Figure 4.13: 2D/3D population level comparison of the viability. **(a)** Images of one spheroid in an anchor and cells in 2D (right) stained with LIVE/DEAD®. Scale bar is 100 μm. **(b)** Evolution of the viability of the spheroids on chip and of the cells in 2D, during a 7-day culture period ($n_{chips} = 3$; $n_{2D} = 4$).

First, LIVE/DEAD® staining enabled to compare 3D and 2D culture conditions at the population level. We found high and similar values over a 7-day culture period (Fig.4.13). The fact that the viability in 3D is consistently slightly lower than in 2D might come from the definition of the viability for these structures (see equation (3.3.5)). Indeed, the number

of dead pixels is probably overestimated in 3D since dead cells out of the focus plane could still lead to positive pixels.

The viability histogram (Fig.4.14 **(a)**), combining all culturing times, shows that not only the mean viability is high but also many spheroids do not have any dead cell (100 % viability). In addition, there are very few spheroids with a viability below 80 %, resulting in a mean viability of 95.9 %. There is a continuous increase of the number of spheroids having a viability ratio from 80 to 99.5 %. We can conclude that the vast majority of spheroids that do not have a 100 % viability only have very few dead cells.

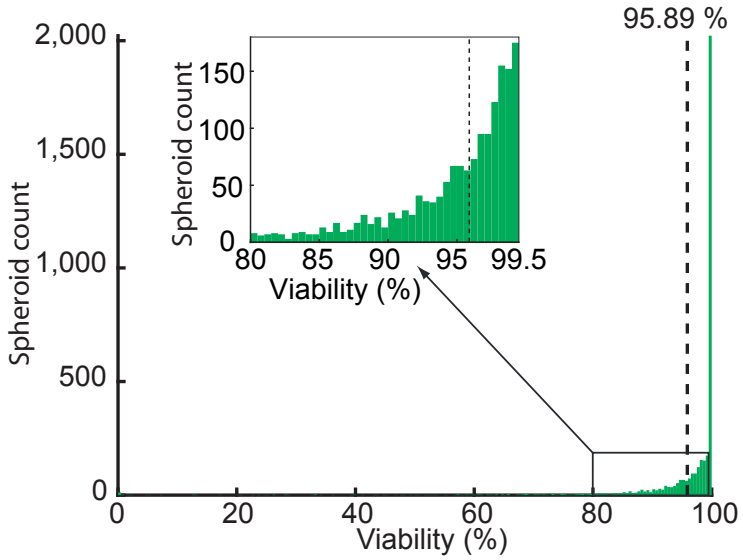

Figure 4.14: Spheroid level analysis of the viability. Histogram of the spheroid viability (n_{spher} = 3,877, n_{chips} = 11). The graph insert shows the part of the histogram between 80 % and 99.5 % viability. Dashed lines indicate mean values.

The cellular level analysis reveals strong spatial heterogeneities in the dead cell location inside the spheroids (Fig.4.15 **(a)**). The tools previoulsly described in 3.4 are used to find that the dead cells are on average significantly closer to the spheroid edge than all the cells (Fig.4.15 **(b)**). This result allows us to calculate for each r/R value the probability for a cell to be dead (Fig.4.15 **(c)**). It is constant at 0.05 for r/R from 0 to 0.8 and then quiclky increases to reach more than 0.2 at the very frontier of the spheroid ($r/R = 1.2$). First, it demonstrates that our spheroids do not have a necrotic core, unlike many of the spheroids in other studies [57]. This can be attributed to the size of these spheroids (an average diameter of 72.9 μm) that is smaller than the oxygen and nutrients typical diffusion lengths [71, 73]. Then, there are two possible explanations for having dead cells preferably at the outside border of the spheroid. Since dead cells are unable to form functional cell-cell junctions they may have been ejected from the spheroid [74]. Alternatively, they may simply have been dead before the spheroid formation step, and thus not incorporated.

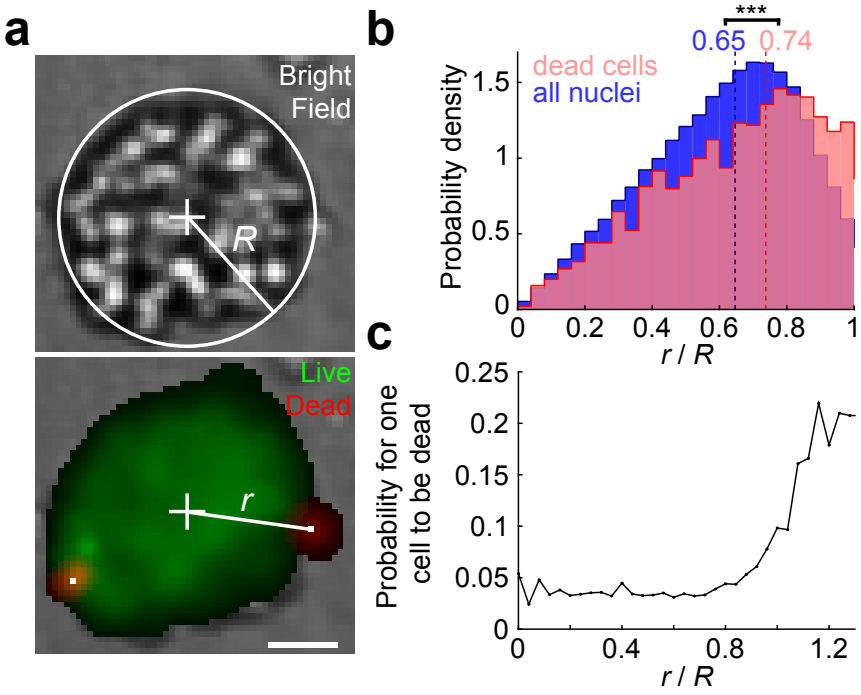

Figure 4.15: Viability data at the cellular level. **(a)** Image of a spheroid shown in bright field (top) and stained with LIVE/DEAD® (bottom). Scale bar is 20 μm. **(b)** Location probability density for the dead cells (red, $n_{dead\ cells}$ = 3,634) and all the detected nuclei with the DAPI experiments (n_{nuclei} = 125,734). Dashed lines: medians. **(c)** Evolution of the probability for one cell to be dead with r / R.

The results presented in this section demonstrate that the hepatocyte spheroids that are created in our microfluidic platform are viable, at least for the 7-day window that we tested. Many of them do not have any dead cell and when some are present, they are likely to be located at the edge of the spheroid.

4.6 Analysis of the cell proliferation

After the demonstration of the high viability of our hepatocyte spheroids, we investigated their proliferation with BrdU staining (see subsection 2.3.1), yielding strong nuclear signal for proliferative cells (see subsection 3.4.2).

We first compared the ratio of proliferating cells in 3D and in 2D conditions (Fig.4.16). We measure an almost 2-fold decrease in the proliferation ratio in 3D (16 %) compared to 2D conditions (30 %). When cells proliferate in gelated agarose, the spheroid applies a force on the hydrogel mesh and has to sustain an opposite reaction since these cells used in this study cannot break this microstructure, unlike highly modified tumour cells [75].

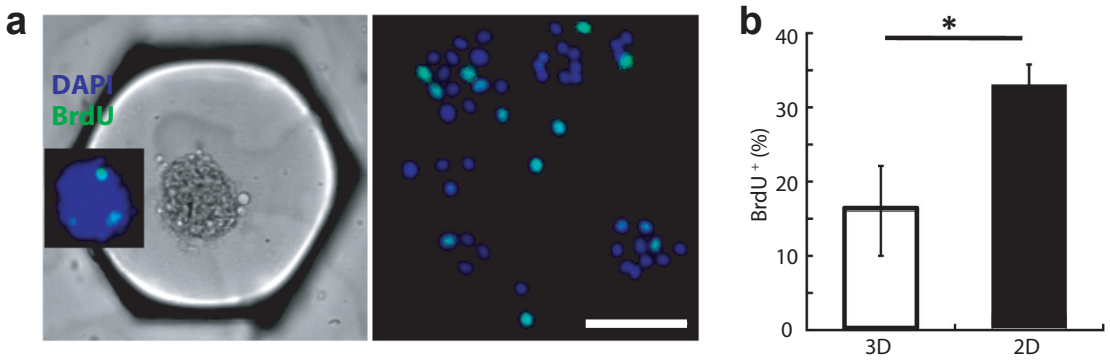

Figure 4.16: Proliferation staining. **(a)** Images of one spheroid in an anchor and cells in 2D (right) stained with BrdU. Scale bar is 100 μm. **(b)** Quantification of the percentage of BrdU$^+$ cells in spheroids on chip and cells in 2D, over a 7-day culture period (n_{chips} = 5; n_{2D} = 4).

The presence of mechanical stress can explain the decreased proliferation rate observed in confined spheroids [76]. This result could appear to be in contradiction with Fig.4.8, since no change in the spheroid diameter is observed in spite of a small but significant proliferation rate. Either the cell density increases slightly over time at constant diameter while the proliferation rate further decreases or the proliferating cells are stuck in the cell cycle between the DNA replication and the mitosis.

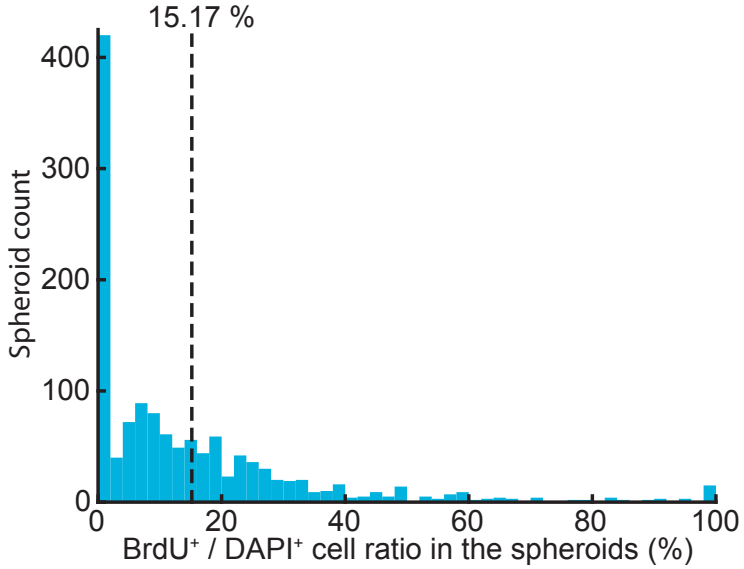

Figure 4.17: Spheroid level analysis of the proliferation. Histogram of the BrdU$^+$ / DAPI$^+$ cell ratio (n_{spher} = 1,311, n_{chips} = 5 chips) in the spheroids. Dashed lines: means.

The spheroid level analysis reveals strong heterogeneities in the population (Fig.4.17 **(b)**) In this case, the distribution of the prolideration rate is broad and many spheroids do not

have any proliferating cell detected. The proliferation rate goes from 0 to 50 % for almost all the spheroids.

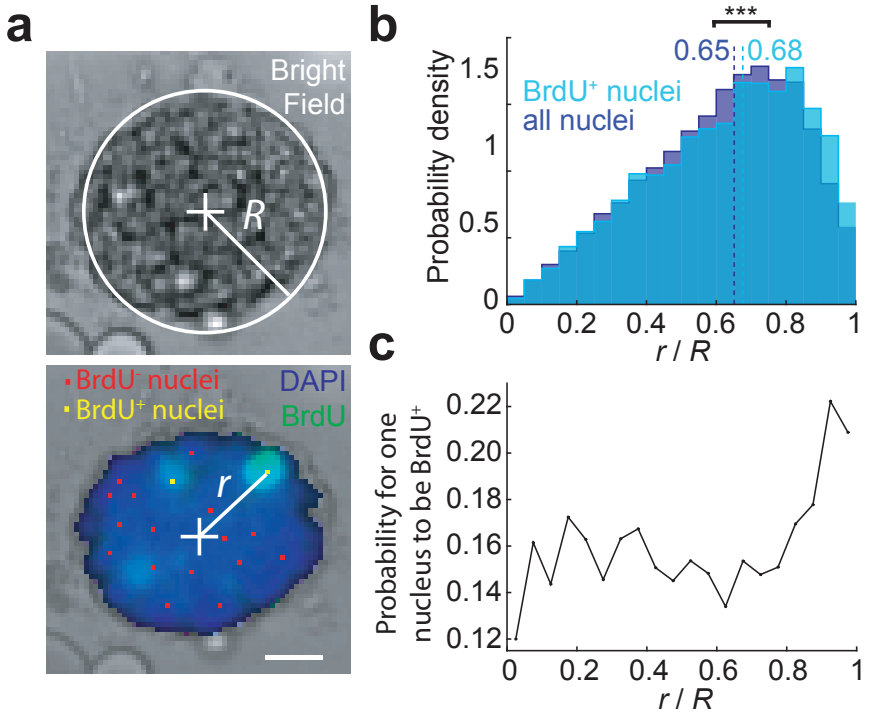

Figure 4.18: Proliferation data at the cellular level. **(a)** Image of a spheroid shown in bright field (top) and stained with BrdU (bottom). Scale bar is 20 μm. **(b)** Location probability density for the BrdU$^+$cells (cyan, n_{cells} = 4,154) and all the detected nuclei (n_{nuclei} = 25,595). Dashed lines: medians. **(c)** Evolution of the probability for one cell to be BrdU$^+$ with r / R.

The detection of the BrdU$^+$ nuclei inside the spheroids is decribed in Fig.4.18. We find, on average, that the proliferating cells are slightly more likely to be located closer to the spheroid edge (Fig.4.18 **(b-c)**). Indeed the probability for one cell to be proliferative is almost constant at 0.15 from $r/R = 0$ to $r/R = 0.8$ and then increases to reach 0.22 close to $r/R = 1$. This observation is also consistent with the solid stress hypothesis [76].

To conclude, the analysis of the BrdU signal reveals some proliferative cells in the spheroids cultured in microfluidic agarose beads. Therefore, our hepatocyte spheroids are viable and proliferative, even if the agarose seems to limit this proliferation.

4.7 Analysis of the spheroid functionality: albumin production

4.7.1 Assessment of the spheroid functionality

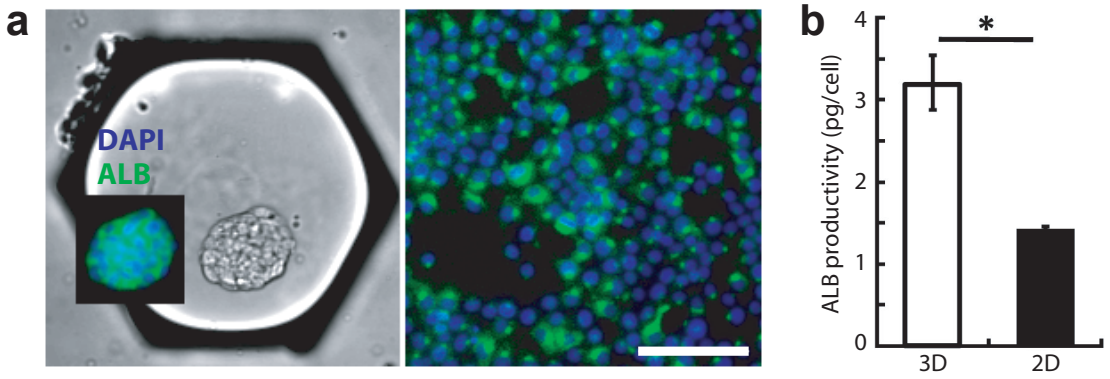

Figure 4.19: Population level analysis of albumin. **(a)** Images of one spheroid in an anchor and cells in 2D (right) stained for intra-cellular albumin. Scale bar is 100 μm. **(b)** Albumin productivity at day 4 by spheroids on chip and cells in 2D, measured by ELISA on the supernatant ($n_{chips} = 2$; $n_{2D} = 3$).

To investigate the functionality of our spheroids we used a fluorescent antibody for intra-cellular albumin (Fig.4.19 **(a)**). In both culture conditions we observe that the DAPI and albumin signal are segregated, which is expected since albumin is a cytoplasmic protein. Then, it is easy to assign an albumin peak to each cell in 2D (that probably corresponds to the Golgi apparatus where many vesicles filled with albumin must travel) whereas the signal is a bit more blurry in 3D because of out of focus intensity. To quantify the albumin production of the cells we performed an ELISA. For the spheroids, the aqueous content of the chamber (chip surpernatant) was harvested and tested. Knowing the volume of the tested samples and the cell concentration, the average albumin productivity can be calculated for each cell after 4 days of culture. The cells in 3D (3.0 pg/cells) were found to be twice as productive as in 2D conditions (1.5 pg/cells).

This increased functionality over 2D conditions was further confirmed at the expression level by qRT-PCR on recovered spheroids. Fig.4.20 **(a)** shows the increased albumin RNA expression in 3D over 2D compared to GAPDH levels. qRT-PCR (Fig.4.20 **(b-c)**) showed an almost 10-fold increase.

This increased functionality over 2D conditions, together with the proliferation and the high viability, demonstrates that our spheroids behave like highly functional microtissues when formed and cultured in microfluidic agarose droplets.

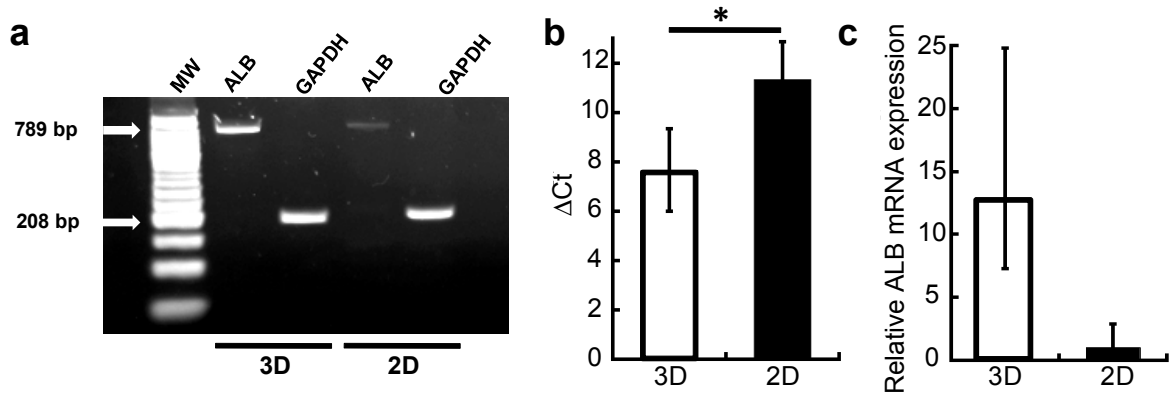

Figure 4.20: Upregulation of the albumin expression in 3D. **(a)** Representative gel of RT-PCR analysis of albumin and GAPDH expression, in 3D and in 2D. **(b)** RT-qPCR analysis of relative albumin expression to GAPDH (ΔCt), in 3D and in 2D ($n_{chips} = 3$; $n_{2D} = 3$). **(c)** RT-qPCR analysis of albumin expression (relative mRNA expression), in 3D and in 2D ($n_{chips} = 3$; $n_{2D} = 3$).

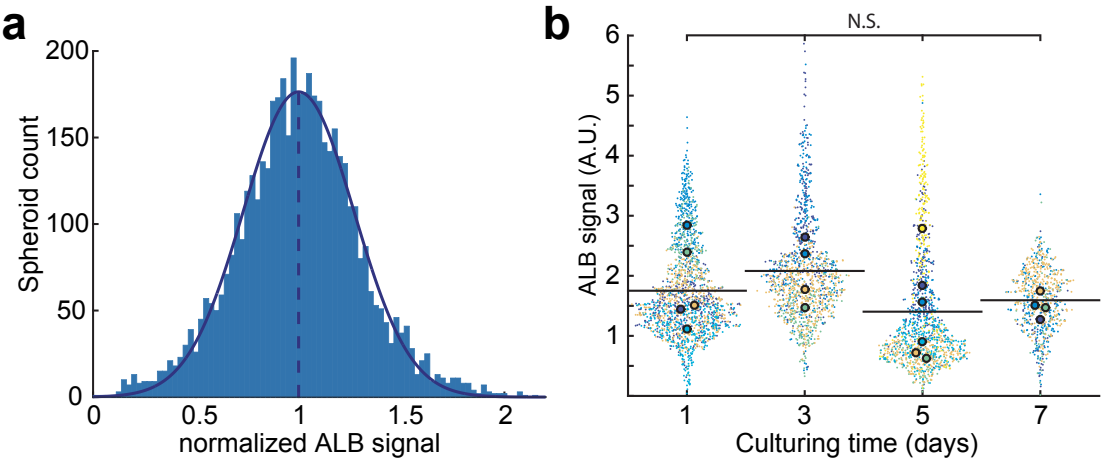

Figure 4.21: Albumin signal at the spheroid level. **(a)** Histogram of the albumin signal normalized per chip. **(b)** Time evolution of the albumin signal. D+1 / D+3 / D+5 / D+7: $n_{chips} = 5$ / 4 / 6 / 4; $n_{spheroids} = 4{,}925$

The albumin signal is also monitored for thousands of spheroids individually (Fig.4.21). When normalized by its mean value in each microfluidic chip, it follows a Gaussian distribution (Fig.4.21 **(a)**). In spite of the analysis of many different chips, we do not see any significant change in the intra-cellular albumin levels over the 7-day culturing time, with both large intra- and inter-chip dispersion of the data (Fig.4.21 **(b)**). This measure gives us an idea of the specific production of intra-cellular albumin per spheroid (whose units could be pg/cell/day) at the time of fixation, which is different from the accumulated albumin over several days of culture (whose units could be pg/cell, like in Fig.4.19). This

measure seems to be highly dependent on the cell type and culturing conditions [73] since some reports support an increase [77, 78], a decrease [79, 64, 80, 81] or a maintenance [82, 68] of the albumin specific production rate in the same time window. Moreover, it is unclear whether the intra-cellular albumin level can robustly predict the actual secretion outside the cells. The number of albumin molecules in cytoplasmic vesicles could reach a plateau and if the intra-cellular transport becomes faster, the actual secretion rate would still increase.

4.7.2 Correlation between the albumin signal and morphological parameters

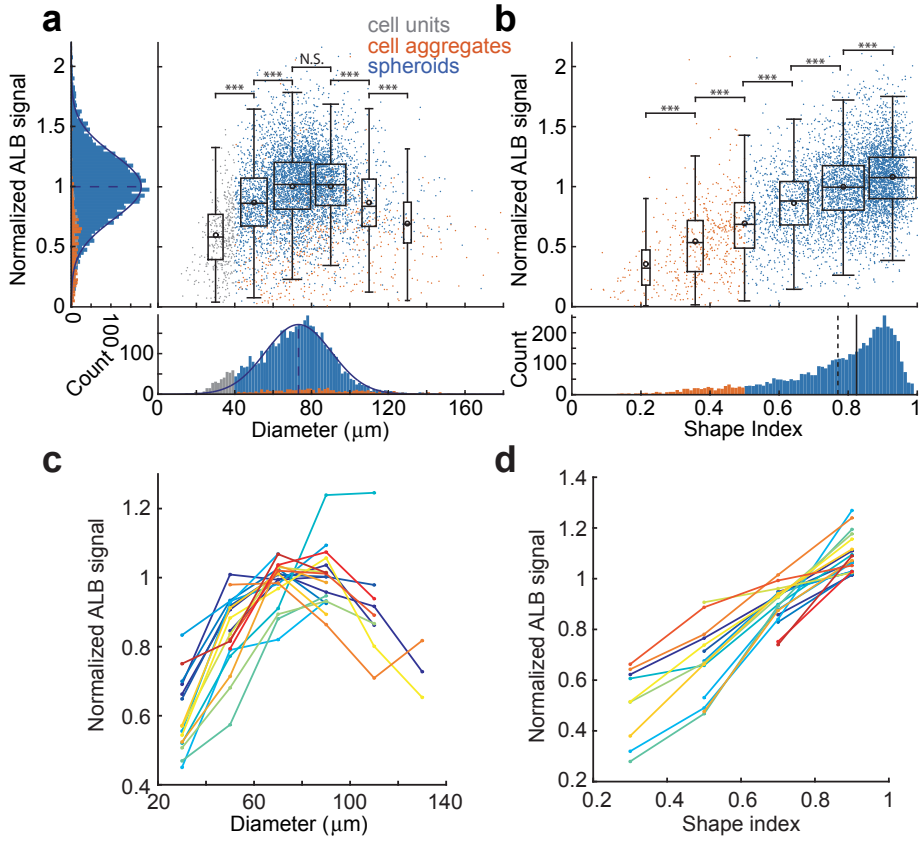

Figure 4.22: Correlation between the functionality and morphological parameters at the spheroid level. Normalized albumin signal for each spheroid vs. **(a)** the spheroid diameter and **(b)** the shape index. The histograms show the distribution of the data along the different axes. Blue curves show Gaussian fits, dashed lines represent the mean and the solid line represents the shape index median. $n_{spheroids} = 4{,}925$, $N_{cell\ aggregates} = 506$, and $n_{units} = 389$. Figures **(c-d)** show the trend for each chip, one color representing one microfluidic chip.

Now that the increased functionality of our hepatocyte spheroids is assessed, we correlate the albumin signal with morphological parameters. It enables to get an insight into the regulatory mechanism involved in the 3D cell culture.

The albumin signal at the spheroid level can be correlated to the spheroid diameter or shape index like the fluorescent signal would be correlated to the forward or side scattered light intensity for single cells in a flow cytometer. Fig.4.22 **(a)** shows a maximum albumin fluorescent level in the 60 to 100 μm range in diameter. This maximum has been previously observed by several groups [80, 73]. More interestingly, we see a clear and unreported correlation between the albumin signal and the spheroid shape index Fig.4.22 **(b)**, with an almost 3-fold increase when the shape index goes from 0.2 to 1. Furthermore, these two trends are consistent across the different microfluidic chips, as shown in Fig.4.22 **(c-d)**.

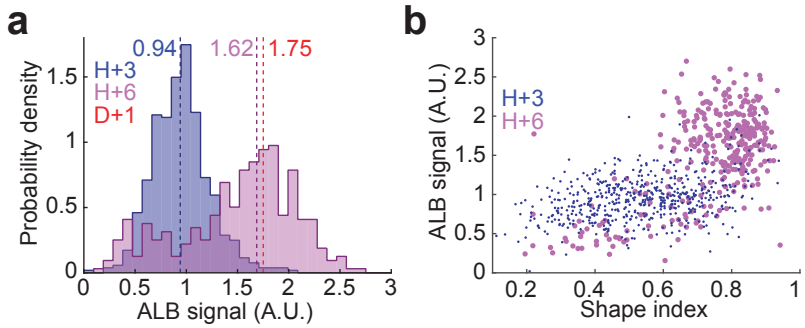

Figure 4.23: Influence of a premature gelation on the albumin signal. **(a)** Histogram of the albumin signal depending on the gelation time (see Fig.4.9 **(a)** for the protocol). The purple and blue dashed lines represent the median of the underlying histograms, the red dashed line show the mean on the D+1 experiments. **(b)** Scatter plot correlating the albumin signal and the shape index at the spheroid level for the H+3 and H+6 experiments.

This dependence of the albumin signal with the shape index has been further investigated by measuring the albumin fluorescent levels in the blockage experiments described in 4.4.2. The distribution of the albumin signal in the H+3 experiment is centered on on much lower value than for the D+1 experiments (Fig.4.23 **(a)**). In the H+6 experiment, the albumin distribution appears to be bimodal with most of the spheroids having a high albumin level and some of them showing lower levels. These differences are nicely explained when the albumin signal is correlated with the shape index at the spheroid level (Fig.4.23 **(b)**). In the H+3 experiment, most of the aggregates have a low shape index (and consequently a low albumin level) and in the H+6 experiment, we can see the two populations: both high shape index and albumin level or both low shape index and albumin level.

This strong correlation between the albumin signal and the shape index supports the critical role of functional cell-cell interactions (notably via E-cahderins and connexin-32) in the spheroid compaction [70] and albumin production [83].

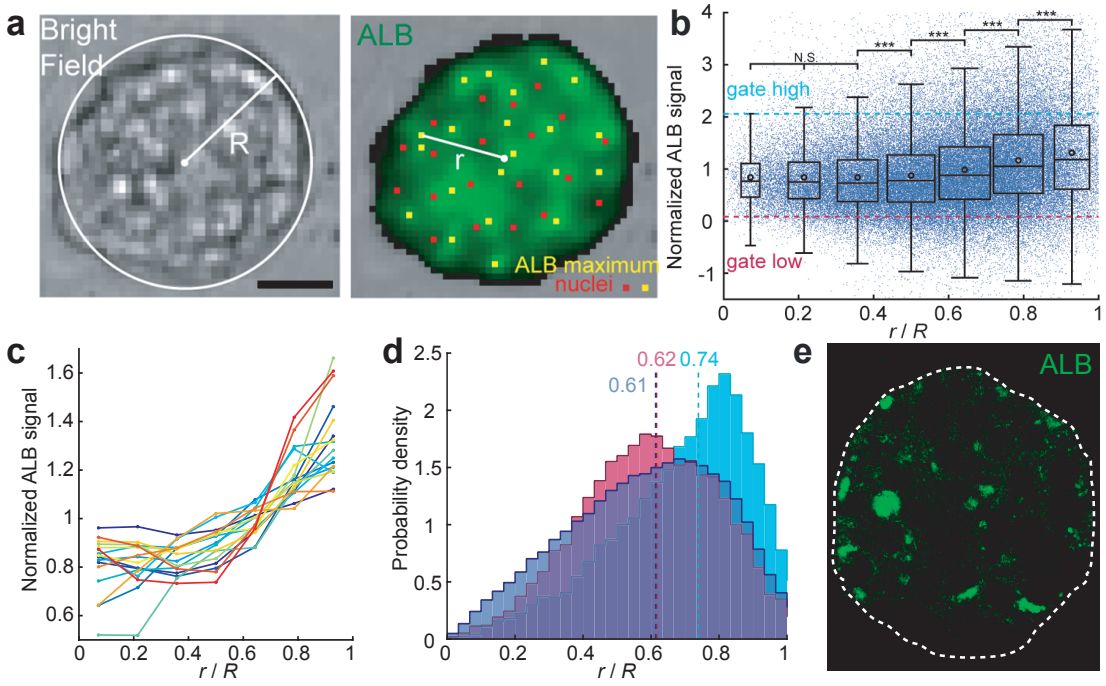

Figure 4.24: Analysis of the albumin signal at the cellular level. **(a)** Image of a spheroid shown in bright field (left) and stained for intra-cellular albumin (right). Scale bar is 20 μm. **(b)** Normalized ALB vs. distance from spheroid center ($n_{ALB\ maxima} = 87.609$, $N_{spheroids} = 4.654$). The cyan and magenta dashed lines represent the first and last deciles of the data. **(c)** Trends per chip. **(d)** Location histograms of all the nuclei (dark blue) and of the two gated populations in **(b)** (magenta: below the first decile, cyan: above the last decile). **(e)** Confocal image of the mid-plane of a spheroid stained for albumin (green). White dashed line shows the spheroid edge.

To analyze the albumin signal at the cellular level we can detect the albumin fluorescent peaks, as described in 3.4.3. Similarly as Fig.4.11, we can find their distance to the spheroid center and thus correlate the normalized albumin signal with r/R (Fig.4.24 **(b)**) at the cellular level. We see a continuous increase of the albumin signal from $r/R = 0.4$ to $r/R = 1$. This trend is consistent across the chips (Fig.4.24 **(c)**) and further confirmed by looking at the location histograms of the 10 % highest and lowest albumin peaks (Fig.4.24 **(d)**). Confocal imaging tends to confirm that highest albumin peaks are more likely to be close to the spheroid edge (Fig.4.24 **(e)**). This increase of the albumin production in cells located at the spheroid border might be a consequence of the mechanical properties of the surrounding agarose [84].

The ability to correlate the functionality with the morphological parameters at the spheroid and cellular level is a unique feature of our microfluidic platform. It allowed us identify a close link between albumin production and the shape index at the spheroid level and to show that the cells close to the spheroid border produce more albumin.

4.8 Selective and dynamic drug perfusion

In this section, we use the selective perfusion techniques discussed in 2.3.2 to culture hepatocyte spheroids under different drug perfusion conditions in the same microfluidic chamber. The viability of the perfused spheroids is followed in real time by live fluorescent staining, allowing us to perform live multiscale cytometry and investigate the dynamic aspects of the drug response.

4.8.1 Chip design, principle and experimental setup

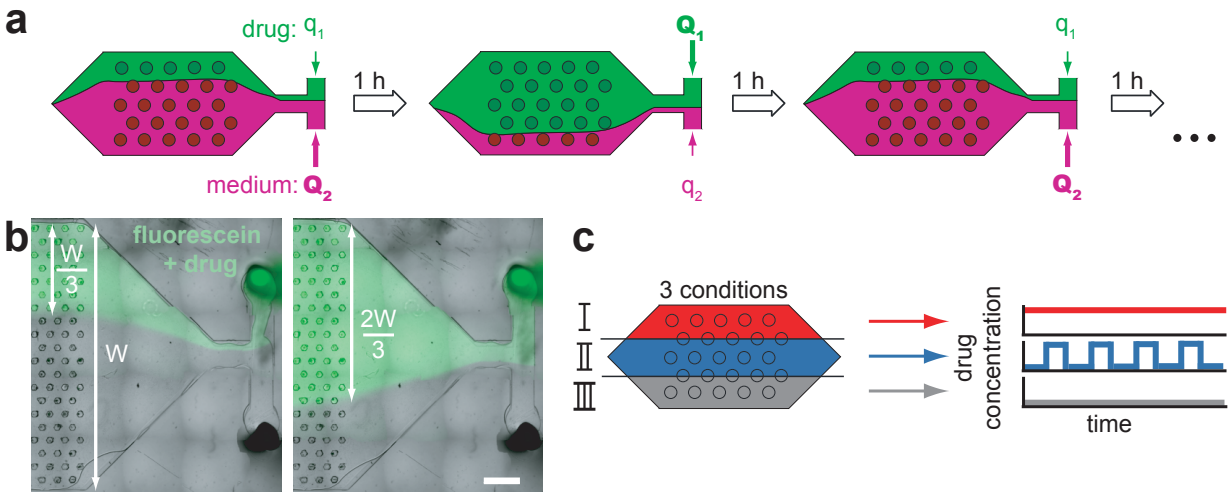

Figure 4.25: Design of the drug perfusion experiment. **(a)** Scheme of the protocol. **(b)** Micrograph of the chip perfusion with different solutions. Fluorescein enables to mark the solution containing the drug. W is the width of the chamber. Scale bar is 1 mm. **(c)** Three different drug expositions protocol are imposed in the same microfluidic chamber.

Two inlets are incorporated at the exit of the culture chamber in order to perfuse the spheroids with 2 different solutions: one contains only culture medium, while the other is supplemented with 30 mM acetaminophen (also known as paracetamol). The control of the relative flow rates enables to regulate spatially and temporally the spheroids exposure to the drug (Fig.4.25 **(a)**). The 2 flow conditions, separating the chamber in 3 zones, as it can be seen on Fig.4.25 **(b)**, are achieved by switching the 2 flowrates every hour between 10 and 30 μL/min, always keeping an overall flowrate of 40 μL/min. This flowrate partition was determined experimentally to achieve an homogeneous 3-part separation of the culture chamber. Although, by assuming a constant flowrate across the chamber width the large flowrate at the inlet should only be twice as large as the small one, not three

times. It is a consequence of the chamber swelling in the central region, perturbing the flow distribution by setting an area of smaller hydraulic resistance in the swollen region. Therefore, hepatocyte spheroids are exposed to three different culture conditions in the same chamber (Fig.4.25 **(c)**). The top part (region I) of the chip is continuously perfused with the drug (red). The middle part (region II) is intermittently perfused with the drug, with a half-period of one hour (blue). The bottom of the chamber (region III) is perfused with culture medium without drug (gray).

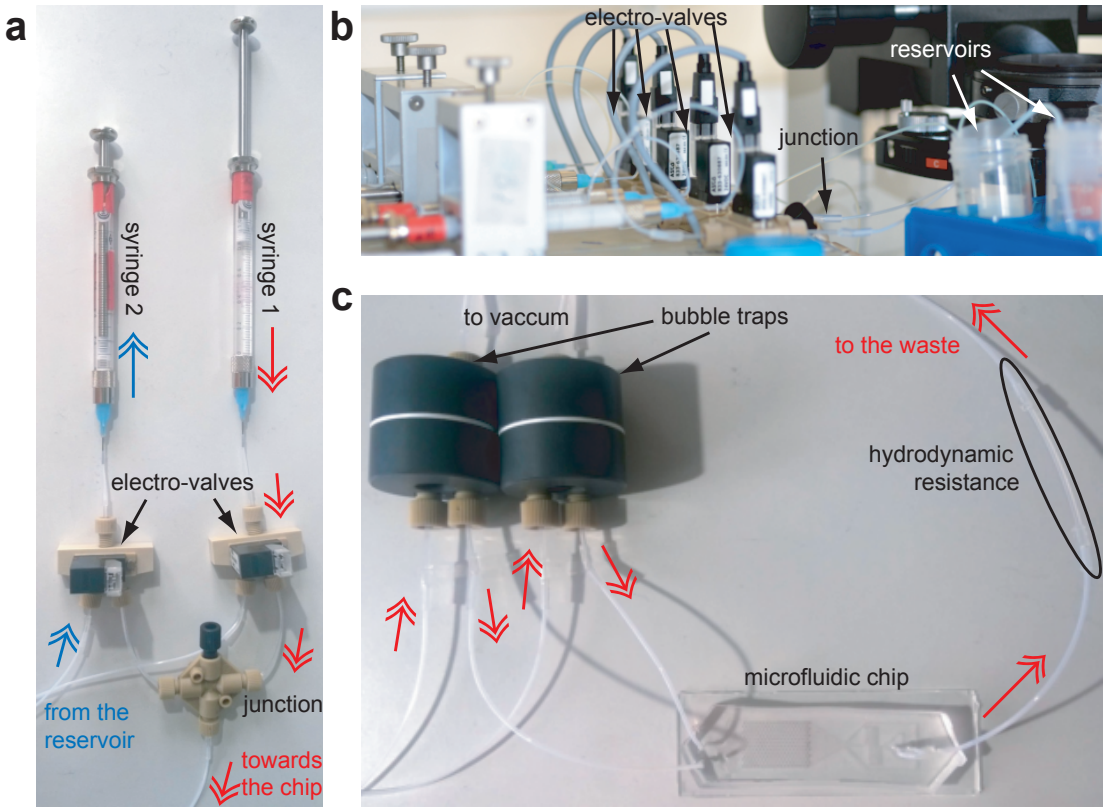

Figure 4.26: Experimental setup for the drug perfusion experiment. **(a-b)** Pictures of the automatized refilling system. **(c)** Picture of the fluidic connections to the microfluidic chip. Red and blue arrows represent respectively the fluidic path of the medium being injected and of the medium refilling one syringe.

Experimental setup for maintaining the perfusion for several hours at 37°C If the flowrates are stopped during this perfusion experiment the integrity of the 3 zones displayed in Fig.4.25 **(c)** is lost because the drug will diffuse and homogeneize in the entire chamber. Nevertheless, the maintenance of the flowrate for several hours under good culturing conditions causes two technical issues that need to be addressed. Indeed, with a 40 μL/min flowrate there is an overall volume of about 30 mL that flows through the chamber in 12 hours. Meanwhile, only small glass syringes with a 1 mL volume can provide

the fine control needed to deliver a constant and accurate flowrate in the 10 to 30 μL/min range. To overcome this issue, we use electro-valves together with programmable syringe pumps (see Fig.4.26 **(a-b)**). Two syringes are used for each solution, while one injects the solution in the chip the other refills at the same flowrate and they switch role every 30 minutes, with the electro-valve selecting the right pathway between the chip and the reservoir. Then, the microfluidic chip and the syringes need to be kept at 37°C because of the cell culture. This temperature favors the nucleation of air bubbles that would completely disturb the flow if injected in the culture chamber. Two strategies are combined to limit this risk Fig.4.26 **(c)**. First, the solution flows through a commercial bubble trap connected to vacuum chamber before being injected through each inlet. Then, an extra hydrodynamic resistance designed to apply a 10 mbar pressure in the chip is added at the outlet of chamber. This way, we change the thermodynamic balance and favor the dissolution of air bubbles.

4.8.2 Live multiscale cytometry

In the multiscale cytometry analysis of the acetaminophen perfusion of our hepatocyte spheroids, we compare the three conditions that are applied in the same microfluidic chamber. Region III (gray) is the control, region I (red) is the area under continuous drug exposure and region II (blue) is the area with an intermittent drug exposure with a half-period of one hour.

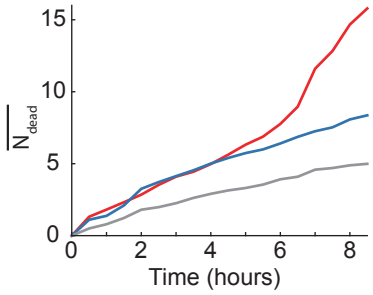

Figure 4.27: Population level analysis of the drug perfusion. Time evolution of the number of dead cells, normalized by the number of spheroids in each region, in the 3 different regions (red = I, blue = II, grey = III).

At the population level (Fig.4.27), we can monitor the evolution of the mean number of dead cells per spheroid. In the control region, we see a slow and continuous increase to reach a mean number of about 4 dead cells per spheroid after 8 hours of perfusion. In region II, the mean number of dead cells increases almost twice as fast. The mortality in the region continuously exposed to the drug is similar than in region II for the 5 first hours and then there is strong acceleration leading to a mean number of 15 dead cells per spheroid at the end of the experiment. These results indicate that indeed the mortality

is higher in the regions exposed to the drug, with a higher mortality for the continuous exposure. Though, it seems that the number of dead cells appear during the experiment in the spheroids of the control region is quite high.

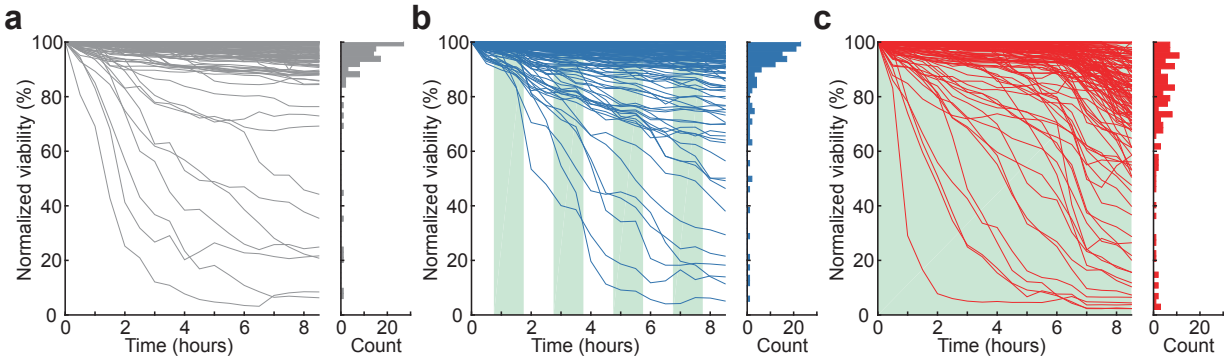

Figure 4.28: Spheroid level analysis of the drug perfusion. Time evolution of the normalized viability for each spheroid in the 3 experimental conditions: **(a)** region III (grey, $n_{spheroids} = 131$), **(b)** region II, (blue, $n_{spheroids} = 133$), **(c)** region I (red, $n_{spheroids} = 106$). The green background indicates the drug perfusion. The histograms indicate the viability distribution at the end of the experiment for each condition.

Looking at the data at the spheroid level provides a much more complete picture of the cell death kinetics (Fig.4.28). The vast majority of the spheroids cultivated in the absence of the drug showed high viability (region III). The cell deaths that were detected on the population scale were concentrated in a small number of spheroids (10 out of 106) that showed a decreased viability in the first hours in culture (Fig.4.28 **(a)**). A similar behavior was observed in region II, though the number spheroids that died was higher (28 out of 133 spheroids) (Fig.4.28 **(b)**). In both of these regions, this led to a final distribution dominated by mostly high-viability spheroids with some low-viability individual cultures, as shown in the final histograms. In contrast, the viability in region I showed very different dynamics. First, a similar rapid decrease in spheroid viability was observed for 25 out of 131 spheroids. But after 6 hours of incubation with the drug, a generalized decrease in viability was observed for 53 out of 131 spheroids (Fig.4.28 **(c)**). The final distribution of viability thus displayed a much lower value and a wider spread compared with the two previous conditions. The dual kinetics of cell death in region I suggest that two different mechanisms take place under continuous exposure to the drug, one of which is fast and the other slow. This observation is consistent with the known mechanisms of the toxicity induced by acetaminophen, which occurs through an initial induction of oncotic necrosis (rapid induction) followed by apoptosis (longer induction) [85]. In the intermittent zone (region II), only the fast mechanism is observed while the slow mechanism is not reached.

The contrast between the three conditions was also visible at the cellular level, as shown in Fig.4.29, where the mean position of the dead cells within the spheroids was plotted as a function of time. In regions II and III, cell death was observed mainly near the boundaries

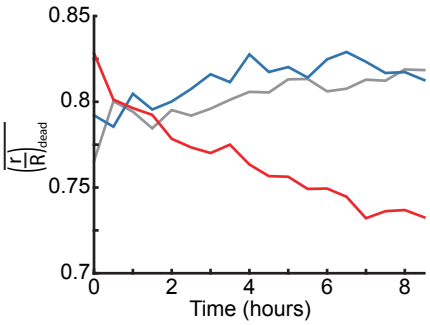

Figure 4.29: Cellular level analysis of the drug perfusion. Time evolution of the mean normalized distance of the dead cells to the spheroid center in the three different regions (red = I, blue = II, grey = III).

of the spheroids, *i.e.* at a normalized distance to the spheroid center $r/R = 0.8$, and remained stationary for the duration of the experiment. In contrast, the location of the dead cells in region I started near the same position ($r/R = 0.8$) but gradually shifted inward. This indicated an increase in the occurrence of cell deaths in the inner parts of the spheroids.

4.9 Conclusion of chapter 5

In this chapter, we formed hepatocyte spheroids for drug toxicity applications. We were able to follow dynamically the spheroid formation process and to identify singular behaviors. The morphological characterization of the spheroid demonstrated their monodispersity and the existence of a cell density gradient oriented towards the spheroid core. The hepatocyte spheroids are also viable, proliferative and exhibit higher functionality when compared to 2D conditions. In addition, we uncovered a non reported correlation between the albumin and shape index at the spheroid level and an increased albumin production for the cells close to the spheroid edge. Finally, multiscale cytometry allowed to study the effects of different dynamic drug exposures in a single microfluidic chip. For instance, there is a progression of cell death to the core of the spheroids which is only observed for a continuous drug exposure.

Although H4-II-EC3 cells have been used for drug testing experiments [86] and express some of the CYP enzymes [87], they remain hepatomas that cannot reproduce the phenotype of the *in vivo* functional hepatocytes. The liver model that we presented could be greatly enhanced by the use of primary hepatocytes or the addition of co-culture [62, 88], for instance by forming heterospheroids with stellate cells.

Chapter 5

Investigating the spatial cues involved in the therapeutic properties of human mesenchymal stem cell aggregates

5.1 Mesenchymal stem cells and their therapeutic applications

Many injuries and diseases result in the formation of defective tissues that cannot be renewed by the organism, like spinal cord injuries, myocardial infracts or neurodegeneration. Sometimes, the impaired tissues can be replaced by a graft from a donor but it is not always possible and there are many compatibility issues between the host and the graft that is recognized as a foreign body. Over the last decades, a growing research effort on stem cells has lead to the concept of cell-based therapies as an alternative to grafts and has hold great promises. Stem cells were first discovered by Becker *et al.* [89], who transplanted bone marrow cells into irradiated mice and observed the formation of spleen colonies *in vivo*. Stem cells indeed bear unique properties:

- **self-renewal**. It means that a single stem cell can support infinitive duplication to generate cells that have the exact same properties.
- **multipotency**. Under the appropriate conditions, stem cells can differentiate into different cell lineages.

Stem cells can be categorized into 2 different types. First, the pluripotent stem cells (embyonic or induced pluripotent stem cells [90]), which can give rise to all the cellular

types of the organism. Therefore, these cells can be used to create organs leading to a great therapeutic potential. However, the use of embryonic stem cells raises significant ethical issues since they can only be harvested from developing embryos. In addition, without complete differentiation, pluripotent stem cells can lead to cancer development while injected *in vivo*. These issues have hindered the applications of pluripotent stem cells in clinical trials. Adult stem cells constitute a second stem cell type. Usually isolated from adult tissues, these cells are not pluripotent but multipotent, meaning that they can differentiate into several cell types but not all.

These adult stem cells were first discovered and characterized in the bone marrow in the 70-80's [91, 92]. When isolated *in vitro*, there is a subset of the bone marrow cell population that have a fibroblastic morphology, create colonies (self-renewal) and differentiate into multiple cell types (multipotency) like adipocytes or osteoblasts [93, 94], mostly from the mesodermal lineage. These cells were first named human mesenchymal stem cells (hMSCs) by Caplan in 1991 [95] and although originally isolated from bone marrow, similar cells were also found in many organs [96]. Mesenchymal stem cells are currently defined by 3 main criteria: plastic adherence, expression of a subset of clusters of differenciation (CD) and *in vitro* differentiation into osteoblasts, adipocytes and chondrocytes [97].

These cells have many potential therapeutic properties, like the establishment of a new bone marrow environment after transplantation [98] or the modulation of the immune system. Interestingly, the transplantation of hMSCs in mice do not trigger any immune response, making them appealing candidates for the treatment of graft versus host disease. Many therapeutic properties of the hMSCs come from their ability to secrete factors with immuno-modulatory and trophic properties [99, 94]. One commonly accepted hypothesis to contextualize these abilities *in vivo* is that hMSCs would sit at perivascular locations, where they are activated by an injury or inflammation to release all these beneficial factors.

The therapeutic properties of hMSCs are currently being investigated in several clinical trials. In october 2016, there were 657 registered trials worldwide on the NIH website (https://clinicaltrials.gov/), mostly in North America, Europe and China (Fig.5.1). They cover many different areas (Fig.5.2) such as bone or cardiac tissue repair, spinal cord injury or neurodegenerative diseases [100, 101].

In many of these applications, the hMSCs help restaining the tissue inflammation, stimulate the growth of new blood vessels on local progenitors and prevent graft versus host disease. There is at least one treatment based on hMSCs that has been approved in Canada and New-Zealand for steroid resistant severe pediatric graft versus host disease (Osiris® Therapeutics) but the vast majority of current clinical trials are in phase I or II (to assess toxicity and efficacy) [101].

Although hMSCs still hold great promises for future clinical applications, the biological mechanisms regulating in their therapeutic functions remain largely unknown. Improving our level of understanding on hMSC biology could help design more relevant and successful

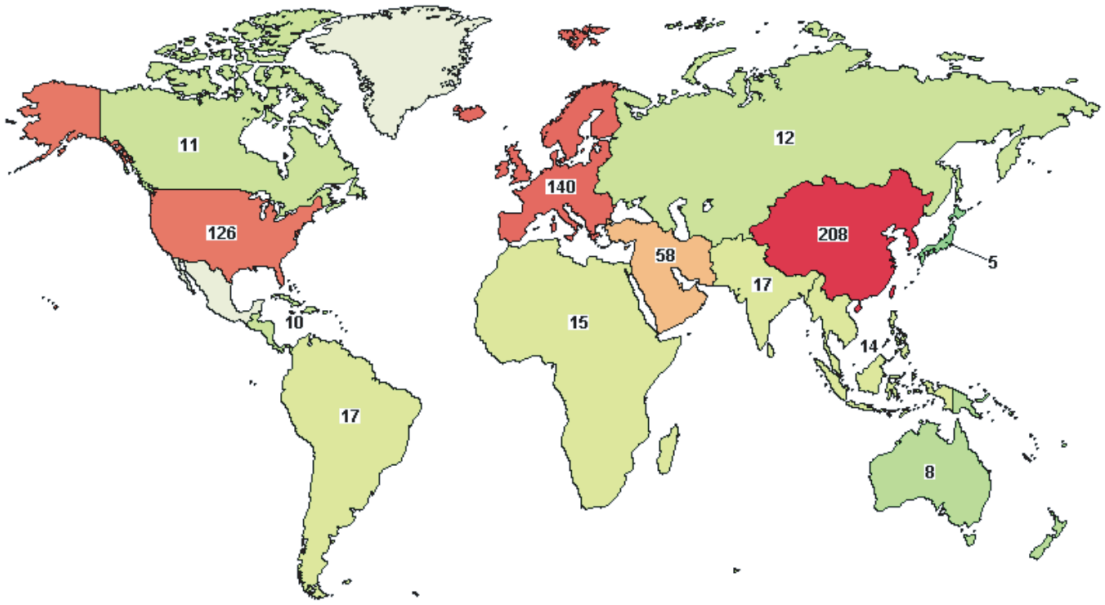

Figure 5.1: Worldwide distribution of clinical trials involving hMSCs. Reproduced from the NIH website, for 657 studies related to hMSCs in october 2016.

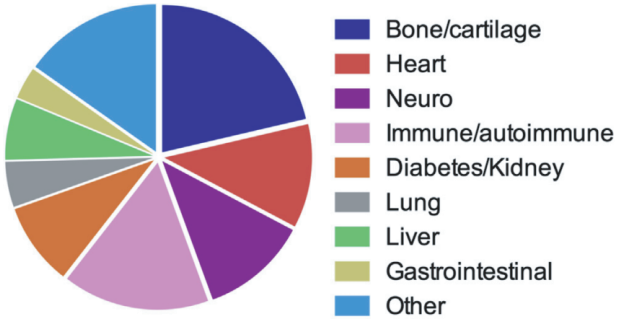

Figure 5.2: Application of the hMSC in clinical trials. Diagram for 352 registered trials in 2015, reproduced from Trounson *et al.* [101].

clinical trials.

Context of the present study. The aggregation of hMSCs have been demonstrated to enhance their antiinflammatory properties [102], probably due to the promotion of cell-cell interactions in 3D (through cadherins or others cellular junctions) [103]. For instance, the tumor necrosis factor α-induced protein 6 (TSG-6) [102], the stanniocalcin-1 (STC-1) and the prostaglandin E2 (PGE2) were upregulated in hMSC aggregates. PGE2 has been demonstrated to resume the inflammation phenotype of macrophages [104]. Bartosh *et al.* [105] proposed a signaling pathway, illustrated in Fig.5.3, explaining the upregulation of the production of these molecules in 3D.

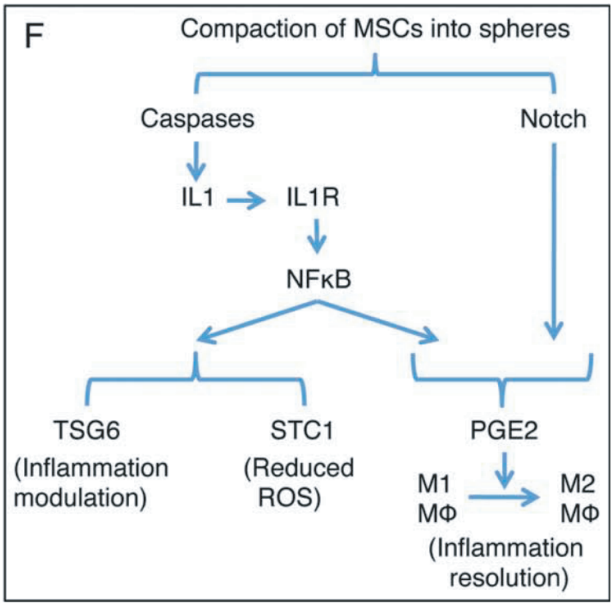

Figure 5.3: Potential signaling pathways regulating hMSC properties in 3D. Proposed signaling pathway for the enhanced production of therapeutic factors in hMSC aggregates, reproduced from Bartosh *et al.* [105]. Abbreviations: IL1, interleukin 1; IL1R, interleukin 1 receptor; NFκB, nuclear factor κB; TSG6 tumor necrosis factor α-induced protein 6; STC1, stanniocalcin-1; ROS reactive oxygen species; PGE2, prostaglandin E2; MΦ, macrophage.

In the present work, we investigated the spatial organization of hMSC aggregates and its potential role for regulating their antiinflammatory properties. The cyclooxygenase-2 (COX2) [104], the only inducible enzyme regulating PGE2 secreation was imaged in our experiments by immuno-cyto-chemistry. We also monitored fluorescently the caspase-3 (Casp3) activity, one of the most important caspases [106] potentially regulating hMSC function in aggregates. The high-throughput and high-content abilities of our platform enable to investigate the spatial heterogeneities in the expression levels of Casp3 and COX2 in hMSC aggregates.

This chapter presents preliminary results as the experiments and analysis remain ongoing. Although we are not in position to answer the main biological question, we demonstrate that our microfluidic platform is suitable for the formation and culture of spheroids with sensitive cells relevant for therapeutic applications.

5.2 Microfluidic design and experimental parameters

To investigate the spatial cues regulating hMSC aggregate functions, which are cells inherently larger than hepatocytes, we need to create aggregates that have a diameter larger

than in chapter 4. Therefore, we designed anchors with a 400 μm diameter. The trapping chamber has a 165 μm height and the anchor depth is 388 μm (see Fig.5.4 **(a)**), which ensures the efficient trapping of agarose droplets (see condition (1.1.4)). The rest of the chip was designed accordingly (see Fig.5.4 **(b)**). The droplets are created at a junction combining flow focusing and a step (from 135 to 150 μm in height, see Fig.5.4 **(c)**) followed by a serpentine emulsification channel with a 450 μm width (see section 1.3). The droplets are homogeneously distributed in the trapping chamber width thanks to diverging rails. There are 270 anchors in the trapping chamber. They have an hexagonal shape and are disposed on an hexagonal pattern with a 950 μm pitch (see Fig.5.4 **(d)**) corresponding to a density of 128 anchors/cm^2. Contrary to the chip used for the hepatocytes, the microfluidic chip for the hMSCs was equipped with a filling chamber that helps to achieve a more reproducible phase change (see Fig.2.4).

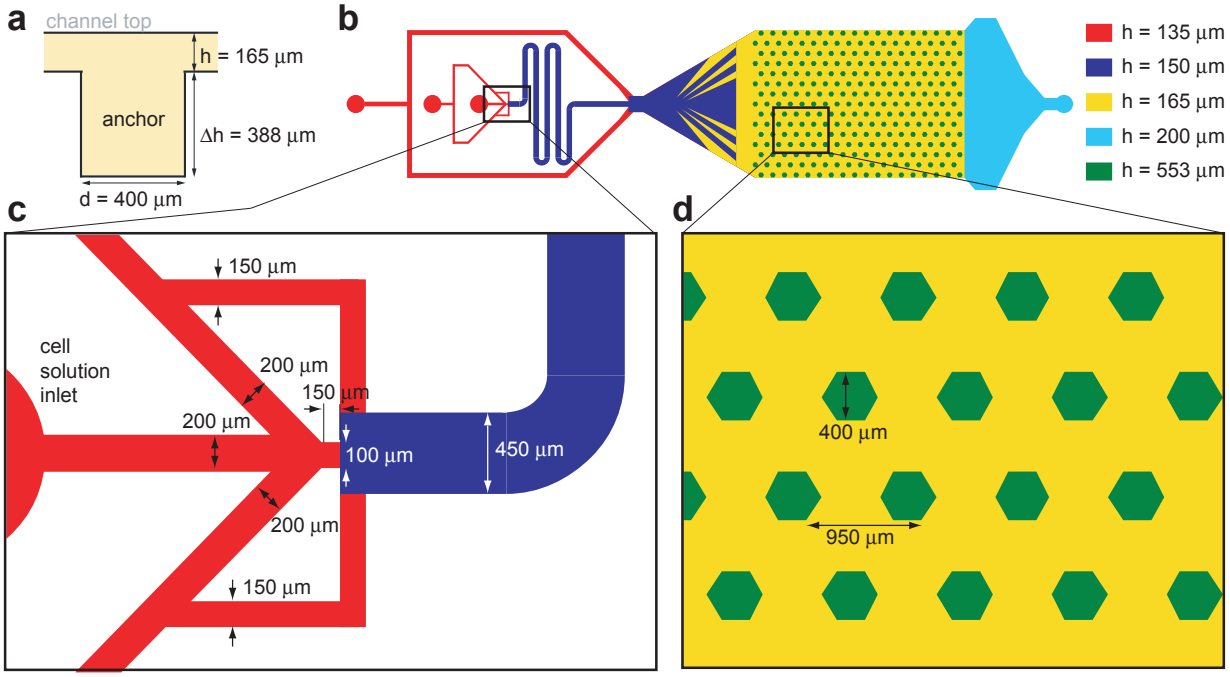

Figure 5.4: Trap and chip design. **(a)** Schematic side view of an anchor with dimensions. Schematic top view of the whole chip **(b)**, the junction **(c)** and the anchors **(d)**.

The anchor volume is 76.6 nL, and the droplets have a volume close to 60 nL. Consequently, the droplets are smaller than the anchors and have an hemispherical bottom interface when trapped. This favors the formation of a single spheroid per droplet after sedimentation. The cell concentration was 6.10^6 cells/mL, which corresponds to an average number of 360 cells per agarose droplet. We used hMSCs are derived from human umbilical cord [93] and 1 % (w/w) Pluronic F-127 was added to the culture medium in order to prevent cell adhesion to the anchor side walls.

As there are only 270 anchors in the chamber, we chose to acquire an image per anchor

(see Fig.3.3) for reconstructing a montage representing the entire array. We used a camera (Hamamatsu) acquiring images with 2048x2048 pixels. At a 10X magnification, the size of the field of view is about 1.3 mm (0.64 μm/pixel), allowing to observe a single centered anchor. This way, as described in subsection 3.1.2, we acquire far more detailed images than in the previous chapter and in a shorter time.

5.3 Morphological characterization

When encapsulated in liquid agarose droplets and immobilized in deep anchors, hMSCs aggregate and create well organized spheroids (see Fig.5.5) when cultured overnight (see chapter 2). They are referred as hMSC aggregates and bear similar morphological properties than in the previous chapter.

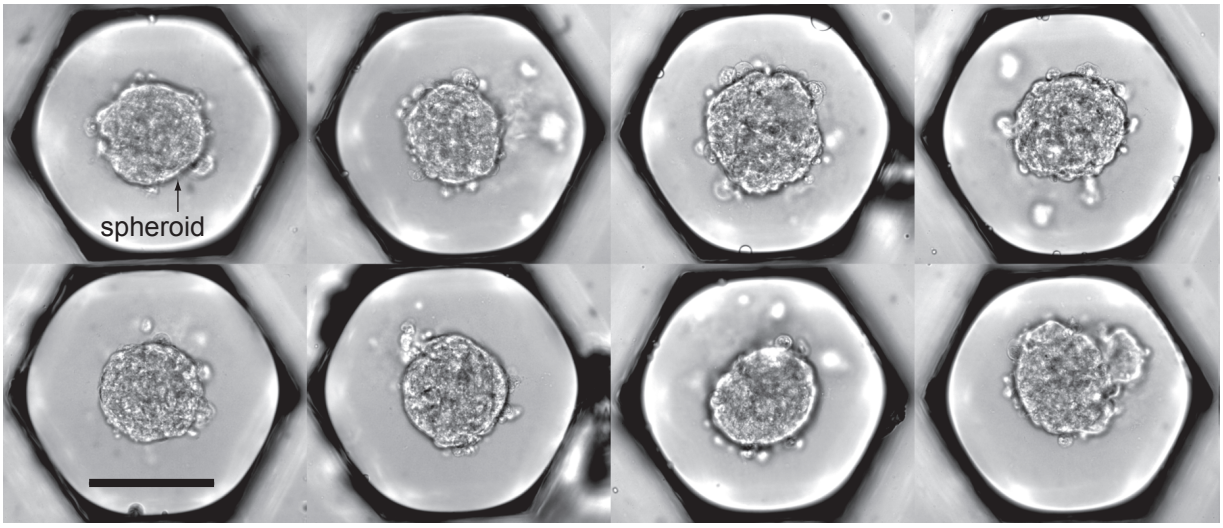

Figure 5.5: Mesenchymal stem cell aggregates. Bright field images of 8 anchors showing well formed hMSC aggregates 1 day after the droplet trapping. Scale bar is 200 μm.

First, their size is controlled by the constant cell concentration in the droplets, as shown in the polydispersity histogram of Fig.5.6 **(a)**. The averaged diameter is 142.1 μm, so they are twice as large as the hepatocyte spheroids studied in chapter 4. The coefficient of variation (CV) of the diameter is 23.5 %, which is similar to the one obtained for hepatocytes. Although the pre-aggregation of the cells is responsible for inhomogeneities in the cellular concentration among the droplets, this CV is also explained by the differences in the mean diameter between different chips. Indeed, for single chips, the mean diameter varies from 110 to 170 μm and the CV ranges from 10 % to 20 %. This high inter-chip variation is probably due to the high incertitude induced by manual cell counting and also explains the flattened shape of the distribution, which is closer to a combination of Gaussian distributions having different means than a single Gaussian.

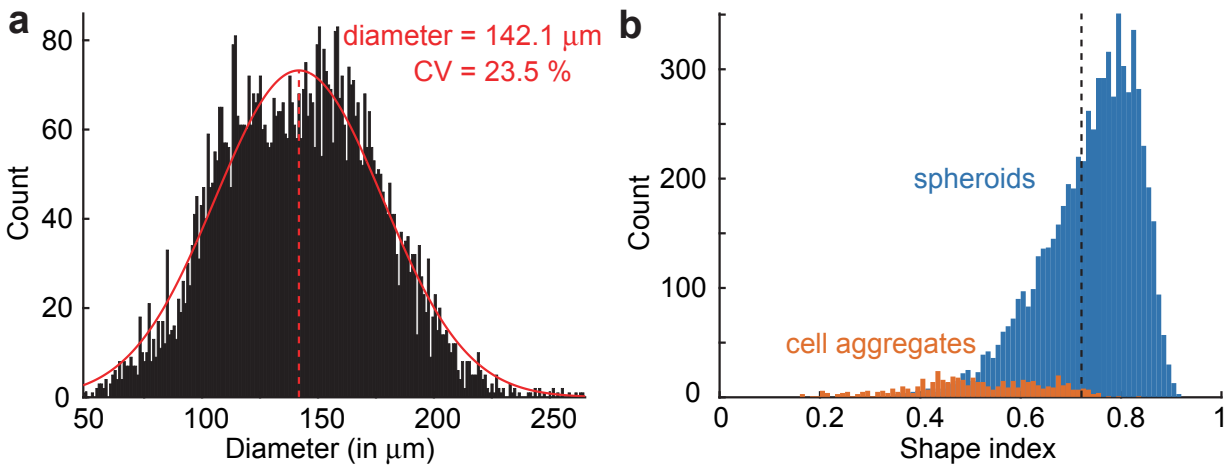

Figure 5.6: Morphological characterization at the spheroid level. Polydispersity **(a)** and shape index **(b)** histograms of the hMSC aggregates. The red line is a Gaussian fit of the polydispersity histogram. The dashed black line represents the median of the shape index distribution. $n_{spheroids} = 6,626$; $n_{cell\ aggregates} = 546$.

Second, the hMSC aggregates have a circular shape as indicated by the skewed shape index histogram of Fig.5.6 **(b)**. In the following parts of this chapter, we only analyze the spheroids, which have a high shape index and ratio of inertia (see section 3.3). The cell aggregates, having either a low shape index or low inertia ratio, are discarded from the analysis.

With the cell concentration used in the droplets, there are about 360 cells in each hMSC aggregate. Consequently, we detect more cells on each image than in the previous chapter and there are more cell layers in each spheroid. Fig.5.7 **(a-b)** shows an example of a Voronoi analysis conducted on a hMSC aggregate which has 6 different detected layers. The hepatocyte spheroids in the previous chapter (see Fig.4.12) had a maximum of 5 different layers. Nevertheless, the trend of a reduced cell diameter while increasing the cell layer number is reproduced (see Fig.5.7 **(c)**) up to the seventh layer.

These results demonstrate that the hMSCs create well organized spheroids, with a controlled diameter and a circular shape. The main morphological difference with the spheroids studied in chapter 4 is the larger size of the hMSC aggregates which are organized in many different cell layers.

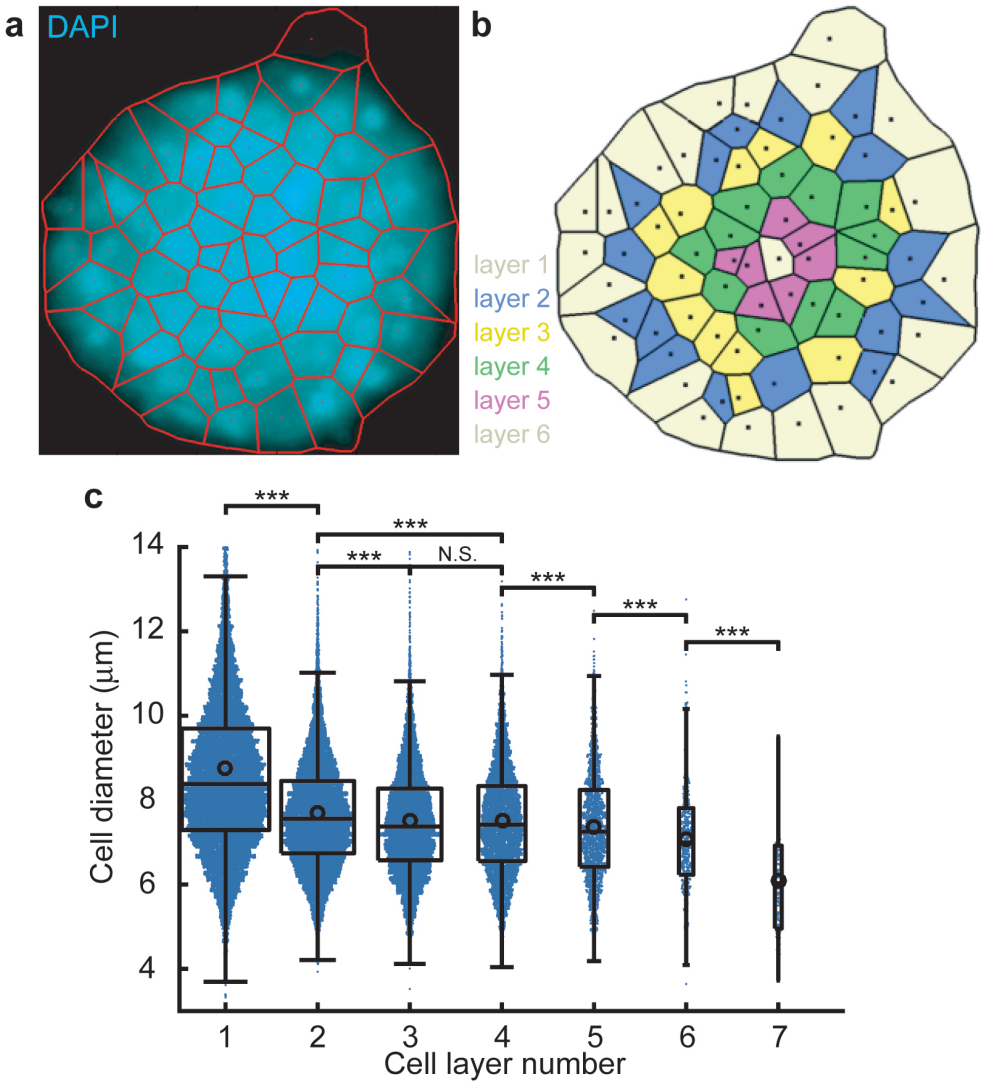

Figure 5.7: Cellular level analysis. **(a)** Image of a hMSC aggregate stained with DAPI (cyan) and overlayed with its corresponding Voronoi diagram (red). $n_{nuclei} = 70$; diameter = 167.1 μm. **(b)** Corresponding scheme showing the cell layer attribution. **(c)** Violin plot of the cell diameter with the cell layer number ($n_{spheroids} = 1,263$; $n_{nuclei} = 67,333$).

5.4 Biological properties of the hMSC aggregates on chip

In order to understand more precisely the influence of aggregation on the secretion of therapeutic factors by hMSCs, we investigated two enzymes which play a role in the secretion of different therapeutic factors (see Fig.5.3).

First, the caspase-3 (Casp3) is a protease which is activated by the aggregation and is also known for playing a major role in apoptosis [107]. We monitor the Casp3 activity with a specific dye (NucView™ 488 caspase-3 substrate) which becomes fluorescent after cleavage by the Casp3 and binding to the DNA in the cell nucleus [108]. Therefore, the nuclear fluorescent level correlates with the activity level of Casp3. Second, we looked at the expression of the cyclooxygenase-2 (COX2). We imaged the COX2 in the hMSC aggregates by immuno-cyto-chemistry. In the PGE2 production pathway proposed by Bartosh *et al.* [105], the Casp3 is first activated and upregulates the production of PGE2, which suggest potential influence on the level of COX2 expression.

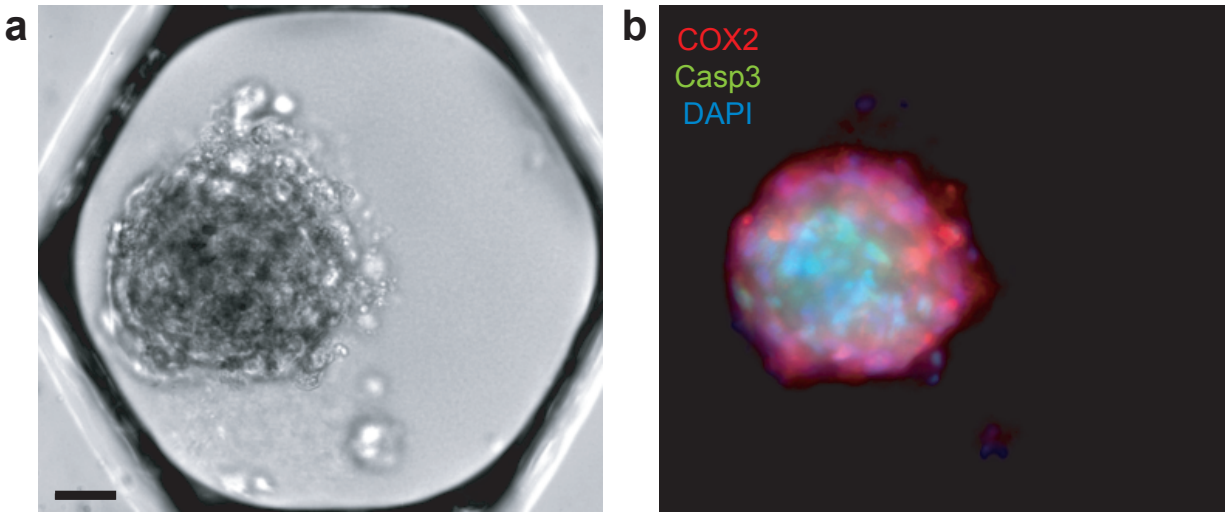

Figure 5.8: Dual Casp3 and COX2 fluorescent staining. Bright field **(a)** and fluorescent **(b)** image of an hMSC aggregate. COX2, Casp3 and DAPI are respectively shown in red, green and blue. Scale bar is 50 μm.

The staining to monitor simultaneously the Casp3 and COX2 was performed in several chips in parallel in an automated fashion (see appendix C). Fig.5.8 shows a typical tri-color staining of a hMSC aggregate for COX2, Casp3 and with DAPI. On the merged image (Fig.5.8 **(b)**), we can see that the distribution of the Casp3 and COX2 signal looks uneven. Some cells have a high Casp3 signal and the COX2 signal looks higher at the edge of the hMSC aggregate. In the following parts of this study, we analyze successively the Casp3 and COX2 signals.

5.4.1 Dynamic expression pattern of the caspase-3 signal

The Casp3 is supposed to be triggered by the aggregation of the hMSCs [104]. In order to investigate the dynamics of this process, we stained and imaged spheroids after 1 and 3 days in culture.

Identifying the cells that have a high Casp3 signal requires a careful analysis. Typical fluorescent images are shown in Fig.5.9. On the top images, the DAPI fluorescent intensity indicates the nuclei locations, while the bottom images show the analysis performed on the Casp3 signal. In order to get a reliable detection of the Casp3$^+$ cells, we first measured the signal after subtraction of the local spheroid background as described in subsection 3.4.3. Then, we determined a threshold for distinguishing the Casp3$^+$ and Casp3$^-$ cell populations as described in subsection 3.4.2. In Fig.5.9, the Casp3$^+$ cells are indicated by white crosses. Fig.5.9 **(a)** shows a hMSC aggregate which has few Casp3$^+$ cells, contrary to one in Fig.5.9 **(b)**, where all the cells are considered Casp3$^-$. Indeed, in the later case, the shape of a cell nucleus was not distinguishable from the Casp3 background. This background has a higher value in the center of the aggregate because of its spherical shape. There are more cells above and underneath the focus plane in the central region of the spheroid. In Fig.5.9 **(c)**, the Casp3 signal is higher and there are more Casp3$^+$ cells than in **(a)**. The images shown in Fig.5.9 **(a-b)** corespond to aggregates that were stained and imaged 1 day after the droplet trapping while the aggregate in Fig.5.9 **(c)** was imaged 3 days of culture.

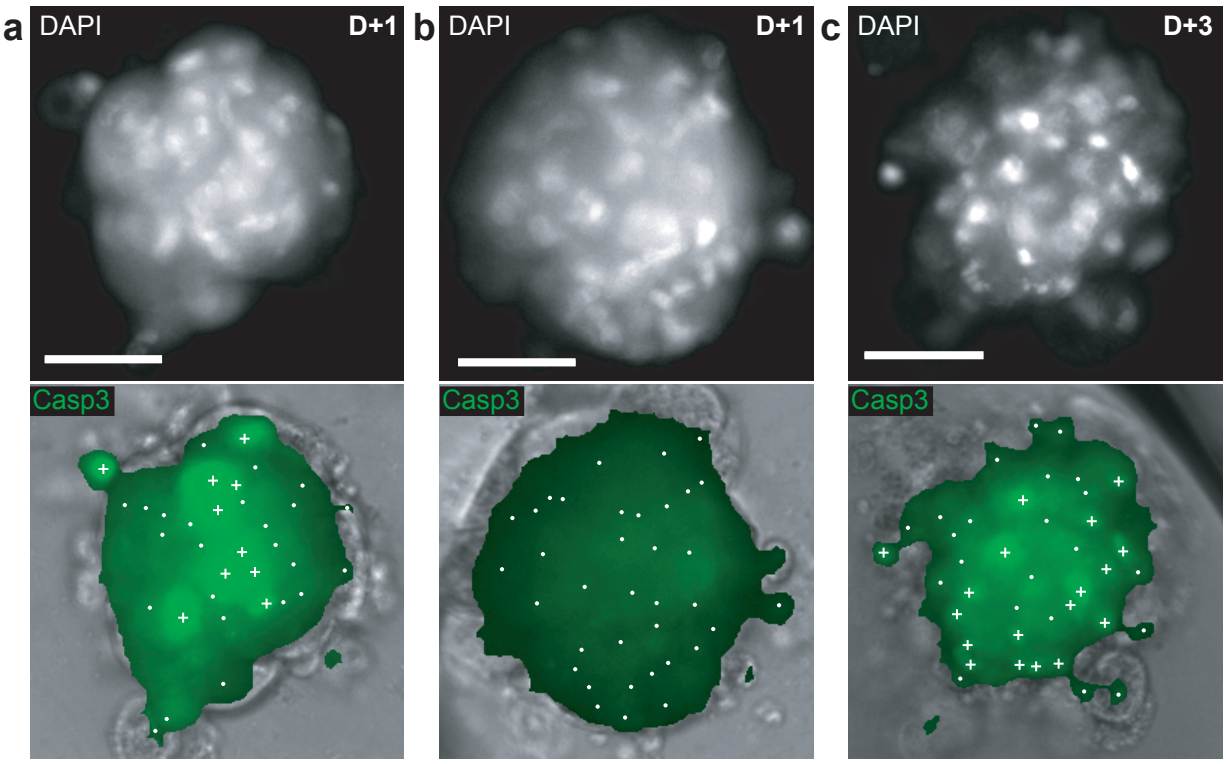

Figure 5.9: Casp3 imaging after 1 or 3 days in culture. Images of the DAPI (top) and Casp3 (bottom) fluorescent intensities for 2 hMSC aggregates after 1 **(a-b)** and 3 days **(c)** of culture. Casp3$^-$ and Casp3$^+$ cells are respectively indicated by white dots and crosses. **(a)** $n_{nuclei} = 34$; diameter = 113.9 μm. **(b)** $n_{nuclei} = 36$; diameter = 128.3 μm. **(c)** $n_{nuclei} = 41$; diameter = 107.8 μm. Scale bars are 50 μm.

The detection of the Casp3$^+$ cells in each hMSC aggregate allows to calculate for each of them the ratio of Casp3$^+$ cells. Fig.5.10 compares this spheroid level data between the 2 culturing times and provides a overview over the entire population. After 1 day of culture (D+1), the hMSC aggregates have between 0 % and 40 % of their cells which are Casp3$^+$, the averaged value being close to 20 %. In turn, after 3 days in culture (D+3), the population distribution is wider and extends up to a ratio of 70 %, with a 32 % average. Therefore, a longer time in 3D culture results in a broader distribution of the Casp3$^+$ ratio centered on a higher value. This indicates a delay in the Casp3 activation which occurs after spheroid formation.

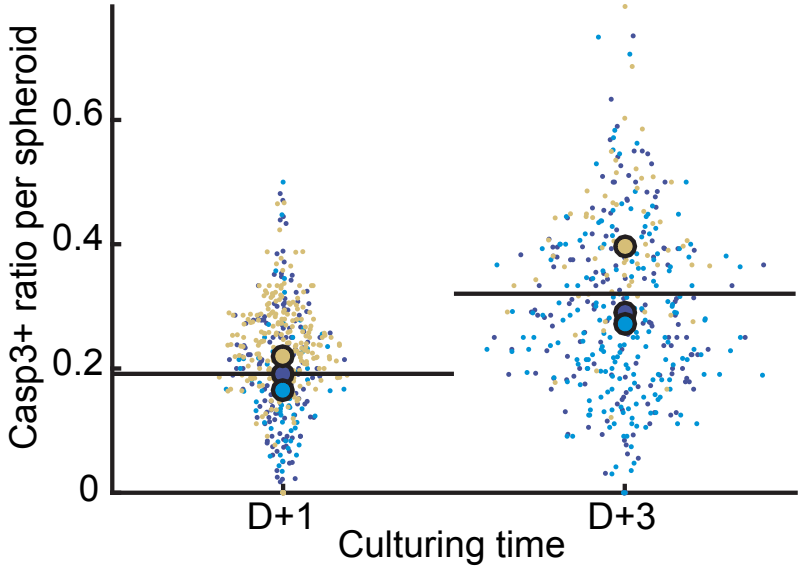

Figure 5.10: Time dependence of the Casp3 signal at the spheroid level. Time evolution of the Casp3$^+$ / DAPI$^+$ ratio in the spheroids. For each time in culture, each color is assigned to a chip, the small and large dots represent respectively the spheroid level data and mean on each chip. The horizontal bars represent the average at the population level. D+1: $n_{spheroids} = 472$; $n_{nuclei} = 26.197$. D+3: $n_{spheroids} = 422$; $n_{nuclei} = 15,620$.

This higher number of Casp3$^+$ cells at D+3 is not the only difference between the two culturing conditions. Indeed, the cellular level analysis provides a more detailed information. Fig.5.11 **(a)** compares at D+1 the probability density of the location (r/R being the normalized distance to the spheroid center) of the Casp3$^+$ cells (green) and all the detected cells (blue) and shows that here is a higher proportion of Casp3$^+$ close to the spheroid center (low r/R values). This trend is confirmed in Fig.5.11 **(b)** which shows the probability of belonging to the Casp3$^+$ population with r/R. This probability is maximum at 0.28 for $r/R = 0.3$, decreases linearly to 0.16 at $r/R = 0.75$ before a sharp increase to reach 0.25 for $r/R = 1$. This result indicates 2 preferential locations for the Casp3$^+$ cells at D+1: close to the spheroid center ($r/R = 0.3$) and at the border of the spheroid($r/R = 1$). These locations might have different explanations. As Casp3 is a hallmark of apoptosis, it

is striking to find a Casp$^+$ cell populations at the border of the spheroid. We previously found similar results when locating the dead cells in hepatocyte spheroids (see Fig.4.15). Therefore, these Casp3$^+$ cells could be dying cells that were excluded from the aggregation. The Casp3$^+$ cell population close to the spheroid center might correspond to the Casp3 activation upon aggregation.

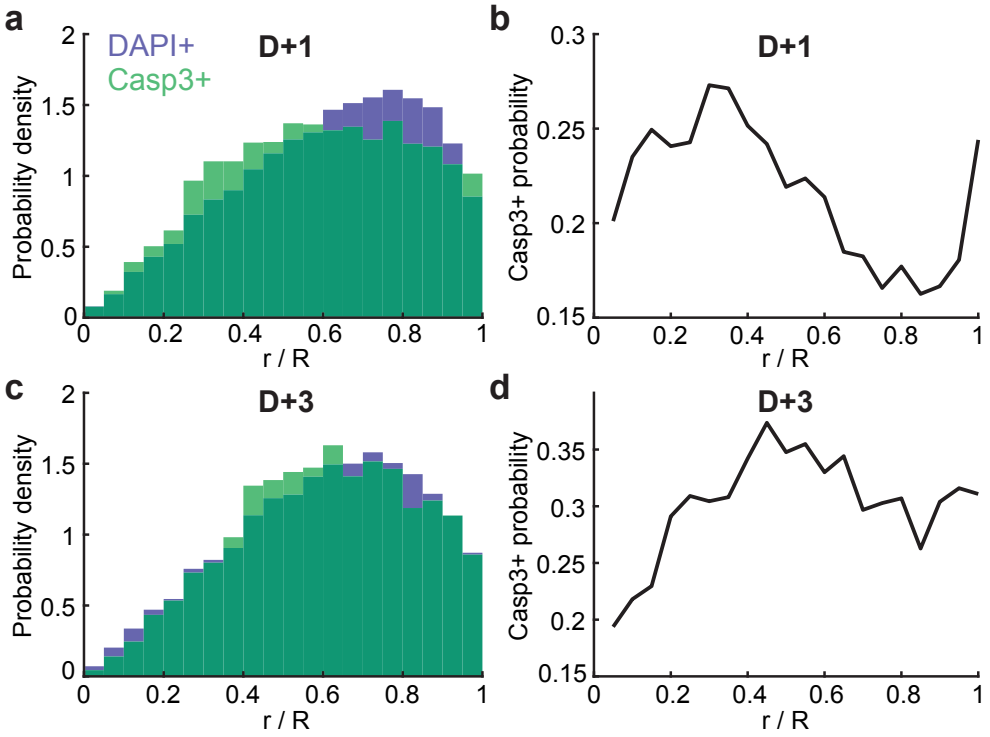

Figure 5.11: Time dependence of the Casp3 signal location at the cellular level. **(a-c)** Location probability density for all the nuclei (DAPI$^+$, blue) and the Casp3$^+$ cells (green) after 1 **(a)** and 3 days **(c)** of culture. r/R is the radial coordinate normalized by the equivalent spheroid radius. **(b-d)** Evolution of the probability for one cell to be Casp3$^+$ with r/R after 1 **(b)** and 3 days **(d)** of culture. D+1: $n_{spheroids} = 472$, $n_{nuclei} = 26,197$. D+3: $n_{spheroids} = 422$, $n_{nuclei} = 15,620$.

A similar analysis is conducted at D+3 (see Fig.5.11 **(c-d)**). The location probability density of the Casp3$^+$ cell population looks quite similar to the one of the entire cell population. The probability to belong to the Casp3$^+$ population increases from 0.2 to 0.37 between $r/R = 0$ and $r/R = 0.45$. For $r/R > 0.5$ the probability decreases slightly but remains almost constant at 0.3. This location pattern is very different from the one obtained at D+1. At D+3, the Casp3$^+$ cells are located inside the spheroids but less often in the core ($r/R < 0.4$). This indicates a propagation of the Casp3 activation over time. If we discard the Casp3$^+$ population at D+1 in the outermost layer of the spheroids, the Casp3 activation begins in the central region and extends gradually with time to the regions closer to the edges. The lower probability to have Casp3$^+$ cells in the center than close to the

edges at D+3 might be due to the fact that these cells in the center were already apoptotic at D+1. As apoptosis progresses at D+3, nuclei become fragmented and are no more able to retain the NucView™ stain.

This hypothesis is supported by the fact that a viability assay at D+3 indicates the presence of a necrotic core inside the hMSC aggregates, as shown in Fig.5.12.

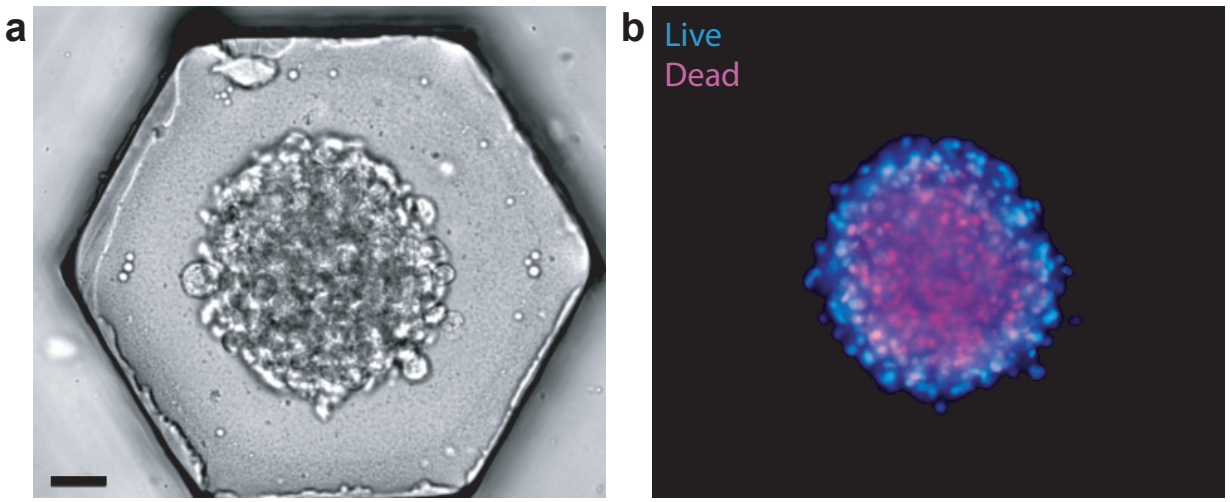

Figure 5.12: Viability at D+3. Bright field **(a)** and fluorescent **(b)** image of an hMSC aggregate. The NucBlue® Live reagent (Live) and propidium iodide (Dead) intensities are respectively shown in blue and red. Scale bar is 50 μm.

5.4.2 Uneven spatial distribution of the cyclooxygenase-2 signal

The COX2 is the only inducible enzyme regulating the production of PGE2. Image analysis was used to quantify the spatial heterogeneities of the COX2 signal inside the hMSC aggregates. Fig.5.13 shows images of 2 typical spheroids of different sizes. The DAPI images (left) allow to detect the nuclei locations and to assign a layer number to each cell (middle). The COX2 intensity (right) is the result of a cytoplasmic immuno-staining, therefore, the intensity cannot be measured as for a nuclear signal. In addition, there was no COX2 peaks and the intensity looks rather homogeneous in each cell, unlike the albumin staining (see subsection 3.4.3). Nevertheless, the COX2 intensity appears higher close to the spheroid border than in the core, in spite of high variation at constant distance to the spheroid center. For instance, in the border part of the spheroid displayed in Fig.5.13 **(a)**, some portions appear brighter than the others (one is highlighted by a white circle) and one part (indicated by a white arrow) has a low intensity similar to the intensity in the core of the spheroid.

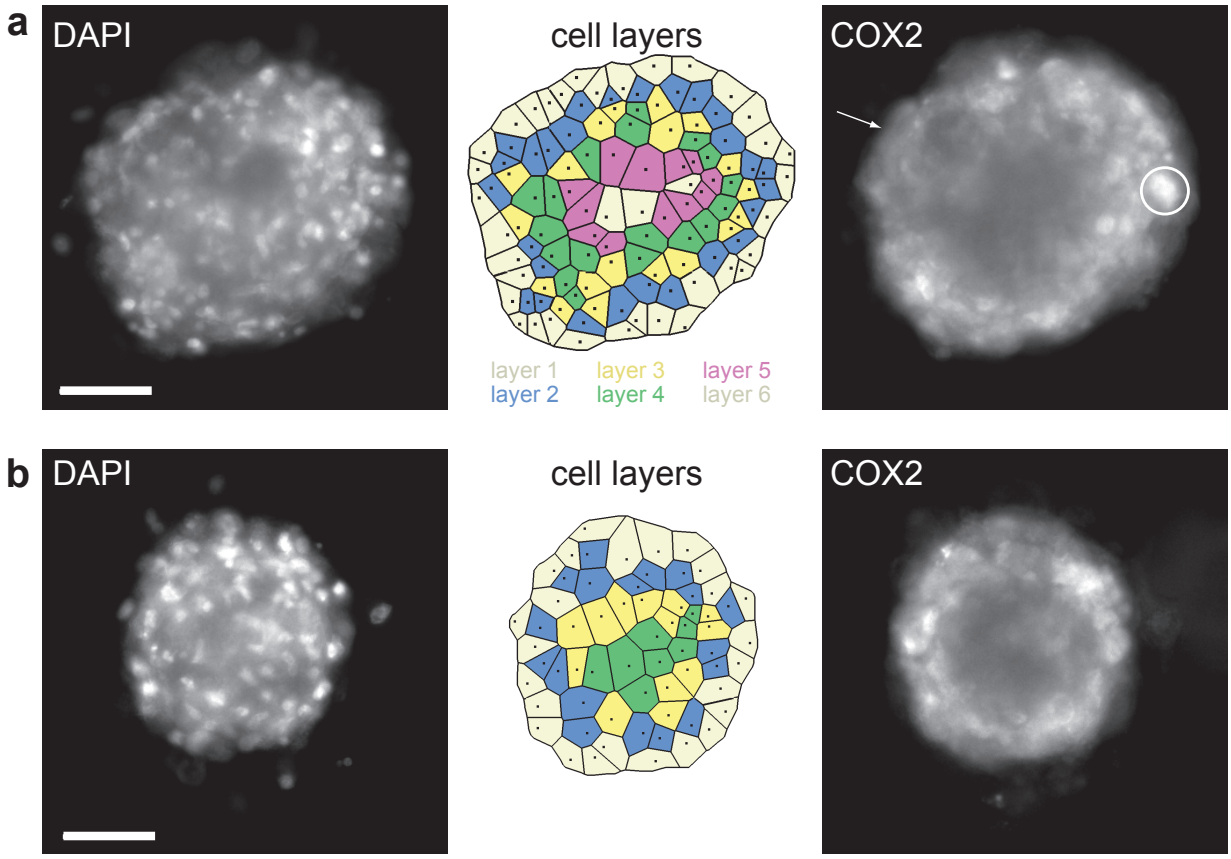

Figure 5.13: COX2 IMAGING. **(a-b)** Images of the DAPI (left) and COX2 (right) fluorescent intensities as well as Voronoi diagrams (middle) for 2 hMSC aggregates. **(a)** $n_{nuclei} = 113$, diameter = 163.6 μm. The white arrow indicates a portion of the hMSC aggregate having a low COX2 intensity even in the border region while the white circle highlights an area with a high COX2 intensity. **(b)** $n_{nuclei} = 64$, diameter = 126.9 μm. Scale bars are 50 μm.

As the Voronoi analysis interpolates the shape of the cells inside the hMSC aggregates, it allows to measure the COX2 signal at the cellular level. The results presented in FIG.5.14 **(a)** indicate that the first 2 layers have a higher COX2 signal than the inner layers. The decrease of the COX2 signal is continuous from the second to the innermost layer. The highest COX2 value is achieved for the second layer. Keeping in mind that some cells detected in the first layer are not well integrated in the spheroid and that we do not control precisely the depth of field, we can say that the highest COX2 signal is achieved for the outermost layers. FIG.5.14 **(a)** also indicates a high standard deviation in the data for each layer, as expected from the observation of the COX2 signal (see FIG.5.13). In addition, this trend is consistently reproduced in each microfluidic chip, as demonstrated by FIG.5.14 **(b)**.

To the best of our knowledge, this reproducible spatial inhomogeneity of the COX2 signal inside hMSC aggregates has never been reported before. Observation of the diffusion

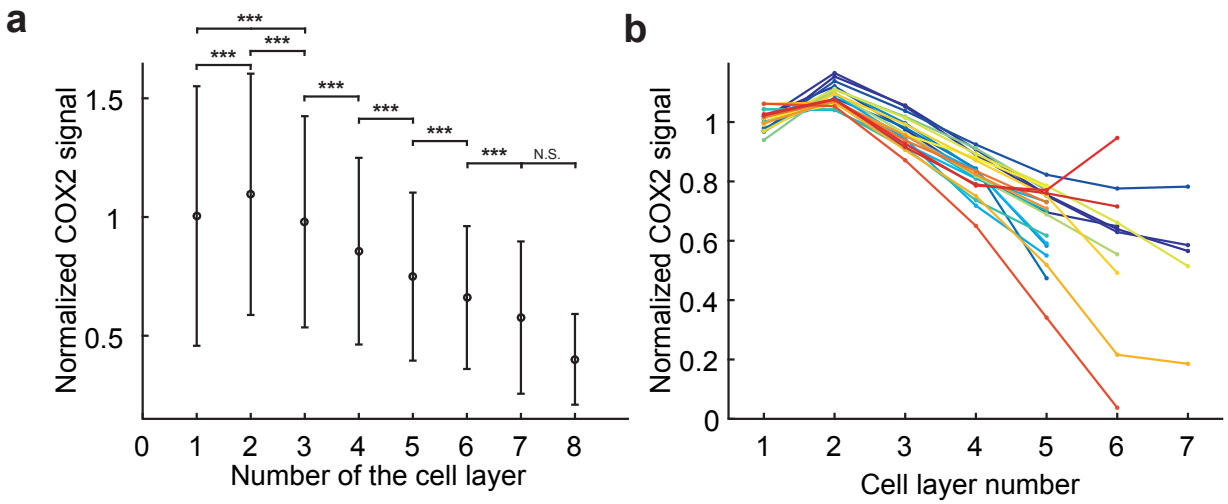

Figure 5.14: Quantification of the spatial distribution of the COX2 signal. **(a)** Evolution of the normalized COX2 signal with the cell layer number. For each cell, the signal was divided by the mean of the chip. Circle and errors bars represent respectively the mean signal and standard deviation per layer. $n_{spheroids} = 5,456$; $n_{nuclei} = 234,458$. **(b)** Evolution of the COX2 trends for each microfluidic chip which are pooled in **(a)**. Each color corresponds to one chip.

of large fluorescently labeled Dextran molecules and homogeneous staining of the spheroids by non specific binding of fluorescent antibodies (without blocking) demonstrate that this is not a effect of the imcomplete diffusion of the antibodies. In addition, the antibody incubation times were long (4 hours for the primary antibody and 2 hours for the secondary antibody).

The induction of the COX2 expression over time (*i.e.* D+1 vs D+3) did not show any significant difference, indicating that if the aggregation of hMSC aggregates upregulates the COX2 expression, this is a fast process reaching a stable expression level 1 day after the droplet trapping.

5.5 Conclusion of chapter 6

In this chapter, we demonstrate the reproducible formation of monodisperse hMSC aggregates in the 400 μm diameter anchors of our microfluidic chip. These spheroids have a diameter close to 140 μm, are circular and organized into up to 8 different adherent cell layers. The *in situ* observation of the Casp3 activity and COX2 expression in the hMSC aggregates reveals distinct spatial location.

First, at D+1, some Casp3$^+$ cells are found in the central region of the spheroids. At

D+3, the number of Casp3$^+$ cells is higher and they are rather located in between the core and the border of the spheroids ($r/R > 0.4$). Second, the COX2 analysis reveals a reproducible higher signal at the spheroid border, regardless of the culturing time.

Bartosh *et al.* [105] hypothesized that the induction of the Casp3 by the aggregation of hMSCs would in turn increase the production of PGE2. In this study, we only investigate the expression level of COX2, not directly the secretion of PGE2. It is possible that the turnover rate of the enzyme or the concentration of the PGE2 precursor are modified at constant COX2 expression level, leading to a modified production of PGE2. Consistently, Casp3 activation did not correlate with COX2 expression, as a result, the signaling pathway that controls directly the expression of COX2 remains unclear. However, it is important to note significant differences between the present work and the results described by Bartosh *et al.* [105]. Indeed, we used hMSCs derived from umbilical cord, not bone marrow and the aggregates we created are encapsulated in agarose droplets.

Further experiments are needed to understand the main cause of the spatial heterogeneities described in this chapter and the regulation of Casp3 and COX2 in hMSC aggregates. However, the presented results demonstrate the suitability of our microfluidic platform for the 3D culture and analysis of cells that are relevant for therapeutic applications, in a high-throughput and detailed manner.

Part III

Concentration gradients and combinatorial chemistry in droplet arrays

In this final part, we further upgrade the microfluidic technology to be able to apply different conditions in the droplets of an high-density array in a controlled manner.

Chapter 6 focuses on the technological aspects allowing the mixing of different reagents in the anchors of a microfluidic chip. We first present the specific anchor design at the heart of this technique as well as the general protocol for combinatorial reactions in high-density arrays. Then, we demonstrate the power of this technique with a proof-of-concept experiment where we perform the combinatorial mixing of colored dyes in a high-density droplet array.

In chapter 7, we combine this technology with 3D cell culture. First, the specific design of the deep anchors needed for spheroid formation is adapted to allow the capture of 2 droplets of different sizes in a single location. Second, we present preliminary results showing that these anchors can be used in a single microfluidic chip to determine precisely the concentration at which a drug affects the viability of hepatocyte spheroids. Finally, we show how this technique can be applied to tissue engineering for controlled spheroid merging and 3D co-culture.

Chapter 6

Capilary traps for combinatorial reactions

In the previous chapters, we have seen how droplet arrays could be used for generating and analyzing high-throughput and quantitative biological data from parallelized 3D cell cultures. Nevertheless, the content of each droplet was the same across the droplet array. It allows, as previously shown, to study in depth the biological variability inherent to cellular models but it would also be useful to test different conditions in the same array. When using hydrogel droplets, it can be done after gelation and phase change by controlling spatially the array perfusion (see section 2.3). If the perfusion can be controlled in time and space, it is difficult to have many different perfusing solutions without increasing significantly the chip design and protocol. In this chapter, we show how we can extend the technology of droplet arrays to perform different reactions in each droplet, regardless of the use of an hydrogel. It allows to perform a high number of different chemical reactions in a single droplet array. This new feature relies on the specific design of the anchors that can trap several droplets with potentially various contents in one location.

6.1 Controlling the number of trapped droplets

In all the previous chapters, the anchors were designed to fit the droplet size. This way, we ensured that only one droplet was trapped per anchor. Here, we consider the case where the anchors are bigger than the droplets. As a result, when a first droplet is trapped, the anchor cavity is not entirely filled and there is some room left for other droplets. Fig.6.1 shows how the size and shape of the anchor can be used to control the number of trapped droplets. In Fig.6.1 **(a-b)**, the anchors have respectively the shape of ellipses and diamonds and each

of them traps 2 droplets. In both cases, the first trapped droplet is in the center of the anchor before the trapping of the second droplet. This way, the droplet is not constrained by the anchor edges and its confinement is minimum. When the second droplet arrives, the first droplet is moved to one side of the anchor and the second droplet is immobilized on the other side. Each droplet surface energy would be further minimized at the center of the anchor but having one droplet on each side of the anchor is the situation that minimizes the surface energy of the two droplet system. The main difference between the two anchor shapes shown in Fig.6.1 **(a-b)** is that in the diamond case, each side of the anchor acts like a diverging rail that drives the droplet towards the central region of the anchor. So when two droplets are trapped in a diamond anchor, they are pushed against one another, ensuring a large contact area between the droplets. Fig.6.1 **(c)** shows anchors that have the shape of a 3 branches star and that can trap 3 droplets, one on each branch. Similarly to the diamond case, each branch of the star has a triangular shape that pushes the droplets against one another. As long as the anchor is bigger than the droplets, many anchor shapes can be used, like the dumbell in Fig.6.1 **(d-f)**, the thick line in Fig.6.1 **(g-h)** or the star with 3 thick line branches in Fig.6.1 **(i)**.

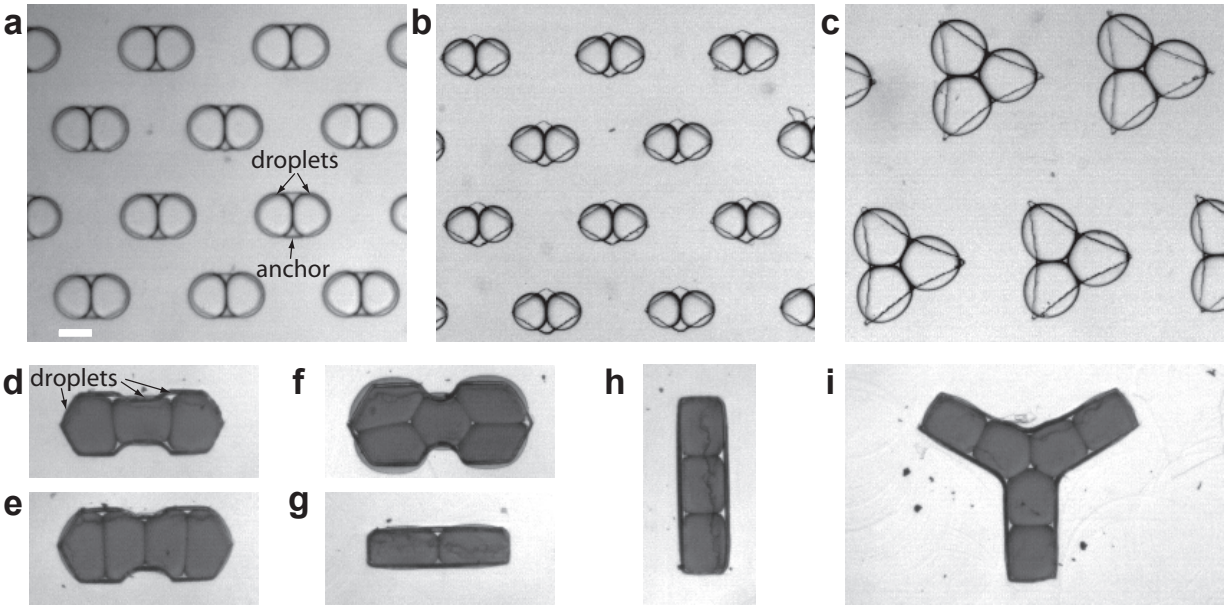

Figure 6.1: Trapping droplets of similar sizes. Images of anchors trapping several identical droplets. **(a-b)** Ovale **(a)** and diamond **(b)** anchors for 2 droplets. **(c)** 3 branches star anchor for 3 droplets. **(d-f)** Dumbell anchors with different dimensions trapping 3 **(d)**, 4 **(e)** and 5 **(f)** dark droplets. **(g-h)** Thick straight line anchors for trapping 2 or 3 droplets. **(i)** Anchor with 6 trapped droplets. For all the images, the chamber height is 100 μm. For **(a-c)**, the anchor depth is 50 μm, for **(d-i)** it is 250 μm. Scale bar is 200 μm for all images.

Trapping several droplets of same size in large anchor is not new. Indeed, Fradet *et al.* [42] showed that two droplets can be immobilized in large circular anchors. Moreover, if

the trapping force is sufficiently low, for instance with a small anchor depth, the external oil flowrate can be increased in order to extract one of the two droplets in each anchor. This way, the anchors can be refilled with a different set of droplets having a similar size but a different content. Therefore, the same 2 different droplets are trapped in each anchor. If these droplets encapsulate different chemical reagents, they can be coalesced to trigger a chemical reaction in the resulting droplet. This technique can be useful but relies on the assumption that the trapping force is sufficiently low for selectively detrapping of 1 of the 2 immobilized droplets. This protocol does not work in the case of anchors exerting a trapping force sufficiently high to prevent the detrapping of the immobilized droplets, and we know from chapter 2 that efficient anchors are of fundamental importance for long-term 3D cell cultures in hydrogel droplets.

Therefore, we want to be able to trap droplets of different contents in the same anchor, in a controlled manner and without assuming a low trapping force. In all of the cases shown in Fig.6.1, the size of the trapped droplets is identical and in Fig.6.2 we show anchors that can trap droplets of different sizes. The basic design is detailed schematically in Fig.6.2 **(a)**. The principle is that the shape of the anchor is designed in order to exert a different trapping force depending on the location inside the anchor. In this example, the anchor shape is a combination of a circle (with a diameter d_1) and a triangle (with a width d_2 and a length d_3). If a droplet has an apparent diameter (when confined) close to d_1 the trapping force will be maximum in the circle, because it results in the higher decrease of confinement and thus, in a high trapping efficiency. On the triangle, only a part of the droplet can enter the anchor cavity, resulting in a low trapping efficiency at this specific location. Consequently, when introducing the white droplets, the first that reaches the anchor is immobilized on the circular part and the triangular part can even help the droplet reaching the circle by acting like a rail. Then, there is some room left in the triangular part of the anchor, and so, a second white droplet can be immobilized. But, as the trapping force for the white droplets is lower in the triangular part than in the circular part, an increase of the external flowrate will lead to the selective detrapping of the droplets that were on the triangular part of the anchor. This way, only the circular part is filled, with a droplet subjected a high trapping force. Moreover, there is no need to change the oil flowrate during the first droplet filling. Indeed, if the filling of the first droplets is directly made at high flowrate, the droplets will only be trapped in the circular part of the anchor. This situation is schematically displayed in Fig.6.2 **(a)** (left scheme) and on the left image of Fig.6.2 **(b)**.

Now, we can introduce smaller droplets (dark droplets on the figure) that can have a content different from the white droplets and that are going to fill the triangular parts of the anchors. The size has been reduced because, in the triangular parts of the anchors, it results in a trapping efficiency higher that the one experienced by the large white droplets. Indeed, for the small droplets a large portion of the volume can enter the triangle cavity and the apparent droplet area in the section of the microfluidic channel (that will determine the magnitude of the drag force) is low. On the contrary, there is only a small portion of the large droplets that can enter the triangle cavity and they have a large apparent area in the

channel section thus, they experience a high drag force. The situation where the anchors are filled with one large white droplet and one small black droplet is schematically represented in Fig.6.2 **(a)** (left scheme) and corresponds to the right image of Fig.6.2 **(b)**. Similarly as Fig.6.1 **(b-c)**, the triangular part of the anchor acts like a rail and helps maintaining a large contact area between the large and small droplets.

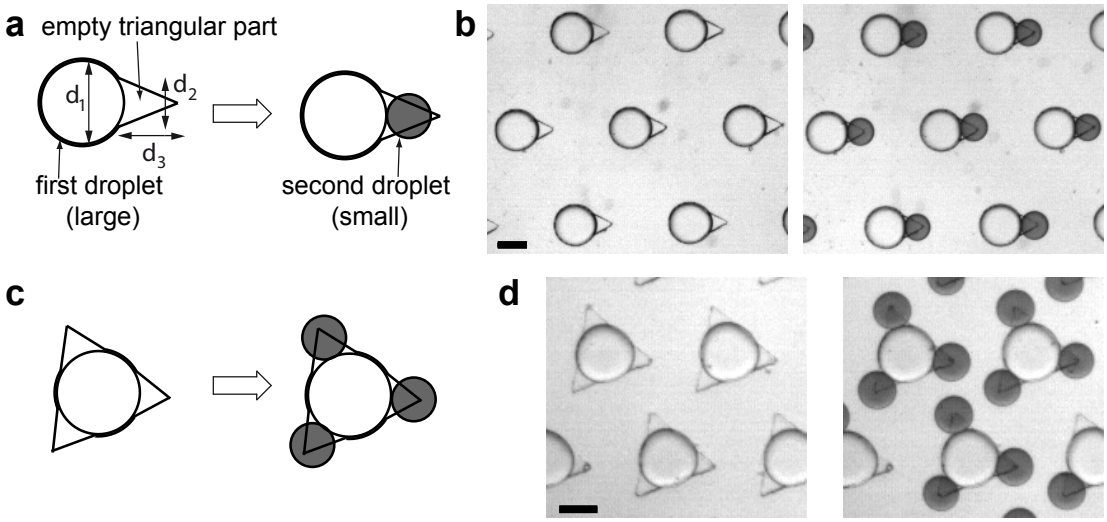

Figure 6.2: Trapping droplets of different sizes. **(a)** Schematic representation of an anchor that can trap 2 droplets of different sizes. d_1 is the diameter of the circle, d_2 and d_3 are respectively the triangle width and length. **(b)** Images of 7 anchors, as described in **(a)**, after the first (left, large white droplets) and second droplet capture (right, small dark droplets). $d_1 = 250\ \mu m$. $d_2 = d_3 = 150\ \mu m$. Chamber height: $h = 100\ \mu$m. Anchor depth: $\Delta h = 50\ \mu m$ **(c)** Schematic representation of an anchor that can trap 1 large and 3 small droplets. **(d)** Images of 3 anchors, as described in **(c)**, after the first and second droplet capture. Scale bars are 200 μm.

This technology is not limited to the capture of 2 droplet of different sizes. Indeed, Fig.6.2 **(c-d)** show that the anchor design can be modified to control the number of large and small droplets that are trapped. In the example shown in Fig.6.2 **(c)**, one large droplet can enter the center of the large triangle and one small droplet can fill each of the 3 corners of the anchor. This is shown on the images of Fig.6.2 **(d)**.

To conclude, with anchors whose shape do not have a revolution symmetry, we can trap a controlled number of large and small droplets. This can be done even if one large droplet experiences a high trapping force.

Tullis *et al.* [109] have shown that droplets of different sizes can be trapped in the same circular anchor (see Fig.6.3). But since the filling is sequential (first, the large droplets, then, the smaller ones) nothing prevents several large droplets from being trapped in the anchor. These additional droplets have to be removed by increasing the external oil flowrate

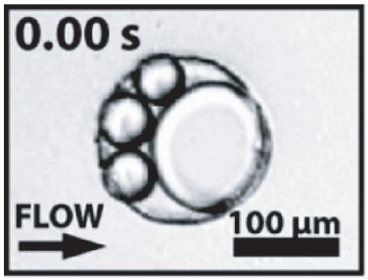

Figure 6.3: Trapping droplet of different sizes - State of the art. Time lapse images showing the trapping of 1 large and 3 small droplets in a single circular anchor (reproduced from Tullis *et al.* [109]). Anchor depth $\Delta h = 15\ \mu m$.

and thus, the trapping efficiency must be low. In addition, the circular shape of the anchor makes it very difficult to control the number of small droplets that are trapped.

In the next section, we will describe how the anchors presented above can be used in a microfluidic chip for creating combinatorial chemical reactions.

6.2 Merging droplets in an array of combinatorial anchors

6.2.1 General protocol

Contrary to the previous chapters, the trapping chamber can be filled with anchors that can trap several droplets. The droplets that will fill the anchors can be produced on chip, similarly to what we have seen in chapter 1. In this case, the droplet size can be controlled by the flowrates at the droplet producing junction but it is difficult to change the droplet content. Indeed, it requires to change the injected aqueous solution and it becomes labor intensive for more than a couple of different solutions. We could also have two different aqueous inlets, that would mix before reaching the junction. Changing the flowrate ratio between the two solutions would allow to control in real time the droplet content. Unfortunately, this procedure would only be possible after a transition time, where the droplet content would not be controlled. Indeed, as the external oil contains surfactants, the 2 aqueous phases need to first enter in contact and then merge before been able to control their mixing. This transition phase would lead to the production of unknown droplets that would still be trapped in the anchor array. Alternatively, the droplets can be produced off chip. For instance, we could inject droplets from a pre-formed library.

Consequently, different protocols can be used with anchors trapping several droplets for the formation of combinatorial reactions, as shown in Fig.6.4. In all of them, the an-

chors are filled with several droplets of different contents. Then, the neighboring droplets are coalesced to mix their content. Fig.6.4 **(a)** describes the use of anchors that can trap 3 droplets of similar sizes (like the ones shown in Fig.6.1 **(c)**) but potentially different contents. As these droplets come from a library, the anchors are filled randomly with different combinations of droplets (1 blue/1 yellow/1 red, 2 blue/1 red etc...). After coalescence, each combination of separated droplets results in a different content after merging. It is worth noting that the number of different mixes is much higher than the initial number of different droplets in the library. This is the result of the combinatorial mixing.

Trapping droplets of different sizes allows to sequentially fill the anchors and thus, to control the content of the droplets trapped at each step. In Fig.6.4 **(b-d)**, we choose the example of the anchors displayed in Fig.6.2 **(b)**, that can trap 1 large and 1 small droplet. Fig.6.4 **(b)** shows the case where all the large droplets and all the small droplets have the same content. Therefore, each anchor is filled with the same droplets, one small and one large, and after coalescence, all merged droplets have the same content across the array. This experiment can be easily done with on chip production of the droplets. The first droplets are produced with a first solution and the second droplets are produced after changing the aqueous inlet and with different flowrates at the junction. Alternatively, Fig.6.4 **(c)** shows the case where all the large droplets have the same content but the small droplets come from a library. This way, there are as many different pairs of droplets as there are different contents in the small droplets of the library, and thus, as there are different merged droplets after coalescence.

In Fig.6.4 **(d)** both the large and small droplets come from a library of different contents. Consequently, after coalescence, there are much more different merged droplets than in the case of Fig.6.4 **(c)**. The protocol explained in Fig.6.4 **(d)** can be used for optimizing the concentration of the 2 reagents of a chemical reaction. The large droplets could encapsulate different concentrations of a reagent A and the small droplets different concentrations of a reagent B. Finding at the end of the experiment the merged droplet in which the reaction was most efficient, for instance by monitoring a fluorescence signal linked to the product concentration, would mean finding the optimum quantities of reagents A and B.

In all these protocols, the final mixing of the neighboring droplets is done by coalescence. This step can be performed with many different techniques [26], comprising the use of electrical fields [110], acoustic waves [111], hydrodynamic forces [112] or surfactant removal [109]. The coalescence step can either be selective, for instance with infra-red laser stimulation [42], or global. In the present work, we chose to trigger rapidly the coalescence by perfusing the entire array with a chemical reagent dissolved in the external fluorinated oil that destabilizes the surfactant.

Chemically-induced coalescence Fluorinated linear alcools are known to increase the surface tension of aqueous droplets stabilized with surfactants in fluorinated oil [113].

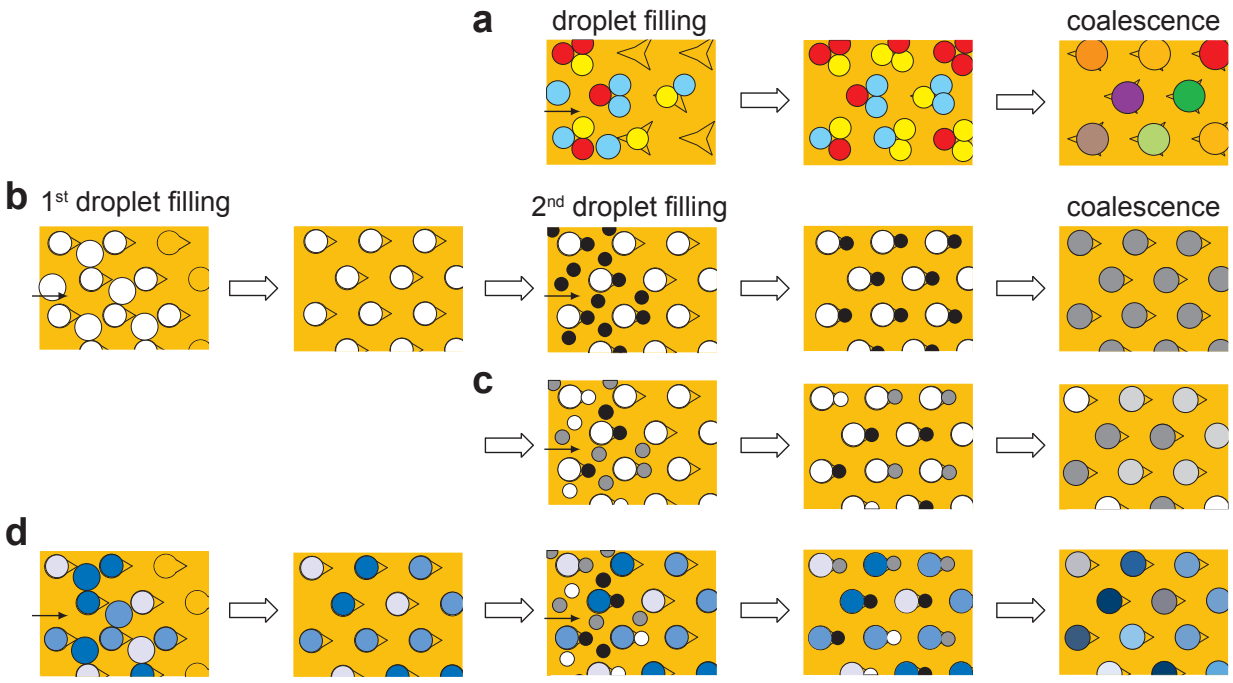

Figure 6.4: Schematized protocols for combinatorial reactions. The anchors are filled with droplets and a coalescence step allows to mix droplets immobilized in the same trap. **(a)** Anchors that can trap 3 droplets of same size. **(b-d)** Protocols for anchors that can trap sequentially 2 droplet of different sizes. **(b)** Case where the content of droplets of same size is similar. **(c)** Case where the first droplets are identical but the second droplets have different contents. **(d)** Case where both the first and second droplets have different contents.

Consequently, they counteract the surfactant effect and destabilize the droplets. Here, we achieve an efficient coalescence by perfusing the droplet array with 1H,1H,2H,2H-perfluooctan-1-ol disolved in the fluorinated oil HFE-7500 at a 20 % volumetric ratio. Fig.6.5 **(a)** shows time lapse images during this perfusion step (perfusion from the left to the right of the image). At first, each anchor is filled with a large white droplet and a small dark droplet. 3 minutes after the beginning of the perfusion, about half of the droplets have coalesced and 4 minutes later all the droplets of the array have been merged. This experiment corresponds to the protocol of Fig.6.4 **(b)** and therefore, all the final droplets have the same content. The varying shades that are seen on the bottom image of Fig.6.5 **(a)** come from the reaction of the dye 2,6-Dichlorophenolindophenol (2,6-DCPIP) with the oxygen in the perfusing oil. Fig.6.5 **(b)** shows time lapse images of the coalescence of 2 droplets followed by the diffusion of the reagents. About 10 seconds after the coalescence, the merged droplet has an homogeneous content. This way, merging stationary droplets allows to study the reaction-diffusion characteristics of a chemical reaction [114]. The kinetics of this process across the array can be investigated with space-time diagrams of the time-lapse images. Fig.6.5 **(c)** is a space-time diagrams over a column of the droplet

array, measuring the timing of the coalescence events in 12 anchors. We can see that in this column and in this line, both close to the central region of the array, all coalescence events occur between the 2nd and 6th minute of perfusion. There is apparently no clear pattern in the coalescence order. At the scale of the entire array, we observe that the very first droplets to coalesce are often in the first columns (the first in contact with the perfusing solution, so on the left side of the array). The last droplets to coalesce are often located on the right side of the array and very close to the chamber side walls.

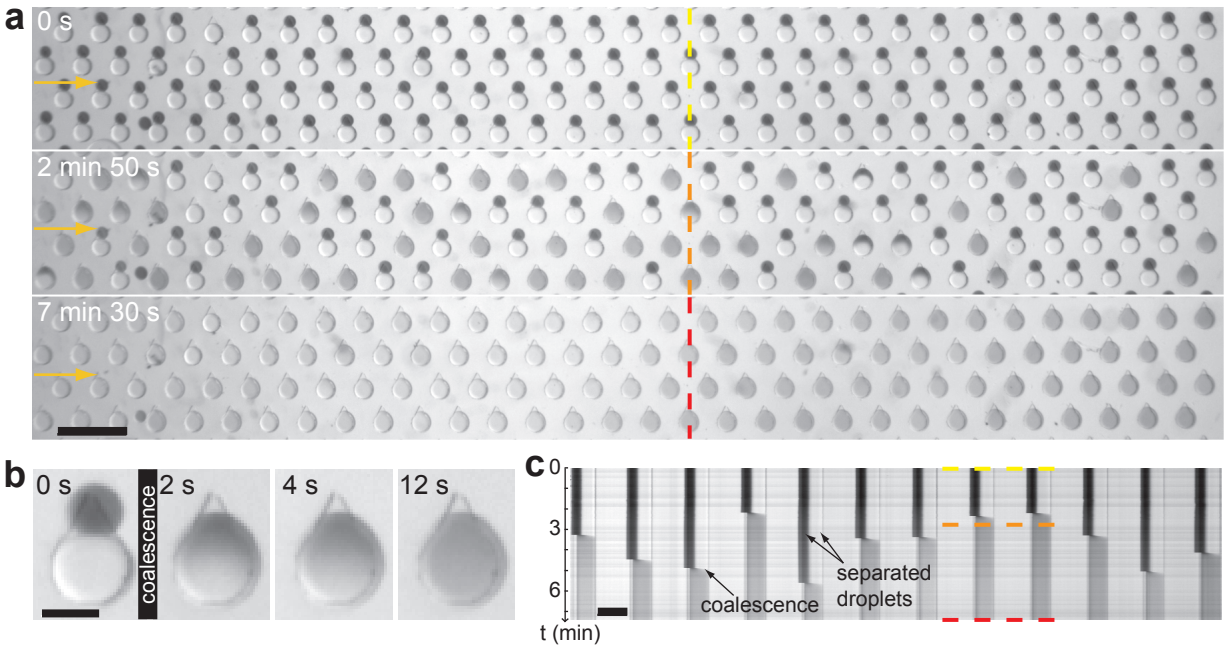

Figure 6.5: Coalescence of the droplet array. **(a)** Time lapse images of 124 anchors at the beginning (top), during (middle) and at the end (bottom) of the coalescence under PFO perfusion. The yellow arrows indicate the direction of the oil flow. Scale bar is 1 mm. **(b)** Time lapse images starting just before the coalescence of 2 neighboring droplets. Scale bar is 200 μm. **(c)** Space time diagrams on a column **(c)** of the droplet array. The location of the pixel line is highlighted in colored dashed lines in **(a)** for three different time points. Scale bar is 500 μm (in the horizontal direction).

This demonstrates that the chemically-induced coalescence is a simple, rapid and effective way to merge all the droplets in an array. As shown in Fig.6.4, the coalescence allows to merge droplets of different contents and thus, to perform the combinatorial mixing of the reagents of a library.

6.2.2 Combinatorial statistics

Combinatorial statistics allows us to predict the number of different droplet contents that will be found after coalescence in a trapping chamber. In this subsection, the parameters are defined as followed:

- n is the number of different contents that are available in a droplet library;
- k is the number of droplets that can be immobilized on a single trap;
- N_{traps} represents the number of anchors in the array;
- $\Gamma_n^{k\neq}$ is the number of different combinations that are achievable with k droplets per anchor and n content in the droplet library, regardless of the number of anchors.

First, we look at the case of anchors capable of trapping droplets of similar sizes (see Fig.6.1). In these anchors, we randomly trap droplets coming from a library, as shown in Fig.6.4 **(a)**. In this case, we count the possible combinations with repeatitions. For instance, with $k = 3$, the combinations of droplet colors (red, yellow, yellow) and (yellow, red, yellow) are not in the same order but both yield the same orange droplet after coalescence. As a result, they are considered as the same combination, even if not originally in the same order. In this context, the number of combinations with repeatitions is [115]:

$$\Gamma_n^{k\neq} = \left(\!\!\binom{n}{k}\!\!\right) = \binom{n+k-1}{k} = \frac{(n+k-1)!}{(n-1)!k!} \tag{6.2.1}$$

This number of different combinations is illustrated in Fig.6.6 **(a)** for anchors that can trap up to 6 different droplets. We see that there can be many different combinations achievable without more than $n = 20$ different droplets in the library. For instance, with $n = 20$, 3 and 6 droplets anchors can generate respectively 1,540 and 177,100 different combinations. With $n = 5$, 2 and 5 droplets anchors can generate respectively 15 and 126 different combinations. This demonstrates the potentiality of anchors with multiple droplets in high-throughput combinatorial chemistry.

For the anchors that can trap 2 droplets of different sizes, (see Fig.6.2 **(a-b)**) the droplets can come from two different libraries (see Fig.6.4 **(d)**) having respectively n_1 and n_2 different contents. In this case, the maximum number of different combinations is simply:

$$\text{anchors for 2 droplets of different sizes} \implies \Gamma_{n_1,n_2}^{k\neq} = n_1 n_2 \tag{6.2.2}$$

because there is in each anchor one droplet from each library.

Now that we know how many different combinations are achievable depending on the anchors design and on the library size, we also need to choose the number of anchors in the array. Indeed, it is useless to be able to create thousands of different combinations if

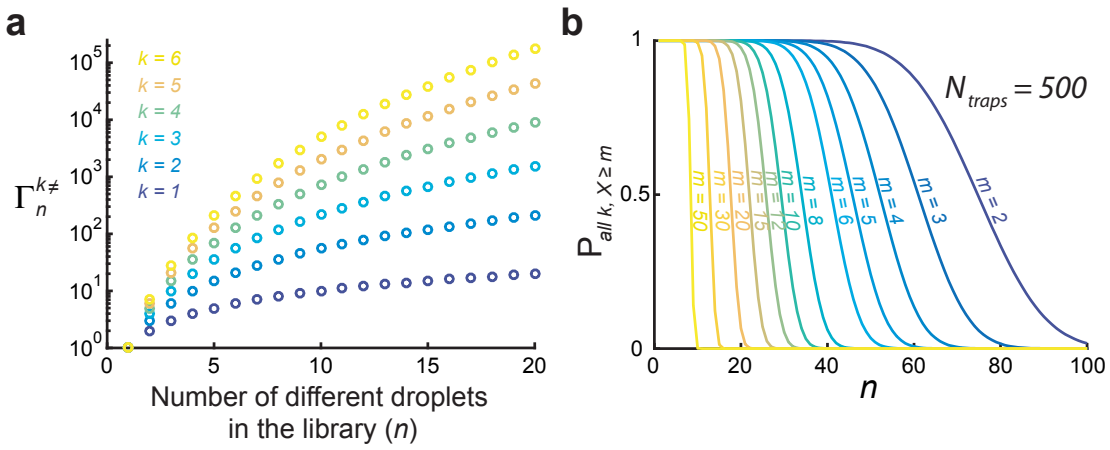

Figure 6.6: Combinatorial statistics. **(a)** Evolution of the number of different combinaisons $\Gamma_n^{k\neq}$ (see equation (6.2.1)) with the number n of different droplets in the library for anchors that can trap $k = 1$ to 6 droplets of the same size. **(b)** Case of an array with $N_{traps} = 500$ anchors for trapping droplets of different sizes. The first droplet is the same in every anchor, the second droplet comes from a library. Evolution of the probability $P_{allk,X\geq m}$ (see equations (6.2.5) and(6.2.6)) to have at least m times each of the possible combinations with the number n of different droplets in the library.

there are not enough anchors to test them. Moreover, we may want to have a minimum number of repetitions for each condition. Here, we consider the protocol of Fig.6.4 **(c)** where 2 droplets of different sizes are trapped with all large droplets identical and the small droplets generated from a library. Therefore, the content of the small droplet is the only parameter that varies. The probability to have one particular small droplet content in one anchor is:

$$p = \frac{1}{n} \tag{6.2.3}$$

Therefore, if X is the number of times that a particular content is found in an array, the probability of having exactly i times this particular content follows a binomial distribution:

$$P(X = i) = \binom{N_{traps}}{i} p^i (1-p)^{N_{traps}-i} \tag{6.2.4}$$

As a consequence, the probability of finding at least m times one particular combination of droplets in the array is:

$$P(X \geq m) = \sum_{i=m}^{N_{traps}} \binom{N_{traps}}{i} p^i (1-p)^{N_{traps}-i} \tag{6.2.5}$$

As the content of the merged droplets depends only on the small droplet there are n different conditions possible. The probability to have at least m times each of the n possible

conditions is:

$$P_{allk,X\geq m} = (P(X \geq m))^n \tag{6.2.6}$$

This probability is displayed in Fig.6.6 **(b)** for $N_{traps} = 500$. For instance, we can see that with $n = 40$ different droplets in the library, the probability to have all combinations at least 5 times is 0.82.

6.3 Combinatorial mixing of colored dyes in a droplet array

In this section, we demonstrate the potential of our microfluidic platform for creating anchored combinatorial reactions by mixing droplets of food dyes. We use anchors that can trap 2 droplets of different sizes (see Fig.6.2 **(a-b)**), the large and small droplets both coming from a library of 5 different concentrations. The production of droplet libraries and the experimental parameters of this proof-of-concept experiment are presented in appendix B.1.

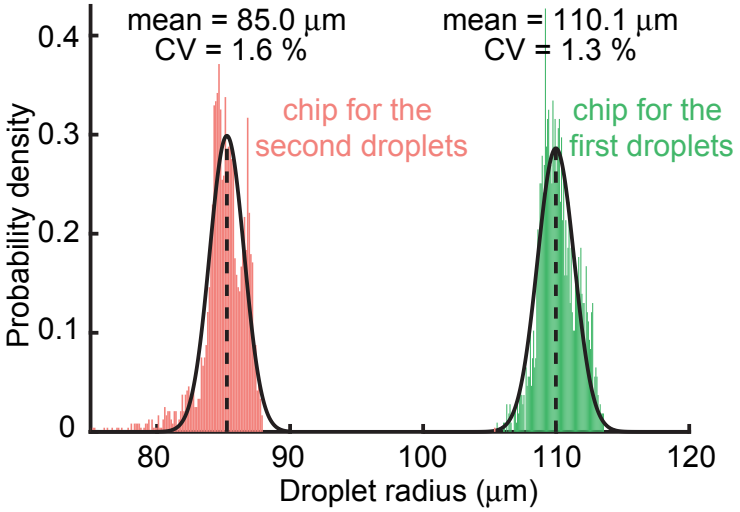

Figure 6.7: Fabrication of libraries of 2 droplet sizes. Polydispersity histogram of the droplets of the first (green, $n_{droplets} = 1,334$) and second (red, $n_{droplets} = 2,001$) libraries. Black lines are Gaussian fits of the data.

In this experiment, the large and small droplet colors vary respectively from yellow to blue and from uncolored to red. The trapping chamber has 388 anchors on a 2 cm^2 area. According to previous notations (see Fig.6.2), the geometrical parameters of the anchors are the following: $d_1 = 250\ \mu m$, $d_2 = d_3 = 150\ \mu m$, $h = 100\ \mu$m and $\Delta h = 50\ \mu m$. Therefore, the volume of the cylindrical section of the anchor is 7,4 nL. In Fig.6.7 **(a)**, we can see a polydispersity histogram for the large (green histogram) and small (pink

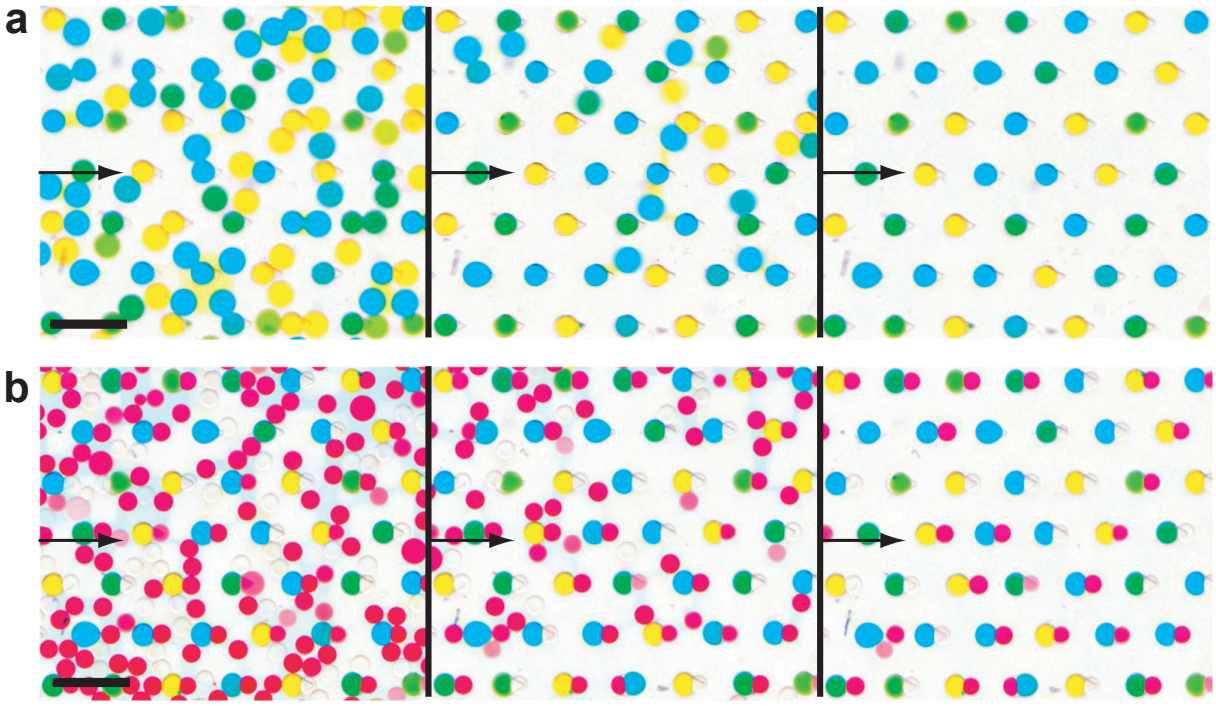

Figure 6.8: Sequential filling of the anchor array. Time lapse images of the first **(b)** and second **(c)** droplet trapping in 46 double anchors. The black arrows represent the direction of the oil flowrate. Scale bars are 1 mm.

histogram) droplets. The small and large droplets have respectively a radius of 85 and 110 μm, which gives volumes of 2.6 and 5.6 nL. Therefore, the large droplets can fill the cylindrical parts of the anchors without filling the triangular parts. This is illustrated in Fig.6.8 **(a)** where every anchor immobilizes a single droplet, either yellow, green or blue. As the triangular parts of the anchors are still empty, the smaller red to uncolored droplets can be trapped. This stage is illustrated in Fig.6.8 **(b)** where every anchor immobilizes a small droplet, either uncolored, pink or red.

At the end of the trapping, we have immobilized in each anchor a large droplet, whose color is either yellow, green or blue, and a small droplet, either uncolored, pink or red. (see Fig.6.9 **(a)**). As each library was produced from segments of 5 different concentrations, there are 25 different possible combinations (see equation (6.2.2) with $n_1 = n_2 = 5$) in the anchors, each one being repeated on average 15.5 times across the array. These combinations lead to different colors for the merged droplets after the coalescence step (which is performed as described in subsection 6.2.1). This situation is displayed in Fig.6.9 **(b)**, that shows the same 80 anchors as in **(a)**. This color covering is illustrated more quantitatively on Fig.6.9 **(c-d)**. The droplets are detected by image analysis, their intensities are computed and displayed in the RGB space. Before the coalescence (Fig.6.9 **(c)**), we can clearly see the difference between the small and large droplets. In the large droplets, we can even

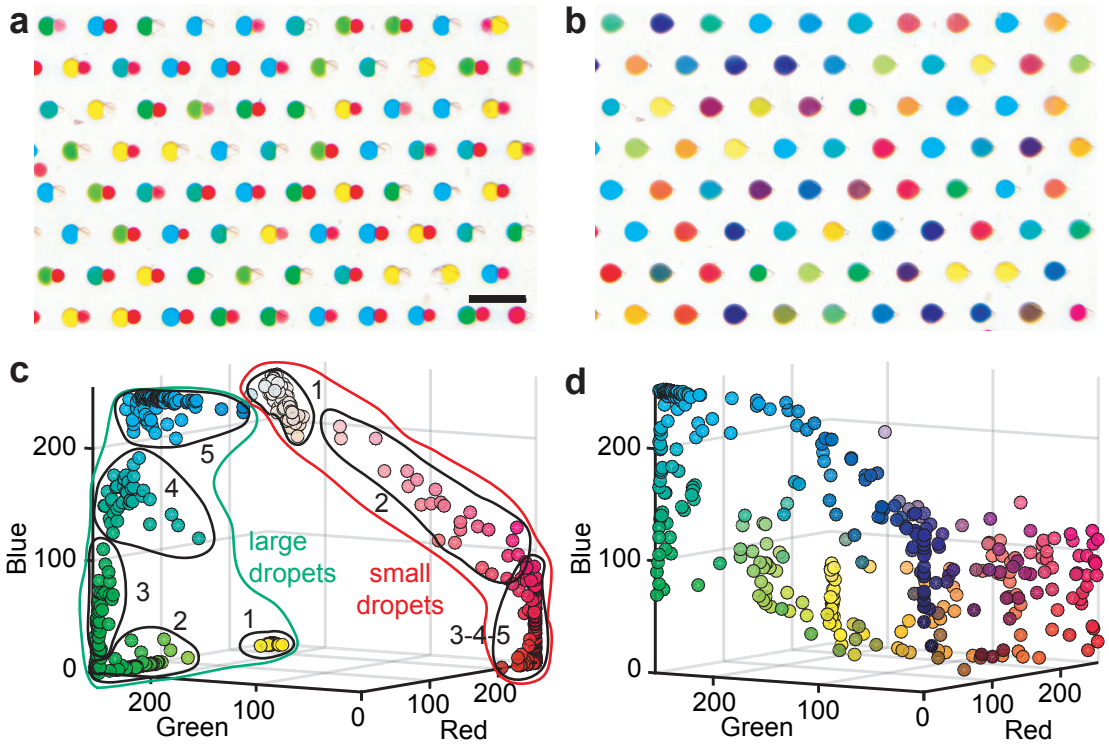

Figure 6.9: Combinatorial mixing of dyed droplets. **(a)** Image of 80 anchors filled with 2 droplets of different sizes. The large droplets have 5 shades of colors from yellow to blue. The small droplets have also 5 different shades from uncolored to red. Scale bar is 1 mm. **(b)** Image of the same anchors as in **(a)** after colescence of the droplet array. **(c-d)** Quantification of the droplets intensities in RGB (8-bit) before **(c)** and after **(d)** the coalescence. The RGB coordinates are used for choosing the color of each dot. $n_{droplets} = 351$.

distinguish the 5 different contents. This is not possible for the small droplets because of the saturation of the red channel. After coalescence (Fig.6.9 **(d)**), the combinatorial mixing results in more dispersed coverage of the RGB space.

This final experiment demonstrates the potential of specifically designed anchors for combinatorial reactions. In the following chapter, we combine this technique with 3D cell culture in microfluidic droplets.

Chapter 7

Use of combinatorial anchors with spheroids

7.1 3D design of the anchors

In order to use the combinatorial anchors with spheroids, their design had to be modified, based on the ones used in chapter 5, with a triangular corner instead of one of the anchor sides. The geometrical parameters of these anchors are defined on Fig.7.1 **(a)**. When loading droplets of appropriate size (see Fig.7.1 **(b)**), they are either immobilized in the hexagonal cavities or, when the hexagonal cavity is already filled, in the triangular parts of these anchors. If we increase the external oil flowrate, all the droplets that were immobilized on the triangular parts of the anchors are removed (Fig.7.1 **(c)**). So far, this behavior is similar to what was observed in the previous chapter, for instance in Fig.6.1 **(b)**. Then, we inject the second droplets (dark droplets in the figure) that are smaller than the ones already immobilized (uncolored droplets). These droplets are created on chip, simply by changing the flowrates at the droplet producing junction. Surprisingly, in spite of an appropriate droplet size, we are only able to immobilize a handful of small dark droplets in the anchors, as shown in Fig.7.1 **(d)** with only one dark droplet immobilized. From the observation of this phenomenon, it looks like the deep anchors induce a modification of the flow lines, as represented in Fig.7.1 **(f)**. Indeed, the dark droplets move in between the anchors without passing above an empty triangular part. It even seems that the only dark droplets that were trapped, were moved from their initial trajectories after collision with another dark droplet.

The most plausible cause of this flow modification is the presence in the chamber of very deep areas (compared to the chamber height) that are also filled with the same oily phase. Therefore, we hypothesized that reducing the height of the triangular parts of the anchors would limit this flow modification and allow a much more systematic trapping of

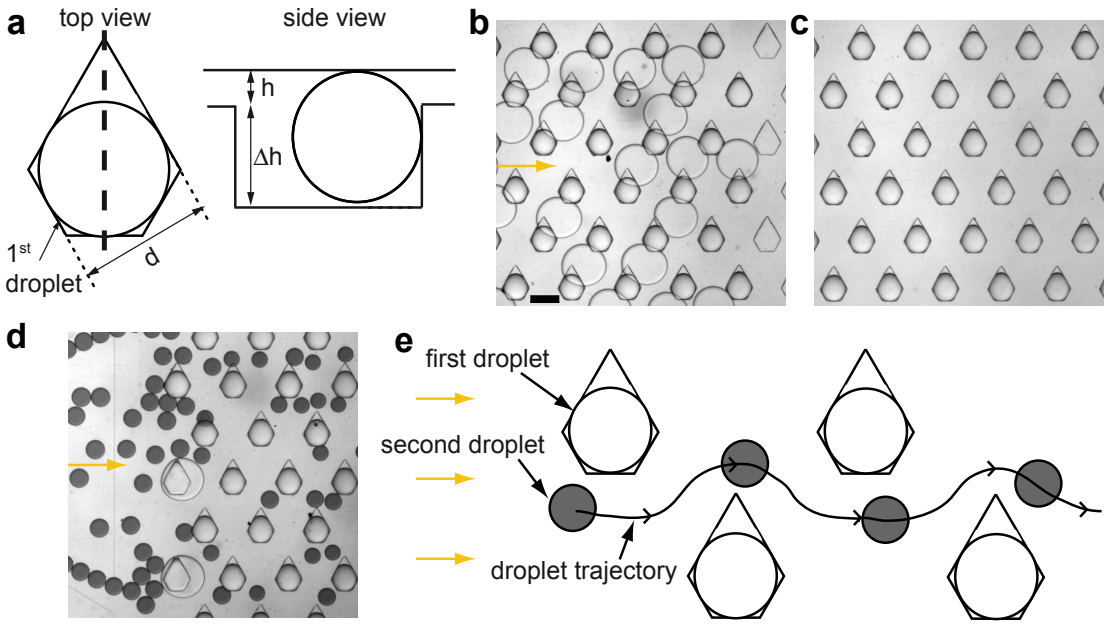

Figure 7.1: Effect of flow modification with deep anchors. **(a)** Schematic top and side view of an anchor designed for trapping two droplets of different sizes. $d = 400\ \mu m, h = 165\ \mu m, \Delta h = 388\ \mu m$. The black dashed line represent the section corresponding to the side view. **(b-c)** Images of the filling 30 anchors with large droplets. The droplets trapped on the triangle area of the anchors **(b)** were removed in **(c)** by increasing the oil flowrate. **(d)** Filling of the array with smaller dark droplets. Scale bar is 500 μm for all images. **(e)** Schematic representation of the small droplet trajectories. Yellow arrows represent the direction of the external oil flow, when there is one.

the small dark droplets.

We basically kept the same anchor design and only changed the height of the triangular part of the anchor, as shown in Fig.7.2 **(a)**. In this case, the depth δh of the triangular part was reduced to 80 μm. This way, the anchor has a 3D design with a different height in each of its two different parts. This design still allows the immobilization of one large droplet (uncolored) in the hexagonal cavity of each anchor, as demonstrated in Fig.7.2 **(b-c)**. As previously hypothesized, it also facilitates the trapping of the smaller dark droplets, as demonstrated in Fig.7.2 **(d-e)**. Although there are still some droplets that can exit the trapping chamber without being immobilized, this ratio is much lower than for the anchors presented in Fig.7.1.

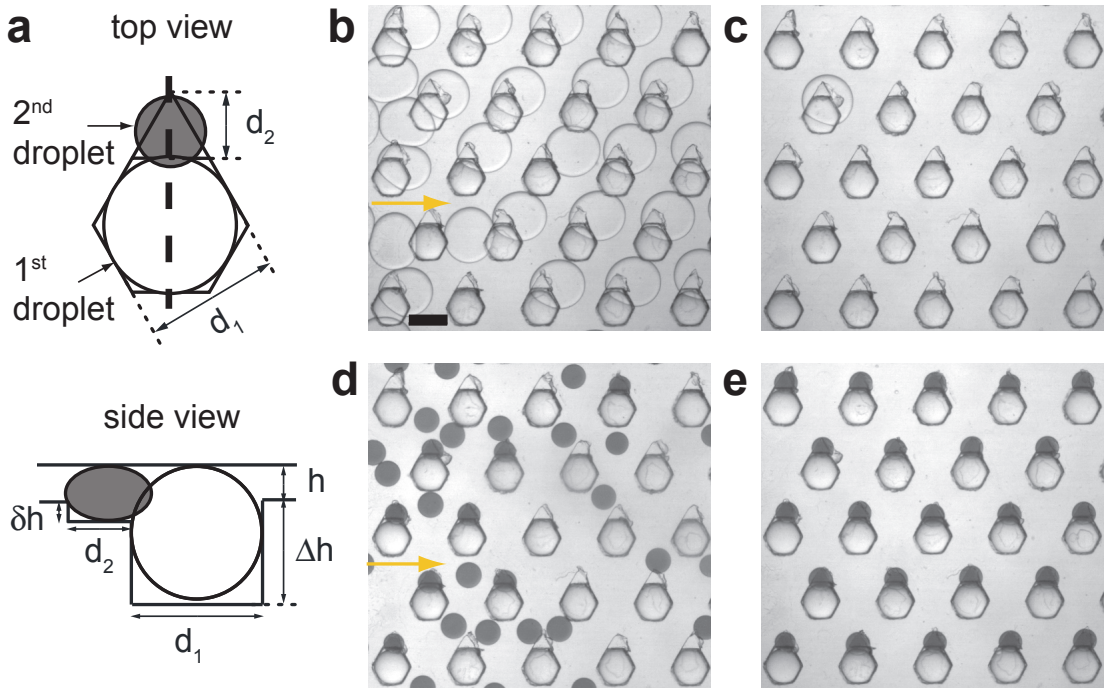

Figure 7.2: Anchor with two different heights. **(a)** Schematic top and side view of 2 droplets trapped in an anchor that has 2 different heights. $d_1 = 400\ \mu m, d_2 = 200\ \mu m, h = 165\ \mu m, \Delta h = 388\ \mu m, \delta h = 80\ \mu m$. The black dashed line represent the section corresponding to the side view. **(b-e)** Time lapse images of the filling of 23 anchors. The first droplets are trapped **(b)**, then, the ones on the triangles are removed **(c)**. The smaller dark droplets are produced, injected **(d)** and trapped **(e)** in the empty triangle of the anchors. Scale bar is 500 μm. Yellow arrows represent the direction of the external oil flow, when there is one.

7.2 Drug toxicity concentration on hepatocyte spheroids - preliminary results

The 3D design of the anchors discussed previously allows the sequential and reproducible trapping of 2 droplets of different sizes in each anchor. The hexagonal cavities of these 3D anchors are sufficiently deep ($\Delta h = 388\ \mu m$) compared to the chamber height ($h = 165\ \mu m$) for the formation and maintenance of 3D cell cultures in agarose droplets. In addition, the triangular parts can be used according to the protocols discussed and demonstrated in chapter 6 to apply different conditions to the spheroids of a droplet array. In this section, we want to explore the possibility to perform a precise drug toxicity test in a single microfluidic chip.

The protocol for this overall experiment is shown in Fig.7.3 **(a)**. The first droplets are all similar and encapsulate H4-II-EC3 cells in liquid agarose. After about 1 day of cul-

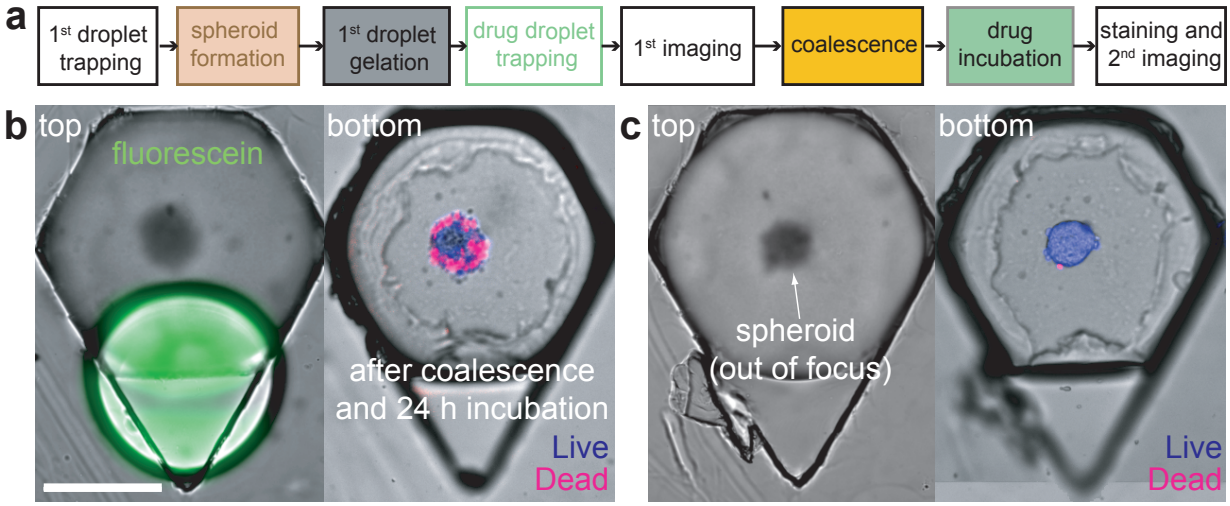

Figure 7.3: Toxicity of acetaminophen on hepatocyte spheroids. **(a)** Protocol for a drug toxicity experiment. **(b)** Micrographs of a 3D anchor after the trapping of a drug droplet (left, acetaminophen + fluorescein) and after the drug incubation (right, viability test after phase change). **(c)** Control case where no drug droplet is trapped. Scale bar is 200 μm.

ture a single spheroid is formed in each anchor and the agarose is gelated. Then, second droplets are trapped in the empty triangular parts of the 3D anchors. They are smaller than the first ones, they are free of hydrogel and contain various concentrations of the drug acetaminophen. These droplets come from a library that is produced from microliter segments with controlled drug concentration (see section B.1). They are fluorescently labeled so that each drug concentration corresponds to a fluorescent level. Therefore, after the trapping of the second droplets, a fluorescence image of the array is taken for assigning a drug concentration to each anchor. After the imaging, the neighboring droplets are coalesced and the drug diffuses quickly throughout the agarose matrix of the merged droplet to reach the spheroid . At this stage, the cells are kept isolated in oil for a 24 hours drug incubation. Finally, the external oil is replaced by an aqueous phase for a fluorescent viabilty test (NucBlue® Live reagent and propidium iodide) and a second fluorescence image of the array is taken. Fig.7.3 **(b)** and **(c)** present some results of a preliminary experiment where droplets containing acetaminophen and fluorescein were immobilized on some of the 3D anchors of an array. In Fig.7.3 **(b)**, we can see that the drug incubation has lead to to low final viability. Fig.7.3 **(c)** represents the control case where no drug was applied, as a consequence, the final viability is high.

These first results confirm that our system is capable of applying locally a drug concentration to a spheroid. In order to test a relevant drug concentration range we need to create a library with a logaritmic evolution of the concentrations [82, 78]. In this case the evolution of the spheroid viability with the drug concentration is expected to follow a sigmoid, as shown in Fig.7.4. For low concentrations, the drug has no effect and the viability is maximum. For high concentrations, all cells are killed by the drug and the viability is

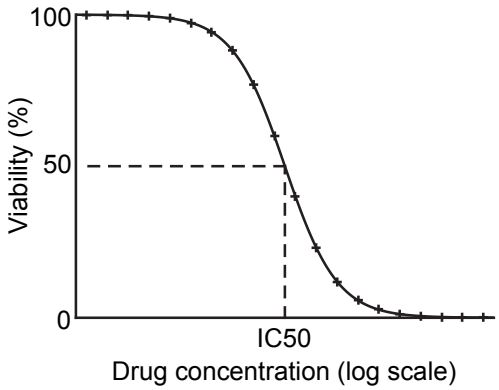

Figure 7.4: Determination of the drug toxicity. Theoretical evolution of the viability of the spheroids with the concentration of drug. The half maximal inhibitory concentration (IC50) is the concentration corresponding to a 50 % viability.

equal to 0 %. The toxicity level of a drug is quantitatively determined by the half maximal inhibitory concentration (IC50), which is the concentration that kills half of the cells during the incubation time. Preliminary tests indicate that a concentration range between 500 μM and 50 mM of acetaminophen (over 2 decades) should be appropriated to see the entire sigmoid.

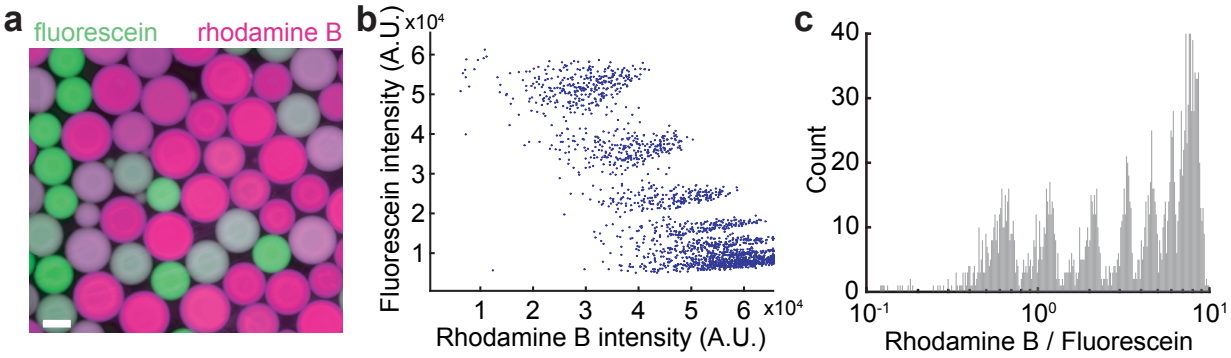

Figure 7.5: Fluorescent labeling over a logarithmic scale. **(a)** Fluorescent image of droplets created from segments with a logarithmic increase of the fluorescein (green) to rhodamine B (magenta) concentration ratio. Scale bar is 200 μm. Height of the microfluidic chip for observation: 100 μm. **(b)** Correlation between the FITC and TRITC signal of each detected droplet. $n_{droplets} = 885$. **(c)** Histogram of the TRITC / FITC intensity ratio of the droplets.

Such an experiment can only be carried out if we are able to distinguish accurately the different concentrations with fluorescent labeling. As the drug concentration increase is logarithmic during the production of the microliter segments, the increase of the fluorescent label concentration also needs to be logarithmic. For increasing our chances of distinguishing the different droplet populations in the library, we chose to use 2 fluorescent

labels at the same time. One of them is added to each of the 2 aqueous solutions used for the segment production, one for the highly concentrated drug solution and one for the dilutant. Therefore, we measure the fluorescence ratio of the 2 labels. Fig.7.5 presents the results of a preliminary experiment that uses fluorescein and rhodamine B over a 2 decade range of concentration with 10 different and regularly spaced values on a logarithmic scale. Fig.7.5 **(a)** shows a fluorescence image of a monolayer of confined droplets from the resulting library in an observation chip. There are more droplets with high rhodamine B levels because the rhodamine B indicates the highly concentrated drug solution, while the fluorescein was added in the dilutant solution. Fig.7.5 **(b)** provides a quantitative correlation for each droplet between the fluorescein and rhodamine B intensities and Fig.7.5 **(c)** shows the histogram of the fluorescence ratio on a logarithmic scale. We can clearly distinguish 7 out of the 10 theoretical different drug concentrations with the ratio histogram. Nevertheless, the detection could be greatly increased by using more appropriate fluorescent dyes. Indeed, if we want to reliability extract quantitative fluorescent signals, many dyes with higher fluorescent intensity and photostability are available commercially. In our preliminary experiment, the rhodamine B is definitely not adapted to quantitative measurements. We can see on Fig.7.5 **(b)** that the spreading of the fluorescent intensity is much higher for the rhodamine B than for the fluorescein. Indeed, rhodamine B leaks from the aqueous droplets, adsorbs into the PDMS walls of the microfluidic chips and even surprisingly leads to the production of bigger droplets at constant flowrates when its concentration increases (see Fig.7.5 **(a)**).

As a summary, we should be able to quickly increase significantly the reliability of the fluorescent detection over a logarithmic scale. Then, we will need to test the agreement between the theoretical and experimental logarithmic concentrations during the segment production. At this stage, we will be able to perform a precise drug toxicity assessment on 3D cell cultures in a single droplet array.

7.3 Application of the sequential droplet merging for tissue engineering

In this section, we explore the cases where cells are encapsulated in the second droplets as well as in the first ones. First, we will discuss the applications where the two droplets are liquid and second, we will see the case where at least one of the two droplets is gelated before the coalescence step.

7.3.1 Controlled merging of spheroids

When both droplets are liquid, the contents can freely mix after the coalescence step. Therefore, we can sequentially put in direct contact several types of cells, initially encapsulated in different droplets.

A first example of protocol is described in Fig.7.6 **(a)**. First, cells are encapsulated in large droplets that fill the hexagonal cavities of the anchors. They can reorganized overnight to create spheroids, as described in section 2.1. Then, we create and trap smaller droplets that encapsulate cells stained with CellTracker™ Red. There are immobilized on the triangular parts of the 3D anchors. The bottom interface of these second droplets looks rather hemispherical since the encapsulated cells are well located in the bottom center after sedimentation (see Fig.7.6 **(b)**). Then, right after the sedimentation, the array is perfused with 1H,1H,1H,2H-perfluorooctan-1-ol dissolved in HFE for triggering the droplet coalescence (see subsection 6.2.1). At this stage, the cell aggregates that began to form in the second droplets sediment to reach the spheroids at the bottom of the merged droplets. This is the situation displayed on the left micrographs (0 h) of the montages in Fig.7.6 **(c-d)**. Here, two different behaviors can be identified. In Fig.7.6 **(c)**, the red cell aggregates are smaller than the spheroids. Therefore, after few hours of culture, the cell aggregates have merged with the initial spheroid, resulting in a single spheroid having one side stained with CellTracker™ Red. Alternatively, the cell aggregates can be bigger than the initial spheroid (Fig.7.6 **(d)**). In this case, after few hours of culture, the cells from the cell aggregate have began to adhere around the initial spheroid.

Consequently, controlling the cell concentration in the second droplets allows to define the spatial organization of the resulting microtissue. Moreover, this operation can be repeated sequentially several times in order to merge more than 2 different droplets.

Fig.7.7 **(a)** presents a protocol with 2 sequential merging events. An additional difference with the protocol of Fig.7.6 is that instead of merging the droplets right after the second droplet trapping, we wait for the second spheroid formation in the small droplets. This way, we only merge well-formed spheroids. The first micrograph of Fig.7.7 **(b)** shows a micrograph of the second droplet trapping (similar to the one in Fig.7.6 **(b)**) and we can see on the second micrograph, taken right after the first coalescence event, two well-reorganized spheroids entering in contact. About 1 day after this coalescence, a third droplet containing cells stained with CellTracker™ Green is trapped in the triangular part of the anchors.

Indeed, since the volume of the second droplets encapsulating the red cells (about 12 nL) was small compared to the volume of the first droplets (about 60 nL), the volume of the resulting merged droplet is entirely contained in the hexagonal cavities of the 3D anchors (76.6 nL), leaving the triangular parts empty and available for trapping other droplets. Micrographs corresponding to this third droplet trapping are shown in Fig.7.7 **(b)**.

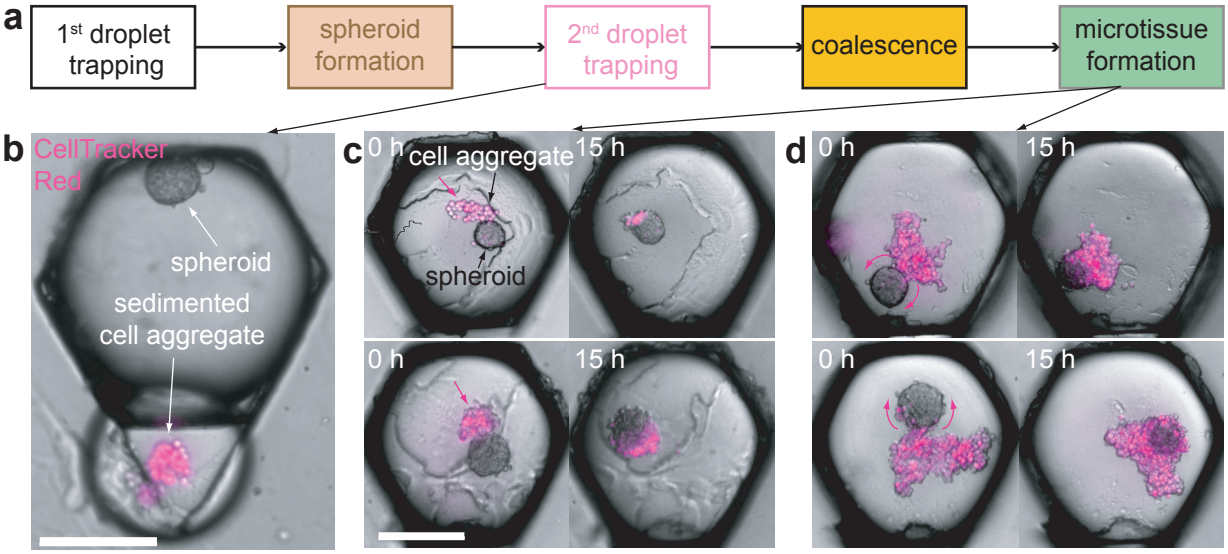

Figure 7.6: Spheroid merging with cell aggregates. **(a)** Protocol for controlled microtissue formation with 2 liquid droplets. **(b)** Micrograph of a 3D anchor before the coalescence step. The cells in the small droplet are stained with CellTracker™ Red. **(c)** Time lapse micrographs of two anchors. The left and right images were taken respectively right after the droplet coalescence and 15 hours after. The red arrows indicate the direction of the merging. **(d)** Time lapse micrographs of two anchors with larger cell aggregates. The red arrows indicate the reorganization movement of the cell aggregates. Scale bar is 200 μm.

When the focus is set on the bottom of the 3D anchor, we can see that the uncolored and red spheroids have merged into to single microtissue having two different cellular contents on opposite sides. When the focus is set at the top of the 3D anchors, we can see the green labeled sedimented cells. After 1 day allowing the reorganization of these cells into a well-formed spheroid, the coalescence of the droplets is triggered again. As a result, the newly formed green spheroid sediment at the bottom of the merged droplet and enters in contact with the uncolored part of the first microtissue. Fig.7.7 **(c)** shows a zoomed image of the resulting microtissue 8 hours after the second coalescence event. We observe a microtissue constituted of 3 different parts coming from the sequential merging of 3 different spheroids.

The spatial organization of these 3 parts in the microtissue depends on the location of the first contact between the green spheroid and the microtissue resulting from the first spheroid merging, right after the second coalescence event. We have identified two main organizations that rely on the location of the contact between the third spheroid compared to the first merging axis. The merging axis, defined on Fig.7.7 **(b)** is the axis created by the centers of the two merging spheroids. In Fig.7.7 **(d)**, the second merging axis (materialized by the green arrows) is almost perpendicular to the first merging axis (red arrows). Therefore, in the resulting tissue, some green cells are in direct contact with red cells and some others

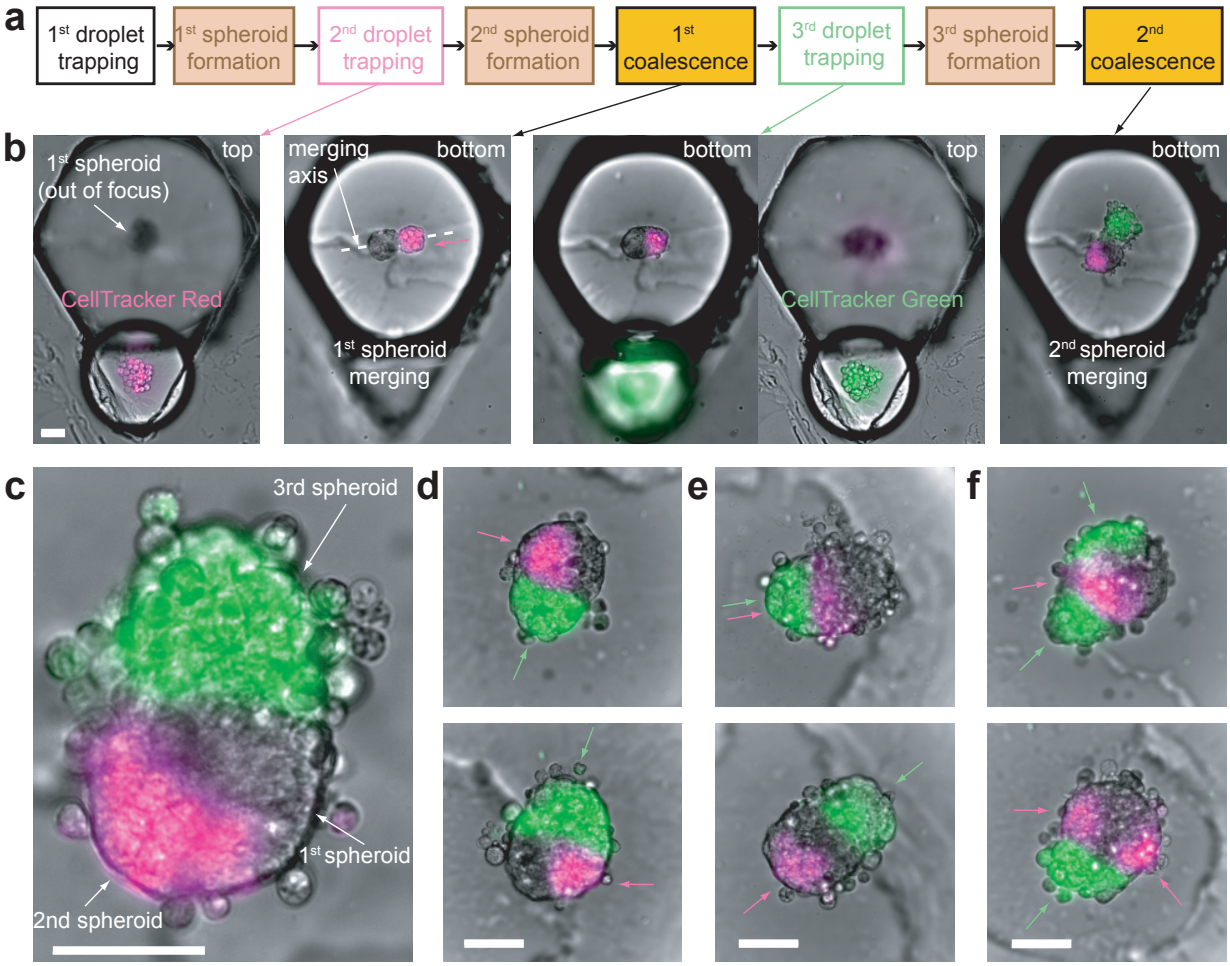

Figure 7.7: Spheroid merging. **(a)** Protocol allowing the controlled merging of spheroids. **(b)** Time lapse micrographs of 2 consecutive spheroid merging events in a single anchor. The cells encapsulated in the second and third droplets are respectively stained with CellTracker™ Red and Green. The focus is either on the bottom spheroids or on the smaller droplet at the top of the anchor. The white dashed line and red arrow represent the merging axis. **(c)** Micrograph of the final microtissue whose fabrication is seen in **(b)**. Image taken 8 hours after the second coalescence. **(d-f)** Micrographs of microtissues created with spheroid merging. The red and green arrows show respectively the directions of the first and second spheroid merging events. In **(d)** these two directions are almost perpendicular and **(e)** there are parallel. In **(f)**, there were 3 consecutive spheroid merging events either with 2 green and 1 red spheroids (top) or with 2 red and 1 green (bottom). Scale bars are 50 μm.

with uncolored cells. The second typical organization is described in Fig.7.7 **(e)**, where the first and second merging axis are almost parallel. In this case, eiher the green cells are only in contact with red cells (top) or only with the uncolored cells (bottom). The microtissue

whose formation is displayed in Fig.7.7 **(b)** and **(c)** belongs to the second category, with almost parallel axis for the first and second spheroid merging.

Finally, this protocol can be further extended by including more droplets and coalescence events, as shown in Fig.7.7 **(f)**. The top micrograph corresponds to a case where the merging of an uncolored and a red spheroid was followed by 2 merging events with a green spheroid. On the bottom micrograph, there were 2 merging events with one red spheroid before the final merging with a green spheroid.

This ability to control temporally and spatially the combination different cellular types in a single microtissue enables many potential applications in tissue engineering when a direct contact between the cellular types is needed.

7.3.2 Separated co-culture

When at least one droplet in the 3D anchors contains agarose and is gelated before the coalescence step, the reorganization that was observed previously is prevented. Indeed, as we mentioned earlier (see subsection 4.4.2), cells cannot adhere or digest the gelated agarose matrix, as a result, there cannot be a direct contact between 2 initially separated microtissues followed by a reorganization.

The case where both the first and second droplets are gelated before coalescence is described in Fig.7.8. The exact protocol is shown in Fig.7.8 **(a)**. Fig.7.8 **(b)** shows time lapse micrographs during the coalescence step. At first, we can see the agarose beads separated from one another. For the first droplets that were immobilized in the hexagonal cavities of the 3D anchors, one spheroid was formed before the gelation. The second droplets encapsulate cells that were stained with CellTracker™ Red. They were quickly gelated after trapping thus, the cells are only roughly organized into sedimented cell aggregates. These droplets also contain fluorescein. This situation is schematically displayed in Fig.7.8 **(c)** with a side view of an 3D anchor. During the time lapse, the array is perfused with 1H,1H,2H,2H-perfluorooctan-1-ol diluted in HFE for triggering the coalescence. We can see in the second micrograph that the coalescence happened in 2 out of 3 anchors. As a result, we can see the fluorescein diffusing from the small to the large beads. In the third micrograph, the beads of the 3 anchors have coalesced and the fluorescein concentration looks homogeneous across the merged beads. As the 2 adjacent agarose droplets were gelated before coalescence, they constitute 2 independant and crosslinked mesh that cannot mix together without significant temperature changes (see section 2.2). Nevertheless, the hydrogel is mainly constituted of water and therefore, when we talk about the coalescence of 2 gelated beads, it means that their aqueous dilutant is shared. Most importantly, we can see on the third micrographs, that the red cell aggregates appear now close to one of the hexagonal cavity side walls. This situation is schematically displayed in Fig.7.8 **(d)** even if at this stage the exact 3D arrangement of the 2 gelated beads remains unclear. In

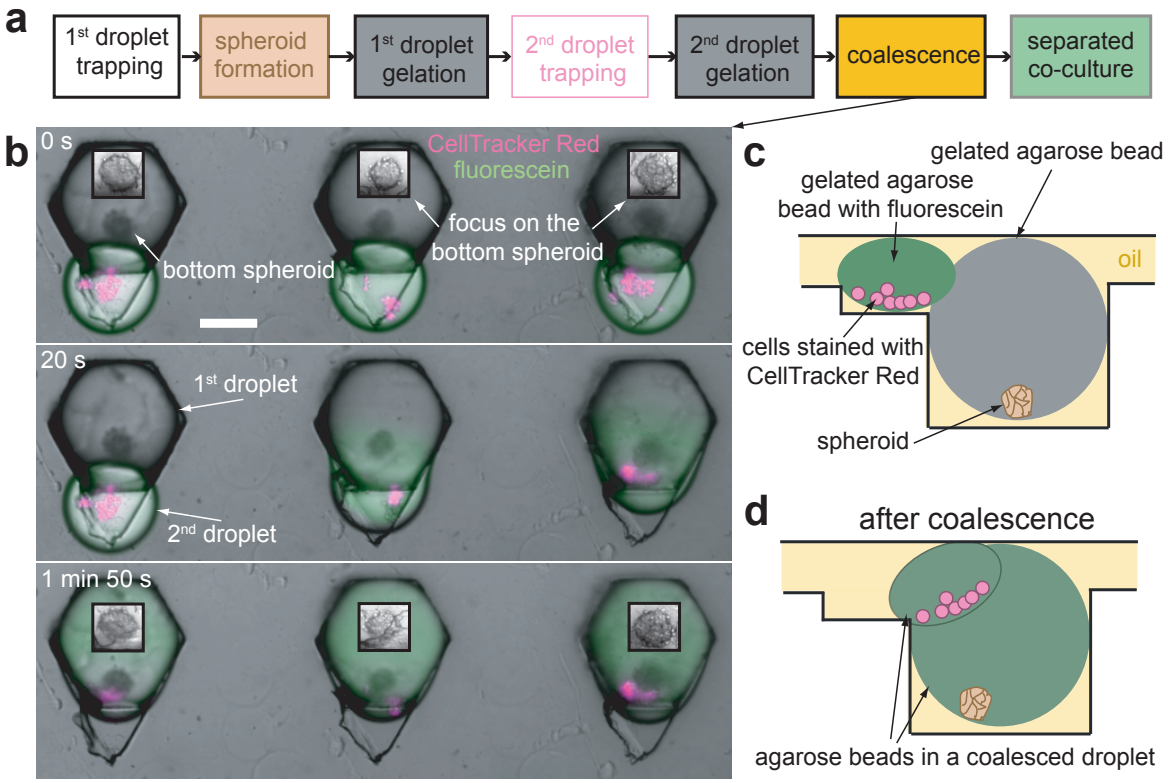

Figure 7.8: Separated co-culture with 2 gelated agarose beads. **(a)** Protocol allowing the formation of separated co-cultures in agarose beads. **(b)** Time lapse micrographs of the coalescence between the droplets. The focus is made on the top droplets, except for the insets that show the bottom spheroids well in focus. The green and red intensities represent respectively the fluorescein and the CellTracker™ Red. Scale bar is 200 μm. **(c-d)** Schematic side view of one anchor before **(c)** and after **(d)** the coalescence.

addition, we can notice that the uncolored spheroids seem to have come closer to the same side wall of the anchor. It could indicate that the coalescence has induced a small rotation of the large agarose beads containing the uncolored spheroids.

This protocol allows to perform a co-culture of 2 different cellular types that can only communicate via paracrine interactions. Indeed, the gelated agarose prevents the direct contact between the 2 cellular types. Meanwhile, chemical communication is still possible, as demonstrated previously by the diffusion of the fluorescein. This way we have created a highly parallelized micro-Transwell plates that allow physically separated co-cultures.

Comparable results can be obtained if only the first droplet contains agarose and is gelated before the coalescence with the second smaller liquid droplets, as shown in Fig.7.9 **(a)**. The micrograph of Fig.7.9 **(b)** shows 4 3D anchors right after the coalescence with droplet containing cells stained with CellTracker™ Red. Like the case of the 2 agarose droplets, the red cells cannot enter in direct contact with the uncolored spheroid and

therefore, they just sit on the top of the agarose beads. A schematic side view of this biological system is shown in Fig.7.9 **(c)**. Adding an extra liquid volume to the gelated agarose bead must result in a liquid droplet encapsulating a slightly smaller agarose bead. As a result, the red cells are just located in the liquid film on the top of the agarose bead.

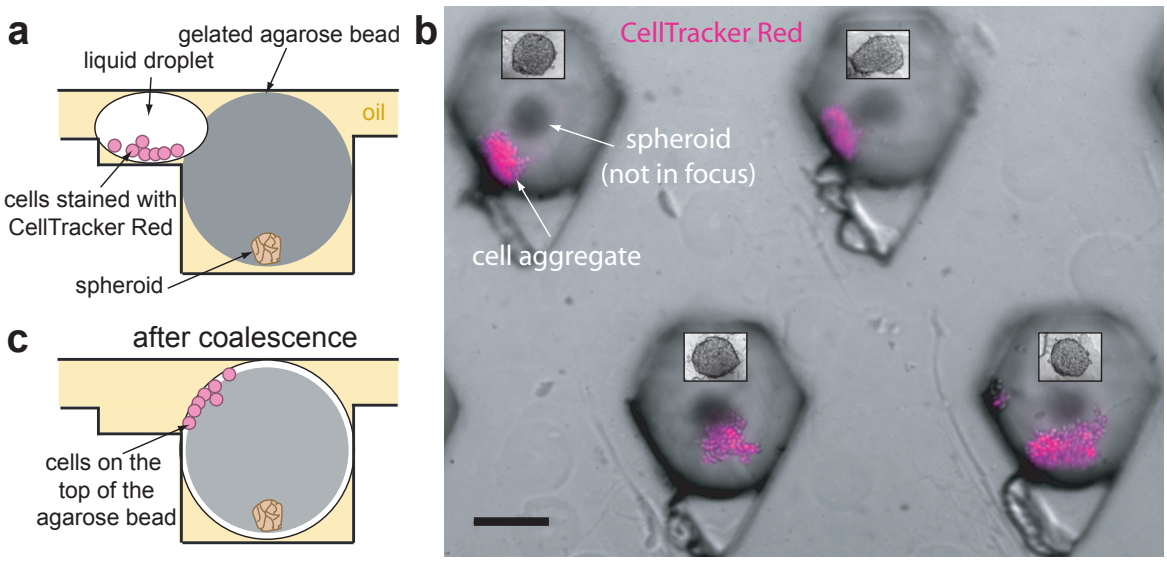

Figure 7.9: Separated co-culture with one agarose bead and one liquid droplet. **(a)** Schematic side view of one anchor before the coalescence. **(b)** Micrographs of 4 anchors with co-culture droplets after the coalescence of an agarose bead and a liquid droplet. The focus is made on the top of the droplets, except for the insets that show the bottom spheroids well in focus. The red intensity represents the cells stained with CellTracker™ Red. Scale bar is 200 μm. **(c)** Schematic side view of one anchor after the coalescence.

Contrary to case of the coalescence of 2 agarose beads, we can see here more clearly the location of the red cells and the initial spheroids remain in the bottom center of the hexagonal cavities of the 3D anchors after coalescence. This format allows also the formation of a co-culture system between 2 cellular types that can only communicate via paracrine interactions. The first difference with the case of the 2 gelated beads comes from the absence of an rigid mesh for the cells that were at first encapsulated in the small droplets. Therefore, they do not feel the rigidity of the gelated agarose. Another significant difference might come from the behavior of these 2 systems during the replacement of the external oil by an aqueous phase. When the small droplets are purely liquid, the added cells are not directly encapsulated in gelated agarose, as a result, we expect them to be easily removed from the surface of the gelated agarose beads. Indeed, they cannot adhere to the surface of these beads. It would allow to choose precisely whenever we want to stop the co-culture conditions in the droplet array. In the case of the combination of the 2 gelated beads it is unclear whether the small bead will remain trapped in the anchor or not.

Conclusion of Part III

In this third part, we modified the design of the anchors in order to be able to trap several droplets in close proximity. When these modified anchors are assembled into an array, we can randomly immobilize different combinations of droplets with potentially different contents in each of them. After having identified these combinations, perfusing the array with a specific chemical allows to efficiently trigger the coalescence of the droplets that were in physical contact. This way, the reagents that were separated in the initial droplets can mix in the merged droplets, creating as many different reactions as there were different combinations in the array.

The droplets can be either produced on chip, notably when droplets of identical contents are needed, or off chip. In the later case, the droplets can come from libraries with many different contents and are simply injected into the trapping chamber. We are able to create or own libraries by controlling the dilution of a solution into microliter segments that are partitioned into nanoliter droplets during their injection into a microfluidic slope (see appendix B). The geometrical parameters and the injection flowrate control the size of the library droplets that needs to be well defined for each anchor design.

In this manuscript, we have mostly focused on an anchor design capable of trapping sequentially two droplets of different sizes. It allows to potentially combine droplets from 2 different libraries, each anchor immobilizing one droplet of each library. This has been demonstrated in section 6.3. It is worth noting that the sizes of the array and of the libraries control the number of different combinations that are achievable in a single microfluidic chip and how many times each condition will be repeated.

Adding a new reagents to a pre-existing droplets is a typical issue of the microfluidic format. This can be solved for instance by using hydrodynamic forces [112, 116] or electro-coalescence [117, 110]. The later technique requires the addition of electrodes close to the microchannels, thus complexifying the microfabrication and experimental setup, but allows the precise control of the coalescence at very high frequencies since the electric field can be actively turned on and off. As an example, picoinjectors [118] can be used to add a picoliter volume to chosen droplets at a kilohertz rate. However, these serial designs often require a precise synchronization between trains of droplets which increase the experimental complexity.

An alternative to the addition of reagents into a droplet can be to directly create droplets by varying the amounts of reagents [24] at the production stage. In this type of protocol, we can only test varying concentrations, not different reagents, and we cannot choose the time for the addition of a reagents since everything is encapsulated together at the droplet production stage.

These techniques for creating microfluidic droplets of different contents have been applied to many fields related to chemistry like combinatorial synthesis [119] that combines libraries of different families of reagents, protein cristallisation [120] with varying salt and protein concentrations or nanoparticles synthesis [121]. With the experimental demonstration of the combinatorial mixing of colored droplets in an anchor array, we have demonstrated that our microfluidic platform can be applied to each of these fields, given that the food dye solutions can be simply replaced by any of the pre-mentioned solutions. We could easily achieve comparable levels of parallelization but we will also benefit from the advantages of static and highly integrated droplet arrays.

Our combinatorial platform becomes even more unique when applied to 3D cell cultures. Indeed, the applications of microfluidic droplet screening to biological systems are so far limited to single cells. We can find nice examples like multidimensional antibiograms on bacteria [122], directed evolution with yeasts [21] or the cytoxocity assessment for single mammalian cells [28]. With our platform, we extend the scope of microfluidic droplet screening to the more biologically relevant 3D cultures. It has required to create 3D combinatorial anchors, allowing the efficient trapping of large hydrogel droplets for the creation and culture of cellular spheroids (see chapter 2) as well as the immobilization of a smaller droplets with a reagent of interest. This feature definitely differentiates our platform from the work of Fradet *et al.* [42] and Tullis *et al.* [109] (see discussions in section 6.1) where multiple droplet trapping is only possible with low trapping efficiency. Moreover, we have largely increase the number of different contents that can be trapped on a single anchor arrays [114] without complicating the microfluidic design and operation.

A first application of our combinatorial platform to 3D cell cultures is presented in section 7.2 with the ability to determine the toxicity concentration of a drug on a microfluidic spheroid array. Simply replacing the library of drug concentrations by a library of drug compounds would allow to shift from toxicity to drug screening experiments. We could also imagine using this platform for the design of personalized cancer treatment. Cells harvested from a patient biopsy could be cultured in 3D conditions in the large droplets and the small droplets could contain various combinations of chemotherapeutical molecules. Finding the most efficient combination of drugs on chip with allow to predict the most efficient personalized cancer treatment. The main advantage of these applications is that they benefit from the high-throughput and low volume capabilities of droplet microfluidics as well as the biologically relevant 3D format.

We have shown in the chapter 7 that the combinatorial 3D anchors can be used for tissue engineering applications and therefore can even increase the relevance of our 3D format. A

first example is the sequential addition of cells to microtissues and the controled merging of pre-formed spheroids (see section 7.3). This feature has been previously demonstrated in the microplate format [123] that does not benefit from the volume reduction or the perfusion capabilities demonstrated earlier in this manuscript. If our proof of concept experiments were conducted with an unique cellular type, it should be very interesting to use this feature with different cellular types. On a theoretical point of view, the easy parallelization of the spheroid merging, together with the image analysis tools developped in part I, could be used to test the differiential adhesion hypothesis [124, 125] that tries to explain why in the case of heterogeneous spheroid formation there can be a segregation between the cellular types, notably between the edge and core of the final microtissue. On a bio-engineering point of view, there are many interesting choices for the cellular types that are put into contact in the same microtissue. Many have already been explored for different applications. Keratinocytes and fibroblasts can be combined for modeling the skin during the test of cosmetic molecules [126], hepatocytes can be co-cultured with stellate cells for reproducing more relevant liver functions [68] or alpha- (producing glucagon) and beta- (producing insulin) cells could be cultured in 3D for creating artificial pancreatic islets that could be implanted in diabetic patients. A second example is the use of agarose droplets in 3D combinatorial anchors for preventing direct contact between the cellular types and only allowing paracrine interactions. This way, each anchor acts like a single Transwell plate. For instance, the anti-inflammatory properties of hMSC aggregates could be tested with undirect co-cuture with stimulated macrophages [102].

Another feature of the 3D combinatorial anchors is their possibility to add control over the hydrogel that encapsulate the cells. Indeed, the agarose is not a biologically relevant hydrogel as it prevents cell adhesion and cannot be digested by the cells. Nevertheless, the spheroid formation would not be possible in usual biological hydrogels. For instance, collagen or Matrigel® can only remain liquid below 4°C and quickly gelate under good culturing conditions (physiological pH and temperature). With 3D combinatorial anchors, we could create spheroids in purely aqueous droplets and only then quickly trap second smaller droplets with a high concentration in hydrogel. After coalescence, the hydrogel would quickly gelate and encapsulate the pre-formed spheroids in a biological matrix. With a similar approach, we could test various hydrogel properties in a single microfluidic chip. In this case, the second droplets would come from an hydrogel library and the gelation would only occur after the coalescence step. For instance, synthetic hydrogels can be used to tune precisely the mechanical, chemical and biological properties of the scaffold [127]. Finally, 3D combinatorial anchors could be used for creating multilayer hydrogel structures. Indeed, a gelated hydrogel droplet in the deep cavity of a 3D anchor can be merged with a second hydrogel droplet whose gelation will only be triggered after coalescence. This will result in the creation of a gelated border around the first core, the 2 hydrogels possibly being different from one another. The operation could be repeated to increase the number of layers.

Conclusion

The aim of my PhD project was the adaptation of droplet microfluidic techniques to the 3D cell culture of adherent mammalian cells. In my opinion, this work has led to 3 main achievements:

- **an highly integrated and versatile microfluidic platform for spheroid culture**. We used droplet manipulation techniques, namely rails and anchors [23], to create high-density droplet arrays in microfluidic chambers. When immobilized in deep anchors, encapsulated cells can adhere one another in order to create a single spheroid per droplet. The use of agarose droplets allows the replacement of the external oil by an aqueous medium on chip. Hence, all kinds of perfusion experiments, including immuno-cyto-chemistry protocols, can be performed *in situ*, without removing the spheroids. In addition, single and viable spheroids can be recovered off chip by the selective melting of an agarose droplet with an infra-red laser. Last but not least, each spheroid of the array can be submitted to different conditions when encapsulated in oil. Indeed, specific combinatorial anchors were designed to trap 2 droplets of different contents in a same location. As these droplets can come from libraries of various contents, their combinatorial mixing is achieved by coalescence in each anchor. We believe that this microfluidic platform combines the numerous advantages of droplet microfluidics and microarrays in the context of 3D cell culture. Namely, our platform enables: low reagent consumption, high-throughput screening in droplets, high-density formation of monodisperse spheroids, hydrogel encapsulation, *in situ* staining and long term culture, spatial and dynamic control of the array perfusion and selective recovery of viable spheroids.

- **an image analysis procedure for high-throughput multiscale cytometry**. The immobilization of the droplets encapsulating cells in anchors enables simple imaging of all the spheroids of the array. Cells can either be monitored over time in each anchor or imaged once after a given time of culture. We designed a custom analysis software which uses the bright field and fluorescent images for computing morphological and biological parameters. Data can either be acquired at the population level, like classical biological results, but also at the spheroid and cellular level *in situ*. We called this analysis procedure multiscale cytometry. In this work, we have generated an unprecedented amount of data. Indeed, we analyzed tens of thousands of individual spheroids and hundreds of thousands of single cells

in their 3D environment and correlated biological function and morphological parameters at the spheroid and cellular level. This would not have been possible with flow cytometry that requires to break microtissues into single cells prior to analysis [128]. In this case, all the structural information of spheroids, which is of paramount importance for understanding their organization and function, would have been be lost. Multiscale cytometry could be used for high-content screening purposes. Some recent exemples demonstrate cellular level analysis of 3D spheroids [129, 130] but every time the results are averaged at the population scale. We believe that displaying the entire cellular level data enables to detect and understand effects which could have been missed by only looking at mean values.

- **the detailed biological study of hepatocyte spheroids and human mesenchymal stem cell aggregates**. The potentiality of our microfluidic platform was demonstrated with 2 different cellular models. First, hepatocyte spheroids were created in the perspective of creating functional liver models for toxicity experiments. We carefully assessed the viability and increased functionality of the cells in the 3D microfluidic format over 2D conditions. Multiscale cytometry revealed a strong correlation between the albumin production and the circularity of the organoids at the spheroid level. At the cellular level, we uncovered an increase of the intra-cellular albumin level close to the spheroid edge. A proof-of-concept experiment was conducted for investigating the effect of different dynamic drug exposures at the population, spheroid and cellular level. Second, we investigated the biological regulation of the therapeutic properties of hMSC aggregates. We discovered spatial and dynamic trends in the expression of Casp3 and COX2, 2 enzymes playing a role in the production of the antiinflammatory factor PGE2.

Further technological development could focus on the hydrogel. For instance, the incorporation of ECM proteins into a synthetic hydrogel that retains the ease of use of agarose is required to encapsulate spheroids into a more biologically relevant environment. The hydrogel matrix could also be used to immobilize antibodies capable of capturing a molecule secreted by an encapsulated spheroid. The small volume of microfluidic droplet would allow to perform fast and highly sensitive ELISA at the spheroid level.

However, we believe that the technology presented in this PhD work is mature and that following work should focus on using this platform for answering biologically relevant questions. As an example, in the context of drug screening, droplet arrays could be used to study the efficiency of the combination of several chemotherapies. Indeed, a cancer patient biopsy could be partionned in a droplet array for spheroid formation (microtumors). Combinatorial anchors could be used to efficiently screen many combinations of drugs at different doses in order to designed a personalized treatment.

The tissue engineering capabilities enabled by combinatorial anchors (see chapter 7) are also of particular interest. The controlled and sequential merging of different 3D cell cultures allows to precisely design co-culture in 3D. With the potential combination of the 3D format, hydrogel encapsulation and co-culture, our microfluidic chip could be used to design organs-on-chips [131] which are *in vitro* systems that closely mimick *in vivo*

conditions for drug screening purposes.

Appendix A

Materials and methods

A.1 Microfabrication

Standard dry film soft lithography was used for the flow focusing device (top of the chip) fabrication, while a specific method for the fabrication of the anchors (bottom of the chip) was developed. For the first part, several layers of dry film photoresist consisting of 33 μm Eternal Laminar E8013 (Eternal Materials, Taiwan) and 15 μm Alpho NIT215 (Nichigo-Morton, Japan) negative films were successively laminated using an office laminator (PEAK pro PS320) at a temperature of 100°C until the desired channel height was reached. The photoresist film was then exposed to UV (LightningCure, Hamamatsu, Japan) through a photomask of the junction, channels and the culture chamber boundaries. The masters were revealed after washing in a 1 % (w/w) K_2CO_3 solution (Sigma-Aldrich). For the anchors fabrication, the molds were designed with RhinoCAM software (MecSoft Corporation, LA, USA) and were fabricated by micro-milling a brass plate (CNCMini-Mill/GX, Minitech Machinery, Norcross, USA). The topography of the molds and masters were measured using an optical profilometer (VeecoWyco NT1100, Veeco, Mannheim, Germany). For the fabrication of the top of the chip, poly(dimethylsiloxane) (PDMS, SYLGARD 184, Dow Corning, 1:10 (w/w) ratio of curing agent to bulk material) was poured over the master and cured for 2 h at 70°C. For the fabrication of bottom of the chip, the molds for the anchors were covered with PDMS. Then, a glass slide was immersed into uncured PDMS, above the anchors. The mold was finally heated on a hot plate at 180°C for 15 minutes. The top and the bottom of chip were sealed after plasma treatment (Harrick, Ithaca, USA).

A.2 Surface treatment, surfactants and oil

Chips were filled 3 times with Novec Surface Modifer (3M, Paris, France), a fluoropolymer coating agent, for 30 minutes at 110°C on a hot plate. It ensures the creation of highly fluorophilic microfluidic chips. The droplets were produced in FC40 with a biocaompatible fluorinated surfactant (RAN Biotechnologies) at a 1 % (w/w) concentration.

A.3 Cell culture

Rat hepatocyte A rat H4-II-EC3 hepatoma cell line (CRL-1600™, American Type Culture Collection, LGC, Molsheim, France) was maintained on T-25 cm^2 flasks (Corning, France) in a standard CO_2 incubator (Binder, Tuttlingen, Germany). The culture medium was composed of Dulbecco's Modified Eagle's medium (DMEM) containing high glucose (Gibco, Life Technologies, Saint Aubin, France) supplemented with 10 % (v/v) fetal bovine serum (Gibco) and 1 % (v/v) penicilin-streptamicine (Gibco). The cells were seeded at $5x10^4$ cells/cm^2 and sub-cultivated every 3 days.

Human umbilical cord derived hMSCs Human hMSCs derived from the Wharton's Jelly of umbilical cord (hMSCs) (ATCC® PCS-500-010, American Type Culture Collection, LGC, Molsheim, France) were obtained at passage 2. hMSCs were maintained in T-175 cm^2 flasks (Corning, France) and cultivated in a standard CO_2 incubator (Binder, Tuttlingen, Germany. The culture medium was composed of Alpha Modified Eagle's medium (α-MEM) (Gibco, Life Technologies, Saint Aubin, France) supplemented with 10 % (v/v) fetal bovine serum (Gibco) and 1 % (v/v) penicilin-streptamicine (Gibco). The cells were seeded at 5.10^3 cells/cm^2, sub-cultivated every week, and the medium was refreshed every 2 days. hMSCs at passage 2 were first expanded until passage 4 (for about 5-6 populations doublings, PDs), then cryopreserved in 90 % FBS / 10 % DMSO and stored in a liquid nitrogen tank. The experiments were carried out with hMSCs at passage 8 to 11 (about 24-35 PDs, after passage 2).

A.4 Staining protocols

Viability assay The cell viability was assessed using LIVE/DEAD® staining kit (Molecular Probes, Life Technologies). The spheroids were incubated for 30 min in PBS containing 1 μM calcein AM and 2 μM ethidium homodimer-1 (EthD1), in flushing 100 μL of the solution. The samples were then washed with PBS and imaged under a motorized fluorescent microscope (Nikon, France).

Detection of intracellular albumin expression The intracellular albumin production was investigated by immunocytotchemisty (ICC), for which all steps were carried out on-chip. The cells cultivated on T-25 flasks or as spheroids on-chip were fixed in a 4 % (w/v) PFA (Alpha Aesar, Heysham, UK) for 30 minutes and permeabilized with 0.2-0.5 % (v/v) Triton X-100 (Sigma-Aldrich) for 5 minutes. The samples were blocked with 5 % (v/v) FBS in PBS for 30 minutes and incubated with sheep polyclonal anti-rat ALB antibody conjugated with FITC solution (ab93322, Abcam, Cambridge, UK) diluted at 1:200 in 1 % (v/v) FBS for 30 minutes. The cells were counterstained with 0.2 μM DAPI for 5 minutes (Sigma-Aldrich), and then washed with PBS. To ensure the specificity of the antibody to the cells' secreted albumin, control cells were permeablized and incubated with a sheep IgG Alexa Fluor 488 isotype (IC016G, R& D systems, Lille, France), following the manufacturer instructions. To verify the absence of contribution of the albumin from the blocking buffer in the fluorescent signal, the cells were treated as above and co-incubated with the anti-rat albumin antibody and 10 μg/mL BSA-tetramethylrhodamine conjugate (Life Technologies) for 30 minutes. The samples were imaged using fluorescent microscope or using confocal microscopy. The absence of fluorescence for the isotype and the BSA-tetramethylrhodamine controls indicated the signal specificity to the cells' produced albumin.

BrdU staining To assess the fraction of proliferative cells within the spheroids or in 2D cultures, the samples were incubated with 10 μM BrdU (BromodeoxiUridne, an analog of thymidine) (B23151, Life Technologies) for 4-8 hours. Cells were fixed in 70 % (v/v) cold ethanol, permeabilized and incubated with anti-BrdU antibody (B35139, Life Technologies), which was diluted at 1:200 (v/v) in 1 % (v/v) FBS. Cells were counterstained with DAPI as above. As a negative control, control cells were stained with anti-BrdU antibody without incubation in the BrdU solution. The absence of fluorescent signal indicated the specificity of the BrdU detection.

Actin staining To interrogate the actin organization of the spheroids of hepatoma compared to 2D cultures, the samples were fixed and permeabilized as above. The samples were incubated with 1:50 (v/v) phalloidin-Alexa®594 (Life Technologies) and counterstained with DAPI (Sigma-Aldrich). The samples were imaged using confocal spinning microscopy (Nikkon, France) or the motorized fluorescent microscope.

Dual caspase-3 and COX-2 staining 2D or spheroid culture of hMSCs were washed in PBS, and incubated with a 5 μM NucView™ 488 caspase-3 substrate (Interchim, Montluçon, France) diluted in PBS. After washing with PBS, hMSCs were fixed with a 4 % (w/v) PFA (Alpha Aesar, Heysham, UK) for 30 min and permeabilized with 0.2-0.5 % (v/v) Triton X-100 (Sigma-Aldrich) for 5 min. The samples were blocked with 5 % (v/v) FBS in PBS for 30 min and incubated with a rabbit polyclonal anti-rat COX-2 primary antibody (ab15191, Abcam, Cambridge, UK) diluted at 1:100 in 1 % (v/v) FBS for

4 hours. After washing with PBS, the samples were incubated with an Alexa Fluor® 594 conjugate goat polyclonal anti-rabbit IgG secondary antibody (A-11012, Life Technologies, Saint Aubin, France) diluted at 1:100 in 1 % (v/v) FBS, for 90 min. Finally, the cells were counterstained with 0.2 μM DAPI for 5 min (Sigma-Aldrich), and then washed with PBS. To ensure the specificity of the antibody to COX-2, control hMSCs were permeablized, fixed and incubated only with the secondary, as above. The absence of fluorescent signal indicated the specific staining for intracellular COX-2.

A.5 ELISA on the secreted albumin

Quantification of secreted albumin The culture supernatants of T-25 cm^2 flasks were collected, while the total medium content of the chip was recovered by flushing the culture chamber with pure oil. An albumin rat ELISA kit (ab108789, Abcam, Cambridge, UK) was used for the albumin quantification, following the manufacturer instructions. Briefly, a standard curve of albumin concentration derived from the serial dilution of an albumin standard solution was generated ($r^2 > 0.9$). The absorbance was measured using a plate reader (Chameleon, Hidex, Finland). The albumin productivity was calculated by normalizing the total amount of secreted albumin by the total number of cells contained in the T-flasks or harvested from the chips. Culture medium was used as a negative control. The absence of signal for the negative control indicated the signal specificity to the albumin produced by the cells.

A.6 RT-PCR on the albumin mRNA

The total spheroids of a 2-day culture period were harvested from the chips, as described above. Alternatively, cells cultured on regular T-flasks were recovered using trypsin after the same cultivation time. The total RNA of 1.10^4 cells were extracted and converted to cDNA using Superscript™ III CellsDirect cDNA synthesis System (18080200, Invitrogen, Life Technologies), following the manufacturer instructions. After cell lysis, a comparable quality of the extracted RNA was observed using a bleach agarose gel and similar RNA purity was obtained by measurement of the optical density at 260 nm and 280 nm using a NanoDrop spectrophotometer (Thermo scientific, Wilmington, DE, USA), between total RNA preparations from 2D and on-chip cultures. The cDNA were amplified using GoTaq® qPCR master mix (Promega, Charbonnieres, France) and primers for ALB and GAPDH (Life technologies, Saint Aubin, France) at the specified melting temperature (T_m) (Table A.1), using a Mini-Opticon™ (Bio-Rad) thermocycler. As negative control, water and total RNA served as template for PCR. To validate the specificity of the PCR reaction, the amplicons were analyzed by dissociation curve and subsequent loading on

Gene	Orientation	Sequence	Product size (bp)	T_m (°C)	qPCR efficiency
Albumin	Forward	GTGTTTCCTGCAGCACAAGG	789	57	103 %
	Reverse	TCAGCACAGCACTTCTCCAG			
GAPDH	Forward	TGTGAACGGATTTGGCCGTA	208	60	98.6 %
	Reverse	GATGGTGATGGGTTTCCCGT			

Table A.1: Primer sequences for the albumin qRT-PCR.

a 2.5 % (w/v) agarose gel and migration at 100 V for 40 min. The PCR products were revealed by ethidium bromide (Sigma-Aldrich) staining, and the gels were imaged using a trans-illuminator. The analysis of the samples non-subjected to reverse transcription (RT-) indicated negligible genomic DNA contamination (i.e. < 0.1 %), while no amplification signal was observed for the water template (NTC). The amount of ALB transcripts was normalized to the endogenous reference (GADPH) (ΔCt), and the relative expression to a calibrator (2D cultures) was given by $2^{-\Delta\Delta Ct}$ calculation. A least three biological replicates of 2D and on-chip cultures were analyzed by at least duplicate measurements. The standard curves for GADPH and ALB were performed using a 5 serial dilution of the cDNA templates, and indicated almost 100 % PCR efficiency (Table A.1).

Appendix B

Production of droplet libraries with different concentrations

B.1 Production of a droplet library

In part I and II, all the produced droplets had the same content. In this appendix, we describe the fluidic and microfluific tools that we used for generating custom droplet libraries.

B.1.1 Creation of segmented flows with programmable syringe pumps

An easy way to create droplets with controlled dilutions of a stock solution is the use of segmented flows [132]. Segments are droplets that have a diameter larger than the tubing. As a result they create a plug in the oil of the tube. The experimental setup is shown in the image Fig.B.1 **(a)**. We use a commercially available cross junction connected to 3 different solutions: the solution of interest, the dilutant and the fluorinated oil. The flows are actuated with a programmable syringe pumps (Cetoni, Nemesys). If the oil flowrate is stopped, the solution of interest and the dilutant can mix at the junction. Therefore, controlling the flowrates of each solution allows to control the mixing. When the desired droplet volume is achieved, the aqueous flowrates are stopped and the oil flowrate is activated, creating a separated droplet. In order to achieve an accurate control of the concentration, these droplets must be sufficiently large, typically in the microliter range. These droplets are called segments. In our case, we chose to impose an overall flowrate always equal to 10 μL/min. So when the segments are created, the two aqueous flowrates are adjusted to keep a constant overall flowrate and achieving the desired ratio of the solution of interest. Fig.B.1

(b) shows the imposed ratio of the colored solution in the image of Fig.B.1 **(a)**. We performed an increase and then a decrease of the colored solution ratio. Segment 1 is an equal mix of the 2 solutions, segments 2, 3, 23 and 24 are supposed to contain only the dilutant and the maximum ratio of colored solution is achieved with segment 12. Alternatively, we can simply impose a linear variation of the flowrate ratio (see Fig.B.1 **(c-d)**).

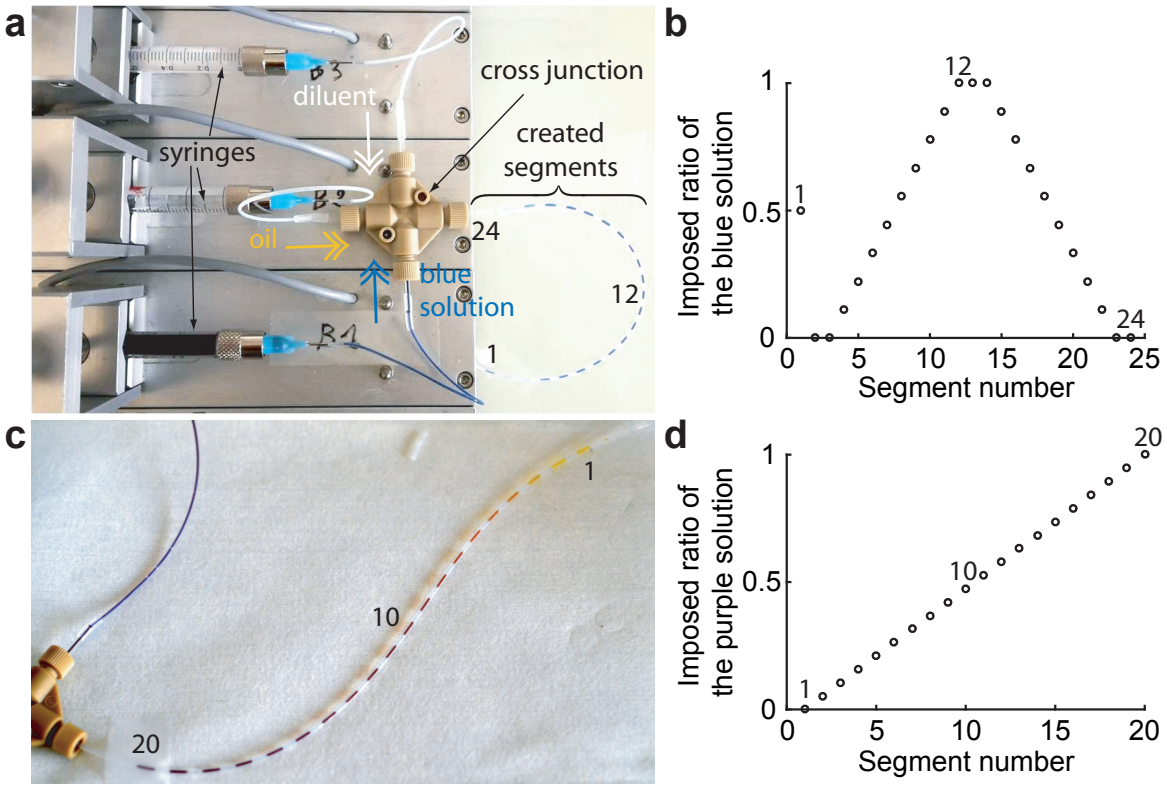

Figure B.1: Segmented flows. **(a)** Image of the experimental setup for the production of segmented flows. **(b)** Graph showing the imposed ratio of the blue solution with the segment number. The segments 1, 12 and 24 are highlighted in the image **(a)**. **(c)** Image of 20 segments produced with the imposed ratios displayed in **(d)**. The segments 1, 10 and 20 are highlighted in the image **(c)**.

B.1.2 Breaking microliter segments into nanoliter droplets with a microfluidic chip

As previously stated, the segments need to be sufficiently large to achieve a good control of their contents. Though, microliter drops can not be easily handled in the microfluidic format. That is why we inject the segments into a microfluidic chip that partitions them in nanoliter droplets. The approach of partitioning large segments into nanoliter droplets for library production has been previously proposed by Kaminski *et al.* [133]. The main

difference with our work comes from the microfluidic design enabling the droplet production.

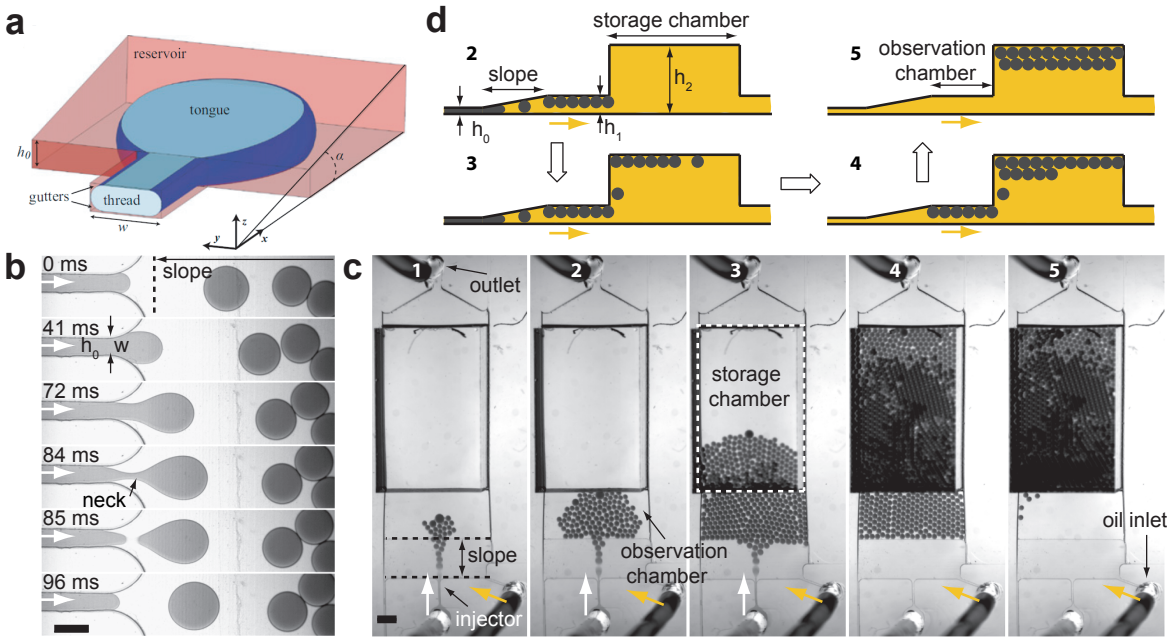

Figure B.2: Producing droplets with a slope. **(a)** Representation of a droplet production in a slope forming an angle α (reproduced from Dangla *et al.* [44]). The injector has a height h_0 and a width w. **(b)** Time lapse images of the droplet production ($\alpha = 8\ \%, h_0 = 40\ \mu m, w = 100\ \mu m$). The dashed line represents the beginning of the slope and the white arrows represent the aqueous flowrate. Scale bar is 200 μm. **(c)** Time lapse images of the entire microfluidic chip for droplet production. Yellow arrows represent the oil flowrate that helps the droplets entering the storage chamber. Scale bar is 1 mm. **(d)** Schematic side view of the chip displayed in **(c)**. Schemes correspond to the steps 2, 3, 4 and 5. h_1 and h_2 are respectively the heights of the observation and trapping chambers.

This microfluidic chip relies on the production of droplets with a slope, as described by Dangla *et al.* [44]. The basic design is explained in Fig.B.2 **(a)**. While the oil remains stationary the aqueous phase is injected into a slope channel. Basically, the deconfinement of the aqueous thread when it progresses along the slope drives the droplet production. Fig.B.2 **(b)** shows time lapse images of the droplet production in one of our microfluidic chips that has a 8 % slope and where we can clearly see the formation and breaking of a neck at the exit of the aqueous injector. The aqueous injector has a constant width w and height h_0. A global view of the microfluidic chip is shown in Fig.B.2 **(c)** (top view) and **(d)** (schematic side view). The chip is composed of an aqueous injector that is connected to the slope beginning. This slope ends when the ceiling and floor of the chamber are parallel again. This area has a height h_1 that is between 1 and 2 droplet diameters. This way, it is easy to observe a monolayer of produced droplets that are not confined. This area is called the observation chamber. Even if the droplet production works while the external oil

remains stationary, we added an oil inlet at one corner of the slope for creating a flow that drives the droplets away from the observation chamber into the storage chamber which has a much higher height h_2. As aqueous droplets are lighter than the fluorinated oil, they ascend to reach the top of the storage chamber where they remain stuck.

This design allows the facile production, observation and manipulation of highly monodisperse microfluidic droplets (see Fig.B.3). This way, the segments that are produced by programming the syringe pumps are partitioned into nanoliter droplets one after the other and all the produced droplets are stored on chip. Before injection of this droplet library into a trapping chamber for combinatorial reactions, we need to ensure that the droplet size matches the design of the anchors.

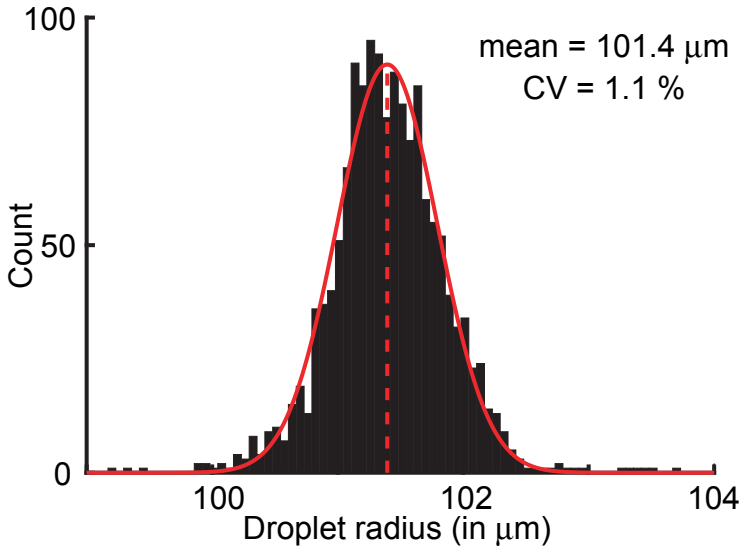

Figure B.3: Control of the droplet size. Polydispersity histogram on 1,500 droplets created with a chip similar than the one in Fig.B.2.

According to the notations in Fig.B.2 **(a-b)**, the geometrical parameters of the chips used for the production of the libraries in section 6.3 are :

- for the large droplets: $w = 100\ \mu m, h_0 = 40\ \mu m, \alpha = 8\ \%$:
- for the small droplets: $w = 90\ \mu m, h_0 = 40\ \mu m, \alpha = 11\ \%$.

The segments were respectively injected in the microfluidic slope at 6 and 0.5 μL/min.

B.1.3 Measure of the generated concentration gradient

Before using droplet libraries to generate combinatorial reaction in anchors, we investigated quantitatively the control of the concentration during the segment production. In order to

do so, we created segments with an increase and decrease of the concentration of colored solution, we partitioned them into nanoliter droplets and measured the droplet intensities in the observation chamber. As we use an absorption dye (2,6-DCPIP), the Beer-Lambert's law applies:

$$log\left(\frac{I}{I_0}\right) = -\epsilon LC \tag{B.1.1}$$

where I and I_0 are respectively the intensity in the droplets and the background intensity, ϵ is the molar attenuation coefficient of the dye, L is the path length of the light, C is the concentration of the absorption dye. Consequently, the experimental concentration ratio is:

$$R_{exp} = \frac{C - C_{min}}{C_{max} - C_{min}} = \frac{log\left(\frac{I}{I_0}\right) - log\left(\frac{I_{min}}{I_0}\right)}{log\left(\frac{I_{max}}{I_0}\right) - log\left(\frac{I_{min}}{I_0}\right)} \tag{B.1.2}$$

where R_{exp} is the experimental concentration ratio of the white solution. Indeed, we chose to indicate with C the concentration of the uncolored solution. This way, the experimental ratio increases when the pixel intensity increases. It means that I_{min} indicates the intensity of a droplet containing only the dye solution. I_{max} indicates the intensity of a droplet containing only the dilutant.

Fig.B.4 **(a-c)** shows the results of this measure in the case of the dilution of the dye followed by an increase of its concentration. Fig.B.4 **(d-f)** shows the results in the opposite case: increase and then decrease of the dye concentration. In these two experiments 43 segments were created: one first segment with only the dye (or the dilutant), then, 20 segments (indicated in red on the figure) for the linear decrease (or increase) of the dye concentration. After this, 1 segment was added before changing again the concentration. Finally, 20 segments (indicated in blue on the figure) for the linear comeback to the initial concentration. The experiment was ended with a last segment for confirming the final concentration. In Fig.B.4 **(a)** and **(d)**, we can see in each case a montage showing images of the nanoliter droplets produced from each segment. These images are taken right after the droplet production, in the observation chamber (see Fig.B.2 **(b)** and **(c)**). They confirm the very high monodispersity of the produced emulsion. In each of these images, we use an homemade Matlab® code to detect the droplets and extract their intensities. These intensities are displayed for each segment in Fig.B.4 **(b)** and **(e)**. It allows to confirm quantitatively the variations of the dye concentration that were observed qualitatively on Fig.B.4 **(a)** and **(d)**.

Nevertheless, as decribed by the equation (B.1.2), we need to take Beer-Lambert's law into account before inferring anything about the actual concentration in the droplets. The experimental ratios of the droplets produced from the segments corresponding to an increase and decrease of the concentration (in red and blue) are compared to the imposed ratios in Fig.B.4 **(c)** and **(f)**. In these figures, the black line represents the agreement between the theoretical and experimental data, the red and blue dots show respectively the

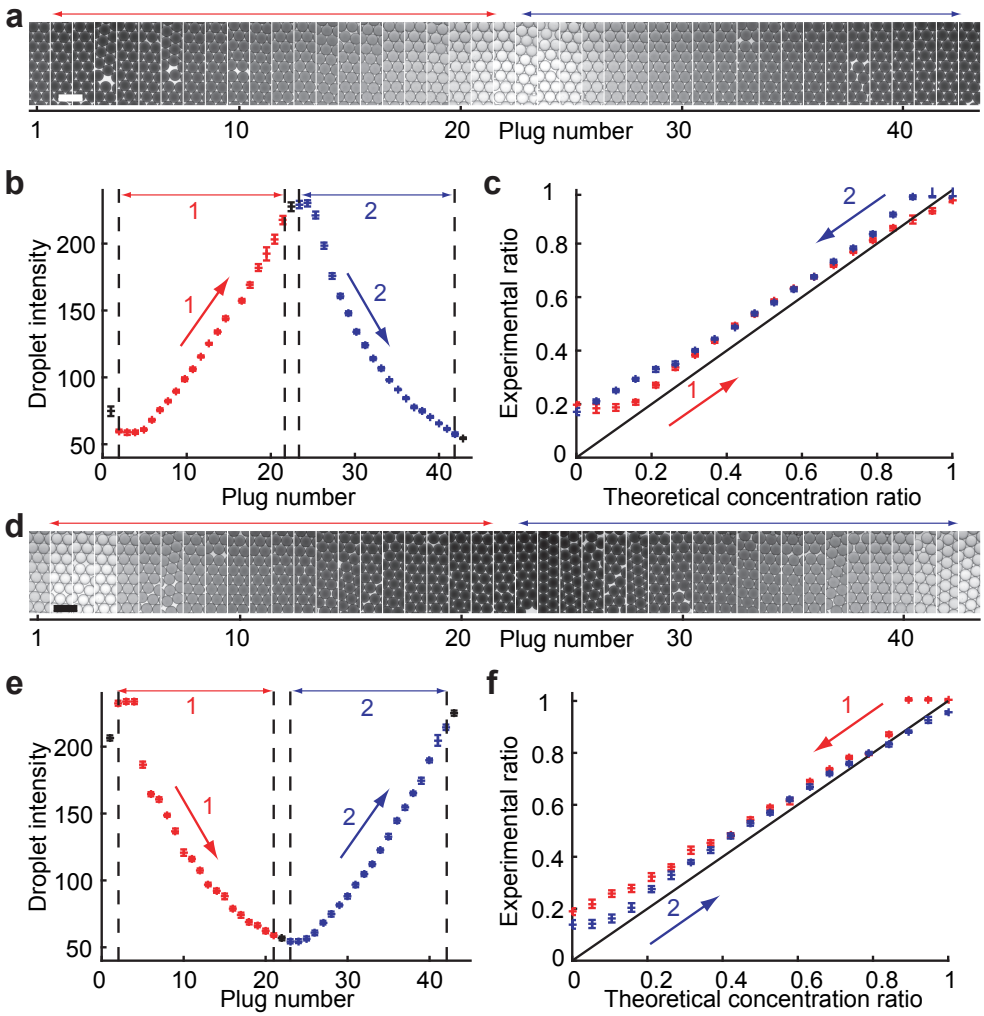

Figure B.4: Measure of the plug concentration ratios. **(a)** Images of droplets created from 43 plugs with a linear decrease and increase of the imposed concentration ratio. **(b)** Evolution of the mean droplet intensity with the plug number. **(c)** Correlation between the experimental and theoretical concentration ratio. The black line equation is $y = x$. **(d-f)** show a similar analysis with a linear increase and decrease of the imposed concentration ratio. The error bar represent the standard deviation on the measured droplets. The data in red and blue represent respectively the first and second concentration variation for each experiment. The data in black represents the plugs that are produced before or after the concentration gradients. Scale bars are 1 mm.

intensities during the first and second concentration change. The analysis of these results is similar whatever the content of the first segment. At first glance, most of the data points remain close to the black line, indicating that the actual dye concentration in the droplets is close the the theoretical one. Then, it is difficult to reach an experimental ratio value below 0.2. The value 0 corresponds to measures with a separate droplet production from

the dye solution only, without extra dilutant. It means that we struggle to reproduce the initial dye concentration, some dilutant must always mix in the created segments. Finally, as the curves corresponding to the increase and decrease of the dye concentration do not overlap exactly, there is an hysteresis in the actual concentration of the droplets. For instance, in Fig.B.4 **(c)**, there is a almost no increase of the experimental ratio for the first 4 red dots staying close to 0.2 while the last dots of the red curve reach the value 1 with a nice and linear increase. The situation is similar when the experimental ratio decreases. The first 3 dots of the blue curve are almost constant at 1, the linear decrease comes only after and is maintained until the lowest value of 0.2.

Therefore, the first segments after the beginning of the linear change of concentration keep a memory of the initial segment concentration and there is a delay for the experimental ratio compared to the theoretical one. This hysteresis can be explained by the mixing and diffusion of the two solutions at the segment producing cross junction. Indeed, when the two aqueous phases are in contact, each solution can diffuse towards the other, consequently when the dilutant is injected we actually inject a mix of dilutant and dye. This has apparently a significant impact when the two aqueous flowrates are very different from one another. This phenomenon could be further investigated by replacing the commercial cross junction with a transparent chip that allows to observe the behavior of the aqueous phase during the segments production.

B.2 Experimental protocol for the sequential production and injection of 2 droplets libraries in a trapping chamber with combinatorial anchors

This section describes the experimental parameters related to the production of the libraries used in section 6.3. We created two sets of segments with 5 different concentrations. In the first case, we mixed a yellow and blue dye and in the second we diluted a red dye with a uncolored solution.

The corresponding fluidic connections are shown in Fig.B.5 **(a)**. We can see the cross junction where the segments are produced and two valves that are used to choose which solutions are injected in the junction. Fig.B.5 **(b)** shows schematically the production of the yellow to blue segments. The yellow solution and the dilutant for the red dye are connected to valve A while the red and blue solutions are connected to valve B. These valves can connect two adjacent ports as indicated by the thick black angled lines. The connection is chosen manually. For both valves, the port number 1 is connected to the junction and their port number 3 is connected to the waste, used when the interior of the valve needs to be cleaned before a change of solution. In the case displayed in Fig.B.5 **(b)**, the yellow and blue solutions are connected to the cross junction, as well as the oil that separates

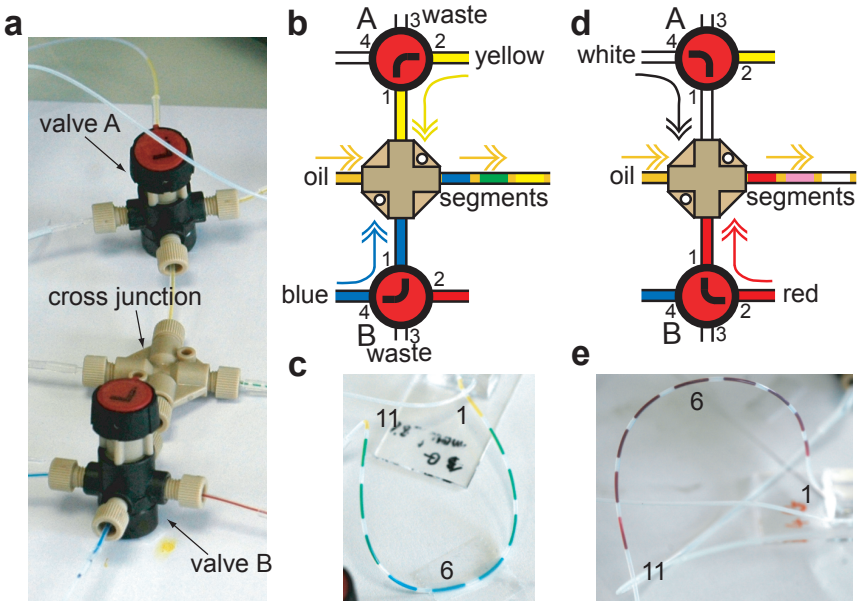

Figure B.5: Protocol for segment creation. **(a)** Image of the connectics around the cross junction that creates the segments. **(b)** Schematized protocol for the production of the first segments. **(c)** Image of the first segments before the droplet production. **(d)** Schematized protocol for the production of the second segments. **(e)** Image of the second segments. Segments 1,6 and 11 are highlighted on images **(c)** and **(e)**.

the segments from one another. As described earlier, it allows to create segments with a linear variation of the concentration ratio between these two solutions. These segments are shown in Fig.B.5 **(c)**, with a linear increase and decrease of the concentration of the blue solution. An extra blue segment (number 6) is added in between the two linear variations, resulting in 11 different segments. Fig.B.5 **(d)** shows the case where the red solution and the dilutant are connected to the cross junction to create the segments that are displayed in Fig.B.5 **(e)**.

Each set of segments is connected and injected in a microfluidic chip for its partition into nanoliter droplets. In our case, the yellow to blue segments will constitute the large droplets in the anchors and the red to uncolored segments will constitute the small droplets. Therefore, we need two different microfluidic chips for the segment partition, each of them with a design adapted to the production of one of the two droplet sizes. Fig.B.6 shows that the 2 droplet producing chips are connected to the trapping chamber via a valve.

This partition is shown schematically in Fig.B.7 **(a)** for the uncolored to red segments. As the segments are injected, droplets of different contents are created. When they reach the storage chamber they ascend and remain trapped at the ceiling level. We can clearly see ascending droplets on the Fig.B.7 **(b)**. Though, once all segments have been injected, the droplets are not well mixed, as shown in Fig.B.7 **(a)**. If they are directly injected in

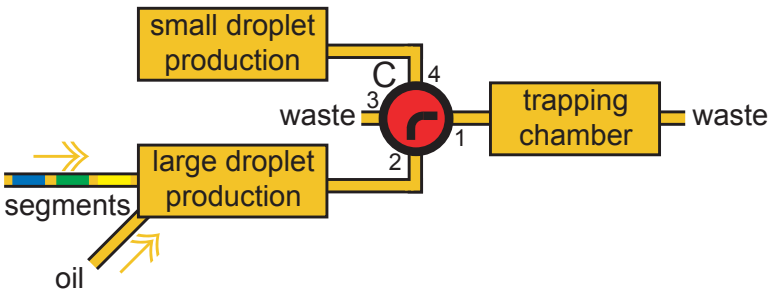

Figure B.6: Protocol for droplet production and trapping. Schematized protocol for the first droplet production and trapping.

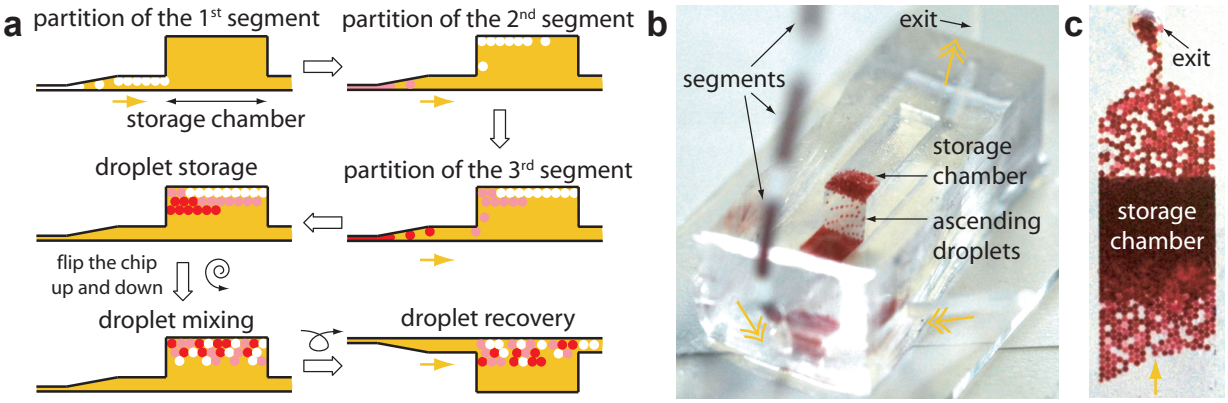

Figure B.7: Partition of the segmented flows and droplet mixing. **(a)** Schematized protocol showing at every step a side view of the droplet production chip. The spiral arrow indicates that the chip is flipped several times to ensure a good mixing of the droplets in the storage chamber. **(b)** Image of an experiment showing the production of the droplets from the segments. **(c)** Top bottom view of a droplet production chip during the droplet recovery after mixing in the storage chamber. Yellow arrows represent the oil flowrate.

the trapping chamber, the proportion of each content will not be equal among the trapped droplets. Some concentrations might even be missed. Therefore, we have designed a storage chamber much bigger than the overall volume of the droplets. By simply flipping the chip up and down several times, we are able to mix the different populations. Finally, the droplets are recovered by simply changing the orientation of the chip (the injector at the top and the storage chamber at the bottom). The droplets are now at the same height as the exit chamber and can be evacuated. This step is shown in Fig.B.7 **(c)**. This is a top view of the chip after the mixing and during the droplet recovery. As the exit is constituted of a channel that has the same height as the observation chamber, we can clearly see a monolayer of exiting droplets and confirm the efficiency of the mixing step.

Appendix C

Automation of the staining protocol

As described in subsection 2.3.1, staining protocols have many successive steps. Therefore, they are labor intensive when performed manually. After each incubation or washing step, the operator needs to change the syringe and may inject an air bubble in the microfluidic chip that will be trapped over an anchor filled with a spheroid. Most of the time, these immobilized air bubbles are much larger than the droplets and cannot be removed by perfusion once immobilized. Consequently, they prevent staining molecules to reach the spheroids in the latter steps of the staining protocol. This can have a dramatic impact on the image analysis that aims at measuring the fluorescent intensity of the immobilized spheroids. Therefore, when the staining protocol was performed manually (that is the case for the data shown in chapter 4), there was a manually pre-processing of the image of the array to discard the anchors with an air bubble. This phenomenon reduces significantly the number of spheroids which can be used for the image analysis. In addition, it is difficult for an operator to control precisely the incubation times when several chips are stained in parallel. In the case of antibodies, the incubation times are long so a difference of few minutes in the incubation time of several chips is negligible but some solutions like DAPI or Triton X-100 require short incubation times (5 min) which need to be well controlled for reproducible results.

To answer this issues, we have automatized the staining protocol, as described in Fig.C.1, with commercially available (Fluigent, Paris, France) pressure controllers and switchs which are interfaced with a computer. Fig.C.1 **(a)** shows the fluidic connections. Switch 1 has 10 inputs that can be selectively linked to one output. Each solution is then connected to a different port of the switch and is actuated by one pressure controller, according to the manufacturer instructions. The second switch is used to choose which chip is going to be perfused. The flowrate is measured in between the switchs and a controlling loop allows to maintain a constant flowrate by adjusting the input pressure when necessary.

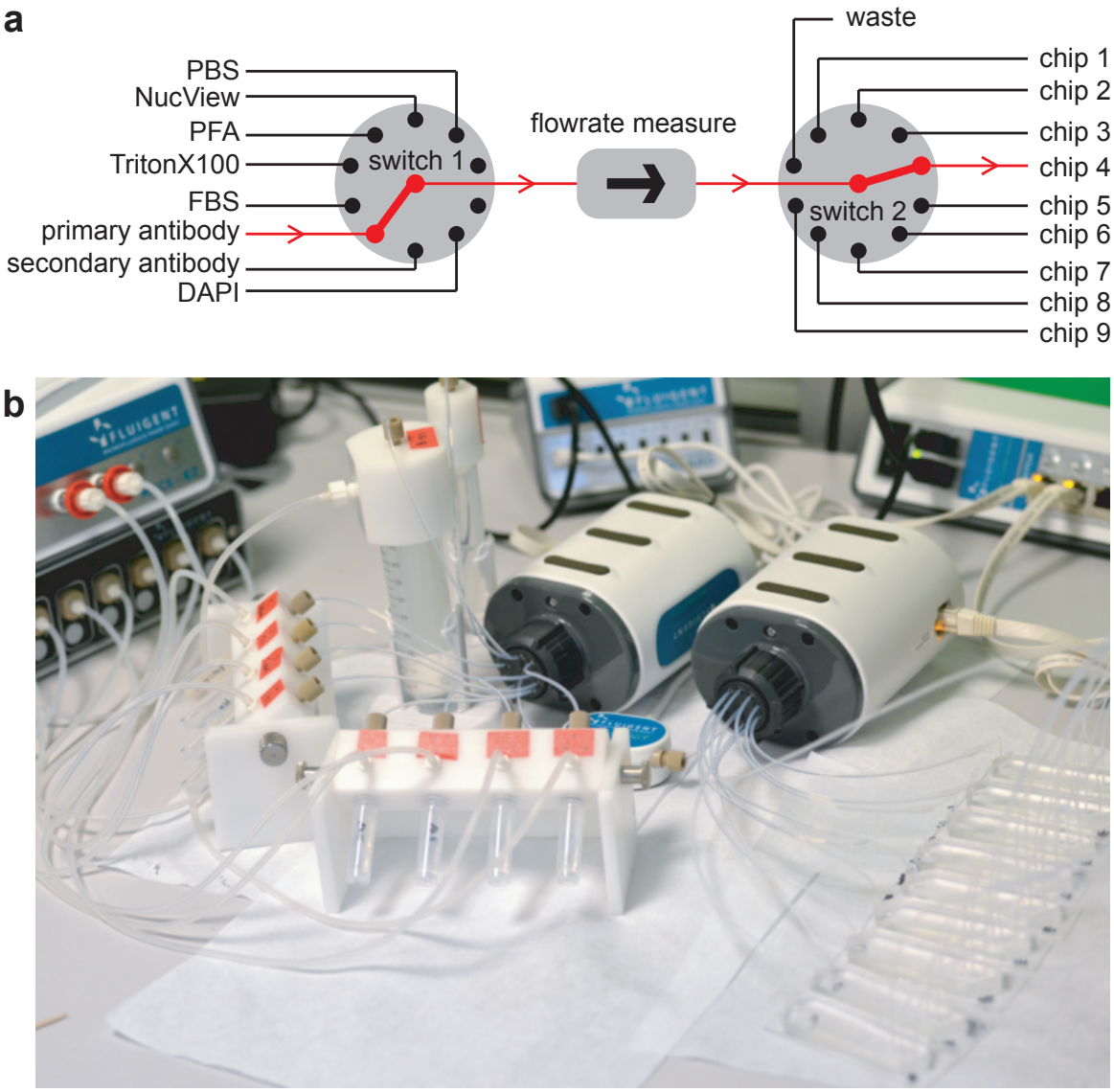

Figure C.1: Automation of the staining protocol. **(a)** Scheme of the fluidic connections for the autoamted staining of 9 microfluidic chips for the culture of hMSC aggregates (see chapter 5). The path leading to the injection of the primary antibody solution into the chip 4 is highlighted in red. **(c)** Image corresponding to the protocol in **(a)**.

The operation of the pressure controllers and of the switchs is entirely controlled by a custom Matlab® code. Each solution is injected sequentially into all the microfluidic chips and the incubation times are controlled with a 1 second precision. This procedure allows the automated, reproducible, bubble-free staining of up to 9 chips in parallel.

Appendix D

Spatial heterogeneities in the fluorescence signal accross the array

The spatial heterogeneities of the signal were investigated at the spheroid level to check whether the location of the immobilized droplets in the array can have an effect on the measured parameters. We analyzed the experiments with the hMSC aggregates after 3 days of culture (1 day in a two phase system and 2 days in culture medium) and averaged the different parameters depending on the location in the array. Fig.D.1 and Fig.D.2 present the results of this analysis with heat maps representing the droplet array. In all cases, the droplets were produced at the right side of the array and the phase change and staining protocol were performed by injecting aqueous solution from the left side of the array.

Fig.D.1 **(a)** shows the mapping of the spheroid diameter, with no visible trend in the noise. The variation of the averaged value in each location is within +/- 12 % of the mean across the array. Therefore, we can say that the droplet location has no significant effect on the spheroid diameter. Fig.D.1 **(b)** shows a similar map for the normalized DAPI signal. Since the mean DNA quantity can be considered as constant at the spheroid level and since the diameter does not change significantly, we expect to have also a constant DAPI signal across the array. Nevertheless, the averaged DAPI signal is consistently higher in the central region of the array, with lower values at the edges of the array (first and last rows and columns). The variation remains within +/- 15 % of the mean. Since it is unlikely to find a biological reason that could explain this small effect, it is possibly due to the chamber swelling during the perfusion of the staining solution. When the chamber swells the hydrodynamic resistance is lower in the central region of the array (where the swelling is maximum). Therefore, the flowrate must be higher in the central part resulting in a higher efficiency of staining.

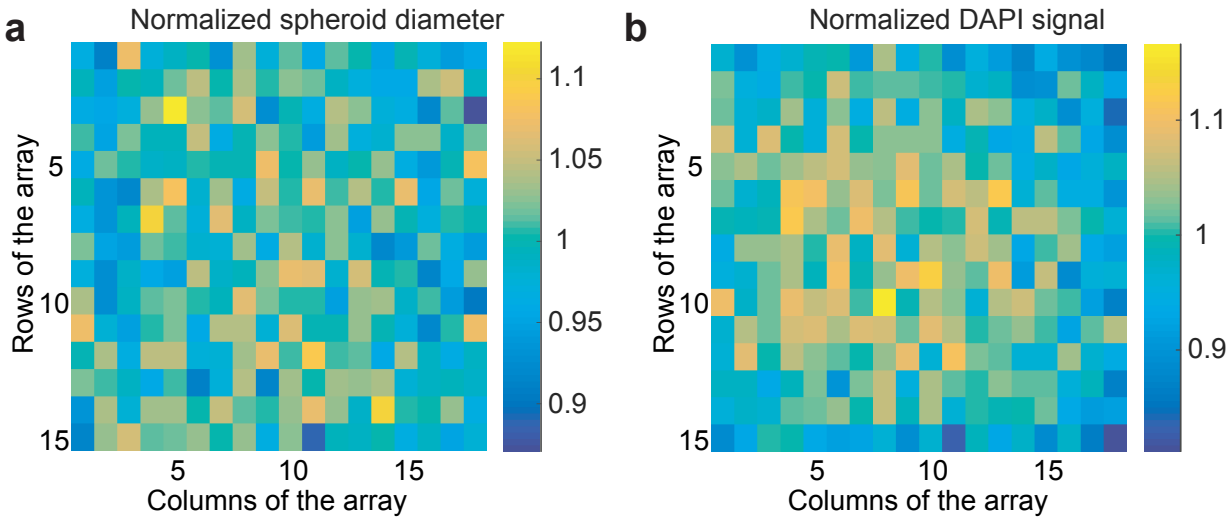

Figure D.1: XY MAPPING OF THE SPHEROID DIAMETER AND DAPI SIGNAL IN THE ARRAY. **(a)** Normalized spheroid diameter and **(b)** DAPI signal. $N_{chips} = 26, N_{spheroids} = 6626$.

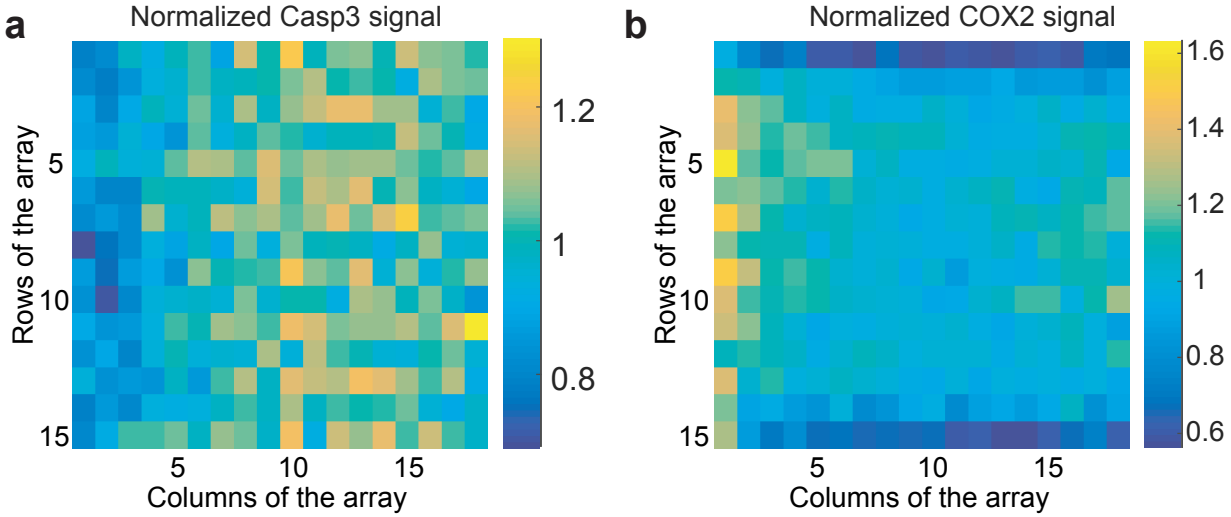

Figure D.2: XY MAPPING OF THE CASP3 AND COX2 SIGNAL IN THE ARRAY. **(a)** Normalized Casp3 and **(b)** COX2 signals. $N_{chips} = 26, N_{spheroids} = 6626$

Similarly, FIG.D.2 shows the variation for the Casp3 and COX2 signals. The Casp3 signal is lower at the left side of the array (FIG.D.2 **(a)**), close to the source of the different aqueous perfusions. This variation is quite high since it extends within +/- 30 % of the mean value. For the COX2, the signal is lower close to the chamber side walls (first and last rows), constant in the central region of the array and lower on the right and left sides (first and last columns), with the highest values reached on the left side of the array (FIG.D.2 **(b)**). In this case the variation is really high, extending within +/- 60 % of the mean value. It is interesting to notice that the area of low Casp3 signal correspond to the area of high

COX2 signal.

The high magnitude of the dependence of these biological fluorescent signals on the droplet location is unexpected and can be explained by several parameters. First, Fig.D.2 **(b)** suggests that there is a significant chamber swelling during the perfusion steps of the staining protocol, potentially leading to inhomogeneous concentrations of the different solutions and to inhomogeneous washing steps. Then, the proximity of the PDMS side walls (permeable to oxygen) might play a role regarding the spatial concentration of the oxygen in the medium. Similarly, a droplet on one side of the array has less neighbors than the other droplets. It could lead to inhomogeneities in the nutrients concentration. Finally, the cells in these experiments were cultured for 2 days in static conditions after the phase change, so they were able to communicate with each other via paracrine interactions. Mesenchymal stem cells are knows for secreting a lot of trophic factors (see section 5.1) so many molecules could have a significant effect on the neighboring spheroids.

Further experiments could help finding the main reasons of these spatial heterogeneities. PIV could help investigating the extend of the chamber swelling, spheroids could be directly stained after the phase change to prevent the establishment of paracrine interactions and specific imaging could allow to determine the oxygen concentration in the array [134]. Understanding these inhomogeneities could help design a microfluidic chamber with similar conditions for all the spheroids of the array, and consequently a lower standard deviation on the fluorescent signals.

Appendix E

Statistics

For the population-level comparison between 2D and 3D conditions, statistical significance was assessed by unpaired two-sample two-tailed Student's t-tests. For the spheroid- and cellular-level data analysis, significance was assessed either by Welch's ANOVA followed by Games-Howell post-hoc procedure. For non-normal distributions, significance was tested using Kruskal-Wallis ANOVA followed by Mann-Whitney U-tests with Sidak's correction for multiple comparisons. *: $p < 0.05$, **: $p < 0.01$, ***: $p < 0.001$, were considered statistically significant. N.S.: non-significant. P-value ranges are only indicated for the highlighted comparisons. In the Tukey box-and-whiskers figures, the boxes represent the first (q_1) and third (q_3) quartiles with the median shown by the line bisecting the box, and the mean is shown with black circles. The whiskers represent 1.5 times the inter-quartile range ($q_3 - q_1$) of the sample. Finally, the box width is proportional to $\sqrt{n}$.

List of Figures

Bibliography

[1] E Cukierman, R Pankov, D R Stevens, and K M Yamada. Taking cell-matrix adhesions to the third dimension. *Science*, 294(5547):1708–1712, 2001.

[2] Michael Hay, David W Thomas, John L Craighead, Celia Economides, and Jesse Rosenthal. Clinical development success rates for investigational drugs. *Nature Biotechnology*, 32(1):40–51, 2014.

[3] Edna Cukierman, Roumen Pankov, and Kenneth M Yamada. Cell interactions with three-dimensional matrices. *Current opinion in cell biology*, 14(5):633–639, 2002.

[4] Adam J. Engler, Shamik Sen, H. Lee Sweeney, and Dennis E. Discher. Matrix Elasticity Directs Stem Cell Lineage Specification. *Cell*, 126(4):677–689, 2006.

[5] Mathieu Vinken, Peggy Papeleu, Sarah Snykers, Evelien De Rop, Tom Henkens, James Kevin Chipman, Vera Rogiers, and Tamara Vanhaecke. Involvement of cell junctions in hepatocyte culture functionality. *Critical reviews in toxicology*, 36:299–318, 2006.

[6] Elliot E Hui and Sangeeta N Bhatia. Micromechanical control of cell-cell interactions. *Proceedings of the National Academy of Sciences of the United States of America*, 104(14):5722–6, 2007.

[7] Steven R Caliari and Jason A Burdick. A practical guide to hydrogels for cell culture. *Nature Methods*, 13(5):405–414, 2016.

[8] Hynda K Kleinman and George R Martin. Matrigel: basement membrane matrix with biological activity. *Seminars in cancer biology*, 15(5):378–86, oct 2005.

[9] Muhannand H Zaman, Alisha L Sieminski, Drew Mackellar, Haiyan Gong, Roger D Kamm, Alan Wells, Douglas A Lauffenburger, and Paul Matsudaira. Migration of tumor cells in 3D matrices is governed by matrix stiffness along with cell-matrix adhesion and proteolysis. *Proceedings of the National Academy of Sciences of the United States of America*, 103(15), 2006.

[10] K A Mosiewicz, L Kolb, A J van der Vlies, M M Martino, P S Lienemann, J A Hubbell, M Ehrbar, and M P Lutolf. In situ cell manipulation through enzymatic hydrogel photopatterning. *Nat Mater*, 12(11):1072–1078, 2013.

[11] Jens M. Kelm and Martin Fussenegger. Microscale tissue engineering using gravity-enforced cell assembly. *Trends in Biotechnology*, 22(4):195–202, 2004.

[12] Francesco Pampaloni, Emmanuel G Reynaud, and Ernst H K Stelzer. The third dimension bridges the gap between cell culture and live tissue. *Nature Reviews Molecular Cell Biology*, 8(october):839–845, 2007.

[13] Eelco Fennema, Nicolas Rivron, Jeroen Rouwkema, Clemens van Blitterswijk, and Jan de Boer. Spheroid culture as a tool for creating 3D complex tissues. *Trends in biotechnology*, 31(2):108–15, feb 2013.

[14] Susan Breslin and Lorraine O'Driscoll. Three-dimensional cell culture: The missing link in drug discovery. *Drug Discovery Today*, 18(5-6):240–249, 2013.

[15] Daniel Mueller, Lisa Krämer, Esther Hoffmann, Sebastian Klein, and Fozia Noor. 3D organotypic HepaRG cultures as in vitro model for acute and repeated dose toxicity studies. *Toxicology in vitro : an international journal published in association with BIBRA*, 28(1):104–12, feb 2014.

[16] Richard M. Eglen and David H. Randle. Drug Discovery Goes Three-Dimensional: Goodbye to Flat High-Throughput Screening? *ASSAY and Drug Development Technologies*, 13(5):150629132900006, 2015.

[17] Jonathan J. Burbaum. Miniaturization technologies in HTS: How fast, how small, how soon? *Drug Discovery Today*, 3(7):313–322, 1998.

[18] Adam Smith. Screening for drug discovery: the leading question. *Nature*, 418:453–459, 2002.

[19] Lorenz M. Mayr and Dejan Bojanic. Novel trends in high-throughput screening. *Current Opinion in Pharmacology*, 9(5):580–588, 2009.

[20] G F Christopher and S L Anna. Microfluidic methods for generating continuous droplet streams. *Journal of Physics D: Applied Physics*, 40:R319–R336, oct 2007.

[21] Jeremy J Agresti, Eugene Antipov, Adam R Abate, Keunho Ahn, Amy C Rowat, Jean-Christophe Baret, Manuel Marquez, Alexander M Klibanov, Andrew D Griffiths, and David a Weitz. Ultrahigh-throughput screening in drop-based microfluidics for directed evolution. *Proceedings of the National Academy of Sciences of the United States of America*, 107(9):4004–4009, mar 2010.

[22] Ralf Seemann, Martin Brinkmann, Thomas Pfohl, and Stephan Herminghaus. Droplet based microfluidics. *Reports on progress in physics. Physical Society (Great Britain)*, 75(1):016601, jan 2012.

[23] Paul Abbyad, Rémi Dangla, Antigoni Alexandrou, and Charles N Baroud. Rails and anchors: guiding and trapping droplet microreactors in two dimensions. *Lab on a chip*, 11(5):813–821, mar 2011.

[24] R F Ismagilov. A Microfluidic System for Controlling Reaction Networks in Time. *Angewandte Chemie (International ed. in English)*, 42(7):767–772, 2003.

[25] Davide Ferraro, Jérôme Champ, Bruno Teste, Marco Serra, Laurent Malaquin, Jean-Louis Viovy, Patricia de Cremoux, and Stephanie Descroix. Microfluidic platform combining droplets and magnetic tweezers: application to HER2 expression in cancer diagnosis. *Scientific Reports*, 6(April):25540, 2016.

[26] Feng SHEN, Yi LI, Zhao-Miao LIU, Ren-Tuo CAO, and Gui-Ren WANG. Advances in Micro-Droplets Coalescence Using Microfluidics. *Chinese Journal of Analytical Chemistry*, 43(12):1942–1954, 2015.

[27] Balint Kintses, Liisa D. van Vliet, S. R a Devenish, and Florian Hollfelder. Microfluidic droplets: New integrated workflows for biological experiments. *Current Opinion in Chemical Biology*, 14(5):548–555, 2010.

[28] Eric Brouzes, Martina Medkova, Neal Savenelli, Dave Marran, Mariusz Twardowski, J Brian Hutchison, Jonathan M Rothberg, Darren R Link, Norbert Perrimon, and Michael L Samuels. Droplet microfluidic technology for single-cell high-throughput screening. *Proceedings of the National Academy of Sciences of the United States of America*, 106(34):14195–200, 2009.

[29] Evan Z. Macosko, Anindita Basu, Rahul Satija, James Nemesh, Karthik Shekhar, Melissa Goldman, Itay Tirosh, Allison R. Bialas, Nolan Kamitaki, Emily M. Martersteck, John J. Trombetta, David A. Weitz, Joshua R. Sanes, Alex K. Shalek, Aviv Regev, and Steven A. McCarroll. Highly Parallel Genome-wide Expression Profiling of Individual Cells Using Nanoliter Droplets. *Cell*, 161(5):1202–1214, 2015.

[30] Jenifer Clausell-Tormos, Diana Lieber, Jean Christophe Baret, Abdeslam El-Harrak, Oliver J. Miller, Lucas Frenz, Joshua Blouwolff, Katherine J. Humphry, Sarah Köster, Honey Duan, Christian Holtze, David a. Weitz, Andrew D. Griffiths, and Christoph a. Merten. Droplet-Based Microfluidic Platforms for the Encapsulation and Screening of Mammalian Cells and Multicellular Organisms. *Chemistry and Biology*, 15(5):427–437, 2008.

[31] Alim Dewan, Jihye Kim, Rebecca H. Mclean, Siva A. Vanapalli, and Muhammad Nazmul Karim. Growth kinetics of microalgae in microfluidic static droplet arrays. *Biotechnology and Bioengineering*, 109(12):2987–2996, 2012.

[32] Linfen Yu, Michael C W Chen, and Karen C Cheung. Droplet-based microfluidic system for multicellular tumor spheroid formation and anticancer drug testing. *Lab on a chip*, 10(18):2424–2432, sep 2010.

[33] Choong Kim, Seok Chung, Young Eun Kim, Kang Sun Lee, Soo Hyun Lee, Kwang Wook Oh, and Ji Yoon Kang. Generation of core-shell microcapsules with three-dimensional focusing device for efficient formation of cell spheroid. *Lab on a chip*, 11(2):246–52, jan 2011.

[34] Yuya Morimoto and Shoji Takeuchi. Three-dimensional cell culture based on microfluidic techniques to mimic living tissues. *Biomaterials Science*, 1(3):257, 2013.

[35] Amy Y Hsiao, Yu-suke Torisawa, Yi-Chung Tung, Sudha Sud, Russell S Taichman, Kenneth J Pienta, and Shuichi Takayama. Microfluidic system for formation of PC-3 prostate cancer co-culture spheroids. *Biomaterials*, 30(16):3020–7, jun 2009.

[36] Hiroki Ota and Norihisa Miki. Microfluidic experimental platform for producing size-controlled three-dimensional spheroids. *Sensors and Actuators A: Physical*, 169(2):266–273, oct 2011.

[37] Mark D Ungrin, Chirag Joshi, Andra Nica, Céline Bauwens, and Peter W Zandstra. Reproducible, ultra high-throughput formation of multicellular organization from single cell suspension-derived human embryonic stem cell aggregates. *PloS one*, 3(2):e1565, jan 2008.

[38] Yi-Chung Tung, Amy Y Hsiao, Steven G Allen, Yu-suke Torisawa, Mitchell Ho, and Shuichi Takayama. High-throughput 3D spheroid culture and drug testing using a 384 hanging drop array. *The Analyst*, 136(3):473–8, feb 2011.

[39] C Holtze, a C Rowat, J J Agresti, J B Hutchison, F E Angilè, C H J Schmitz, S Köster, H Duan, K J Humphry, R a Scanga, J S Johnson, D Pisignano, and D a Weitz. Biocompatible surfactants for water-in-fluorocarbon emulsions. *Lab on a chip*, 8(10):1632–9, oct 2008.

[40] Jean-Christophe Baret. Surfactants in droplet-based microfluidics. *Lab on a chip*, 12(3):422–33, feb 2012.

[41] Rémi Dangla, Sungyon Lee, and Charles N. Baroud. Trapping Microfluidic Drops in Wells of Surface Energy. *Physical Review Letters*, 107(12):124501, sep 2011.

[42] Etienne Fradet, Craig McDougall, Paul Abbyad, Rémi Dangla, David McGloin, and Charles N Baroud. Combining rails and anchors with laser forcing for selective manipulation within 2D droplet arrays. *Lab on a chip*, 11(24):4228–34, dec 2011.

[43] Emilie Verneuil, Maríaluisa Cordero, François Gallaire, and Charles N Baroud. Laser-induced force on a microfluidic drop: origin and magnitude. *Langmuir : the ACS journal of surfaces and colloids*, 25(9):5127–34, may 2009.

[44] Rémi Dangla, S Cagri Kayi, and Charles N Baroud. Droplet microfluidics driven by gradients of confinement. *Proceedings of the National Academy of Sciences of the United States of America*, 110(3):853–8, jan 2013.

[45] Etienne Fradet, Yonatan Lopez, and Charles N Baroud. The physical mechanisms of step emulsification. *Journal of Physics D: Applied Physics*, 46, 2013.

[46] Venkatachalam Chokkalingam, Stephan Herminghaus, and Ralf Seemann. Self-synchronizing pairwise production of monodisperse droplets by microfluidic step emulsification. *Applied Physics Letters*, 93(25):254101, 2008.

[47] Jean-Christophe Baret, Felix Kleinschmidt, Abdeslam El Harrak, and Andrew D Griffiths. Kinetic aspects of emulsion stabilization by surfactants: a microfluidic analysis. *Langmuir : the ACS journal of surfaces and colloids*, 25(11):6088–93, jun 2009.

[48] David J Collins, Adrian Neild, Andrew DeMello, Ai-qun Liu, and Ye Ai. The Poisson distribution and beyond : methods for microfluidic droplet production and single cell. *Lab on a Chip*, 15(17):3439–3459, 2015.

[49] Jeffrey D. Martin and Steven D. Hudson. Mass transfer and interfacial properties in two-phase microchannel flows. *New Journal of Physics*, 11, 2009.

[50] N Pernodet, M Maaloum, and B Tinland. Pore size of agarose gels by atomic force microscopy. *Electrophoresis*, 18(1):55–58, 1997.

[51] Jaaky Narayanan, Jun-Ying Xiong, and Xiang-Yang Liu. Determination of agarose gel pore size: Absorbance measurements vis a vis other techniques. *Journal of Physics: Conference Series*, 28:83–86, 2006.

[52] Peng Chen, Xiaojun Feng, Dongjuan Chen, Chao Liu, Wei Du, and Bi-Feng Liu. Investigating intercellular calcium waves by microfluidic gated pinched-flow. *Sensors and Actuators B: Chemical*, 234:583–592, 2016.

[53] María Cordero, Emilie Verneuil, François Gallaire, and Charles Baroud. Time-resolved temperature rise in a thin liquid film due to laser absorption. *Physical Review E*, 79(1):011201, jan 2009.

[54] Olivier Frey, Patrick M Misun, David a Fluri, Jan G Hengstler, and Andreas Hierlemann. Reconfigurable microfluidic hanging drop network for multi-tissue interaction and analysis. *Nature communications*, 5(May):4250, jan 2014.

[55] K Kwapiszewska, a Michalczuk, M Rybka, R Kwapiszewski, and Z Brzózka. A microfluidic-based platform for tumour spheroid culture, monitoring and drug screening. *Lab on a chip*, may 2014.

[56] Bishnubrata Patra, Chien-Chung Peng, Wei-Hao Liao, Chau-Hwang Lee, and Yi-Chung Tung. Drug testing and flow cytometry analysis on a large number of uniform sized tumor spheroids using a microfluidic device. *Scientific Reports*, 6(October 2015):21061, 2016.

[57] Kévin Alessandri, Bibhu Ranjan Sarangi, Vasily Valérïévitch Gurchenkov, Bidisha Sinha, Tobias Reinhold Kießling, Luc Fetler, Felix Rico, Simon Scheuring, Christophe Lamaze, Anthony Simon, Sara Geraldo, Danijela Vignjevic, Hugo Doméjean, Leslie Rolland, Anette Funfak, Jérôme Bibette, Nicolas Bremond, and Pierre Nassoy. Cellular capsules as a tool for multicellular spheroid production and for investigating the mechanics of tumor progression in vitro. *Proceedings of the National Academy of Sciences of the United States of America*, 110(37):14843–8, sep 2013.

[58] Hon Fai Chan, Ying Zhang, Yi-Ping Ho, Ya-Ling Chiu, Youngmee Jung, and Kam W Leong. Rapid formation of multicellular spheroids in double-emulsion droplets with controllable microenvironment. *Scientific reports*, 3:3462, jan 2013.

[59] Christian Siltanen, Maliheh Yaghoobi, Amranul Haque, Jungmok You, Jeremy Lowen, Masoud Soleimani, and Alexander Revzin. Microfluidic fabrication of bioactive microgels for rapid formation and enhanced differentiation of stem cell spheroids. *Acta Biomaterialia*, 34:1–8, 2016.

[60] Pooja Sabhachandani, Vinny Motwani, Noa Cohen, Saheli Sarkar, Vladimir Torchilin, and Tania Konry. Generation and Functional Assessment of 3D Multicellular Spheroids in Droplet Based Microfluidics Platform. *Lab on a Chip*, 16(3):497–505, 2016.

[61] Kay S Mcmillan, Marie Boyd, and Michele Zagnoni. Transitioning from multi-phase to single-phase microfluidics for long-term culture and treatment of multicellular spheroids. *Lab on a Chip*, 16(18):3548–3555, 2016.

[62] Lucas T Vu, Rebekah R Less, and Padmavathy Rajagopalan. The promise of organotypic hepatic and gastrointestinal models. *Trends in biotechnology*, 32(8):406–413, may 2014.

[63] Yusuke Sakai, Seita Yamagami, and Kohji Nakazawa. Comparative analysis of gene expression in rat liver tissue and monolayer- and spheroid-cultured hepatocytes. *Cells Tissues Organs*, 191:281–288, 2010.

[64] J. Landry, D. Bernier, C. Ouellet, R. Goyette, and N. Marceau. Spheroidal aggregate culture of rat liver cells: Histotypic reorganization, biomatrix deposition, and maintenance of functional activities. *Journal of Cell Biology*, 101:914–923, 1985.

[65] Franziska van Zijl and Wolfgang Mikulits. Hepatospheres: Three dimensional cell cultures resemble physiological conditions of the liver. *World Journal of Hepatology*, 2(1):1–7, 2010.

[66] Tammy T Chang and Millie Hughes-Fulford. Molecular mechanisms underlying the enhanced functions of three-dimensional hepatocyte aggregates. *Biomaterials*, 35(7):2162–71, 2014.

[67] Linda G Griffith, Alan Wells, and Donna Beer Stolz. Engineering Liver. *Hepatology*, 60(4):1426–1434, 2014.

[68] Sau Fung Wong, Da Yoon No, Yoon Young Choi, Dong Sik Kim, Bong Geun Chung, and Sang-Hoon Lee. Concave microwell based size-controllable hepatosphere as a three-dimensional liver tissue model. *Biomaterials*, 32(32):8087–96, nov 2011.

[69] M. A. Saber, M. A. Zern, and D. A. Shafriz. Use of in situ hybridization to identify collagen and albumin mRNAs in isolated mouse hepatocytes. *Proceedings of the National Academy of Sciences of the United States of America*, 80:4017–4020, 1983.

[70] Ruei-Zeng Lin, Li-Fang Chou, Chi-Chen Michael Chien, and Hwan-You Chang. Dynamic analysis of hepatoma spheroid formation: roles of E-cadherin and beta1-integrin. *Cell and tissue research*, 324(3):411–22, jun 2006.

[71] Dirk Drasdo and Stefan Höhme. A single-cell-based model of tumor growth in vitro: monolayers and spheroids. *Physical Biology*, 2(3):133–147, 2005.

[72] Emmanouhl S. Tzanakakis, Linda K. Hansen, and Wei Shou Hu. The role of actin filaments and microtubules in hepatocyte spheroid self-assembly. *Cell Motility and the Cytoskeleton*, 48:175–189, 2001.

[73] Rachel Glicklis, Jose C Merchuk, and Smadar Cohen. Modeling mass transfer in hepatocyte spheroids via cell viability, spheroid size, and hepatocellular functions. *Biotechnology and bioengineering*, 86(6):672–80, jun 2004.

[74] Jennifer L. Luebke-Wheeler, Geir Nedredal, Le Yee, Bruce P. Amiot, and Scott L. Nyberg. E-cadherin protects primary hepatocyte spheroids from cell death by a caspase-independent mechanism. *Cell Transplantation*, 18(12):1281–1287, 2009.

[75] Gang Cheng, Janet Tse, Rakesh K Jain, and Lance L Munn. Micro-environmental mechanical stress controls tumor spheroid size and morphology by suppressing proliferation and inducing apoptosis in cancer cells. *PloS one*, 4(2):e4632, jan 2009.

[76] Fabien Montel, Morgan Delarue, Jens Elgeti, Danijela Vignjevic, Giovanni Cappello, and Jacques Prost. Isotropic stress reduces cell proliferation in tumor spheroids. *New Journal of Physics*, 14, 2012.

[77] Rui M Tostões, Sofia B Leite, Margarida Serra, Janne Jensen, Petter Björquist, Manuel J T Carrondo, Catarina Brito, and Paula M Alves. Human liver cell spheroids in extended perfusion bioreactor culture for repeated-dose drug testing. *Hepatology (Baltimore, Md.)*, 55(4):1227–36, apr 2012.

[78] Sreenivasa C. Ramaiahgari, Michiel W. Den Braver, Bram Herpers, Valeska Terpstra, Jan N M Commandeur, Bob Van De Water, and Leo S. Price. A 3D in vitro model of differentiated HepG2 cell spheroids with improved liver-like properties for repeated dose high-throughput toxicity studies. *Archives of Toxicology*, 88(5):1083–1095, 2014.

[79] Colleen M. Brophy, Jennifer L. Luebke-Wheeler, Bruce P. Amiot, Harris Khan, Rory P. Remmel, Piero Rinaldo, and Scott L. Nyberg. Rat hepatocyte spheroids formed by rocked technique maintain differentiated hepatocyte gene expression and function. *Hepatology*, 49:578–586, 2009.

[80] Elien Gevaert, Laurent Dollé, Thomas Billiet, Peter Dubruel, Leo van Grunsven, Aart van Apeldoorn, and Ria Cornelissen. High throughput micro-well generation of hepatocyte micro-aggregates for tissue engineering. *PloS one*, 9(8):e105171, jan 2014.

[81] Daniel Mueller, Anika Koetemann, and Fozia Noor. Organotypic Cultures of Hepg2 Cells for In Vitro Toxicity Studies. *Journal of Bioengineering and Biomedical Sciences*, 01(S2), 2011.

[82] Patrina Gunness, Daniel Mueller, Valery Shevchenko, Elmar Heinzle, Magnus Ingelman-Sundberg, and Fozia Noor. 3D organotypic cultures of human HepaRG cells: a tool for in vitro toxicity studies. *Toxicological sciences : an official journal of the Society of Toxicology*, 133(1):67–78, may 2013.

[83] Jun Yang, Akira Ichikawa, and Toshie Tsuchiya. A novel function of connexin 32: Marked enhancement of liver function in a hepatoma cell line. *Biochemical and Biophysical Research Communications*, 307:80–85, 2003.

[84] Bae Hoon Lee, Myung Hee Kim, Jae Ho Lee, Dror Seliktar, Nam-Joon Cho, and Lay Poh Tan. Modulation of Huh7.5 Spheroid Formation and Functionality Using Modified PEG-Based Hydrogels of Different Stiffness. *Plos One*, 10(2):e0118123, 2015.

[85] Kazuyoshi Kon, Jae-Sung Kim, Hartmut Jaeschke, and John J Lemasters. Mitochondrial permeability transition in acetaminophen-induced necrosis and apoptosis of cultured mouse hepatocytes. *Hepatology*, 40(5):1170–1179, 2004.

[86] Willem G E J Schoonen, Joe C R Stevenson, Walter M A Westerink, and G. Jean Horbach. Cytotoxic effects of 109 reference compounds on rat H4IIE and human HepG2 hepatocytes. III: Mechanistic assays on oxygen consumption with MitoXpress and NAD(P)H production with Alamar Blue??? *Toxicology in Vitro*, 26(3):511–525, 2012.

[87] Hisako Fujimura, Naoko Murakami, Satoko Miwa, Chinami Aruga, and Wataru Toriumi. The suitability of rat hepatoma cell line H4IIE for evaluating the potentials of compounds to induce CYP3A23 expression. *Experimental and Toxicologic Pathology*, 64(5):527–533, 2012.

[88] Sangeeta N Bhatia, Gregory H Underhill, Kenneth S Zaret, and Ira J Fox. Cell and tissue engineering for liver disease. *Science Translational Medecine*, 6(245), 2014.

[89] A.J. Becker, E.A. McMulloch, and J.E. Till. Cytological Demonstration of the Clonal Nature of Spleen Colonies Derived from Transplanted Mouse Marrow Cells. *Nature*, 197(487):912–914, 1963.

[90] Kazutoshi Takahashi and Shinya Yamanaka. Induction of Pluripotent Stem Cells from Mouse Embryonic and Adult Fibroblast Cultures by Defined Factors. *Cell*, 126(4):663–676, 2006.

[91] a J Friedenstein, I I Piatetzky-Shapiro, and K V Petrakova. Osteogenesis in transplants of bone marrow cells. *Journal of embryology and experimental morphology*, 16(3):381–390, 1966.

[92] Paolo Bianco, Pamela Gehron Robey, and Paul J. Simmons. Mesenchymal Stem Cells: Revisiting History, Concepts, and Assays. *Cell Stem Cell*, 2(4):313–319, 2008.

[93] Pierre Moretti, Tim Hatlapatka, Dana Marten, Antonina Lavrentieva, Ingrida Majore, Ralf Hass, Cornelia Kasper, and Abstract. Mesenchymal Stromal Cells Derived from Human Umbilical Cord Tissues: Primitive Cells with Potential for Clinical and Tissue Engineering Applications. *Advances in biochemical engineering/biotechnology*, 123(July 2015):29–54, 2010.

[94] Arnold I. Caplan and Diego Correa. The MSC: An injury drugstore. *Cell Stem Cell*, 9(1):11–15, 2011.

[95] Arnold I Caplan. Mesenchymal stem cells., 1991.

[96] Lindolfo da Silva Meirelles, Pedro Cesar Chagastelles, and Nance Beyer Nardi. Mesenchymal stem cells reside in virtually all post-natal organs and tissues. *Journal of cell science*, 119(Pt 11):2204–13, 2006.

[97] M Dominici, K Le Blanc, I Mueller, I Slaper-Cortenbach, Fc Marini, Ds Krause, Rj Deans, a Keating, Dj Prockop, and Em Horwitz. Minimal criteria for defining multipotent mesenchymal stromal cells. The International Society for Cellular Therapy position statement. *Cytotherapy*, 8(4):315–7, 2006.

[98] Benedetto Sacchetti, Alessia Funari, Stefano Michienzi, Silvia Di Cesare, Stefania Piersanti, Isabella Saggio, Enrico Tagliafico, Stefano Ferrari, Pamela Gehron Robey, Mara Riminucci, and Paolo Bianco. Self-Renewing Osteoprogenitors in Bone Marrow Sinusoids Can Organize a Hematopoietic Microenvironment. *Cell*, 131(2):324–336, 2007.

[99] Lindolfo da Silva Meirelles, Aparecida Maria Fontes, Dimas Tadeu Covas, and Arnold I. Caplan. Mechanisms involved in the therapeutic properties of mesenchymal stem cells. *Cytokine and Growth Factor Reviews*, 20(5-6):419–427, 2009.

[100] Stefan Bajada, Irena Mazakova, James B. Richardson, and Nurredin Ashammakhi. Updates on stem cells and their applications in regenerative medicine. *Journal of tissue engineering and regenerative medicine*, 4(7):169–183, 2008.

[101] Alan Trounson and Courtney McDonald. Stem Cell Therapies in Clinical Trials: Progress and Challenges. *Cell Stem Cell*, 17(1):11–22, 2015.

[102] Thomas J Bartosh, Joni H Ylöstalo, Arezoo Mohammadipoor, Nikolay Bazhanov, Katie Coble, Kent Claypool, Ryang Hwa Lee, Hosoon Choi, and Darwin J Prockop. Aggregation of human mesenchymal stromal cells (MSCs) into 3D spheroids enhances their antiin fl ammatory properties. *Proceedings of the National Academy of Sciences of the United States of America*, 107(31):13724–13729, 2010.

[103] Sébastien Sart, Ang-Chen Tsai, Yan Li, and Teng Ma. Three-Dimensional Aggregates of Mesenchymal Stem Cells: Cellular Mechanisms, Biological Properties, and Applications. *Tissue engineering. Part B, Reviews*, 20(5):1–46, 2013.

[104] Joni H. Ylöstalo, Thomas J. Bartosh, Katie Coble, and Darwin J. Prockop. Human mesenchymal stem/stromal cells cultured as spheroids are self-activated to produce prostaglandin E2 that directs stimulated macrophages into an anti-inflammatory phenotype. *Stem Cells*, 30(10):2283–2296, 2012.

[105] Thomas J. Bartosh, Joni H. Ylöstalo, Nikolay Bazhanov, Jessica Kuhlman, and Darwin J. Prockop. Dynamic compaction of human mesenchymal stem/precursor cells into spheres self-activates caspase-dependent il1 signaling to enhance secretion of

modulators of inflammation and immunity (PGE2, TSG6, and STC1). *Stem Cells*, 31(11):2443–2456, 2013.

[106] Faris Q Alenzi, Mahmoud Lotfy, and Richard Wyse. Swords of cell death: caspase activation and regulation. *Asian Pacific journal of cancer prevention : APJCP*, 11(2):271–80, 2010.

[107] a G Porter and R U Jänicke. Emerging roles of caspase-3 in apoptosis. *Cell death and differentiation*, 6(2):99–104, 1999.

[108] Hui Cen, Fei Mao, Ida Aronchik, Rholinelle Joy Fuentes, and Gary L Firestone. DEVD-NucView488: a novel class of enzyme substrates for real-time detection of caspase-3 activity in live cells. *The FASEB journal : official publication of the Federation of American Societies for Experimental Biology*, 22(7):2243–2252, 2008.

[109] Jonathan Tullis, Chong Lak Park, and Paul Abbyad. Selective Fusion of Anchored Droplets via Changes in Surfactant Concentration. *Lab on a Chip*, 14(17):3285–3289, 2014.

[110] Biddut Bhattacharjee and Siva a. Vanapalli. Electrocoalescence based serial dilution of microfluidic droplets. *Biomicrofluidics*, 8(4):044111, jul 2014.

[111] Muhsincan Sesen, Tuncay Alan, and Adrian Neild. Microfluidic on-demand droplet merging using surface acoustic waves. *Lab on a chip*, 14(17):3325–3333, jun 2014.

[112] Nicolas Bremond, Abdou R. Thiam, and Jérôme Bibette. Decompressing emulsion droplets favors coalescence. *Physical Review Letters*, 100(2):1–4, 2008.

[113] Ilke Akartuna, Donald M. Aubrecht, Thomas E. Kodger, and David a. Weitz. Chemically induced coalescence in droplet-based microfluidics. *Lab Chip*, 15(4):1140–1144, dec 2014.

[114] Etienne Fradet, Paul Abbyad, Marten H Vos, and Charles N Baroud. Parallel measurements of reaction kinetics using ultralow-volumes. *Lab on a chip*, 13(22):4326–30, oct 2013.

[115] Richard A. Brualdi. *Inroductory Combinatorics - Fifth Edition*. 2010.

[116] Linas Mazutis and Andrew D Griffiths. Selective droplet coalescence using microfluidic systems. *Lab on a chip*, 12(10):1800–6, apr 2012.

[117] Max Chabert, Kevin D. Dorfman, and Jean Louis Viovy. Droplet fusion by alternating current (AC) field electrocoalescence in microchannels. *Electrophoresis*, 26(19):3706–3715, 2005.

[118] Adam R Abate, Tony Hung, Pascaline Mary, Jeremy J Agresti, and David a Weitz. High-throughput injection with microfluidics using picoinjectors. *Proceedings of the National Academy of Sciences of the United States of America*, 107(45):19163–19166, 2010.

[119] Ashleigh B. Theberge, Estelle Mayot, Abdeslam El Harrak, Felix Kleinschmidt, Wilhelm T. S. Huck, and Andrew D. Griffiths. Microfluidic platform for combinatorial synthesis in picolitre droplets. *Lab on a Chip*, 12(7):1320, 2012.

[120] J Lance, Bo Zheng, L Spencer Roach, and Rustem F Ismagilov. Screening of Protein Crystallization Conditions on a Microfluidic Chip Using Nanoliter-Size Droplets. *Journal of the American Chemical Society*, 125(37):11170–11171, 2003.

[121] Matthias Thiele, Joanne Zi En Soh, Andrea Knauer, Daniell Malsch, Ondrej Stranik, Robert Müller, Andrea Csáki, Thomas Henkel, J. Michael Köhler, and Wolfgang Fritzsche. Gold nanocubes - Direct comparison of synthesis approaches reveals the need for a microfluidic synthesis setup for a high reproducibility. *Chemical Engineering Journal*, 288:432–440, 2016.

[122] Jialan Cao, Dana Kürsten, Steffen Schneider, Andrea Knauer, P Mike Günther, and J Michael Köhler. Uncovering toxicological complexity by multi-dimensional screenings in microsegmented flow: modulation of antibiotic interference by nanoparticles. *Lab on a Chip*, 12(3):474, 2012.

[123] Amy Y. Hsiao, Yi Chung Tung, Xianggui Qu, Lalit R. Patel, Kenneth J. Pienta, and Shuichi Takayama. 384 hanging drop arrays give excellent Z-factors and allow versatile formation of co-culture spheroids. *Biotechnology and Bioengineering*, 109(5):1293–1304, 2012.

[124] Malcom S. Steinberg. Reconstitution of tissues by dissociated cells. *Science*, 141(3579):401–408, 1963.

[125] Steve Pawlizak, Anatol W. Fritsch, Steffen Grosser, Dave Ahrens, Tobias Thalheim, Stefanie Riedel, Tobias R. Kie??ling, Linda Oswald, Mareike Zink, M. Lisa Manning, and Josef A. K??s. Testing the differential adhesion hypothesis across the epithelial-mesenchymal transition. *New Journal of Physics*, 17(8):83049, 2015.

[126] Yuya Morimoto, Risa Tanaka, and Shoji Takeuchi. Construction of 3D, layered skin, microsized tissues by using cell beads for cellular function analysis. *Advanced healthcare materials*, 2(2):261–265, feb 2013.

[127] A Ranga, S Gobaa, Y Okawa, K Mosiewicz, A Negro, and M P Lutolf. 3D niche microarrays for systems-level analyses of cell fate. *Nature communications*, 5:4324, jan 2014.

[128] Bruce S Edwards and Larry A Sklar. Flow Cytometry: Impact on Early Drug Discovery. *Journal of biomolecular screening*, 20(6):689–707, 2015.

[129] Carsten Wenzel, Björn Riefke, Stephan Gründemann, Alice Krebs, Sven Christian, Florian Prinz, Marc Osterland, Sven Golfier, Sebastian Räse, Nariman Ansari, Milan Esner, Marc Bickle, Francesco Pampaloni, Christian Mattheyer, Ernst H. Stelzer, Karsten Parczyk, Stefan Prechtl, and Patrick Steigemann. 3D high-content screening for the identification of compounds that target cells in dormant tumor spheroid regions. *Experimental Cell Research*, 323(1):131–143, 2014.

[130] Oksana Sirenko, Trisha Mitlo, Jayne Hesley, Steve Luke, Windsor Owens, and Evan F. Cromwell. High-Content Assays for Characterizing the Viability and Morphology of 3D Cancer Spheroid Cultures. *ASSAY and Drug Development Technologies*, 13(7):402–414, 2015.

[131] Eric W. Esch, Anthony Bahinski, and Dongeun Huh. Organs-on-chips at the frontiers of drug discovery. *Nature Reviews Drug Discovery*, (March):1–13, 2015.

[132] Anette Funfak, Regina Hartung, Jialan Cao, Karin Martin, Karl Heinz Wiesmüller, Otto S. Wolfbeis, and J. Michael Köhler. Highly resolved dose-response functions for drug-modulated bacteria cultivation obtained by fluorometric and photometric flow-through sensing in microsegmented flow. *Sensors and Actuators, B: Chemical*, 142(1):66–72, 2009.

[133] Tomasz S Kaminski, Slawomir Jakiela, Magdalena a Czekalska, Witold Postek, and Piotr Garstecki. Automated generation of libraries of nL droplets. *Lab on a chip*, 12(20):3995–4002, 2012.

[134] Paul Abbyad, Pierre-Louis Tharaux, Jean-Louis Martin, Charles N Baroud, and Antigoni Alexandrou. Sickling of red blood cells through rapid oxygen exchange in microfluidic drops. *Lab on a chip*, 10(19):2505–12, oct 2010.

université PARIS-SACLAY
ÉCOLE DOCTORALE
INTERFACES
Approches Interdisciplinaires : Fondements, Applications et Innovation

Titre : Cytométrie multi-échelle de cultures cellulaires 3D dans des tableaux de billes de gel microfluidiques

Mots clefs : Microfluidique, culture cellulaire 3D, gouttes d'hydrogel, analyse d'images haut-débit, hépatocytes, cellules souches mésenchymales

Résumé : Les conditions du corps humain ne sont pas reproduites fidèlement par la culture cellulaire traditionnelle en 2D. Dans cette thèse, des cultures cellulaires 3D sont réalisées dans une plateforme microfluidique hautement intégrée. Des cellules mammifères adhérentes sont encapsulées dans des gouttes immobilisées dans un tableau de pièges capillaires à haute densité. Dans chaque goutte, les cellules se réorganisent pour former un unique microtissu 3D et fonctionnel appelé sphéroïde. L'utilisation d'un hydrogel permet d'allonger le temps de culture et de perfuser le tableau avec des solutions aqueuses, par exemple pour de l'immuno-cyto-chimie. Un unique sphéroïde, viable, peut aussi être extrait de cette puce microfluidique. Des données quantitatives sont extraites à haut débit au niveau de la population, du sphéroïde (dizaines de miliers de sphéroïdes) et au niveau cellulaire *in situ* (centaines de miliers de cellules) grâce à de l'imagerie de fluorescence et au dévelopement d'un code d'analyse d'image. Une première preuve de concept a été obtenue en démontrant la viabilité, la prolifération et la fonctionalité de sphéroïdes d'hépatocytes et en les corrélant à des paramètres morphologiques. Ensuite, des aggrégats de cellules souches mésenchymales ont été produits et les hétérogénéités spatiales dans l'expression de protéines impliquées dans leurs propriétés thérapeutiques ont été étudiées. Enfin, cette technologie a été encore dévelopée pour permettre d'appliquer des conditions biochimiques différentes dans chaque goutte. La production et la culture de sphéroïdes dans cette plateforme microfluidique peut mener à des dévelopements importants dans beaucoup de domaines tels que l'analyse de la toxicité des médicaments, le criblage de médicaments à haut débit, le traitement personnalisé du cancer, l'ingénierie tissulaire ou la modélisation de maladies.

Title : Multiscale cytometry of 3D cell cultures in microfluidic hydrogel droplet arrays

Keywords : Microfluidics, 3D cell culture, hydrogel droplets, high-throughput image analysis, hepatocytres, mesenchymal stem cells

Abstract : Conventional 2D cell culture fails to reproduce *in vivo* conditions. In this PhD thesis, 3D cell culture is implemented into a highly integrated microfluidic platform. Adherent mammalian cells are encapsulated in droplets immobilized on a high density array of capillary traps called anchors. In each droplet, the cells reorganize into a single functional 3D microtissue called spheroid. The use of an hydrogel allows to extend the culturing time in microdroplets and to perfuse the array with aqueous solutions, for instance for immuno-cyto-chemistry. A single and viable spheroid can also be selectively retrieved from the microfluidic chip. High throughput and quantitative data is extracted at the population, spheroid (tens of thousands of spheroids) and cellular level *in situ* (hundreds of thousands of cells) thanks to fluorescent imaging and a custom image analysis software. As a first proof of concept, the viability, proliferation and functionality of hepatocyte spheroids were demonstrated and correlated with morphological parameters. Drug toxicity experiments were also performed on this liver model. Then, human mesenchymal stem cell aggregates were produced and the spatial heterogeneities of the expression of proteins involved in their therapeutic properties were investigated. Finally, this technology was further developed to enable applying different biochemical conditions in each droplet. The production and culture of spheroids in this microfluidic platform could lead to major advances in many fields such as drug toxicity, high throughput drug screening, personalized cancer treatment, tissue engineering or disease modeling.

Université Paris-Saclay
Espace Technologique / Immeuble Discovery
Route de l'Orme aux Merisiers RD 128 / 91190 Saint-Aubin, France